Cool Wolf-Rayet Central Stars and their Planetary Nebulae

A Thesis submitted for the Degree

of

Doctor of Philosophy of the University of London

by

Orsola De Marco

Department of Physics & Astronomy

University College London

University of London

September 1997

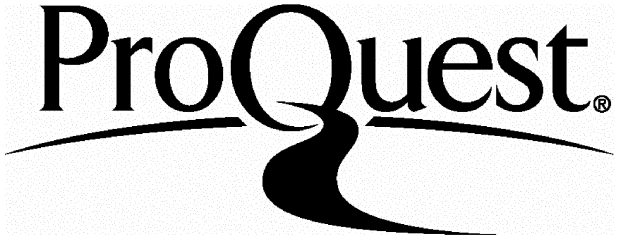

To Chikky Wikky

Acknowledgement

My first, hugest 'thank–you' goes to my supervisors Mike Barlow and Pete Storey for the patience, the help and ... the patience. In the same breath I also have to thank Paul Crowther for showing me quite a few things about Astronomy and Astronomers. For Serena Viti, my Ph.D. sister, I have almost no words: pointy–tit Venusia with pint–over–head on orgasmitronic–bike lost in the middle of the night in Kentish Town, is only the outer skin of the immense joy of having met her. All my love and thanks to Mattieu, the Strou–dog, Chrissy and Herdy Gerdy for the parties on balcony, at Chrissy's, in A25, Housman Room, dinner, Housman Room, dinner, cinema, Housman Room, dinner, Paris, ... ultimately for all the 'togetherness'. A brontoflop of gratitude to John Deacon for all the wee tapes, the convolution thinghy–me–jig and the technical support and to Martin Clayton for the IRAF fun hours. My collaborators Geoff Clayton, George Jacoby, Robin Kingsburgh and Martin Cohen are thanked to make me discover the world beyond Mike and Pete, and especially Geoff for lots of support during the groundhog days. Muchas gracias to Martin Guerrero for the PN fun book, and the images of M 4–18 and to Wolf–Rainer Hamann for lending me his spectra. Many thanks to Simon Jeffery for the CCP7 Cray hours and to Tony Lynas-Grey for the confidence boosters and all the drinks. Thanks to Nick Achilleos for the integrals and the MHD lectures and to John McManus for opening my office every time I forgot my keys! Finally, my eternal gratitude goes to Bob Wilson for backing my Perren Fund application. Last I would like to thank my mothers Carla Colavolpe and Marcella Massironi and fathers Gualtiero De Marco and Giancarlo Viaro for the endless support, love and encouragement though the London years.

Abstract

The research presented in this thesis is concerned with the properties of Wolf–Rayet central stars and their planetary nebulae (PN).

Radial and nebular expansion velocities, reddenings and distances have been derived using different methods. A detailed analysis of the nebular physical parameters and abundances has been carried out for the PN of four cool Wolf–Rayet central stars, based on high resolution optical and UV spectroscopy. For the same sample, HST and ground–based images are presented. Photoionization modelling of the PN is undertaken using different model stellar atmospheres and a comparison with empirically derived parameters is carried out.

Non–LTE Wolf–Rayet stellar atmosphere modelling is described to the winds of two central stars with WC10 spectra. From this, stellar parameters are derived which are compared with estimates from independent model codes.

The theory of low–temperature dielectronic recombination is applied and a method for the direct determination of the wind electron temperature is developed and applied to one WC11 and four WC10 central stars. Direct analysis of the stellar emission line spectrum of three of the four WC10 central stars is carried out using recombination line theory. A comparison is made between abundances derived using the non–LTE models and from recombination line analysis. Parameters derived from the non–LTE Wolf–Rayet models are used in an investigation of optical depth effects in the wind recombination lines. From this it is shown, for the first time, that low–lying lines usually considered to be optically thick and hence unsuitable for abundance determination, can be employed without substantial systematic effects. On the other hand, lines arising from dielectronic states are found to yield systematically lower abundances due to their being in LTE with the continuum.

A classification system for Wolf–Rayet central stars is also developed, consistent with the classification of massive Wolf–Rayet stars.

Contents

List of Tables

List of Figures

Chapter 1

Introduction

This thesis is devoted to the study of the physics and evolution of Wolf–Rayet central stars of planetary nebulae (WR CSPN). WR CSPN form a subgroup of all CSPN (about 10–15%) which, with little or no hydrogen in their atmospheres, are mainly composed of helium, carbon and oxygen and possess fast, dense and extended stellar winds. Their spectra can mimic to perfection the spectra of massive ($\sim 50 M_\odot$) Pop. I WR stars of the carbon sequence (WC), despite having a completely different evolutionary history.

Approximately once every year a new star of mass $\geq 1 M_\odot$ is born in our Galaxy. Ninety nine times out of a hundred, this star is less massive than $\sim 10 M_\odot$ and, if it is a single star or in a wide binary, it will become a central star of planetary nebula in its old age (Iben and Renzini 1983). Because of their number and the amount of gas they eject, central stars of planetary nebulae are responsible for the enrichment of the interstellar medium (ISM) and the chemical evolution of galaxies. The nebulae they release at the very end of their lives (called planetary nebulae or PN) are tools in the study of the Distance Scale and stellar populations in other galaxies. Therefore the understanding of physical processes in planetary nebulae and their central stars is functional not only to understanding their evolution, but is also basic in a wider astrophysical sense. Moreover H–deficient central stars can be fitted into the general context of the little understood phenomenon of hydrogen deficiency in the atmospheres of a diverse stellar sample (e.g.

massive WR stars or white dwarfs). Lastly, the energetics of massive WR winds are still under dispute, since the mechanism by which momentum is transfered to the stellar envelope is still largely unknown. The addition of non–massive counterparts to the already studied massive WR stars, provides a further testing 'field' though which constraints can be added in the development of wind driving theories.

In this thesis, I present a detailed study of four cool WR central stars. I followed lines of investigation that span the techniques of spectroscopy (of both stars and nebulae) and imaging and I used different observational and theoretical methods. I think that this multi–sided approach can make connections that are not possible if only one aspect of PN science is tackled, although it allowed me to analyse only a limited sample. Abundance analysis of the PN in my sample was carried out since it is a powerful tool in determining whether a [WC] central star followed or not a similar evolutionary path to other [WC] central stars or indeed to regular H–rich PN central stars.

The relationship between the star and its nebula was also investigated through a combination of stellar wind modelling and PN photoionization modelling: by modelling the stellar wind spectrum one obtains the stellar continuum flux distribution which in turn can be used to model the PN. If the PN model is successful in reproducing observables such as nebular line fluxes, one might feel justified in believing the stellar flux distribution is a more accurate representation to the real stellar flux than the more commonly used blackbody energy distributions. In doing this one has therefore used the PN as a probe for the stellar energy output. On the other hand the stellar modelling has provided us with a more accurate PN model which returns more reliable information as to the physics of the PN itself.

Imaging is useful in complementing a variety of activities: it is essential in determining the inner and outer radii of the ionized region in a PN, which is one of the inputs to the PN modelling. It can also help to explain the shape of nebular lines and therefore to reveal more information as to the velocity structure of the PN. For these reasons images of the studied objects were always keenly sought.

Recombination line analysis of the stellar atmosphere might appear redundant, since models derive elemental abundance ratios while taking into account the radiation transfer as a whole, and hence can be believed to be much more trustworthy. On the other hand it is useful to be able to check on the models in a more direct way. It is also important to be able to know if past recombination line analysis can be trusted or has to be disregarded hence throwing away years of research. Moreover modelling of WR winds is computationally time and money consuming, while recombination line analysis is faster and simpler. I therefore used this method to derive wind abundances for our sample. Following the same philosophy I adopted and further developed a method to determine the wind electron temperature in the wind. This is needed by the recombination line analysis and once again allows us to compare model results with independently determined physical parameters.

My work started as a study of one object (CPD–56°8032). It then was naturally extended to a spectroscopic twin of my first star (He 2–113), for which data were also available. Interest in the stellar class pushed me to apply for more observing time and a third member of the class (M 4–18) was added to the list. The fourth object (SwSt 1) was analysed because of its peculiarities had made it controversial, swinging in and out of the stellar class to which CPD–56°8032, He 2–113 and M 4–18 also belong; for this object high quality spectra were also available and, although it is considerably different from the other three, it would have been a real shame not to tackle it.

In the Sections that follow I will relate some of the background to my work. I will provide some statistics and explain the main advances in the understanding of WR central stars. The principal names in the field will be introduced and the Reader will be guided through the zoo of stars related to WR central stars. The methods and technicalities will be summarised in Chapter 2, so that the Chapters that follow are left free of lengthy explanations. Chapter 3 describes the observations and the data reduction of all the data presented in the course of this thesis. Chapter 4 started as a project in collaboration with P.A. Crowther to classify cool WC stars, although P.A. Crowther later took the lead

in extending it to the hotter WC and WO stars. The Chapter is therefore a result of our combined efforts although I acknowledge P.A. Crowther for about 60% of the overall work. Chapters 5, 6 (in collaboration with P.A. Crowther) and 7 develop a full analysis of CPD–56°8032 and He 2–113. In Chapter 8 the nebular analysis of M 4–18 and SwSt 1 is carried out. I finally draw my conclusions in Chapter 9 and lay the bases for future work. Appendix A shows lightcurves for some of my sample stars briefly discussing the variability properties, in Appendix B I give a brief account of the Quantum Defect method to calculate the energy of transitions that are not observed in the laboratory and finally in Appendices C, D and E I show the spectra on which all the analysis was carried out, complete with line identification.

1.1 Low and Intermediate Mass Stars: from Main Sequence to White Dwarf

All single stars born with masses between 1 and $\sim 10 M_{\odot}$ spend most of their life burning hydrogen in their cores ($\sim 10^{10}$ yr for a $1 M_{\odot}$ star, $\sim 10^{8}$ yr for a $5 M_{\odot}$ star; Bowers 1984). Once hydrogen is exhausted in the centre the star leaves the main sequence, crosses the Hertzsprung Gap (the Hertzsprung–Russell diagram for a $5 M_{\odot}$ star is shown in Fig. 1.1) and ascends the Red Giant Branch (RGB). At the tip of the RGB the star ignites the helium that was the by-product of the hydrogen burning. The ignition happens under degenerate conditions for stars less massive then 2.3 $M_{\odot}$, while for more massive stars the core simply reaches a temperature sufficient for helium burning by the triple–alpha process.

The star then burns helium in its core producing carbon and oxygen. When helium becomes exhausted in the core, it keeps burning in a shell source. The star has at this stage an onion–like structure, with a carbon–oxygen degenerate core, which is not burning, a helium shell source and a hydrogen shell source. These layers are protected by a large hydrogen–rich envelope into which the products of previous nucleosynthesis have been

mixed by the first and/or second dredge–ups (Becker and Iben 1979; Iben and Renzini 1983).

The star is at this stage near the base of the Asymptotic Giant Branch (AGB; L∼10-2000$L_{\odot}$, T_{eff}∼4000K). As the helium shell source dumps its ashes onto the helium–exhausted core, its mass increases (Paczynski 1971) causing an increase in luminosity at virtually constant temperature. The stellar radius simultaneously expands and the star acquires a giant structure for the second time.

Near the tip of the AGB, the star experiences a series of thermal pulses (thermally pulsating AGB or TPAGB) due to the helium shell undergoing sudden thermonuclear runaway episodes. The number and frequency of these episodes depends on the mass of the star, although it is not clear exactly what relationship ties these quantities (Iben 1975). Nor is it clear just how much mass is lost during the AGB (Reimers 1975, see also Iben and Rood 1970, while for an observational counterpart see, e.g., Knapp et al. 1982).

All studies of AGB stars are limited by the copious amounts of dust that is produced by these fairly cool objects, so that we can only take educated guesses at how much mass is lost during the AGB, based on the properties of the surrounding dust, knowledge of which is in itself pretty scarce. The TPAGB is responsible for the 'production' of central stars: it is thought that the heavy mass loss during the TPAGB diminishes the hydrogen burning rate causing the giant star to be unable to maintain its large structure (Shklovski 1956; Paczynski 1971; Kwok 1981). As a consequence the energy balance dictates a slow expansion of the envelope to infinity and the PN is ejected. The phase in the thermal pulsation cycle at which this slow ejection occurs determines the type of central star that will emerge from the AGB and is possibly the cause for the differentiation of H–rich and H–deficient CSPN.

In order to describe the different phases between two successive pulses, Iben (1984, 1995) introduced the parameter $\phi=\delta M_H/\Delta M_H$, where ΔM_H is the mass of the matter though which the hydrogen shell burns between pulses and where δM_H is the mass of the helium buffer layer when departure from the AGB happens, which is 0 at the first

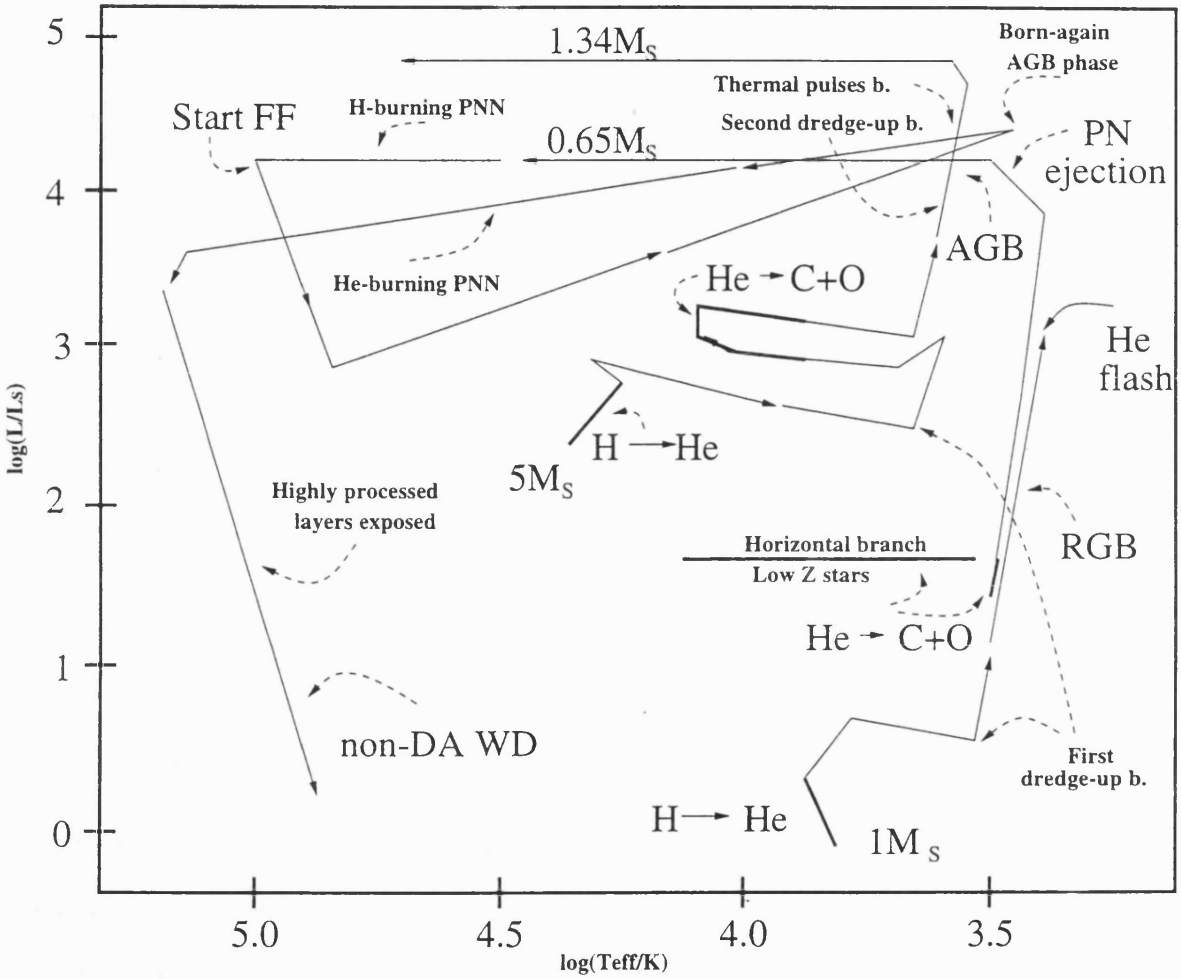

Figure 1.1: Evolutionary tracks for a 1 and a 5 $M_\odot$ stars plotted on the log(T_{eff})–log(L) plane (reproduced from Iben 1984, 1985). The thick segments mark the section of the tracks where nuclear burning is taking place. A 'b.' means 'begins'. The subscript 'S' substitutes the symbol $\odot$. 'PNN' stands for 'Planetary Nebula Nucleus', while 'FF' stands for 'Final Flash'. The CSPN of 1.34 $M_\odot$ might continue to become a white dwarf or might undergo a FF event. For the 0.65 $M_\odot$ CSPN I have traced the *born-again* evolution although not all remants of that mass will become *born-again* (see text)

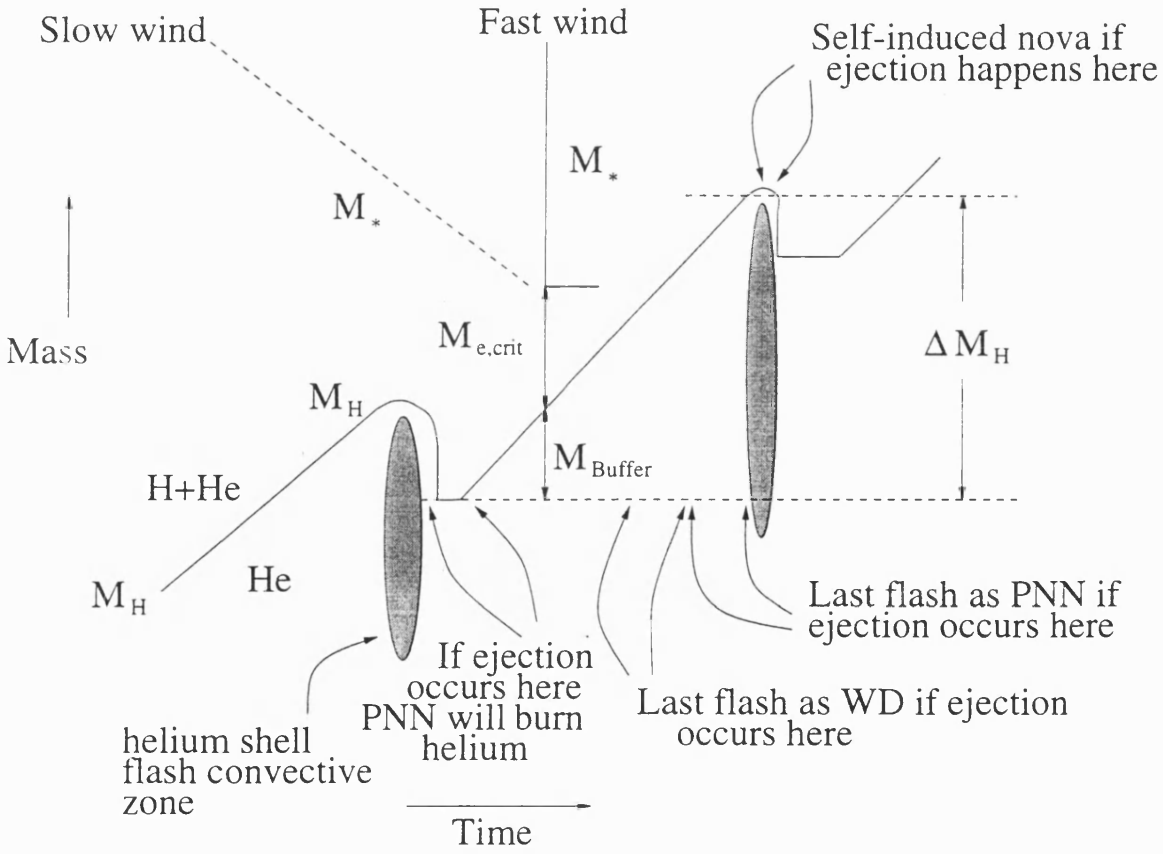

Figure 1.2: Consequence of AGB termination as a function of where in thermal pulse cycle the mass of the H-rich envelope reaches the critical value $M_{e,crit}$; from Iben 1995

pulse and 1 at the next. If departure from the AGB happens $0<\phi<0.75$ (case A in Iben 1995, or case I in Iben 1984), the central star remnant continues to burn hydrogen and evolves to the blue in consequence of a decreasing envelope mass (M_e) . If M_e decreases below a critical value $M_{e,crit}$, hydrogen burning ceases. The star then evolves along a track of constant radius becoming a DA White Dwarf (WD), i.e. a WD with He/H$<10^{-4}$ by number.

If departure from the AGB happens during the quiescent helium burning (after the luminosity spike induced by the thermal pulse – case B or cases V and VI), that star continues to burn helium. If when helium stops burning, the mass of the hydrogen shell above the helium shell is greater than $M_{e,crit}$, hydrogen re–ignites. There is the further possibility that all the hydrogen rich layers are lost ($M_{e,crit}\sim0$), in which case the products of helium nucleosynthesis are exposed (such layers should be characterised by number abundance ratios of C/He=0.06, N/He=0.11 ^{22}Ne/He=0.0005 and O/C=0.04–0.12; Iben 1995). A special case of this (case C or IV) is when departure happens at the pulse, bypassing the third dredge-up that follows. In either case the central star evolves into a WD where carbon diffuses outward and hydrogen inward thus meeting in the helium buffer layer. If this layer is small enough that carbon and hydrogen mix the star experiences a hydrogen runaway becoming a self–induced nova.

If the star departs from the AGB late during the last phase of quiescent hydrogen burning ($0.85<\phi<1.0$ – case D or III), when the helium buffer layer has had time to grow, but has not quite had time to reach the critical mass to undergo a flash, the central star will burn hydrogen, thus adding helium to the buffer layer. This causes this layer to increase in mass and pass the threshold for the flash, which therefore happens when that star has already started its journey on the horizontal PN track. The star then returns to the top of the AGB with a new, *born–again* planetary nebula around it. If no mass were lost at this stage, evolution would proceed as in case B and one anticipates the rebirth of a super–wind which would prevent the re–ignition of hydrogen at the end of the helium burning phase. This second mass loss exposes the helium–nitrogen layer and layers that

have experienced partial helium burning (enriched in carbon and oxygen).

Lastly, when $0.75<\phi<0.85$ (case E or II), hydrogen burning is extinguished before a final flash can happen. However, the loss of power caused by the turning off of burning allows compression of the helium layer due to gravity and helium re–ignites. The large power generated by helium burning is transported out by a convective region which reaches and engulfs the H– rich layer (contrary to what happens in case D, where hydrogen is still burning at the beginning of the flash). The schematic in Fig. 1.2 summarises these five phases.

Observational counterparts to the case E *born–again* scenario are A 30 and A 78 with an inner, H–deficient nebulosity embedded in a larger, low surface brightness and H–rich PN (Hazard et al. 1980, Jacoby and Ford 1983). Both these central stars are H–deficient and have WR/*wel* spectra. Another case, V605 Aql, is known to have experienced a nova outburst around 1919–1921. It has now developed a similar PN configuration to A 30 and A 78. Its central star, which after the outburst resembled an R CrB (see Section 1.3) star, has now a WC spectrum (Bond, Ciardullo and Meakes 1993). Moreover, the [WC4][1] central star of NGC6751 has abundances (calculated by Hamann and Kösterke 1993) which bear some resemblance to the abundance mixes predicted for the *born–again* scenario (Iben et al. 1983). FG Sge is another good *born–again* candidate: it was observed to brighten by ~5 mag between 1900 and 1970 (cf. Herbig and Boyarchuk 1968; Langer, Kraft and Anderson 1974). Today it has a spectrum reminiscent of the R CrB stars, although with a normal hydrogen abundance, it cannot be identified as a *bona fide* R CrB star (Herbig and Boyarchuk 1968; Iben, Tutukov and Yungelson 1996).

There are many other indications of the *born–again* phenomenon in action: Sion, Liebert and Wesemael (1985) and Mendez et al. (1986) have suggested that there is an evolutionary link between [WR] central stars and PG1159 stars (hot pulsating WDs). Indeed some PG1159 stars show similarities in the abundances (e.g. Werner, Heber and

[1] the [] notation was introduced by van der Hucht et al. (1981) to distinguish WR central stars from Pop. I WR stars

Hunger 1991). Moreover the similarity in the frequency of the WC-type nuclei and DB WD stars suggests it as an evolutionary possibility (Monk, Barlow and Clegg 1988).

In conclusion, there is a strong suggestion that WR central stars are associated with the *born–again* scenario, although amongst the WR central star sample there are many examples whose characteristics cannot be reconciled with the *born–again* scenario, hence leaving the post–AGB evolution as the only choice.

1.2 Wolf–Rayet Stars Big and Small

1.2.1 Massive Wolf–Rayet Stars

Classical Wolf–Rayet stars represent the final stage of the lives of massive (M_i=60-100$M_\odot$) stars, before they end as Type II supernovae. They were discovered at the end of last century by Wolf and Rayet (1867) who noticed bright lines in the spectra of several stars in Cygnus.

Massive WR stars[2] are characterised by hot and dense stellar winds. Their spectra exhibit broad emission lines mainly of helium, nitrogen, carbon and oxygen, sometimes associated with blue–shifted absorptions. No photospheric absorption lines are observed. WR stars are subdivided into two sequences: the WN or nitrogen sequence, whose stars exhibit line of helium, nitrogen and carbon and the WC or carbon sequence, whose members have no nitrogen lines. The classification scheme sorts WN and WC stars in order of increasing ionization. On Table 1.1 I reproduce the subdivision of the WC group since, as we will see later, only the members of this group bear resemblance to the spectra of WR CSPN.

Typically Pop I WC stars have wind speeds ranging between 1300 and 3200 km s^{-1}, mass loss rates between 1.5 to 12 $\times$ 10^{-5} $M_\odot$/yr, luminosities between 50 000 and 300 000 $L_\odot$ and effective temperatures (formally defined by the Stephan–Boltzmann relation at optical

[2]Massive WR stars have come to be called Pop. I as a means of differentiating them from central stars, despite CSPN not necessarily being population II stars. In this thesis I will use many of the names created to distinguish the two groups.

Table 1.1: Massive Wolf–Rayet (WC) optical classification criteria (Conti, Massey and Vreux 1990)

WC types	carbon emission lines	other emission criteria
WC4	C IV(λ5801,12) strong & C III(λ5696) weak or absent	O V(λ5592) moderate
WC5	C III(λ5696) $\ll$ C IV(λ5801,12)	C III(λ5696) $<$ O V(λ5592)
WC6	C III(λ5696) $\ll$ C IV(λ5801,12)	C III(λ5696) $>$ O V(λ5592)
WC7	C III(λ5696) $<$ C IV(λ5801,12)	C III(λ5696) $\gg$ O V(λ5592)
WC8	C III(λ5696) $\approx$ C IV(λ5801,12)	O V(λ5592) weak or absent
WC8.5	C III(λ5696) $>$ C IV(λ5801,12)	C II absent, O V(λ5592) weak or absent
WC9	C III(λ5696) $>$ C IV(λ5801,12)	C II present, O V(λ5592) weak or absent

depth 2/3 – see Section 2.2.3) between 35 000 and 57 000 K (van der Hucht 1996).

1.2.2 WR Central Stars of PN

Already in the late 30's (Beals 1938) it was noticed that some WR star were central stars of planetary nebulae. However the discrimination of whether any WR star was a massive Pop I star or a central star of PN could not be resolved in a clear–cut way, since massive WR stars can also be associated with ring nebulae; in the literature we find repeated references to this dilemma: in 1971 Smith and Aller compared the CSPN BD+30°3639 with the Pop I WR star HD184738, stating that '... there is no *clear* reason for supposing that [BD+30°3639] is not a planetary nebula.' Another example is the dispute over the WN8 star M 1–67, believed to be a central star, but proven to be a massive WR star surrounded by stellar ejecta (Crawford and Barlow 1991). In short there is no *single* discriminatory parameter to discern between the two types of objects observationally and only a complete analysis of all the physical properties can give an indication of whether a particular WR is a massive or a [WR] CSPN.

In fact some differences that have been established between the two groups raise more doubts than answer questions: for instance, if the classical classification scheme for Pop I WR (Smith, Sarah and Moffat 1990) together with the extension to the classification to

cooler subtypes (Tylenda et al. 1993, Chapter 4) is followed, massive WR stars cluster between subtypes WC5 and WC9, while [WR] CSPN cluster in subtypes WC2 to WC5 and WC8 to WC11 (Mendez and Niemela 1982). It is not clear whether some selection effect is at work here, or whether the classification scheme is actually indicating a physical truth.

Leaving for the moment the comparison between massive WR stars and WR CSPN, let us concentrate on the group of central stars with a WR nucleus. It is established that about 15% of all central stars have a WR type nucleus. Another 10% have a hydrogen–deficient spectrum which cannot be strictly classified as WC due to the presence of photospheric absorption lines. Some of these spectra (called by Tylenda et al. (1993) *weak emission line stars*) resemble *Of* spectra, while others are so hybrid as to defy any attempts at classification (Chapter 4). However, due to their similar hydrogen–deficient character *wels* are often included in studies of WR central stars.

When attempts are made at determining characteristics that help in discriminating between the H–rich and H–deficient/WR central star groups, we find ourselves at a loss. In terms of spatial distribution, there seems to be no difference between the H–poor and H–rich groups (Acker, Gorny and Stenholm 1996, Gorny and Stasinska 1995, Pottasch 1996). The expansion velocities of the PN around WR central stars seem to be higher (averaging about 30 km s^{-1}) than those of the *wels* or the H–rich central stars' ($\sim$ 20 km s^{-1}) although there is a very large scatter. Moreover, the hotter WR central stars seem to exhibit higher PN expansion velocities than the cooler ones. This would make sense if the PN velocity developed somewhat as the central star evolved. However it would then remain to be explained why some hot WR central star have low expansion velocity PN. The expansion velocity does not seem to be correlated to the central star luminosity.

On two different occasions Pottasch (1996, 1997) showed amazement at the fact that the abundances of the elements do not show any changes when one analyses PN around H-deficient and H–rich stars. In particular, he finds the fact that PN with WR central stars show an average hydrogen content, in complete disagreement with the H–depleted

nature of the atmosphere of the central star: "The central star apparently knows that it must stop losing large amounts of mass once the hydrogen–rich envelope has been ejected" (Pottasch 1996). However the abundance studies carried out so far show that the estimates are often in disagreement. Differences in the adopted reddenings, electron temperatures and electron densities are the main reasons for discrepant abundances; these in turn rely on sensitive line flux measurements which may change from spectrum to spectrum. In particular, it has been suggested that the use of the Ionization Correction Factors (ICF) to account for unobserved ionizations stages might lead to large discrepancies (Dopita 1997). One of the largely accepted conclusions that the C/H abundance in PN with H–deficient central stars is the same as in PN around H–rich ones, will be reconsidered in this study.

Accurate distances to galactic PN would allow one to discover if WR CSPN have the same luminosities as non–WR CSPN. However distances to galactic PN are not known accurately. A variety of methods (see Sec. 2.2.2) are employed in the literature which use both statistical and individual approaches. So it must be kept in mind that distances have large error bars, and conclusions can be drawn only when these error bars can be taken into account.

In conclusion, there is no clear distinction between WR CSPN and H–rich CSPN apart from the tautological fact that the WR CSPN have a WR spectrum! Indeed the PN around WR stars are similar in all aspects to the PN with *wel* stars and H–rich nuclei: spatial distribution, nebular abundances, surface gravities, temperatures and luminosities. The only difference seems to be a relatively higher nebular expansion velocity and more far–IR emission in some of the WR and *Of*–WR CSPN. This provides very little on which to base a separate evolution for the WR CSPN and does not clarify the nature of the WR phenomenon in the context of low–mass stellar evolution.

1.3 Related Stars: HdC, EHe and R CrB

On the topic of hydrogen–deficient stars two meeting have taken place: the first in Mysore (India) in 1985[3] and the second – in which I took part, in Bamberg (Germany) in 1995[4]. The Bamberg meeting encompassed all the problems still to be tackled in the study of all H–deficient stars. Of particular interest to this thesis are the reviews on H–deficient giants, and of these I chose the one by David Lambert to briefly discuss three classes of stars that might be related to WR central stars.

200 years ago Edward Piggot communicated to the Royal Astronomical Society that a star he was observing in the constellation of the Northern Crown underwent drastic declines in magnitude with a period he reckoned to be of 10.5 months and that he attributed to rotation. Today we know that R Coronae Borealis, the star that Edward Piggot was observing, has continued to exhibit deep declines but that its period is not 10.5 month. In fact, to the best of our knowledge, that star does not have a period. R Coronae Borealis was the first of 32 galactic stars observed to show such behaviour: today we know them as the R CrB stars.

R CrB stars are H–deficient G or F giants (although a few hotter exceptions have been identified). They are characterised by deep (up to 8 magnitudes) declines that are now thought to be due to dust formation in the stellar envelope (Loreta 1934; O'Keefe 1939; Woitke, Goeres and Sedelmayr 1996). As the dust cloud is pushed far from the star by radiative pressure, it obscures the photosphere and induces changes in the observed spectrum. A very good review of R CrB stars is presented by Clayton (1996). However, no matter how much observational material has been accumulated, we still lack a good theory on their origin.

Before I briefly outline the formation scenarios of R CrB stars and why they might be

[3] Hunger K., Schönberner D. and Rao N.K. (editors) 1986, 'Hydrogen–Deficient Stars and Related Objects', IAU Colloquium No. 87, Reidel, Dordrecht.

[4] Jeffery C.S. and Heber U. (editors) 1996, 'Hydrogen Deficient Stars', ASP Conference Series No. 96, ASP, San Francisco.

related to WR central stars, it is important to mention that H–deficient stars are divided into three groups, whose members might or might not be related to WC central stars: the *carbon–normal* group, whose members do not appear to have carbon enrichment, the *carbon–rich* group and the *carbon–strong* groups (Jeffery 1994). The *carbon–rich* comprises R CrB stars (including the hot R CrB stars with temperatures ~20 000 K (e.g. V 348 Sgr, Leuenhagen and Hamann 1994)), H–deficient Carbon stars (HdC), Extreme Helium stars (EHe) and helium sub–dwarfs O^+ (HesdO^+) stars. HdC stars are spectroscopically similar to R CrB stars, but they are not observed to decline (analyses of their properties were carried out by Warner 1967, Schönberner 1975, Cottrell and Lambert 1982, cited in Jeffery 1994), while EHe stars are much hotter (A or B spectral type), with strong He I lines (e.g. HD 124448, Popper 1942). HesdO (Drilling 1983) show strong He II absorption lines. Husfeld et al. (1989) analysed a group of HesdO for which they found indications of high L/M ratios and abundances similar to the EHe stars; this group is referred as the HesdO^+. In a tentative evolutionary chain, HdC stars are seen as precursors of R CrB stars which in turn should evolve into hot R CrB/EHe stars. These then turn into HesdO^+ stars and then into non DA–white dwarfs (Jeffery 1994, Shönberner 1996 and references therein). Finally, the *carbon–strong* group includes WC central stars, O(C) and PG1159 stars. PG1159 stars are pulsating white dwarfs (McGraw et al. 1979) sometimes associated with PN (e.g. NGC 246). O(C) stars are spectroscopically very similar to PG1159 stars (Leuenhagen 1994).

It has been suggested (e.g. Iben 1996; Iben et al. 1996) that the origin of the HdC–R CrB–hot R CrB/EHe evolutionary chain might also originate from a *born–again* type scenario (in the same way as some [WR] central stars – Section 1.1). Alternatively, HdC stars and their progeny might be the product of the merger of two white dwarfs. Both scenarios have theoretical and observational flaws and at the moment there is no clear winner. What is not excluded is that both evolutionary scenarios might be responsible for the formation of H–deficient giants.

The link between R CrB and H–deficient central stars (a topic that is partly tackled

in the course of this thesis) is not only a theoretical possibility, but is also reinforced by observational considerations. To give some examples, the WR (WC10) central star CPD–56°8032 has been observed to decline in brightness (Pollacco et al. 1992, Lawson and Jones 1992, 1996), its V–magnitude lightcurve resembling a typical R CrB lightcurve, despite the smaller depth (one instead of several magnitudes). Not only this, but the well known R CrB–type, EHe star V348 Sgr has a spectrum of the WC type (Leuenhagen, Heber and Jeffery 1994) despite some variations connected to its dust formation cycle. Finally, the central star of A 58, V 605 Aql, developed an R CrB spectrum after a brightening event in the years 1917-1921 (Lundmark 1921), although it now has a WR–type spectrum (Seitter 1987).

1.4 A Special Case: Binary Stars

According to Noam Soker, most if not all central stars are in binaries or even multiple systems where one or more stellar or sub-stellar components orbit the central star proper. In his contribution to the PN meeting that took place in Groningen (Holland) in September 1996. Soker (1997) advocated that 60–70% of all central stars have or did have companions that helped shape the nebula the way we now observe it.

However, since this scenario is not yet generally recognised, we prefer here to give the more conventional explanation of how binaries fit into the story. In fact binary systems have so often been called into the picture in connection to H–deficient giants to warrant a short explanatory section in this thesis. At least half of the stars are born in binaries with a period short enough that they will influence each other's evolution. It is also thought (Yungelson et al. 1993; Iben 1995) that half of all binaries will expel a shell of nebular material as a consequence of matter flowing from the primary, more evolved star, onto the companion at such a rate that the companion will not be able to accommodate it. This matter will then form a hot blanket of material which will engulf both stars to form a 'common envelope,' which will then be driven from the system by energy liberated in a frictional interaction between the common envelope material and the stars orbiting within

it (Garcia–Berro and Iben 1994).

A common envelope might ensue either when the more massive of the two stars stops burning hydrogen at its centre and becomes a giant for the first time (Case B), or when the primary star becomes a giant for the second time (Case C), i.e. when it is ascending the AGB. In either case, the expanding atmosphere of the giant star fills its Roche lobe and starts transferring mass to its companion though the inner Lagrangian point.

Case B events initiated by low–mass primaries will not lead to observable PN unless the mass of the remnant is larger than $\sim 0.4 M_{\odot}$ and unless the final Roche lobe radius after the common envelope event is smaller then $\sim 1 R_{\odot}$. Remnants less massive than 0.3 $M_{\odot}$ achieve surface temperature less than 30 000 K (the temperature necessary to ionise the nebula and make it visible) and if Roche lobe radii are much less then $1 R_{\odot}$, remnants as massive as 0.4 $M_{\odot}$ take more than 10^4 yr to evolve to surface temperatures of more than 30 000 K (Iben and Tutukov 1985, 1986, 1993; Iben and Livio 1993) .

Common envelope events in binary AGB stars may be responsible for the formation of bipolar PN, as the drag forces set up as the ejected wind passes by the companion set up a density contrast between matter along the polar axes and matter on the equatorial plane. However, while about 80% of all PN are bipolar only 13 PN are known to have close binary central stars. Of course it is not excluded that single stars might develop differential wind ejection as a consequence of rotation and/or magnetic fields. This possibility, however, remains to date only a qualitative speculation. There is no evidence that any of the WR central stars has a binary companion, although, as for the H–rich group, about 80% of the WR central stars have bipolar or axisymmetric nebulae.

1.5 PN: Dynamics of Formation

Morphologies of PN have always been thought to hold important clues as to the evolution of the central star. In 1978 Kwok, Purton and FitzGerald developed a key idea in the explanation of how PN morphologies develop: a fast wind from the central star ploughs into gas ejected by the star during its giant phase. This model, known as interactive

stellar wind model (ISW), can also explain the asphericity of most PN on the grounds of an aspherical gas ejection during the giant phase, and modelling codes based on ISW do reproduce most of the observed morphologies in PN. This model has been developed since with the inclusion of time dependency that can take into account a rapidly evolved central star (see for instance Mellema 1997).

The cause of the aspherical giant wind is however still unknown and this constitutes at the moment one of the major challenges. Among the possible explanations are strong magnetic fields during the giant phase, fast rotation or the action of a binary companion. Any of these agents would act to concentrate the wind into a torus–like structure around the star. The subsequent fast wind would then plough into a medium of uniform density and create an asymmetric PN.

A schematic showing the dimensions of the WR central star–PN system can be found in Fig. 1.3.

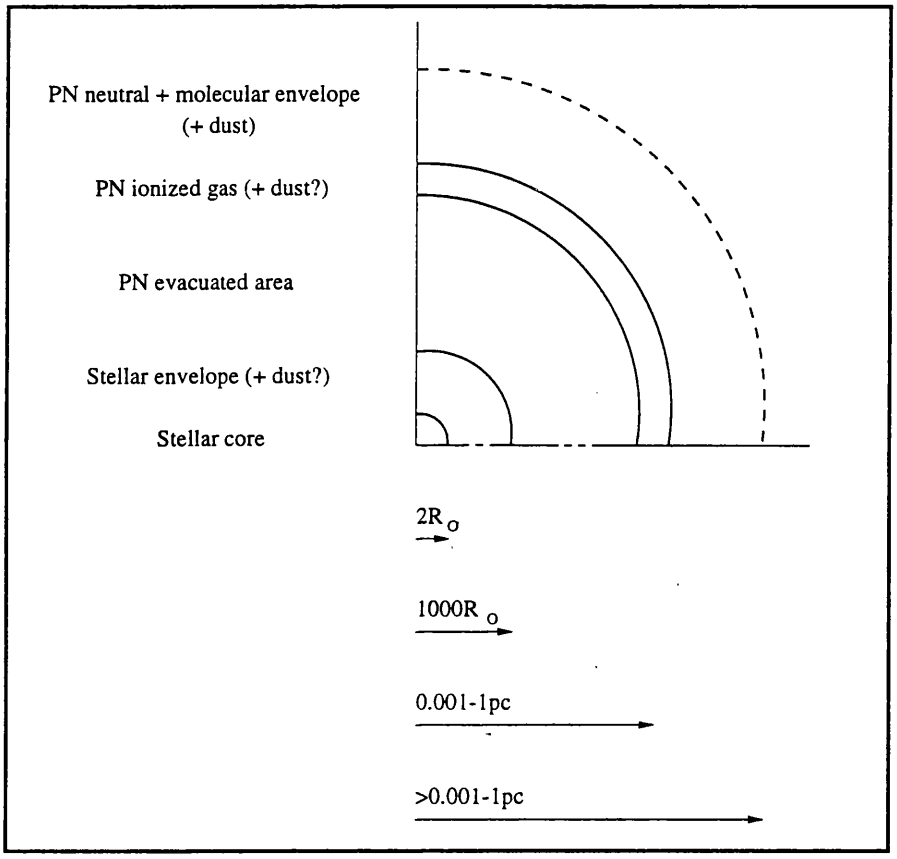

Figure 1.3: Approximate dimensions of the WR central star and its PN. The size of the ionized region in a PN is extremely variable, both due to its radial expansion and to the continuing ionizing of the gas by the evolving central star. The neutral region can extend much further than the ionized region; its size is highly dependent on the amount of mass lost by the star during the AGB.

Chapter 2

Astrophysical Methods and Computational Tools

In this Chapter I will describe the techniques that I have used in the course of this thesis; it is divided into two Sections, dealing with the stellar wind and the nebula.

2.1 Stellar Atmospheres and Winds

By a stellar atmosphere, we mean the fuzzy interface between the stellar interior and the ISM. It can also be considered as a blanket of gas that the photons produced by the stellar furnace have to cross in order to escape. Since the interior of the star is completely opaque to our telescopes (with the exception of particles such as neutrinos which will not interest us here), we can think of stars as solid spheres within which hot plasmas undergo nuclear processes. The power produced as a result of these processes emerges at the surface of the sphere with a black body spectrum characteristic of the star's internal energy.

If the stellar atmosphere consists of only a thin and stationary layer, the emergent blackbody spectrum will have its energy redistributed to longer wavelengths and a series of absorption lines will appear where the atmospheric material absorbed radiation. Surrounding the photosphere, Wolf–Rayet stars have extended, expanding envelopes which we call winds. Many types of stars are known to have winds; amongst these, WR stars

have the most energetic winds known. A WR stellar wind, due to its density and temperature characteristics, reprocesses the emergent flux from the photosphere away from the black–body distribution that it first had when it emerged from the stellar core. The spectral appearance of a WR wind is dominated by emission lines. No absorption lines are visible, apart from the blue–shifted P–Cygni type absorptions (so called because of the prototype star on which these features were first observed). These are not normal photospheric absorptions, but are a result of the expanding gas absorbing the continuum at a wavelength which is blue–shifted in the rest frame of the line.

2.1.1 Stellar Winds: a Direct Approach

Emission lines are very useful in the direct determination of wind abundances and can also give indications of physical conditions in parts of the wind. Abundances derived in this way provide a useful check on the abundances derived from bulk modelling of the stellar atmosphere (e.g. Hillier 1989; Hamann et al. 1992; Section 2.1.2). Moreover, the large amount of computing time needed to construct models spanning a large spectral range makes direct methods all the more appealing. For cool WC stars it is possible to measure a substantial number of unblended lines of all the ions present and hence to derive total abundances by summing the individual ionic contributions.

It is well known that the winds of Wolf–Rayet stars have considerable ionization stratification (e.g. Hillier 1988). However Smith and Hummer (1988) have shown (in their Sect. 7.4) that, even in a stratified wind, the elemental abundances are exactly given by the sum of the individual ionic emission measures, provided that the inner radius down to which line and continuum opacity permits line emission to be observed is the same for each species. This is usually the case for recombination lines observed in similar spectral regions (e.g. the optical), since the depth of the recombination line is normally determined by a slowly varying continuum opacity. Problems arising from line opacity were thought to be significant (e.g. Kingsburgh, Barlow and Storey 1995) for low–lying transitions. We will demonstrate in Chapter 7, that this is not necessarily the case: although line optical

depth still needs considering, its effect on the abundance determination might not be as severe as previously thought. We also assumed that the O II and C II lines originate in similar regions, together with the He I lines.

Since effective recombination coefficients and collisional rates are temperature dependent, the wind electron temperatures needed to calculate the emission measures need to be known. Most studies either fit a blackbody to the stellar continuum to derive the temperature, or simply adopt an electron temperature that is 'appropriate' for the ionization stage of the wind being studied. In the case of WC10 WR central stars it was found (Barlow and Storey 1993) that lines arising from low–temperature dielectronic recombination of $C^{2+}+e^{-}$, could be observed and could be exploited for the direct determination of the wind electron temperature. This method is revised in this thesis (Chapter 7) and applied to 5 cool WC stars. The C^{2+} ion is the dominant ion stage of carbon in the wind of WC10 stars and this method diagnoses the average temperature in the C^{2+} line formation region.

The details of the procedures to determine the wind electron temperature and abundances are described in detail in Chapter 7.

2.1.2 Stellar Winds: the Standard Model

Wolf–Rayet stars have complex atmospheres and no matter how applicable the direct approach is, the only way to determine their structure is to construct a model that can take into account all the processes that take place in the stellar wind and reproduce the spectral appearance of the star.

The challenge of deriving the mathematical relations that explained the way photons propagate in a thick moving medium was first described by Castor, Mihalas and Hummer in the 60's and 70's (e.g. Castor 1970). Within the last ten years the first codes that could synthesize the emergent spectrum from WR stars started to appear, e.g. Hillier (1987) and Wessolowski, Schmutz and Hamann (1988).

In WR atmospheres, among other problems, the assumption of Local Thermodynamic Equilibrium (LTE) breaks down as the level populations are very far from their LTE values.

An extremely anisotropic radiation field is established and a strong temperature gradient arises. Because of the dense wind, the continuum is formed beyond the subsonic region, with the result that the wind is optically thick in the continuum at all wavelengths. Moreover the steep velocity gradient makes it difficult to solve the radiative transfer equation in the observer's frame so that a co–moving frame (CMF) solution has to be adopted.

Below I summarise the basic theory of WR atmospheres, while later I will describe the particular choices that the Hillier code makes. This Section is mostly a synopsis of P.A. Crowther's Ph.D. thesis (1993) introduction.

2.1.2.1 Radiative Transfer and Lambda Iteration

The standard transfer equation for a one dimensional plane parallel static model atmosphere is:

$$\left(\frac{1}{c}\frac{\partial}{\partial t} + \mu\frac{\partial}{\partial z}\right) I(z,\nu,t) = \eta(z,\nu,t) - \chi(z,\nu,t)I(z,\nu,t) \tag{2.1}$$

where z is the direction measured upward towards the external observer, $\mu = cos\ \theta$ (where θ is the angle between the line of sight and the direction of propagation of the radiation), $I(z,\nu,t)$ is the specific intensity, $\eta(z,\nu,t)$ is the emission coefficient (or emissivity) and $\chi(z,\nu,t)$ is the extinction coefficient (or opacity). In the time independent case, the optical depth $\tau(z,\nu)$ and source function $S(z,\nu)$ are defined in the usual manner,

$$d\tau(z,\nu) = -\chi(z,\nu)dz, \tag{2.2}$$

$$S(z,\nu) = \eta(z,\nu)/\chi(z,\nu). \tag{2.3}$$

Substituting Eqs. 2.2 and 2.3 in Eq. 2.1 we obtain:

$$\mu\frac{dI_{\mu\nu}}{d\tau_{\mu\nu}} = I_{\mu\nu} - S_\nu. \tag{2.4}$$

whose formal solution (in the case of complete frequency redistribution and no overlapping continuum) is:

$$I_{\mu\nu} = \Lambda_{\mu\nu}[S] \tag{2.5}$$

or, more usefully,

$$J_\nu = \Lambda_\nu[S], \quad \text{where} \quad J_\nu = \frac{1}{2}\int_{-1}^{1} I_{\mu\nu} d\mu \quad \text{and} \quad \Lambda_\nu = \frac{1}{2}\int_{-1}^{1} \Lambda_{\mu\nu} d\mu, \tag{2.6}$$

or,

$$\bar{J} = \Lambda[S], \quad \text{where} \quad \bar{J} = \int J_\nu \phi_\nu d\nu \quad \text{and} \quad \Lambda = \int \Lambda_\nu \phi_\nu d\nu, \tag{2.7}$$

where J_ν and $\bar{J}$ are the mean and frequency–averaged mean intensities and ϕ_ν is the normalized absorption profile. Since the Λ operator acts on a continuous function of position (source function), it should be represented by an infinite matrix. However for practical purposes we express it as a finite matrix, acting on a vector of source function values at discrete points. We can rewrite Equation 2.6 as,

$$J_d = \sum_{d'}^{D} \Lambda_{dd'} S_{d'}, \tag{2.8}$$

where d is the atmospheric depth index. In the case of a two level atom, from Mihalas (1978) the statistical equilibrium equation, under the above assumptions, can be rewritten as,

$$S = (1 - \epsilon)\bar{J} + \epsilon B, \tag{2.9}$$

where ϵ is the collisional destruction probability and B is the Planck function.

The problem therefore, is one of a coupling between the physical variables. There is a coupling of depth with frequency and angle and in the multi-level case an additional coupling of source functions in different transitions via the statistical equilibrium equation.

Auer and Mihalas (1969) developed a set of equations that, through complete linearization, described the interaction of the photons with the material and how information is transfered from one point in the envelope to the next in the stellar envelope. Their solution is however very memory limited and not practical for computational adaptation.

Substituting Eq. 2.7 into Eq. 2.9 we see that, since Λ is linear, the resulting equation is solvable in one step by matrix inversion. In practice the matrix Λ can be enormous and this solution may be not practical. An alternative method can be found by rewriting the solution equation in 'iterative' form, so that through an appropriate choice of the initial source function one can iterate to the correct solution. This solution however, has the problem that lambda iteration tends to stabilize the iterative process and a small relative correction in the iteration process is no guarantee of convergence.

The next advance in solving the statistical equilibrium equation came with the idea of splitting a linear operation into two parts (Cannon 1973). The Λ operator is split as $\Lambda^* + (\Lambda - \Lambda^*)$, where Λ^* is a suitably chosen operator. If $\Lambda^*=0$ we recover the slow–convergence solution, wile if $\Lambda^* = \Lambda$ we return to the costly matrix inversion. The choice of a viable Λ^* operator is therefore important and far from trivial (methods on the construction of such an operator are found in Scharmer 1981, Olson, Auer and Buchler 1986, or in the review by Rybicki (1991)).

Three groups have tackled the problem for extended atmospheres, and found different practical solution methods. These are, in chronological order, the Kiel group (now Potsdam; Hamann 1985, Hamann and Wessolowski 1990 and Kösterke, Hamann and Kosomol 1992), Hillier (Hillier 1983, 1987a and 1990b) and the Munich group (Puls 1991). Only the code resulting from the efforts of Hillier (who used a tridiagonal solution technique for the transfer problem) will be used in the course of this thesis and will be explained in Section 2.1.3.

2.1.2.2 Extended Spherically Expanding Atmospheres

An extended atmosphere is one where the outer radius is much larger then the stellar core radius. In this way, at any point in the atmosphere the radiation coming from the core subtends a different solid angle.

In such a situation the solution of the transfer equation and of its moments can be noticeably simplified by introducing a spherical grid of points which sample the whole

atmosphere. Boundary conditions are imposed such that at the outer boundary (R) the monochromatic Eddington factor h_ν is:

$$h_\nu = \int_0^1 I(R,\mu,\nu)\mu d\mu / \int_0^1 I(R,\mu,\nu)d\mu, \tag{2.10}$$

while at the inner boundary the 'diffusion approximation' is imposed, i.e.:

$$H_\nu(r_c) = \frac{1}{3}\left(\frac{1}{\chi_\nu}\left|\frac{\partial B_\nu}{\partial r}\right|\right)_{r_c}, \tag{2.11}$$

where $H_\nu(r_c)$ is the monochromatic Eddington flux calculated at the inner boundary, i.e. the surface of the core r_c. Moreover the integral of H_ν over all frequencies at the core boundary must be equal to the integrated flux $L/(16\pi^2 r_c^2)$. r_c has to be sufficiently deep in the atmosphere that the diffusion approximation still holds. A ray–by–ray solution at each frequency along a grid of impact parameters p_i is performed. In this way the variation of the mean intensity as a function of z and p is equivalent to the variation as a function of $\mu = \cos\theta$. Solution of the transfer equation and of its moments along rays parallel to the line of sight and intersecting each radial grid point allows us to obtain the emergent flux.

The lines emergent from an extended, radially expanding atmosphere with a defined photospheric surface receive contributions from material with different velocity and emissivity characteristics. Radiation is received directly (we will assume here that the envelope is completely transparent) from every region of the envelope apart from the region directly behind the stellar disk (bounded by the photosphere; Fig. 2.1).

The matter projected on the stellar disk can either (a) simply emit radiation without significant reabsorption – in which case we would obtain a violet–shifted emission, or (b) absorb the incident photospheric radiation and scatter it out of the line of sight – in which case we would obtain a violet–shifted absorption dip characteristic of P–Cygni profiles. From the matter in the emission lobes to the side of the disk we receive either thermal photons or scattered photons from the stellar and diffuse radiation fields. The velocity field along the line of sight does so that the emission from the lobes produces symmetric line profiles extending from blue side to the red side of the line's rest wavelength.

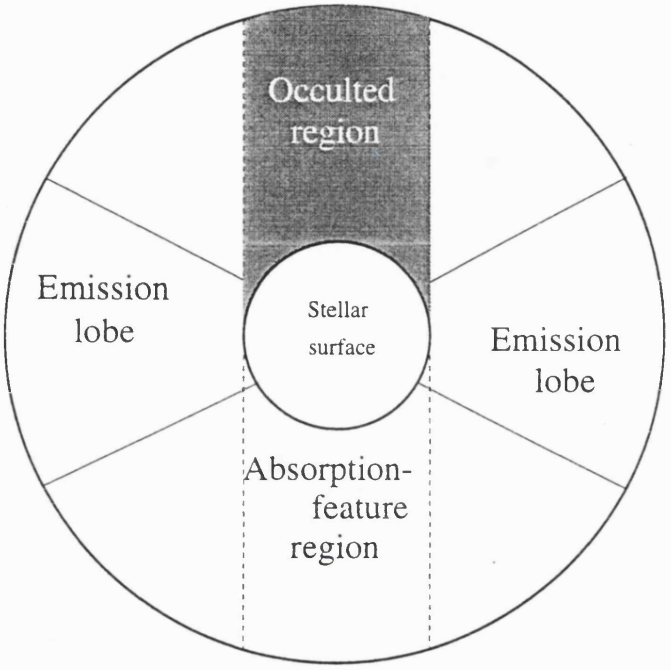

Figure 2.1: Schematic diagram of expanding envelope surrounding a stellar surface. The material in the occulted region is blocked from view by the stellar disk and cannot be seen by an external observer (Figure 14-7 from Mihalas 1978)

Because of occultation we will not observe the material with the highest red–shift, although if the size of the disk is small compared to the envelope, occultation effects can be negligible. The maximum flow velocity can be obtained by measuring the position of the blue edge of the P–Cygni feature (or of the emission feature if no absorption is present)[1]. The emitting volume can be huge compared to that of the star and in some cases the peak of strong emission lines can be several times the continuum level value.

2.1.2.3 The Sobolev Approximation and the Co–Moving Frame

Sobolev (1958, 1960) realised that a steep atmospheric velocity gradient allowed one to simplify the radiation transfer problem. He considered the problem from the point of view of an ion moving outward in the atmosphere at a certain velocity. Only photons coming from ions with small relative velocity would be absorbed by equivalent transitions of the reference ion, since if the relative velocity were too high, photons would be Doppler shifted out of the wavelength bracket within which they can interfere.

This also introduced the idea of the CMF, i.e. a frame of reference that is co–moving with the expanding material. In this way the opacity and emissivity become isotropic and the calculation needs only to be carried out over a frequency interval broad enough to contain the line profile. Within the CMF the transfer equation is solved by means of the Sobolev approximation for which we introduce the escape probability (β) and a probability of penetration (β_c) as follows:

$$\bar{J}(r) = (1-\beta)S(r) + \beta_c I_c(\nu_0), \tag{2.12}$$

where $I_c(\nu_0)$ is the continuum intensity from the stellar disk and

$$\beta = \int_0^1 \frac{1-e^{-\tau(r,\mu)}}{\tau(r,\mu)} d\mu, \tag{2.13}$$

[1]More precisely, one should measure the maximum negative velocity at which all the continuum has been absorbed (V_{black}), but that is not always possible

$$\beta_c = \int_{[1-(R_c/r)^2]^{\frac{1}{2}}}^{1} \frac{1 - e^{-\tau(r,\mu)}}{\tau(r,\mu)} d\mu. \tag{2.14}$$

The local optical depth $\tau(r,\mu)$ is

$$\tau(r,\mu) = \chi_l(r)/(V/r)/(1+\sigma\mu^2), \tag{2.15}$$

where V is the radial velocity at radius r,

$$\chi_l(r) = \frac{\pi e^2}{mc} f_{ij}[N_i - g_i N_j/g_j]/\nu_D, \tag{2.16}$$

$$\sigma = \frac{\partial \ln V}{\partial \ln r} - 1 \quad \text{and} \quad \nu_D = \nu_0/c, \tag{2.17}$$

the other symbols having their usual meaning.

For WR atmospheres, the inner boundary R_c is a function of frequency, so that Hillier (1987a) substituted β_c with β_c', where β_c' takes into account the change in continuum depth with frequency.

2.1.3 The Hillier WR Modelling Code

The model code used in this thesis has been written by D.J. Hillier (1990 – called CMFGEN). It consists of a helium atmosphere with provisions to include, carbon, oxygen, nitrogen and silicon, although any of these elements can be omitted (e.g. we did not make use of nitrogen since it is below detectability in WC stars). Spherical geometry and time independence are assumed, as are particular prescriptions for mass–loss ($\dot{M} = 4\pi r\rho(r)v(r)$), luminosity and velocity law. The code has been extensively used and modified by Crowther (1993) .

The equation of radiative transfer is solved for all lines and at all frequencies, subject to the constraint of radiative and statistical equilibrium. The problem of the coupling of all variables at all grid points in the atmosphere is solved by an Approximate Newton–Raphson operator (Hempe and Schönberg 1986). At every iteration step the new level populations are estimated.

Heavy element line–blanketing is only superficially dealt with, although a recent modification of the code (Hillier and Miller 1997) does include it. The Sobolev approximation,

with a correction for the diffuse radiation field, can be used in the case of specific lines with the advantage of speeding up calculations. However, there might be limitations in the calculation of line profiles (Hamann 1981) and it was not used during the course of this thesis.

•Velocity law.

The velocity law is assumed for WR winds to have the form:

$$v(r) = \frac{v_0 + (v_{\max} - v_0)(1 - R_*/r)^\beta}{1 + (v_0/v_{\rm core})\exp[(R_* - r)/\Delta R]}, \tag{2.18}$$

where R_* is the 'core' radius, v_0 is of order 100 km s^{-1}, $v_{\rm core}$ the core expansion velocity (order of 1 km s^{-1}), $\Delta R_* = 0.01 R_*$ and β is the adopted velocity law. Typically an outer radius of around 200-1000 R_* is used (we used $500 R_*$) depending on the particular model. The use of differing velocity forms requires a trivial modification in the code although due to the particular solution techniques the velocity must monotonically grow with radius.

• Computation of the lines equivalent widths.

Instead of undertaking the lengthy calculation to derive the line's equivalent width (EW) in the observer's frame, Hillier (1990) derived an approximation that deals with the line in the CMF, yielding EWs that differ only 5% from EWs calculated in the correct observer's frame way.

• Using the code.

CMFGEN is currently run in the Cray J90 supercomputer facility at the Rutherford Appleton Laboratory. It consists of 10 000 lines of main program and about 40 000 lines of subroutines and libraries. It reads the atomic data needed for the calculations from a series of parameter files which can be implemented separately. It also reads the model atom from a separate file: in this way the number or atomic levels in each species, the number of depth points etc. can be changed.

Once the model atom is decided the stellar parameters are input by editing the VADAT file. These parameters consist of the stellar radius (which governs the temperature structure), luminosity, mass–loss and abundances of the included atomic species. Additionally

this file sets the convergence and divergence thresholds. Last, the VADAT file contains the 'switches' that control the use of 'lambda' iterations (which have the effect of damping the level populations changes at every iteration – useful for the first few iterations of a new model) and the use of the Sobolev approximation.

It is convenient to start any new model from an existing, previously converged model. To obtain convergence in successive models care must be taken that changes in the VADAT file parameters are not too large. This is of course also dependent on the model atom used. Running a model from a previous model is a budget of resources: a considerable change in one parameter means that other parameters must be kept constant not to overload the program. To run a model in a new parameter space a set of intermediate models have to be run with parameters changing by small amounts from the previous models.

The convergence (or indeed divergence!) of a model is monitored though the file OUTGEN, into which the level population changes at each iterations are written. Convergence is reached when level populations do not vary more than a few percent for a few iterations. The code considers a model divergent if the population changes by about a factor of 10^6 between iterations and it will automatically interrupt execution. When convergence is reached, the set of output files can be transferred to the local machine for computation of the line profiles (for direct comparison with observational data) and for determination of the wind structure. The number of iterations needed to reach convergence is highly dependent on the set of parameters.

The wind structure information (such as electron temperature, electron density and ionization stratification as functions of radius) is extracted by the program DISPGEN (run on a local machine) which reads from the file RVTJ. The approximate equivalent widths are stored in the file EWDATA for comparison with the data. Synthetic profiles are computed by a series of routines. At present this is a very tedious process but a new model code (Hillier and Miller 1997) is already operational that outputs the whole spectrum without having to create the individual profiles.

- **Profile calculation.**

Profiles are first computed in the CMF using Gaussian lines for both emission and absorption parts with widths determined by Doppler broadening, following which the more accurate observer's frame profile is computed using electron scattering information from CMF as input. Output files from the CMF_PRO and OBS_PRO codes are read by the program PLTPRO which outputs ASCII files with the profile information. Electron scattering contributes to the wings of the profiles (e.g. Castor, Smith and van Blerkom 1970) and must be taken into account (the code uses the method of Mihalas, Kunasz and Hummer 1976). The electron scattering is calculated in the CMF using an iterative technique and then transferred to the observer's frame.

• **Atomic data.**

Below I summarize the atomic data used by the the Hillier WR modelling code. I made no alterations and problems with poor atomic data will be emphasised in Chapter 6.

Table 2.1: Adopted collisional rates

Ion	Rate from:
	Collisional excitation rates
Hydrogenic ions	routine by David Hummer (p.c.)[a]
He I[b]	Auer and Mihalas (1973), Mihalas and Stone (1968)
He I forbidden rates (n=2 states)	Berrington, Fon and Kingston (1982)
O II $2p^3$ ^{4}S°, ^{2}D°, ^{2}P°	Mendoza (1983)
O III $2p^2$ ^{3}P, ^{1}D, ^{1}S	Mendoza (1983)
C III $2s^1$S, $2p^3$P°, $2p^1$P°,	Berrington et al. (1985) and Dufton et al. (1978)
C III $2p3p^3$P, $2p^2$ ^{1}D, $2p^2$ ^{1}S	as above
C IV $2s-2p$, $2s-3$, $2p-3$	Cochrane and McWhirter (1983)
Other metals[c]	expression of van Regemorter (1962)
	Collisional ionization rates
Hydrogenic ions	Klein and Castor (1978)
He II ($n \geq 12$)	Hillier (1987a)
Other cases	formula of van Regemorter (1962) and Blaha (1969)

[a] Uses fits from Giovanardi et al. (1987) and Giovanardi and Palla (1989)

[b] Individual treatment for $n \leq 4$; singlets and triplets grouped together for n>4

[c] All metal states treated individually except C IV (and isoelectronic ions) which are grouped by quantum number for $n \geq 5$

• Collisional excitation and ionization rates are summarised in Table 2.1.3:

- Einstein A coefficients are given in terms of the transition oscillator strength f and the B coefficients calculated from the A value (Table 2.2).

Table 2.2: Adopted oscillator strengths

Transition	Oscillator Strength from:
Hydrogenic ions ($j < 20$)	Smith and Glennon (1966)
Hydrogenic ions ($j > 20$)	$f_{ij} = 1.96 g_{ij} (j)^{-3} (i)^{-5} (i^{-2} - j^{-2})^{-3}$ (bound-bound Gaunt factors g_{ij} given by Burgess (1959))
He I ($n \geq 5$)	Green, Rush and Chandler (1957)
He I ($n < 5$)	Opacity Project
Metals (except C III)	Opacity Project
C III	Pete Storey (p.c.; including the effects of core polarization)
Semi-forbidden (e.g. C III] λ1909)	Nussbaumer and Storey (1981, 1982, 1983, 1984)

- The photoionization cross-sections are listed in Table 2.3.

- Low temperature dielectronic recombination (LTDR, Storey 1983) is taken from Nussbaumer and Storey (1983, 1984) for C III and O III-V. High temperature dielectronic recombination (HTDR, Burgess 1965) is not presently incorporated. HTDR does becomes important above ~20 000 K and so will not be expected to contribute strongly to the ionization balance of cool WC central stars whose ions have low ionization potential.

- The **bound–free opacity and emissivity** due to level n have the form

$$\chi_\nu = [N_n - N_n^* \exp(-h\nu/kT)]\alpha(\nu, n) \tag{2.19}$$

$$\eta_\nu^* B_\nu(T) \tag{2.20}$$

where the asterisk indicates the LTE value and $\alpha(\nu, n)$ is the photoionization cross-section. For a hydrogenic ion, the free-free opacity is given by

$$\chi_\nu = 3.69 \times 10^8 Z^2 \nu^{-3} T^{-0.5} g_{\rm ff} N_e N_i [1 - \exp(-h\nu/kT)], \tag{2.21}$$

where cgs units are used and where the value of the free-free Gaunt factor $g_{\rm ff}$ was obtained from a table of Kurucz (1970). The electron scattering opacity is given by

$$\chi_{es} = 6.65 \times 10^{-25} N_e, \tag{2.22}$$

Table 2.3: Adopted photoionization cross-sections

Ion	Cross-section from:
Hydrogenic ions (charge Z)	$\alpha(\nu, n) = 2.815 \times 10^{29} Z^4 g_{bf} n^{-5} \nu^{-3}$ [a]
He I [b] ($n \leq 3$)	Kurucz (1970)
He I ($n = 4$ s and p states)	Ilmas and Nugis (1982)
else	Hydrogenic approximation
Metals	Opacity Project [c]
C III $2s2s$, $2s3l$, $2s4s$	Sakhibullin, Auer and van der Hucht (1982)
$2p^2$, $2p3d$, $2p3p$	Sakhibullin, Auer and van der Hucht (1982)
O II $2p^3$ ^{4}S°, ^{2}D°, ^{2}P°	Henry (1970)
O III $2p^2$ ^{3}P, ^{1}D, ^{1}S, $2p^3$ ^{5}S°	Hidalgo (1968), Henry (1970)

[a] Bound-free Gaunt factors g_{bf} for $n \leq 10$ computed using the formulae of Mihalas (1967) and set to unity otherwise.

[b] Since photoionization of He I is important for heating the stellar wind, recombinations to higher levels were included by treating them as dielectronic recombination to the $2s$, $2p$ states weighted according to Case B recombination theory (Osterbrock 1974).

[c] While cross-sections do not directly influence line strengths, they do affect ionization structure which can affect line strengths! In the case of C IV and isoelectronic ions, cross-sections are relatively simple and so the Opacity Project expressions of Peach, Saraph and Seaton (1988) are used, while for other ions, power law fits of the form given by Seaton (1958) are made to the cross-sections of the lowest states with the hydrogenic approximation adopted otherwise.

and following Mihalas, Kunasz and Hummer (1975)

$$\eta_{es} = 6.65 \times 10^{-25} J_c, \tag{2.23}$$

was adopted, where J_c is the local mean continuum intensity.

2.2 Gaseous Nebulae

Planetary Nebulae, like H II regions, belong to the class of gaseous photoionized nebulae. Gaseous nebulae have an emission line spectrum dominated by the forbidden lines of ions like O III and N II. In addition, the permitted lines of hydrogen are common to most nebulae as well as, but in a much weaker fashion, the recombination lines of He I (He II occurs only in the highest ionization PN and only very rarely in H II regions). A longer exposure spectrum will also reveal the presence of other recombination lines of C II, C III, O II etc.. Gaseous nebulae have a weak continuum spectrum consisting of atomic (chiefly free–bound transitions of the Paschen and Balmer continua) and reflection (but only for H II regions where starlight is scattered by dust) components. In the radio regime PN emit strong radiation associated mainly with Bremsstrahlung emission.

The main source of ionizing radiation for a PN is the UV radiation from a hot (T_*>30 000 K) central star. Photons with E>13.6 eV ionize hydrogen (the most abundant element) and liberate electrons which, by means of collisions with other electrons and ions, maintain a Maxwellian velocity distribution with temperature between 5 000 and 20 000 K. Collisions of electrons and ions excite low–lying levels of the ions. The probability of a downward transitions from these levels is very low, but at the low nebular densities (N_e < 10^4 cm^{-3}) the probability of collisional de–excitation is even lower, so almost every excitation leads to the emission of a photon, cooling the nebula.

Thermal electrons are recaptured by ions and at every point in the nebula the degree of ionization is fixed by a balance of photoionization and capture. The higher the temperature of the central source the higher the ionization of the PN. However a high degree of ionization of the nebula does not necessarily mean a high nebular temperature since this

is determined by the kinetic energy of the electrons and the abundance of coolants. In the recombination processes, recaptures occur to high levels of the ions and the excited levels then decay to lower levels and then ultimately to the ground. In this way line photons are emitted and this is the origin of the H I Balmer and Paschen lines observed in almost all PN. In addition to the line and continuum spectra PN also have an infrared continuum spectrum which derives from thermal radiation of the dust associated with the gas.

2.2.1 Electron Temperatures, Densities and Abundances from Emission Lines

The temperature of a nebula may be determined from ratios of intensities of pairs of emission lines, specifically those emitted by a single ion from two levels with considerably different excitation energies. A few ions, of which [O III] and [N II] are the best known examples, have energy structures that result in emission lines from two different upper levels. The energy diagram for [O III] is shown in Fig. 2.2(a).

From the figure it is clear that the relative rates of excitation of the ^{1}S and ^{1}D states depend on the electron temperature T_e, and so the relative strength of the 5007+4959 Å and 4363 Å lines is a direct measure of electron temperature. Before the method of how this is practically achieved is outlined, a short digression is in order.

The calculation of a relation for the relative emissivities of the lines mentioned above proceeds from the derivation of an expression for the cooling rate by collisionally excited lines, i.e. how much energy is lost by electrons as a result of excitation of ionic states.

For an ion with a single excited level, in the limit of very low electron density, every collisional excitation is followed by the emission of a photon and the cooling rate per unit volume is therefore (Osterbrock 1989):

$$L_C = N_e N_1 q_{12} h\nu_{21} = N_2 A_{21} h\nu_{21}, \tag{2.24}$$

where N_e is the electron density, N_1 is the population of the ground level, q_{12} is the collisional excitation rate, h is the Planck constant, ν_{21} is the transition frequency and

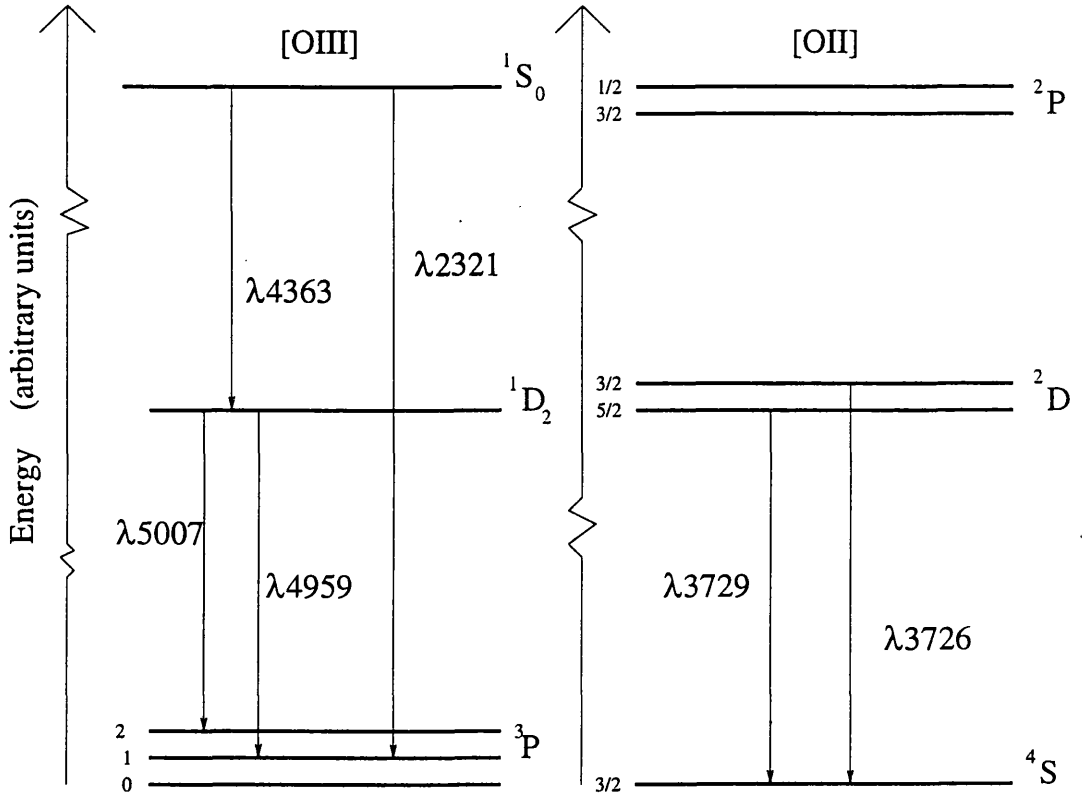

Figure 2.2: Energy level diagram for the lowest terms of [O III](a) and [O II](b) (from Osterbrock 1989, pp. 64 and 132)

A_{21} is the radiative transition probability. The total collisional de–excitation rate per unit volume per unit time is:

$$N_e N_2 q_{21} = N_e N_2 \int_0^\infty v\sigma_{21} f(v) dv = N_e N_2 \frac{8.629 \times 10^{-6}}{T^{1/2}} \frac{\Omega(1,2)}{\omega_2} \tag{2.25}$$

where the integrand is the Maxwellian–averaged collision cross–section (σ_{21}), ω_2 is the statistical weight of the upper level and $\Omega(1,2)$ is the collision strength and is a function of the electron kinetic energy, but is often approximately constant near the ionization threshold.

If the electron density is sufficiently high, the collisional de–excitation is not negligible and the cooling rate is reduced (this has different effects on lines deriving from upper states with different energies). The equilibrium equation for the balance between the excitation and de–excitation rates of the excited levels is in general:

$$N_e N_1 q_{12} = N_e N_2 q_{21} + N_2 A_{21}, \tag{2.26}$$

so that from Eq. 2.24 we obtain:

$$L_C = N_e N_1 q_{12} h\nu_{21} \left[\frac{1}{1 + \frac{N_e q_{21}}{A_{21}}} \right]. \tag{2.27}$$

It can be seen that as $N_e \rightarrow 0$ we recover Eq. 2.24, but as $N_e \rightarrow \infty$,

$$L_C \rightarrow N_1 \frac{\omega_2}{\omega_1} e^{-\chi/kT} A_{21} h\nu_{21} \tag{2.28}$$

the thermodynamic equilibrium cooling rate. Some ions have only two low–lying levels and can be treated by this simple formalism, but most ions have more levels and collisional and radiative transitions can happen between any of the levels. For the O^{++} and N^+ ions, there are 5 levels and the equilibrium equation thus becomes:

$$\sum_{j \neq i} N_j N_e q_{ji} + \sum_{j>i} N_j A_{ji} = \sum_{j \neq i} N_i N_e q_{ij} + \sum_{j<i} N_i A_{ij}, \tag{2.29}$$

which, together with the total number of ions $N = \sum_j N_j$, can be solved for the relative population in each level and then for the collisionally excited population cooling rate

$$L_C = \sum_i N_i \sum_{j<i} A_{ij} h\nu_{ij}. \tag{2.30}$$

In the low–density limit, $N_e \rightarrow 0$, this becomes a sum of terms like Eq. 2.24, but if

$$N_e q_{ij} > \sum_{k<i} A_{ik} \tag{2.31}$$

for any i and j, collisional de–excitation is not negligible and the complete solution must be used. In fact, for any level i, a critical density $N_c(i)$ may be defined as

$$N_c(i) = \sum_{j<i} A_{ij} / \sum_{j \neq i} q_{ij} \tag{2.32}$$

so that for $N_e < N_c(i)$, collisional excitation of level I is negligible but for $N_e > N_c(i)$ it is important.

The average electron density in a nebula can be measured by observing the effects of collisional de–excitation. This can be done by comparing two lines from the same ion with upper levels with similar excitation energies so that the relative excitation rates at the two levels depend only on the ratio of collisional strengths. If the two levels have different radiative transition probabilities or different collisional de–excitation rates, the relative populations of the two levels will depend on the density and the ratio of intensities of the lines they emit will likewise depend on the density. Two good examples are [O II] λ3729/λ3726. and [S II] λ6716/λ6731 (see Fig. 2.2(b) for [O II])

The relative populations of the various levels and the resulting line emission coefficients may be found by setting up the equilibrium equations for the populations of each level as previously described. However direct physical reasoning easily shows what is involved. In the low density limit, the relative excitation rates of the upper levels of, say, [O II] λ3729 and λ3726 are proportional to their statistical weights and the ratio of the two lines is simply 1.5. In the high density limit collisional excitation and de–excitation set up a

Boltzmann population ratio and the relative strength of the two lines are in the ratio of their statistical weights ($j_\lambda 3729/j_\lambda 3726$=0.30). The transition between the high and the low density limits is different for the two upper levels (3×10^3 cm^{-3} for λ3729 and 1.6×10^4 cm^{-3} for λ3726) and thus the ratio is sensitive to density within this regime.

The study of the abundance patterns in PN has helped not only in determining the nucleo–synthetic paths during the stellar previous history, but it can also be used to determine abundance gradients in our and external galaxies and in the study of stellar populations.

Once electron temperature and density are determined, abundances can be found from regular recombination lines or from forbidden lines that have been collisionally excited. This was carried out using the RATIO and EQUIB programs (written by I.D. Howarth and modified by S. Adams). Recombination line theory can be applied in the same way as for stellar winds (cf. Sec. 2.1.1 and Chapter 7). Moreover, while the relative strength of recombination lines are not particularly temperature sensitive, the electron density of the gas must be known quite accurately since the effective recombination rates ($\alpha_{eff}N_eN_p$), do vary quite steeply with it. Of particular interest are hydrogen recombination lines, which, in the optical spectral range, are the Balmer lines. PN abundances are traditionally cited as number ratios of an element with respect to hydrogen. For Hβ the observed (de–reddened) intensity is given by the integral:

$$I_{H\beta} = \frac{1}{4\pi}\int N_pN_eh\nu_{H\beta}\alpha^{eff}_{H\beta}(He^0,T)ds, \qquad (2.33)$$

where N_p and N_e are the proton and electron densities, $\alpha^{eff}_{H\beta}$ is the $H\beta$ effective recombination coefficient and the other quantities have their usual meaning. Less abundant ions have weaker permitted lines, that need large telescopes to be observed. However some of these lines are also exited by resonance–fluorescence and cannot be used to derive abundances in any straightforward way. So for abundance determination for elements other than hydrogen or helium one often has to resort to forbidden lines. For these lines the emissivity depends more strongly on the temperature:

$$I_\nu = \frac{1}{4\pi}\int N_i N_e h\nu q_{1,2}(T) b ds$$

$$= \frac{1}{4\pi}\int N_i N_e h\nu \frac{8.63\times 10^{-6}}{T^{1/2}}\frac{\Omega(1,2)}{\omega_1} b ds, \tag{2.34}$$

in the low–density limit, where b is the fraction of excitation to level 2 that are followed by emission of a photon in the line observed. The programs EQUIB and RATIO were used to compute electron density and abundances from the measured diagnostic line fluxes.

2.2.2 Extinction and Distances

Extinction of stellar (or nebular) light by the intervening medium must be carefully taken into account if we want to know the real flux emerging from the object of interest. Interstellar extinction is expressed in a magnitude scale:

$$m(\lambda_2) - m(\lambda_1) = m_0(\lambda_2) - m_0(\lambda_1) + A(\lambda_2) - A(\lambda_1) \tag{2.35}$$

where m is the observed magnitude at a particular wavelength, m_0 is the magnitude in the absence of extinction and A is the extinction measured in magnitudes. $A(\lambda_2) - A(\lambda_1)$ is called the *differential extinction* and is denoted $E(\lambda_2 - \lambda_1)$. Generally extinction is quoted either as A_v – the extinction at V (λ=550 nm), or as E(B–V) – the differential extinction between B (λ=440 nm) and V. From Eq. 2.35 and the above definition it is simple to derive:

$$2.5\log\left\{\frac{I(B)/I(V)}{F(B)/F(V)}\right\} = E(B-V), \tag{2.36}$$

where F is the observed flux, I is the intrinsic or de-reddened flux and m_0 is the relative magnitude of the star before extinction. However, in order to determine $E(B-V)$ we would have to know the theoretical ratio of fluxes at B and V before extinction, which is not known. A way around it, is to use values of the fluxes in different hydrogen Balmer lines for which theoretical ratios can be determined making certain assumptions and then transform the differential extinction in this baseline to the familiar $E(B-V)$.

Theoretical ratios of Balmer line fluxes are calculated using the Case B hydrogen recombination coefficients of Storey and Hummer (1995), for a nebula with electron density $N_e = 10^4$ cm^{-3} and $T_e = 10^4$ K. From Howarth (1983) we then adopt the following polynomial fits to the optical galactic reddening:

$$X(x) = R + 2.04(x - 1.83) + 0.094(x - 1.83)^2 \quad \text{for } 1.83 \leq x \leq 2.75 \tag{2.37}$$

and

$$X(x) = R + 2.56(x - 1.83) - 0.993(x - 1.83)^2 \quad \text{for } 1.83 \leq x \leq 2.75, \tag{2.38}$$

where $X(x) = A(\lambda)/E(B-V)$, $x = 1/\lambda$ and R is the ratio of total to differential extinction $(A(\lambda)/E(B-V))$ and is taken to be 3.1, a value which is found suitable for most galactic lines of sight.

From Eqs. 2.37 and 2.38 it is straightforward to derive:

$$A_v = 3.1 \times \frac{E(H\beta - H\alpha)}{k\beta - k\alpha}, \tag{2.39}$$

where k is a constant which depends on the Balmer line chosen. Eq. 2.39 can be adapted to any combination of the Balmer lines for which fluxes can be measured. The logarithmic extinction at $H\beta$, $c(H\beta)$, can be derived from Eqs. 2.37 and 2.38 to be $c(H\beta) = 0.4(R + 0.53)E(B-V)$.

Optical extinction laws do not necessarily apply to the UV and IR regions of the spectrum. This is due to the different agents responsible for the extinction of light at different wavelengths. Moreover, what is strictly an interstellar extinction law might not hold once the extinction is due to circumstellar material, which might have a different composition and optical properties from the interstellar material mix. This is why other methods for the determination of the extinction constant have been devised. Amongst them, one can use a technique based on the comparison of radio and $H\beta$ fluxes. The theoretical $H\beta$ flux is calculated using a method given in Milne and Aller (1975) according to the formula:

$$\frac{S(5GHz)}{I(H\beta)} = 3.05 \times 10^{-18} t^{0.4} ln(9900t^{3/2})(1 + y^{+} + 3.7y^{++}), \qquad (2.40)$$

where $S(5GHz)$ is the observed 5 GHz radio flux (in units of W m^{-1} Hz^{-1}), $I(H\beta)$ is the theoretical $H\beta$ flux (in units of ergs cm^{-2} s^{-1}), t is the electron temperature (in units of 10^4 K) and y^{+} and y^{++} are the ratios of singly and doubly ionized helium to singly ionized hydrogen, respectively. The extinction at $H\beta$ can then be derived from

$$c(H\beta) = \log\left(\frac{I(H\beta)}{F(H\beta)}\right), \qquad (2.41)$$

where $F(H\beta)$ is the observed $H\beta$ flux. $c(H\beta)$ can then be converted to $E(B-V)$ using the reddening law of Howarth (1983) as described above.

Distances to galactic PN are *the* problem in PN studies, as almost all parameters depend on distance. For this reason a multitude of methods have been proposed, each with its bag–load of assumptions. In the course of this thesis we did not adopt many of the more conventional methods, since most of them are of a statistical nature and are not appropriate for the treatment of individual objects. Hence the specific distance determinations carried out in this thesis will be discussed in Chapters 5 and 8. Here, some of the most adopted distance methods are summarised.

Right after ejection, PN are optically thick to Lyman continuum photons, but as they expand the density drops until all the envelope is ionized. Once all the envelope is ionized and the mass of ionized hydrogen has become constant the PN becomes optically thin. Eventually, once the stellar ionizing photon flux diminishes, the PN may become again optically thick. Therefore there are two main methods by which to determine the distance to a PN, each dealing with the optically thin and optically thick cases.

The **Vorontsov–Veliamynov method** (optically thick case) verges on the assumption that all optically thick PN have the same magnitude ($\log F(H\beta) = -9.0$) at 1 Kpc (Barlow 1987) . Then the distance is given by:

$$D(\mathrm{kpc}) = \left(\frac{I(H\beta_{thick})}{I(H\beta)}\right)^{1/2}, \tag{2.42}$$

where $I(H\beta)_{thick}$ is 1×10^{-9} ergs cm^{-2} s^{-1} and $I(H\beta)$ is the dereddened $H\beta$ flux. This method is only applicable for intermediate and high excitation PN, i.e. if $(y^{+} + y^{++})$>0.06.

The **Shklovsky method** relies on the assumption that the mass of ionized hydrogen for optically thin PN is constant. The distance is given by:

$$D(\mathrm{kpc}) = 0.160 \left(\frac{\gamma M_H^2 t^{-0.913}}{\epsilon \theta^3 I(H\beta)}\right)^{1/5}, \tag{2.43}$$

where γ is the ratio of electron density to the density of ionized hydrogen, ϵ is the filling factor, M_H is the mass of ionized hydrogen and θ is the angular radius in arcsec. It was shown by Barlow (1987) that for a sample of LMC PN (which have known distances) the mass of ionized hydrogen is in a small enough range for the method to work ($M_H = 0.33 \pm 0.08 M_{\odot}$ for Type I PN and $M_H = 0.189 \pm 0.043 M_{\odot}$ for non–Type I PN).

Finally, it was shown by Minkowski (1965) that the application of either method to an inappropriate PN leads to an overestimation of the distance hence if both methods are applied the smaller of the two values should be adopted.

2.2.3 PN and the Measurement of Stellar Effective Temperatures

Stellar effective temperatures are essential to be able to position CSPN on the HR diagram and thus compare models with observations. However, the concept of effective temperature in the WR wind loses somewhat its meaning: it makes more sense to talk about the electron temperature of the gas at the various depth points in the extended atmosphere, than to try and define an effective temperature as such. HR diagram track models (e.g. Vassiliadis and Wood 1994) follow the time evolution of stars whose outer boundary is defined and that radiate as blackbodies. In order to obtain a quantity that can be compared with the modelled effective temperatures, we must therefore define an outer boundary for our WR stars. To this aim, we define the effective temperature of a WR star, as the temperature in the Stefan–Boltzman relation at a depth in the wind that corresponds to a mean Rosseland

optical depth (τ_{Ross}) of 2/3, i.e. the surface of the star becomes a function of wind density and opacity! Therefore two WR stars at the same evolutionary stage (i.e. with very similar cores), but with different envelopes, would have different effective temperatures. This would then place them at different locations in the HR diagram, biasing the conclusions that can be made. The second problem is that the emergent flux from a WR atmosphere is not blackbody. In Chapter 6 the application of the Zanstra method to WR stars using different stellar model flux distributions will be fully discussed.

Traditionally, the four methods by which stellar effective temperatures are determined are the **Zanstra** method, the **colour temperature** method, the **ionic abundance ratio** and the **energy balance** or **Stoy** method. In the Zanstra method (Zanstra 1931) the ionizing photons from the central star can be counted by measuring the flux in a single nebular hydrogen recombination line (usually $H\beta$) or in the nebular free–free radio continuum. The number of ionizing photons can be interpreted in terms of a temperature if the continuum flux from a central star in a given frequency band is known. The difficulties are that (1) it is only applicable if the PN is optically thick to the ionizing radiation (in all directions) and (2) if the central star is observable.

The colour temperature method measures the shape of the stellar continuum, but measurements are needed from as long a baseline as possible, needing accurate UV fluxes. These are available only for the brightest stars, with errors becoming increasingly more important for hotter stars. The ionic abundance method deduces the shape of the stellar continuum from the ratio of two successive ionization stages in the PN. Many ratios are necessary to accurately define the spectrum to very short wavelengths. A good measurement of the nebular spectrum is thus required and at least a rough modeling of the nebular structure is necessary. In this way the shape of the spectrum below 912 Å is found. The method does not require the measurement of the central star and can be used for optically thick or thin nebulae.

The energy balance method (or Stoy method) shows that the average excess energy per ionising photon can be found from the ratio of the intensity of collisionally excited lines to

$H\beta$. Only the nebular spectrum has to be known, thus it is more suitable to measure the temperature of faint stars then the first two methods. It is applicable to optically thick and thin nebulae, it is independent of the nebular model (although electron temperature and density have to be known). The only drawback is that cooling lines over the entire spectrum must be measured.

In Tab. 2.4 we summarise the main observational techniques which have brought advances in the understanding of the evolution of central stars and their PN.

Table 2.4: Summary of the main uses of observations at different wavelengths

Wavelength	Telescope	Main application
UV	HST,IUE	Detection of the 2200 Å feature for reddening determination. Detection of the 1909 C III] and 2326 C II] lines for C/H nebular abundance determination. Detection of the 1515 C IV line for determination of the V_∞ of the stellar wind.
	HST	Imaging carbon ejecta for *born-again* central stars.
Optical	AAT, WHT, INT	Detection of the Balmer lines for reddening and nebular abundances. Detection of nebular forbidden lines: T_e, N_e and abundances. Nebular imaging (in [O III], [N II], [S II]).
	HST	All of the above, but with much better results!
Near IR	UKIRT	Detection of optically thin stellar wind lines for abundance analysis.
	UKIRT	Imaging of hot dust and molecular envelopes.
Far IR	IRAS, ISO	Detection of spectral dust features.
	IRAS, ISO	Imaging of hot dust and molecular envelopes. Detection of IR fluxes for distance determination by the bolometric luminosity method.
Radio	VLA	Imaging at high resolution of ionized regions. Distances determination by expansion velocity.

2.2.4 Morphology and Classification

Abundances in PN trace both the abundances of the ISM from which the star has formed and the surface abundance of the progenitor AGB star. In all PN progenitor stars, the products of nucleosynthesis have been dredged up to the surface and the ejected nebula is enriched in helium and nitrogen, but some appear to have been particularly enriched in these elements.

Type-I PN were defined by Peimbert and Torres–Peimbert (1983) as having N/O≥5 *and* He/H≥0.125. They are often bipolar showing pronounced filamentary structure. They also show a wide range of ionization stages and are overall believed to have evolved from more massive than average stars with main sequence mass >2.4 $M_{\odot}$ (Peimbert and Serrano 1980) [2], and thus to have formed out of a more enriched ISM.

However, Kingsburgh and Barlow (1994) redefined Type–I PN by one single criterion: "...any galactic PN whose N/O ratio exceeds 0.8 is a Type–I PN". They conclude that such a PN must have undergone envelope–burning conversion to nitrogen of primary carbon raised to the hydrogen envelope by the third dredge–up". Their Type–I criterion does not involve helium for which no increasing trend (in the log(N/O) vs. log(He/H) plane, see their Fig. 4) was observed.

As to the morphology of PN, numerous classification criteria have been devised to try and group different PN and connect different PN shapes with different evolutionary paths. Greig (1972) divided his PN sample into 'binebulous' and circular, showing that the 'binebulous' type exhibited, on average, higher forbidden line strength and a higher distance from the galactic plane (although this was only a small difference). Zuckerman and Aller (1986) classified their sample of 180 PN into bipolar, round, disk–like and annular; they also found an anti-correlation of the abundance of heavy elements with galactic latitude. Balick (1987) divided PN into round, elliptical and butterfly and Icke, Balick and Frank (1992) demonstrated that all three types could be reproduced by the dynamical interaction of AGB and post–AGB (central star) winds. With time and better observations, the morphological schemes became more elaborated, with the introduction of stellar, elliptical, bipolar, point–symmetric and irregular PN by Schwartz Corradi and Melnik (1992) and the further definition of corollary characteristics, such as the presence of single or double–halos (e.g. Stanghellini and Pasquali 1995).

[2] Kingsburgh and Barlow (1994) note that it is interesting that this mass limit roughly corresponds to the point above which helium–burning precedes non–degenerately in the cores of AGB stars (Iben and Renzini 1983).

A thorough morphological scheme is presented in the IAC Morphological Catalogue (Manchado et al. 1996), where the smallest morphological differences have been taken into account. I am not going to list all the classes here, since very few morphological considerations are made in this thesis. Worth mentioning, however, is one particular morphology that seems to be associated with the *born–again* scenario: the IAC Catalogue classifies Abell 78 as an 'Esm', or elliptical with inner structure and multiple shell. PN such as A78 are likely to arise from a *born–again* event (Jacoby and Ford 1983; see Chapter 1), where the second ejection has sent hydrogen–depleted material plunging into the outer, older and hydrogen–rich PN. Other objects with similar morphology are A 30 (Jacoby and Ford 1993) and V 605 Aql (Bond et al. 1993).

From imaging of PN, angular diameters can be derived and, if the distances and expansion velocities are known, one can calculate an expansion age of the nebula. This has been thought to give an idea of the evolutionary timescales since the nebular ejection. However the ejection event is not a simple phenomenon in which the shell is ejected at constant velocity and then coasts out till the time when its surface brightness decreases below detectability. The ejection event might be multiple, the velocity might change in the course of time and, most important, shocks and ionization fronts play an important role in the appearance of the PN. Additionally if the PN is radiation–bounded there is no telling how far the neutral material surrounding the ionized region extends. This is the case for young, low excitation PN, like the ones that are the subject of this thesis.

2.2.5 The Harrington Photoionization Code

Photoionization modelling of PN is the best way to test the internal consistency of empirical derivations. In the Harrington photoionization code, the PN is considered as a hollow spherical shell, sampled by a network of grid points (in a way similar to the WR stellar code, see Section 2.1.2). The program has two segments, the first to calculate the thermal structure and ionic distribution and the second to evaluate the emission line spectrum and other observables. A full description of the computer program is found in Harrington 1967

and 1968, and Harrington et al. 1982. Below I summarise the main characteristics of the code.

If we let N_{ij} denote the number of ions of species i in the j^{th} ionization stage, we can write the equation of ionization equilibrium for adjacent stages as:

$$N_{i,j+1} = \theta_{ij} N_{ij}, \tag{2.44}$$

where

$$\theta_{ij} = \frac{\Phi_{ij} + \beta'_{ij} N(H^+)}{N_e \alpha_{ij} + \beta_{ij} N(H^0)} \tag{2.45}$$

and where

$$\Phi_{ij} = \int_{\nu_{ij}}^{\infty} \frac{4\pi J(\nu)}{h\nu} a_{ij}(\nu) d\nu \tag{2.46}$$

is the photoionization rate per ion (a_{ij} being the photoionization cross–section and ν_{ij} the threshold frequency), N_e is the electron density, α_{ij} is the rate of recombinations (including dielectronic recombination) summed over all levels of the j^{th} ion, β_{ij} is the rate of charge transfer and β'_{ij} the rate of the inverse process.

The quantity λ_{ij} is then defined:

$$\lambda_{ij} = \prod_{n=1}^{j-1} \theta_{in}, \quad \text{for} \quad j \geq 2, \tag{2.47}$$

with $\lambda_{i1} = 1$, from which the explicit expression for N_{ij} can be constructed:

$$N_{ij} = N_H A_i \lambda_{ij} \left(\sum_{n=1}^{M_i} \lambda_{in} \right)^{-1}, \tag{2.48}$$

where $N_H = N(H^0) + N(H^+)$ is the total number density of hydrogen, A_i is the total abundance of element i in ionization stage j relative to hydrogen and M_i is the number of ionization stages considered for element i. The N_{ij} can thus be evaluated for any electron density N_e, temperature T_e and radiation field J(ν). The equation for the electron density is:

$$g(N_e,T) = N_e - \sum_i \sum_{j=2}^{M_i} (j-1)N_{ij} = 0. \tag{2.49}$$

The equation of thermal balance is:

$$f(N_e,T_e) = \sum_i \sum_{j=1}^{M_{i-1}} N_{ij}\Psi_{ij} - \sum_i \sum_{j=2}^{M_i} N_e N_{ij}(\beta_j^{ff} + \beta_{ij}^{fb}) -$$

$$\sum_i \sum_{j=1}^{M_i} N_{ij} \left(\sum_{u=2}^{L_{ij}} P_{ij}(u) \sum_{l=1}^{u-1} A_{ul} h\nu_{ul} \right) = 0, \tag{2.50}$$

where

$$\Psi_{ij} = \int_{\nu_{ij}}^{\infty} \frac{4\pi J(\nu)}{h\nu} a_{ij}(\nu)(h\nu - h\nu_{ij}) d\nu \tag{2.51}$$

is the rate of energy input by photoionization per ion, β_j^{ff} is the free–free energy loss, β_j^{bf} is the energy lost by recombining electrons, and the last term represents the cooling when the low–lying energy levels of the ions are collisionally excited and decay by emission of radiation.

The statistical equilibrium equation is solved for the level populations of each ionic species as determined by radiative de–excitation and collisional excitation and de–excitation. When the total number of levels considered for a particular species is 2 or 3, the explicit solution for the populations is simple enough to be used. This is not the case for ions like O^{2+} and O^{+}, for which more sophisticated solution methods need to be applied.

In the evaluation of the cooling term, all levels of ions within about 10 eV of the ground state are included, along with the n=2 and 3 levels of hydrogen. The equations for the electron density (Eq. 2.49) and the equation of thermal balance (Eq. 2.50) are solved by two–dimensional Newton–Raphson iteration (Harrington 1968).

In the evaluation of Eqs. 2.46 and 2.51, the frequency range is divided into 50 intervals, bounded by the ionization thresholds of the ions considered. The radiation field mean intensity $J(\nu)$ is divided into its attenuated stellar component ($J^S(\nu)$) and diffuse nebular ($J^D(\nu)$) parts. Specific treatment of some components of the diffuse radiation field is

required. For instance the problem of the He^+ Lyα radiation is complex and approximation is necessary (Weyman and Williams 1969; Harrington 1972).

Given the stellar radiation field, the density distribution of the nebula and its chemical composition, an initial model is constructed by a modified on–the–spot approximation. Initially the diffuse radiation field is set to zero at each grid point. Eqs. 2.49 and 2.50 are then solved for N_e, T_e and N_{ij} and the emission coefficients for the diffuse radiation ($4\pi j(\nu)$) are computed. The assumption is then made that some fraction f of the diffuse radiation is absorbed on the spot ($J^D(\nu) = fj(\nu)/k(\nu)$, where $k(\nu)$ is the continuum opacity). This solution is iterated at each grid point until there is no further change in $J^D(\nu)$.

Next the emission coefficients and optical depth from the on–the–spot approximation are used to solve the spherical radiative transfer problem and $J^D(\nu)$ is evaluated at all the grid points and frequencies. This is done using the Feautrier method in a cylindrical coordinate system, as discussed by Hummer, Kunasz and Kunasz (1973) and Leung (1976). Rays tangent to each shell, and up to 10 rays though the hollow core, are used. A new ionization model is then constructed with this $J^D(\nu)$ field and the process iterated to convergence. A few iterations are generally sufficient to reach convergence (i.e. the difference in the temperature structure throughout the shell is less then a few parts in 10^4 between successive iterations).

The atomic data employed by the Harrington code are summarised in Section 10.6 and Table 13 of Harrington at al. (1982).

Chapter 3

Observations and Data Reduction

3.1 Echelle Spectroscopy of CPD–56°8032, He 2–113, SwSt 1 and M 4–18

CPD–56°8032, He 2–113 and SwSt 1 were observed with the 3.9 m Anglo-Australian Telescope (AAT) on May 14 and 15 1993 using the 31.6 l/mm UCL Echelle Spectrograph (UCLES), with a 1024×1024 pix^2 Tektronix CCD as detector. Four settings of the CCD were needed in order to cover the entire echellogram: two adjacent ones in the far-red and two in the blue. Complete wavelength coverage was obtained from 3600 Å to 9500 Å. At each wavelength setting, 5 arcsec wide-slit spectra were obtained for absolute spectrophotometry, and 1.5 arcsec narrow–slit spectra for maximum resolution (R=50,000). For SwSt 1 narrow–slit spectra were obtained only in the range 4100–5400 Å. The continuum signal-to-noise ratios ranged from 20 to 60, depending on exposure time and the brightness of the object. A log of the observations is presented in Table 3.1.

M 4-18 was observed by the Isaac Newton Group staff as part of a service night (November 27, 1996), with the 4.2 m William Hershell Telescope (WHT). To obtain a resolution similar to the one achieved by UCLES, the Utrecht Echelle Spectrograph (UES) was used in conjunction with a 2048×2048 pix^2 Tek CCD chip. Only one setting was obtained in the range 4200–5850 Å; two exposures lasting 2400 sec were sufficient to

achieve a continuum signal–to–noise of 40.

The data were reduced using the IRAF (V2.10)[1] package at the UCL STARLINK node. Wavelength calibration was with respect to comparison Th-Ar arc exposures. Absolute flux calibration for the UCLES data was with respect to the B3IV star HD 60753, whose energy distribution has been measured by Oke (1974, 1992). The flux calibration was achieved by first flat-fielding, background subtracting, and wavelength calibrating the spectrum of HD 60753. Next a comparison was made between the counts in every wavelength bin (of 2–Å width) and the tabulated Oke fluxes in that bin. This was achieved by locating about 30 points per order on the continuum of the standard star, and fitting them to a polynomial in wavelength, allowing the creation of a calibration curve (counts vs. flux units) for every order of the standard spectrum. This curve was then applied to the target star to convert counts to flux units. Care was needed to create a calibration curve free of glitches. Misfittings of the echelle orders could occur if the order of the fitting polynomial was too high; conversely a low order polynomial could miss real flux changes. The join between successive orders was a measure of how successful the flux calibration had been.

The UCLES echelle orders were then merged to produce continuous spectra for CPD–56°8032, He 2–113 and SwSt 1 extending from 3600 Å to 9500 Å. Subsequent data reduction was carried out with the Starlink DIPSO package (Howarth and Murray 1991), particularly heavy use being made of the ELF suite of emission-line fitting subroutines.

After flux calibration, the narrow–slit spectra of CPD–56°8032, He 2–113 and SwSt 1 were scaled up to the continuum levels of the wide–slit spectra. For CPD–56°8032, the blue spectra were obtained during the first night, which was not photometric. In order to scale the blue part of its spectrum to the correct level, we calculated a 'scaling' factor from the flux in the nebular hydrogen lines. This was done by taking the ratio between the measured Hβ flux and that measured from a wide–slit spectrum taken in photometric conditions in 1981 (see Section 3.2). The scaling factor was 1.42 ± 0.04. After this factor

[1]IRAF is written and supported by the National Optical Astronomy Observatories (NOAO) in Tucson, Arizona. http://iraf.noao.edu/

was applied to the blue spectrum of CPD–56°8032, the alignment with the red part was almost perfect[2].

The UES spectra of M 4–18 were flux–calibrated using the HST standard G191B2b. However the narrow slit used might have resulted in a non–photometric spectrum. In fact a comparison of the UES spectrum of M 4–18 with a photometric spectrum of M 4–18 obtained at the Isaac Newton Telescope (INT) in July 96 (see Section 3.3), revealed the UES spectrum to have a continuum level approximately 20% higher than the IDS spectrum, although with an overall similar shape. To scale the UES spectrum of M 4–18 to the continuum level of the INT photometric spectrum, the continua of both spectra were fitted using second order polynomia. The polynomia were then divided to obtain a calibration curve that could then be applied to the narrow–slit UES spectrum to scale it to the level of the wide–slit INT spectrum.

3.2 RGO Spectrograph Spectrum of CPD–56°8032

On 1981 July 22, a spectrum of CPD–56°8032 was taken with the 3.9 m AAT using the RGO Spectrograph 25–cm camera with an IPCS as detector. A log of the observations is presented in Table 3.2. A 1200 l mm^{-1} grating, blazed in the red, was used in first order to acquire spectra longwords of 5000 Å at a dispersion of 33 Å mm^{-1} and was used in second order to obtain spectra shortwords of 5000 Å at a dispersion of 16 Åmm^{-1}. Appropriate order-sorting filters were used. The wavelength coverage per spectrum was about 1000 Å and 500 Å in first and second order, respectively. When using a narrow slit (1.0–1.5 arcsec), the instrumental resolution, as judged from the FWHM of comparison arc lines, was typically 0.98 Å and 0.50 Å, in first and second order (the instrumental resolution was lower, though, at the edges of the detector field). With a wide slit (8.3 arcsec), the

[2]Despite the blue part of our 1993 CPD–56°8032 spectrum having been scaled to the 1981 spectrum, the values of the Hβ fluxes listed in Chapter 5 for the two spectra differ by about 5%. This is due to a subsequent remeasuring of the 1993 Hβ flux. However, the new value is within the errors associated with flux measurements and is not considered to be a cause of concern.

instrumental resolution was 3.0 Å and 1.5 Å in first and second order, respectively.

Spectra were obtained at eight different grating settings, yielding complete wavelength coverage between 3600–8700 Å, with the wavelength overlaps between adjacent spectra being typically about 120 Å. At each wavelength setting, narrow-slit spectra (for maximum resolution) and wide-slit spectra (for absolute spectrophotometry) were obtained. The data were reduced by M.J. Barlow using the AAO SDRSYS package, written by J. Straede. Wavelength calibration was with respect to comparison Cu–Ar arc exposures and absolute flux calibration was with respect to the DA white dwarf W485A, whose energy distribution has been measured by Oke (1974). Subsequent data analysis was also carried out within the Starlink DIPSO package (Howarth and Murray 1988).

After flux calibration, the narrow–slit spectra were scaled up to the continuum levels of the wide–slit spectra. Regions where strong emission lines had caused detector saturation were replaced by the equivalent regions from spectra, obtained immediately adjacent in time, which used a neutral density filter to reduce the count–rate. Finally, the resulting absolutely calibrated narrow–slit spectra were merged to produce a continuous spectrum extending over 14000 pixels from 3600–8700 Å. A log of the RGO observations is presented in Table 3.2.

3.3 Long–Slit Spectra of H–Deficient Central Stars

Spectroscopy of a sample of 19 H–deficient central stars was obtained on July 17–23, 1996 at the 2.5 m Isaac Newton Telescope (INT), using the Intermediate Dispersion Spectrograph (IDS) in conjunction with a 385×578 pix^2 GEC CCD and the 235 mm camera. Wavelength coverage between 3800 and 6800 Å was achieved using the R1200B/Y grating (four settings; resolution 1.5 Å for a 1.5 arcsec slit), the R632V (two settings; resolution 3 Å for a 1.5 arcsec slit) and the R300V grating (one setting; resolution 6 Å for a 5 arcsec slit). The signal–to–noise ranged between 80 and 100. The R1200B/Y grating was used for the cooler stars which have thinner lines, while the R632V setting was used for the hotter stars. The R300V setting was used solely to obtain the whole spectrum in one

Table 3.1: Log of the 1993 UCLES observations of He 2–113, CPD–56°8032 and SwSt 1. Only the second night was photometric

Star	Run	Central wavelength (Å)	Date 1993, May	Exposure time (sec)	Slit width (arcsec)	Airmass	Seeing (arcsec)
He 2–113	102	4622	14	500	1.5	1.71	2
	105	4622	14	600	1.5	1.60	2
	107	4622	14	600	1.5	1.54	2
	123	4622	14	600	1.5	1.08	4
	125	4622	14	600	1.5	1.09	4
	176	6827	15	600	5.0	1.67	2
	178	6960	15	600	5.0	1.59	2
	180	4622	15	400	5.0	1.54	2
	236	6827	15	1200	1.5	1.29	2
	239	6960	15	1200	1.5	1.40	2
CPD–56°8032	120	4622	14	600	1.5	1.28	4
	121	4622	14	600	1.5	1.25	4
	122	4622	14	600	1.5	1.23	4
	133	4622	14	300	5.0	1.11	2.5
	134	4622	14	300	5.0	1.11	2.5
	204	6827	15	500	5.0	1.42	1.5
	206	6960	15	500	5.0	1.39	1.5
	241	6960	15	1200	1.5	1.19	2
	242	6827	15	1200	1.5	1.23	2
SwSt 1	126	4622	14	900	1.5	1.24	3
	128	4622	14	900	1.5	1.25	3
	129	4622	14	300	5.0	1.14	2.5
	210	6827	15	900	5.0	1.62	2
	212	6960	15	600	5.0	1.50	2
	214	4622	15	300	5.0	1.43	2
	216	3712	15	500	5.0	1.38	2
	218	6827	15	60	5.0	1.32	2
	220	6960	15	60	5.0	1.31	2

Table 3.2: Log of the 1981 July 22 RGO Spectrograph observations of CPD–56°8032

Run	Setting's starting wavelength (Å)	Setting's ending wavelength (Å)	Exposure time (sec)	Slit width (arcsec)	ND Filter[a] (dex)
32,34	5007	5968	500,500	0.7	none,0.7
36,37	5007	5968	450,200	0.7	0.7,1.3
40,41,42	5850	6811	500,320,200	0.8	none.1.0,0.34
44,45	5850	6811	300,200	8.3	0.7,1.3
46,47,48	6773	7723	240,100,150	8.3	0.34,1.3,0.7
50,51,52	6773	7723	500,180,80	1.2	none,0.7,1.0
55	7748	8698	1000	3.5	none
57	7748	8698	400	8.3	none
59	3325	3805	900	1.5	none
62	3325	3805	321	8.3	0.34
63,64	3775	4255	300,100	8.3	0.7,1.0
66,67	3775	4255	650,120	1.5	0.34,0.7
70,71	4247	4727	650,120	1.5	0.34,1.0
73,74	4247	4727	100,250	8.3	1.0,0.7
75,76	4591	5050	250,120	8.3	0.34,0.7
78,79,80	4591	5050	200,400,100	1.5	none,0.34,0.7

[a]The Neutral Density filter was introduced to reduce the counts so the strongest lines would not saturate.

setting with a wide slit (5 arcsec) in order to achieve absolute flux calibration.

The flux standards adopted were the B2 IV star BD+33°2642 and the Op star BD+28°4211 which have been recalibrated recently (Oke 1992). Flux calibration was achieved by scaling the narrow–slit spectra to the wide–slit as already described in in Section 2.1. Wavelength calibration was with respect to a Cu–Ne arc (for the red settings) and a Cu–Ar arc (for the blue settings). A log of the INT observations is presented in Table 3.3.

Table 3.3: Exposure times (s) for the 1996 July 17–23 IDS observations of II–deficient central stars of PN

Star	Spectral type[a]	Setting and central wavelength (Å) R1200B 4090	R1200B 4870	R1200Y 5650	R1200Y 6430	R632V 4440	R632V 5990	R300V 5330
V 348 Sgr	EHe(pec)	300						600
K 2–16	[WC11]	600,600	300,600	600,600	300,600			50,100
IRAS 17514–1555	[WC10]	2400,2400	1800,1800	1800,1800	1800,1800			1000,600
M 4–18	[WC10]	600,750	500,600	450,450	30,400,450		600,600	120
IRAS 21282+5050	WEL	1200,2400	600,1800,1800	1800,1800	900,1800			300,300
NGC 6543	*wel*	60,60,120	10,60	60,60	10,60,120			20,20
NGC 6567	*wel*	600,1200	60,600,1200	100,600	60,450,600			10,180
NGC 6629	*wel*	300,600	100,300,600	100,600	100,200,600			60,60
Cn 3–1	*wel*	300,300	60,300	300,300	30,300,600			60,10
M 1–46	*wel*	600,600	600	300,600	100,500,600			50,100
A 78	*wel*	300,600	300,500	400,400	400,400			30,120
NGC 246	PG1159	120,120	120,240	200	200,300			30,120
BD+30°3639	[WC9]	60,60	10,60	60	1,6,60			10,2
He 2–459	[WC9]	1800	300,900		300,900	1800,1800	1800	60,300,600
NGC 40	[WC8]	120,180	60,120	60	60,600			10,30
NGC 6751	[WC4]					600,1000	600,600	300,600
IC 1747	[WC4]					600,1800	3001500	100,600
NGC 7026	[WC3]					60,900,1200	60,450,800	60,600
NGC 6905	[WC2]					600,600	600,900,1500	600

[a]Spectral classification for WC stars according to the quantitative scheme developed in Chapter 4.

The average night seeing was 1.1" on the 17^{th}, 18^{th} and 22^{nd}, 1.0" on the 19^{th}, 1.2" on the 23^{rd}, 1.4" on the 20^{th} and 1.5" on the 21^{st}.

Chapter 4

Quantitative Classification of WC Stars

Up until very recently the spectral classification of WR stars was based on a system developed for photographic plates, was highly subjective to an individual observer and so was limited in its usefulness. The advent of linear digital detectors has facilitated the easy quantification of the WR classification system, allowing objective spectral classifications for WN2–8 stars (Smith, Shara and Moffat 1996), WN9–11 stars (Smith, Crowther and Prinja 1994), WC4–9 stars (Smith, Shara and Moffat 1990) and WO1–5 stars (Kingsburgh, Barlow and Storey 1995). However alternative qualitative schemes (e.g. Méndez and Niemela 1982) are still generally followed for WC–type CSPN, leading to systematic differences from massive WC stars. For example, Acker, Gorny and Cuisinier (1996) identified the CSPN M1–25 as a [WC6] star following Méndez and Niemela (1982) which should be classified [WC5] according to the scheme of Smith et al. (1990). In addition, stars showing a late WC (WCL) appearance, first identified as a class by Webster and Glass (1974), have remained poorly distinguished despite efforts by Hu and Bibo (1990). Beyond the WC9 subclass, all WC–type stars known are CSPN. Quantitative spectroscopy has been carried out for a subset of these by Leuenhagen, Hamann and Jeffery (1996),

Table 4.1: Log of observations for programme WC and WO stars, including narrow band *ubvr* photometry (following Smith 1968b). Spectral classifications are taken from Smith et al. (1990) for massive WC stars and Tylenda et al. (1993) or Acker et al. (1996) for CSPN, except for SwSt1, IRAS 17514–1555 (Hu and Bibo 1990) and IRAS 21282+5050 (Cohen and Jones 1987). Sources for intrinsic colours are discussed in the text, with interstellar reddenings probably reliable to ±0.05 mag (E(B–V)=1.21 E_{b-v}, Turner 1982)

Star	Alias	PN G	Sp. Type	Telescope/ Instrument	Epoch	Sp. Coverage (Resolution Å)	v mag	$(b-v)$ mag	E_{b-v} mag
HD 193949	NGC 6905	061.4–09.5	[WC3]	2.5m INT-IDS	Jul 96	3700–6800 (3.0)	14.45	0.11	0.38
HD 210092	NGC 7026	089.0+00.3	[WC3/4]	2.5m INT-IDS	Jul 96	3700–6800 (3.0)	14.26	1.01	1.28
HD 11758	IC 1747	130.2+01.3	[WC4]	2.5m INT-IDS	Jul 96	3700–6800 (3.0)	15.06	1.01	1.28
HD 177656	NGC 6751	029.2–05.9	[WC4]	2.5m INT-IDS	Jul 96	3700–6800 (3.0)	14.47	0.49	0.76
HD 192103	WR135		WC8	2.5m INT-IDS	Sep 91	3800–7300 (2.5)	8.44	0.21	0.41
HD 826	NGC 40	120.0+09.8	[WC8]	2.5m INT-IDS	Jul 96	3700–6800 (1.5)	11.82	0.15	0.35
HD 164270	WR103		WC9	3.9m AAT-RGO	Nov 92	3700–7300 (1.7)	8.94	0.18	0.38
HDE 313643	WR106		WC9	2.5m INT-IDS	Jul 96	5200–6800 (3.0)	12.40	0.91	1.11
	LS15 (WR119)		WC9	2.5m INT-IDS	Jul 96	5200–6800 (3.0)	12.48	0.77	0.97
	MR90 (WR121)		WC9	2.5m INT-IDS	Jul 96	5200–6800 (3.0)	12.33	1.14	1.34
HD 184738	BD+30°3639	064.7+05.0	[WC9]	2.5m INT-IDS	Jul 96	3700–6800 (1.5)	10.30	0.09	0.29
He 2–459		068.3–02.7	[WC9]	2.5m INT-IDS	Jul 96	3700–6800 (1.5)	17.26	1.30	1.50
He 2–99	LSS 3169	309.0–04.2	[WC9]	3.9m AAT-UCLES	May 93	4050–5300 (0.2)	13.33	0.09	0.29
HD 167362	SwSt1	001.5–06.7	[WC10]	3.9m AAT-UCLES	May 93	3400–9900 (0.2)	11.77	0.22	0.51
	IRAS 17514–1555	012.2+04.9	[WC11]	2.5m INT-IDS	Jul 96	3700–6800 (1.5)	16.03	0.76	1.05
	M4–18	146.7+07.6	[WC11]	2.5m INT-IDS	Jul 96	3700–6800 (1.5)	14.14	0.02	0.31
He 2–113	He 3–1044	321.0+03.9	[WC11]	3.9m AAT-UCLES	May 93	3400–9900 (0.2)	11.93	0.55	0.84
	K2–16	352.9+11.4	[WC11]	2.5m INT-IDS	Jul 96	3700–6800 (1.5)	12.89	0.26	0.55
He 3–1333	CPD–56°8032	332.9–09.9	[WC11]	3.9m AAT-UCLES	May 93	3400–9900 (0.2)	10.87	0.27	0.56
	IRAS 21282+5050		[WC11]	2.5m INT-IDS	Jul 96	3700–6800 (1.5)	14.38	1.32	1.59

in Chapter 6 and by Leuenhagen and Hamann 1997, while two early WC (WCE) CSPN have been studied by Koesterke and Hamann (1997). It is important to develop and utilise *consistent* classification criteria for both CSPN and massive WC stars in order to understand and test the apparent absence of WC5–7 stars amongst CSPN.

In Section 4.1, we list additional observations of several WC stars. In Section 4.2, we present a new quantitative classification scheme for WCL stars that forms a natural extension to the existing scheme of Smith et al. (1990), and that applies equally to CSPN and to massive stars. In Section 4.3, we consider whether WCE or WO spectral classifications are more appropriate for higher ionization stars, both CSPN and massive stars. Section 4.4 provides a brief summary.

4.1 Observations

The observations described in Chapter 3 were complemented by additional spectroscopy of HD 192103 (WR135), obtained with the INT-IDS, 500mm camera and 400×590 pixel GEC CCD in 1991 September. 400 lines/mm V and R gratings provided complete spectral coverage between $\lambda\lambda$3800–7300 in seven overlapping wavelength settings (see Crowther et al. 1995 for details of the reduction). Additional AAT observations of HD 164270 (WR103) were obtained in 1992 November using the RGO Spectrograph, 250mm camera, Tektronix CCD and 1200V grating, covering $\lambda\lambda$3680–6000 in three overlapping settings (see Crowther, Hillier and Smith 1995 for details).

We found some quantitative spectroscopic data for CSPN available in the literature. Seven late WC (WCL) have been observed by Leuenhagen, Hamann and Jeffery (1996). Two early WC (WCE) CSPN have been studied by Koesterke and Hamann (1997), while Wolf–Rainer Hamann has kindly provided us with observations of four high excitation CSPN (NGC 1501, 5189, 5315 and PB6), two of which were previously presented in Hamann (1996). We will also use spectroscopy of the CSPN Sand 3 observed by Barlow, Blades and Hummer (1980), and include our previously unpublished red spectroscopy of He 2-99 obtained with the AAT–RGO spectrograph.

For massive WC4 and WC9 stars, quantitative visual spectroscopy is available from Torres and Massey (1987) and Smith et al. (1990). The hot R CrB star V348 Sagittarii, which has in the past been classified WC12, has been observed by Leuenhagen, Heber and Jeffery (1994).

As already pointed out, the signal–to–noise ratio of all the INT spectroscopy was about 100, while for the AAT spectra it ranged between 30 and 60. No spectra had a signal–to–noise ratio lower than about 20. In order to use the classification system developed in the course of this Chapter, spectra should have a signal to noise ratio higher than about 20 and include all the diagnostic lines used for primary and secondary criteria. As for the resolution, the coolest WCL stars (i.e. WC11–10) cannot be classified if the spectral resolution is lower than about 50 km s^{-1}, while for WC9–8, a value of 1000 km s^{-1} is sufficient. For WC7–5 a resolution of at least 2000 km s^{-1} is required, while for the WO stars a value of 3000 km s^{-1} should be considered as an upper limit.

4.1.1 Photometry and Emission Line Strengths

In Table 4.1, we include narrow–band synthetic photometry (following Smith 1968b) obtained by convolving each of our flux calibrated datasets with suitable Gaussian filters. Intrinsic colours for WC stars have been obtained from test non–LTE model atmosphere calculations. It is found that $(b-v)_0 \sim -0.27$ mag for WCE stars (Willis et al. 1997), $(b-v)_0 \sim -0.20$ mag for WC8–9 stars (Crowther 1997), $(b-v)_0 \sim -0.29$ mag for WC10–11 stars (Chapter 6) and $(b-v)_0 \sim -0.27$ mag for late O stars (Crowther and Bohanan 1997). From these intrinsic colours, estimates of interstellar (and/or circumstellar) reddenings can be made and are included in Table 4.1. Note that the colour excess for IRAS 21282+5050 is based on our reclassification to a late O star (Section 4.2.2). In many cases, our photometric magnitudes differ greatly from previously published values that were obtained from Johnson photometry or from direct images and that suffered from significant stellar and nebular contamination.

In Table 4.2, we present selected emission line equivalent widths (W_λ) and dereddened

Table 4.2: Emission equivalent widths, W_λ (in Å), dereddened line fluxes, I_λ (in 10^{-12} erg cm^{-2} s^{-1}) of various classification diagnostics, plus the FWHM C III λ5696 or C IV λλ5801-12 (in Å). Fluxes are uniformly dereddened using interstellar extinctions from Table 4.1. IRAS 21282+5050 is omitted since it is no longer classified as a WC star (see text)

Star	FWHM		O VIλ3818		C IIλ4267		He IIλ4686		O VIλ5290		O III-Vλ5590		C IIIλ5696		C IVλ5808		He Iλ5876	
	λ5696	λ5808	W_λ	I_λ	W_λ	I_λ	W_λ	I_λ	W_λ	I_λ	W_λ	I_λ	W_λ	I_λ	W_λ	I_λ	W_λ	I_λ
NGC 6905	–	36.5	349.0	40.7	–	–	99.0	4.3	31.0	0.7	6.5	0.1	–	–	87.0	1.3	–	–
NGC 7026	–	63.0	108.0	140.0	–	–	87.0	28.6	44.0	7.7	31.4	3.9	–	–	86.5	11.4	–	–
IC 1747	–	36.0	<30	<70	–	–	82.0	45.0	10.2	2.4	53.0	10.0	–	–	416.0	57.2	–	–
NGC 6751	–	52.0	46.0	24.0	–	–	270.0	43.0	31.5	3.1	112.0	7.1	–	–	2270	135.0	–	–
HD 192103	37.8	26.9	5.5	88.0	17.5	210.0	81.0	1190	6.5	34.8	12.3	71.7	189.0	1300	215.0	1450	49.0	310.0
NCG 40	28.0	21.7	5.4	3.4	14.0	6.6	54.0	23.0	–	–	18.3	3.4	140.0	29.0	164.0	32.0	25.0	4.6
He 2-459	34.9	29.4	–	–	25.0	5.4	50.0	9.4	–	–	17.2	1.2	244.0	26.0	99.5	9.6	41.0	3.4
He 2-99	16.6	15.6	–	–	23.7	4.1	26.7	23.0	–	–	20.0	1.5	245.0	18.0	96.0	5.8	41.0	3.2
HDE 313643	18.3	30.0	–	–	22.4	81.0	16.9	52.0	–	–	5.2	6.3	196.0	240	71.0	71.0	55.9	54.0
LS 15	16.7	32.6	–	–	19.5	46.0	11.2	27.0	–	–	4.4	3.5	192.0	120.0	62.0	30.0	46.0	21.0
HD 164270	18.0	30.0	–	–	24.8	160.0	13.8	100.0	–	–	4.6	15.5	235.0	690.0	69.0	170.0	56.5	155.0
MR 90	18.2	28.7	–	–	22.9	220.0	12.0	110.0	–	–	3.1	7.7	206.0	450.0	58.0	130.0	47.5	110.0
BD+30° 3639	14.1	–	–	–	15.6	25.0	11.3	18.0	–	–	4.0	3.0	172.0	120.0	39.0	25.0	27.5	15.0
SwSt1	5.4	–	–	–	1.5	1.2	2.9	2.1	–	–	0.5	0.2	32.9	12.0	6.3	2.2	3.4	1.1
IRAS 17514-1555	5.8	–	–	–	24.5	2.9	2.2	0.2	–	–	1.0	0.05	26.3	1.4	4.1	0.2	24.9	1.3
CPD-56°8032	4.0	–	–	–	24.5	61.0	1.4	2.4	–	–	1.0	0.8	17.9	15.0	2.4	2.1	22.6	17.0
M 4-18	3.5	–	–	–	11.4	0.64	1.0	0.03	–	–	0.3	0.01	14.4	0.33	0.9	0.02	11.3	0.03
He 2-113	2.9	–	–	–	9.6	31.0	0.6	1.5	–	–	0.3	0.3	14.5	18.0	1.5	1.6	9.6	11.0
K 2-16	3.3	–	–	–	4.1	2.0	<0.1	<0.01	–	–	<0.1	<0.01	3.6	0.57	<0.1	<0.01	3.3	0.51

fluxes (I_λ) that will be used as classification criteria for WC stars. It is important to emphasise that all equivalent widths and fluxes used for our quantitative classification are *emission* measurements, with P Cygni absorption components neglected. In the case of the C IV λ5801–12 doublet for WCL stars, we add emission components together when they are resolved (true for all stars cooler than WC9). He II λ4686 is only well resolved from C III λ4650 in WC9 and later subtypes. It is likely that certain line measurements include contributions from other unidentified features, though these are (reasonably) anticipated to affect all stars in a similar manner. Nebular contributions to emission lines were removed through subtraction by Gaussian fits (using the ELF suite of programmes within DIPSO). Although equivalent width measurements provide our principal diagnostic criteria, we have included line flux measurements in Table 4.2 since the stellar continuum may be significantly affected by the nebular continuum, especially for extragalactic PN. Since this preferentially contaminates at longer wavelengths, line equivalent width ratios at different wavelengths will be differentially affected. All fluxes were dereddened using the colour excesses determined in Table 4.1 and the standard Galactic reddening law of Howarth (1983) assuming R=3.1.

4.2 Classification of WCL Stars

4.2.1 Previous WCL Schemes

The current optical classification scheme for WC stars is based upon measurements of carbon and oxygen emission lines, namely C III λ5696, C IV λ5801–12 and O III-V λ5590 (Smith et al. 1990). The carbon lines, together with the λ4650 blend, represent the strongest emission features in the visual spectra of WC stars, and are relatively well separated for all subtypes, although C IV λ5801–12 suffers from some contamination from He I λ5876 for those stars showing the broadest line spectra. The oxygen feature is used principally to distinguish between WC4–6 stars, since it is extremely weak at later spectral types.

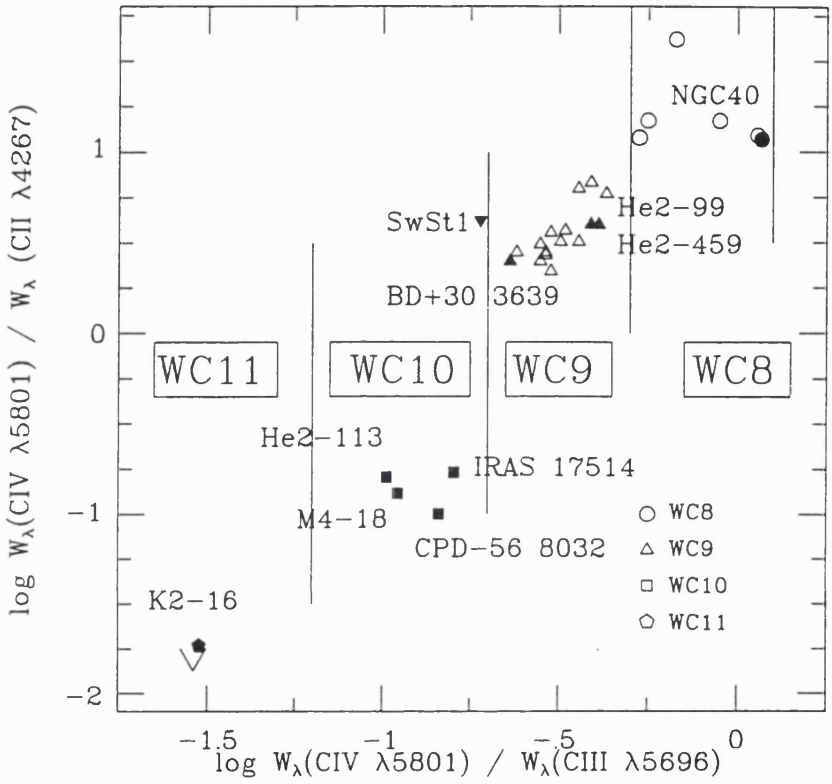

Figure 4.1: Emission line equivalent width ratios for our principal and secondary criteria for WCL stars (filled: CSPN, open: massive Pop I) including measurements for massive WC8–9 stars from Torres and Massey (1987). The natural separation between subtypes is apparent, with divisions marked as solid lines. Similar relations are provided by line flux ratios listed in Table 4.1. SwSt1 (inverted triangle) is given a WC9 classification because of our secondary criterion (see text)

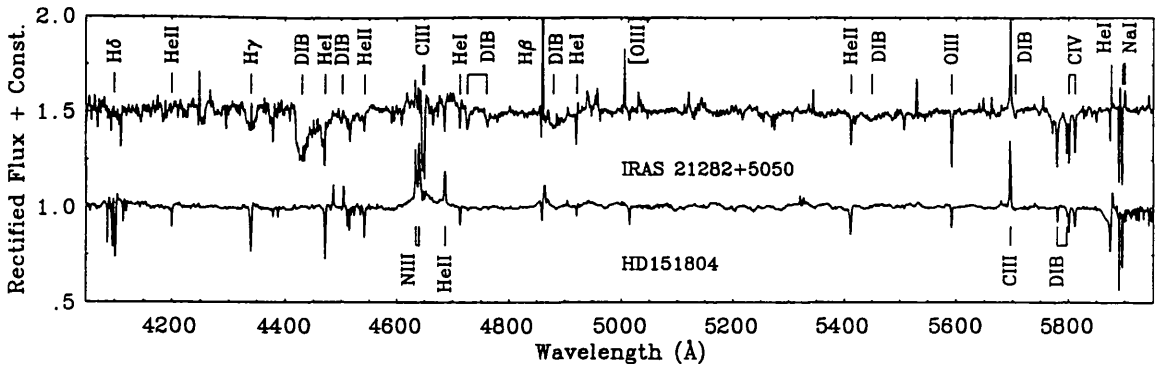

Figure 4.2: Spectral comparison of IRAS 21282+5050, previously classified as WC11 (Cohen and Jones 1987), with HD 151804 (O8 If, Crowther and Bohanan 1997) showing an extremely similar spectral morphology in the yellow, though differing substantially in the blue (especially around He II λ4686), probably as a result of abundance differences. Note the presence of strong diffuse interstellar bands (DIBs) at λ4430, λ4760, λ4880, λ5780 and λ5797 (Herbig 1995)

Webster and Glass (1974) noted that the nuclei of CPD-56°8032, He 2-113, M 4-18 and V348 Sgr have spectra in which C II emission lines dominate those of C III, implying spectral types later than WC9, the latest that had been defined at that time for massive WC Wolf–Rayet stars (Smith 1968a). Carlson and Henize (1979), on the basis of data from Swings and Struve (1943), classified SwSt1 as WC10 and inferred still later spectral types for the four stars discussed by Webster and Glass (1974). van der Hucht et al. (1981) were the first to classify the four nuclei discussed by Webster and Glass (1974) as WC11 (their Table IX).

To date, the only attempt at a more quantitative classification was made by Hu and Bibo (1990) for WC10–12 subtypes, based on C II-IV lines, including C II λ5641–62. We were motivated to develop an improved scheme for WCL stars because of the apparently contradictory classification provided for CPD–56°8032 by Hu and Bibo (1990). For this star, a WC11 classification was proposed, signifying no C IV $\lambda\lambda$5801–12 emission, yet our spectra clearly show P Cygni emission for this doublet (see Section 4.2.4). Acker et al. (1996) have suggested that the scarcity of [WC10] CSPN relates to the definitions from

Hu and Bibo (1990) being poorly linked to earlier subclasses, and proposed renaming the [WC10] subclass to [WC10–11].

4.2.2 New WCL Classification Scheme

We have adopted the C IV λ5801–12/C III λ5696 ratio as our primary classification diagnostic for WCL stars, providing consistency with the scheme of Smith et al. (1990). Unfortunately, their secondary criterion O III-V λ5592/C III λ5696 suffers from variations in C/O abundances, and becomes a crude discriminator of spectral subclass for WCL stars because of the weakness of the O III λ5592 feature. We have therefore sought alternative secondary diagnostics, that are preferably strong, relatively unblended features from the same element in the yellow–red part of the spectrum. We find that C IV $\lambda\lambda$5801–12/C II λ4267 and He II λ4686/He I λ5876 provide useful discriminators between WC8–11 subclasses. Although C II λ4267 is difficult to measure in stars suffering from high interstellar reddening, it remains superior to alternative C II diagnostics, such as C II λ5640–62 proposed by Hu and Bibo (1990), which is extremely weak and consequently difficult to measure for stars of subtype earlier than WC10. Alternative C II features at longer wavelengths have the disadvantage of either being badly blended (C II λ6578–82 with [N II] λ6583), or lying in a rarely observed part of the spectrum (C II λ7231–7237). Although helium diagnostics are severely blended with carbon features in WCE stars (C III-IV λ4650 and C IV $\lambda\lambda$5801–12), the narrower emission lines of WCL stars allow reliable He II λ4686 and He I λ5876 measurements to be made for most WCL stars in our sample (with the possible exception of He 2–459).

In Fig 4.1, we illustrate our primary and secondary classification line ratios for WCL stars, including and massive (open symbols) and CSPN (filled symbols) WC stars. Since our observational sample includes only a small fraction of known massive WC8–9 stars, we have included our own measurements of 16 other WC8–9 stars from the spectrophotometry of Torres and Massey (1987). Boundaries between subtypes are marked. Note the natural breaks between subclasses WC8–9, 10 and 11 in both line ratios and line strength. This

remains unexplained.

Overall, our measurements support the classification criteria adopted by Smith et al. (1990), with the exception of the WC8–9 boundary. We have revised this from W_λ(C IV)/W_λ(C III)=0.4 to 0.5 as this appears to represent a more natural division. Following Smith et al. (1990), He 2–459 [with W_λ(C IV)/ W_λ(C III)=0.41] would be classified as a [WC8] star, while He 2–99 [with W_λ(C IV)/W_λ(C III)=0.39] would be defined as a [WC9] star, despite showing a very similar spectral morphology. Our revised criteria yields a [WC9] classification for both stars. HD 117297 (WR53) is the only massive WCL star reclassified relative to Smith et al. (1990): with W_λ(C IV)/W_λ(C III)= 0.43, it changes from WC8 to WC9.

Table 4.3 summarises the primary (C IV/C III) and secondary (C IV/C II, He II/He I) classification criteria, with examples for each class. L302 in the SMC (Monk, Barlow and Clegg 1988) provides a useful test of our flux ratio criteria, since its continuum is heavily contaminated by its nebula. Both our primary and secondary flux ratio criteria support the previously derived WC8 classification for this star, with possible nebular He I contamination affecting the helium criterion.

C III λ5696 emission is not restricted to WC stars, and is observed in many other emission line stars including late O stars (Crowther and Bohanan 1997), and 'weak emission line' (*wel*) CSPN. Tylenda, Acker and Stenholm (1993) defined *wel*'s as stars with weak and narrow C IV $\lambda\lambda$5801–12 emission, and with C III very weak or undetectable. In order to avoid confusion between WCL, O–type and *wel*'s for stars in which the stellar continuum is well defined, we shall impose two additional criteria necessary for a WCL–type classification, namely sufficient C III λ5696 emission ($W_\lambda \geq$3Å) plus emission ($W_\lambda \geq$1Å) either at C II λ4267 or C IV $\lambda\lambda$5801–12. Obviously, these criteria do not apply to high excitation WCE stars since C III λ5696 has negligible strength in WCE and WO stars (Section 4).

To illustrate the border region, we now discuss IRAS 21282+5050 which Cohen and Jones (1987) classified as a [WC11] star. This is a heavily reddened emission line star (E(B–V)=1.92 mag from Table 4.1) that has received little attention to date. Our

Table 4.3: Quantification of WC11–5 and WO4–1 subclasses based on emission equivalent width ratios (W_λ) or dereddened line flux ratios (I_λ), providing a natural connection to Smith et al. (1990) for most WC spectral types. To exclude O–type and weak emission line stars from WC or WO classifications, additional criteria include W_λ(C III λ5696)$\geq$3Å and either C II or C IV emission for WCL stars, and W_λ(C IV λ5808)$\geq$10Å and either C III or O VI emission for WCE or WO stars

Subtype	FWHM (Å)	Primary	Secondary	Additional Criteria	Examples
	C III λ5696	C IV λ5808/C III λ5696	C IV λ5808/C II λ4267	He II λ4686/He I λ5876	
		log W_λ or log I_λ	log W_λ	log W_λ	
WC11	~3	≤ -1.2	≤ -1.5	He II λ4686 absent	K2–16
WC10	3–6	-1.2 to -0.7	-1.5 to -0.2	≤ -0.8	CPD–56°8032
WC9	30±15	-0.7 to -0.3	-0.2 to $+1.0$	-0.8 to $+0.1$	He 2–99, HD 164270
WC8	40±10	-0.3 to $+0.1$	$\geq$1.0	$\geq$0.1	HD 192103, NGC40
	C IV λ5808	C IV λ5808/C III λ5696	C III λ5696/O V λ5590	O VI λ3818/C IV λ5808	
		log W_λ or log I_λ	log W_λ or log I_λ	log W_λ	
WC7	45±20	$+0.1$ to $+0.6$	$\geq$0.1		HD 156327
WC6	50±20	$+0.6$ to $+1.5$	-0.4 to $+0.7$	≤ -0.3	HD 165763, M1–25
WC5	70±20	$\geq$1.5	≤ -0.4	≤ -0.3	HD 32257, NGC 5315
	C IV λ5808	O VI λ3818/O V λ5590	O VI λ3818/C IV λ5808	O VII λ5670/O V λ5590	
		log W_λ	log W_λ	log W_λ	
WO4	60±20	-0.3 to $+0.25$	-1.5 to -1	$\ll$0.0	MS4, NGC1501
WO3	90±30	$+0.25$ to $+0.6$	-1 to $+0.2$	$\ll$0.0	Sand 2, NGC7026
WO2	160±20	$+0.6$ to $+1.1$	$\geq +0.2$	$\leq$0.0	Sand 4
WO1	40±10	$\geq$1.1	$\geq +0.2$	$\geq$0.0	NGC 6905

observations cover a greater spectral range at a superior resolution than Cohen and Jones and reveal that W_λ(C III λ5696)=2Å, with neither C IV $\lambda\lambda$5801–12 nor C II λ4267 observed in emission. Therefore, this star fails both of our WCL criteria. It appears to be a peculiar O–type star, as illustrated in Fig. 4.2 where we compare its blue and yellow spectrum with that of the O8 If star HD 151804 (Crowther and Bohanan 1997). In the yellow part of the spectrum, the similarities with the O supergiant are striking, specifically, the C III λ5696 emission and weak He I λ5876 P Cygni profile. However in the blue, the spectra are quite different, with He II λ4686 in *emission* in HD 151804 and in *absorption* in IRAS 21282+5050, and with strong C III $\lambda\lambda$4647–51 absorption in the latter, possibly as a result of chemical peculiarities. From comparison with spectral standards from Walborn and Fitzpatrick (1990) we propose an O9–9.5 classification for IRAS 21282+5050 based on the observed He II λ4542/He I λ4471 ratio and absence of Si III $\lambda\lambda$4552–4573. A Iab supergiant luminosity class is implied from the observed C III λ5696 emission coupled with He II λ4686 absorption (Walborn, private communication). However, since it has strong UIR emission with a symmetric mid-IR dust nebula, it is almost certainly a young H–deficient CSPN.

Optical spectra of the hot R CrB star V348 Sgr have previously been discussed by Leuenhagen et al. (1994). On the basis of the Hu and Bibo (1990) scheme, they suggested a [WC12] classification because C II emission is present and C III-IV and He II are absent. They commented on the similarity of its absorption line spectrum to those of extreme He–stars (e.g. DY Cen). Since C III λ5696 is absent in V348 Sgr (Dahari and Osterbrock 1984), it *fails* our WCL criteria; the ionization state is too low (20kK, according to Leuenhagen and Hamann 1994). In support of this exclusion, we recall the original definition of a WR star from Beals (1938), 'emission bands due to atoms of *high* ionization potential' are required. We suggest an alternative, though not completely satisfactory, classification for this unique object of 'peculiar extreme He–star'. Exclusion of such low ionization spectral types from the WC sequence is analogous to exclusion of lower ionization stars from the WN sequence (that extends to WN11 provided He II λ4686 emission is present); such stars

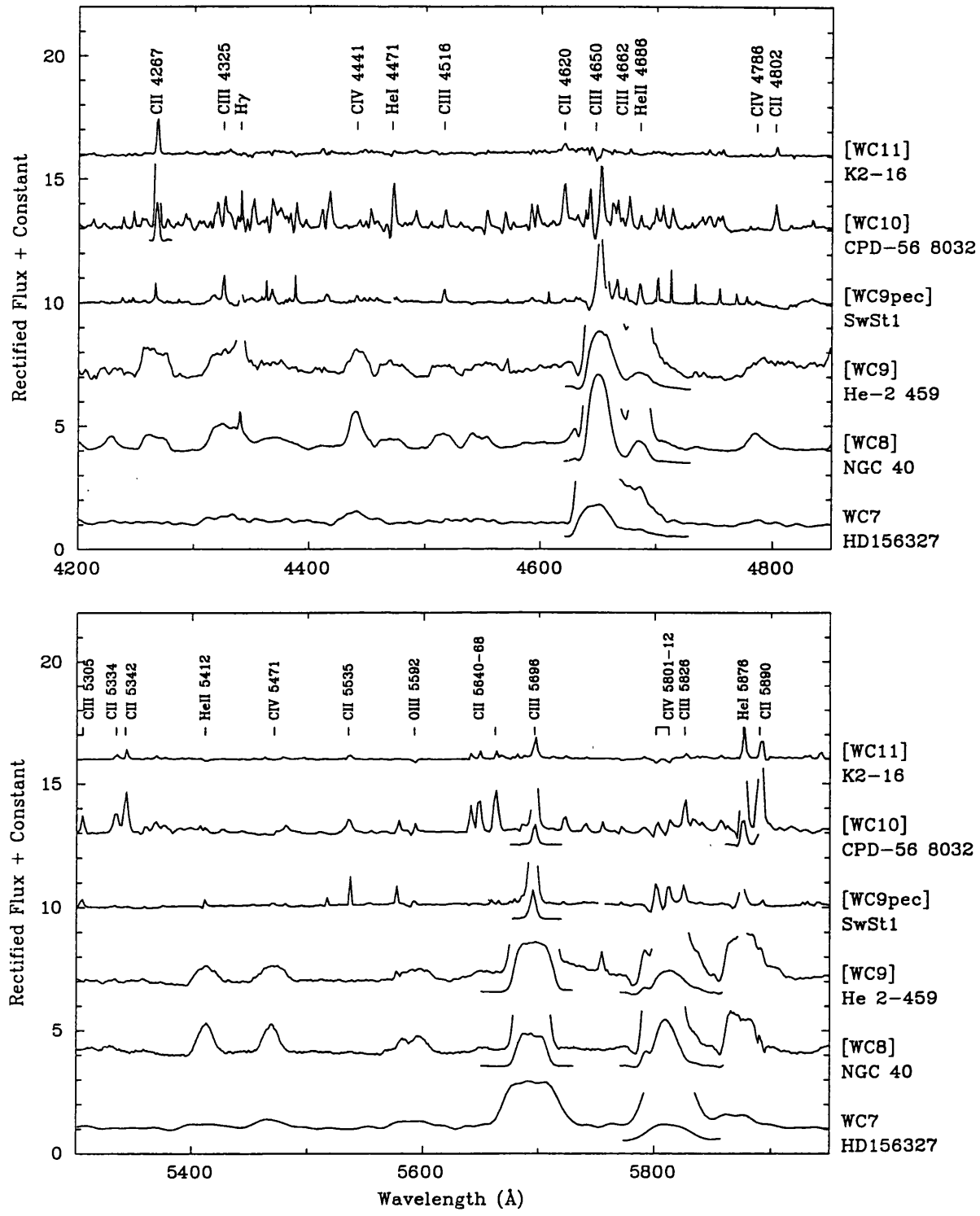

Figure 4.3: Spectral comparison of WC7–11 stars between $\lambda\lambda$4200–4850 and $\lambda\lambda$5300–5950, sorted by new spectral type, demonstrating the change in ionization. Spectra are rectified, separated by 3 continuum units, with very strong lines shown divided by a factor of four, offset by 0.5 continuum units, for clarity

are given P Cygni–type (B Ia$^+$) classifications.

Fig. 4.1 confirms the conclusion of Méndez et al. (1991) that there is no clear distinction in line strength between massive WCL stars and WCL–type CSPN, contrary to the early suggestion by Smith and Aller (1971). Nor is there any separation in line width. In our sample, CSPN show both the broadest (He 2–459) and narrowest (BD+30° 3639) line widths among WC9–type stars. Apart from the absence of massive WC stars with spectral type later than WC9, only the presence or absence of the nebula distinguishes between massive and CSPN WC stars (see also the Proceedings of the "Workshop on PN with WR–Type Nucleii", Lundström and Stenholm eds., 1996).

4.2.3 Remarks on Individual Objects

While the classification scheme described above readily accommodates most stars, some remarks are necessary relating to particular objects showing unusual spectral characteristics:

- **SwSt1** (HD 167362) defies WC spectral classification in any of the proposed schemes. Both Smith and Aller (1969) and Méndez et al. (1991) suggested a composite Of-WR classification, Carlson and Henize (1979) and Hu and Bibo (1990) proposed a WC10 classification and Tylenda et al. (1993) suggested that it was a *wel* star. The latter classification is certainly not appropriate for SwSt1 since very weak C III emission is expected for *wel* stars, yet W_λ(C III λ5696)=33Å for SwSt1 – stronger than in all WC10–11 stars. Neither is an Of-WR classification appropriate since the criterion for an Of star (Conti 1976) is "photospheric lines uncontaminated by wind emission in the visual spectrum" and Méndez et al. (1991) demonstrated that the usual O star classification (photospheric) absorption line at He II λ4542 is blue–shifted, i.e. affected by wind emission. From Fig. 4.1, our primary classification criterion supports a WC10 subclass (as proposed by Carlson and Henize 1979), although it lies very close to the WC9 boundary. The line widths are more representative of WC10 than WC9. However, measurements based on alternative high resolution

spectroscopy indicate W_λ(C IV)/W_λ(C III)=0.27, characteristic of a WC9 star and stellar He I and C II signatures are very weak, i.e. *both* our secondary criteria indicate WC9. We suggest a WC9pec classification for this star.

- **K2–16** appears to have a significantly lower ionization than the other late type CSPN in Fig. 4.1, yet it was given the same classification by Tylenda et al. (1993). Our revised classification criteria make K2–16 the sole CSPN in the WC11 subclass.[1] However, we note that W_λ(C III λ5696)/W_λ(C II λ4267)=0.88 for this star lies within the range observed for WC10 stars, namely 0.73–1.5, which implies that its difference from WC10 stars is a result of lower wind density rather than lower ionization. A *wel* classification is not appropriate since C IV $\lambda\lambda$5801–12 is not present in emission. Strictly speaking, we should exclude a WR classification for K2–16, since photospheric features appear to be present in its spectrum (the spectral resolution of our observations is insufficient to verify significant wind contamination). An Of-WR(C) classification is inappropriate, because He II λ4686 is in absorption. An alternative would be to assign a peculiar O–WC10 classification. However, we feel that WC11 better indicates the close similarly to WC10 spectra and is more useful for our understanding of its nature.

4.2.4 WCL Spectral Atlas

Fig. 4.3 presents spectra of our programme WCL stars that cover our spectral diagnostics. They are ordered by new spectral subclass. For uniformity, spectra were rebinned to 1Å per resolution element; strong features are re–scaled so that weak features are still clear. As previously discussed, WC8–9 and WC10–11 stars are very distinct in their line strengths and ratios.

[1]The massive WC9 star WR104 (Ve 2–45) has recently displayed spectral variability revealing a temporary WC11 spectrum (Crowther 1997).

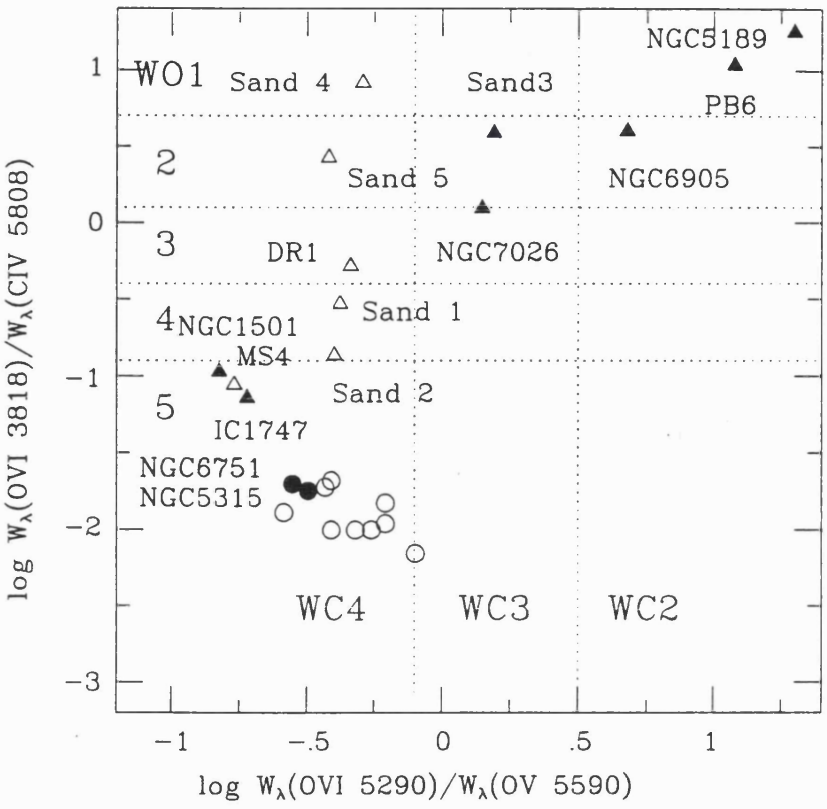

Figure 4.4: Emission line equivalent width ratios for the principal classification criteria for WCE stars according to Méndez and Niemela (1982), namely O VI λ5290/O V λ5590 versus the principal criteria for WO stars according to Kingsburgh et al. (1995), namely O VI $\lambda\lambda$3811–34/C IV $\lambda\lambda$5801–12. WC4 stars are presented as circles, WO stars as triangles, with filled (open) symbols for CSPN (Population I) stars. Clearly, an individual star can be assigned different spectral types and classes on the basis of the different schemes followed

4.3 Classification of WCE and WO Stars

High excitation WC–type CSPN are presently classified on a different scheme (Méndez and Niemela 1982) from Population I WC and WO stars (Smith et al. 1990; Kingsburgh et al. 1995). In this Section we investigate whether the classification schemes can be, or indeed should be, unified.

4.3.1 Current WCE and WO Schemes

For high ionization CSPN showing negligible C III λ5696 emission, Méndez and Niemela (1982) suggest classification into WC2–4 subtypes using diagnostics lines: O V λ5590, O VI λ5290 and O VII λ5670. For the Population I Sanduleak (1971) stars that show extremely strong O VI $\lambda\lambda$3811–34 emission, Barlow and Hummer (1982) introduced the WO subclass; this sequence was later quantified by Kingsburgh et al. (1995) using the diagnostics O IV λ3400, O V λ5590 and C IV $\lambda\lambda$5801–12. Population I stars without strong O VI emission are left in the WC4 subclass of Smith et al. (1990). The three schemes yield different classifications for the same spectrum: e.g. NGC 6905 would be classified [WC3] in the scheme of Méndez and Niemela (1982), [WC4] in the scheme of Smith et al. (1990), and [WO2] in the scheme of Kingsburgh et al. (1995). Since the primary WO subclass criterion depends on C/O line ratios, both ionization and composition effects play a role in this scheme.

In Fig. 4.4 we present equivalent width ratios of our programme WCE CSPN stars, supplemented by 6 WO stars (Kingsburgh et al. 1995), 3 WC4 stars in the Galaxy and 5 WC stars in the LMC (Torres and Massey 1987). The horizontal axis shows the ionization ratio W_λ(O VI λ5290) /W_λ(O V λ5590) of the Méndez and Niemela (1982) scheme, while the vertical axis indicates the primary WO criterion of Kingsburgh et al. (1995), namely W_λ(O VI $\lambda\lambda$3811-34)/ W_λ(C IV $\lambda\lambda$5801-12). Clearly, depending on one's preference, individual stars may presently be assigned either a WCE or WO spectral classification.

However, both schemes suffer from certain limitations. The primary WO1–5 diagnostic of Kingsburgh et al. (1995) involves both ionization and C/O abundance effects. From

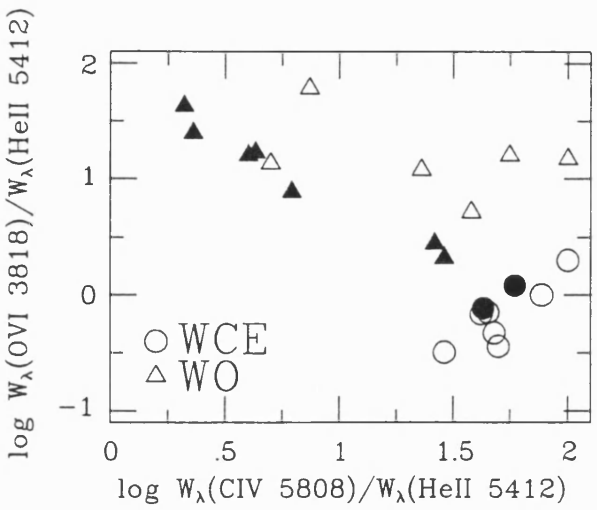

Figure 4.5: Comparison between the equivalent width ratios W_λ(C IV λ5805)/W_λ(He II λ5412) and W_λ(O V λ5590)/W_λ(He II λ5412) for massive WO and WCE stars (open), and their CSPN counterparts (filled). This demonstrates the absence of a systematic difference between C/He ratios for massive WC and CSPN. The low O V/He II ratios in some CSPN is as a result of extremely high excitation (e.g. NGC 6905).

Fig. 4.4 this is incapable of distinguishing between WO stars, such as Sand 5, and ultra–high ionization CSPN, such as NGC 6905. Meanwhile, the complex qualitative scheme of Méndez and Niemela (1982) successfully distinguishes between Sand 5 and NGC 6905, but is unable to separate between WO and WC4 stars.

4.3.2 A Unified Scheme for WCE and WO Stars?

In our revision to the WCE and WO classification scheme, we first consider whether the existing Population I and CSPN Wolf–Rayet stars should remain separate, or instead be unified. To answer this question we first consider whether we would expect chemical differences between these stars. In massive WCE and WO stars, carbon and oxygen are produced continuously in the non–degenerate He–burning core, and are exposed by mass–loss stripping. Meanwhile, in CSPN carbon and oxygen are produced during thermal pulses at the degenerate bottom of the He–shell, produced ~10% of the time, which are

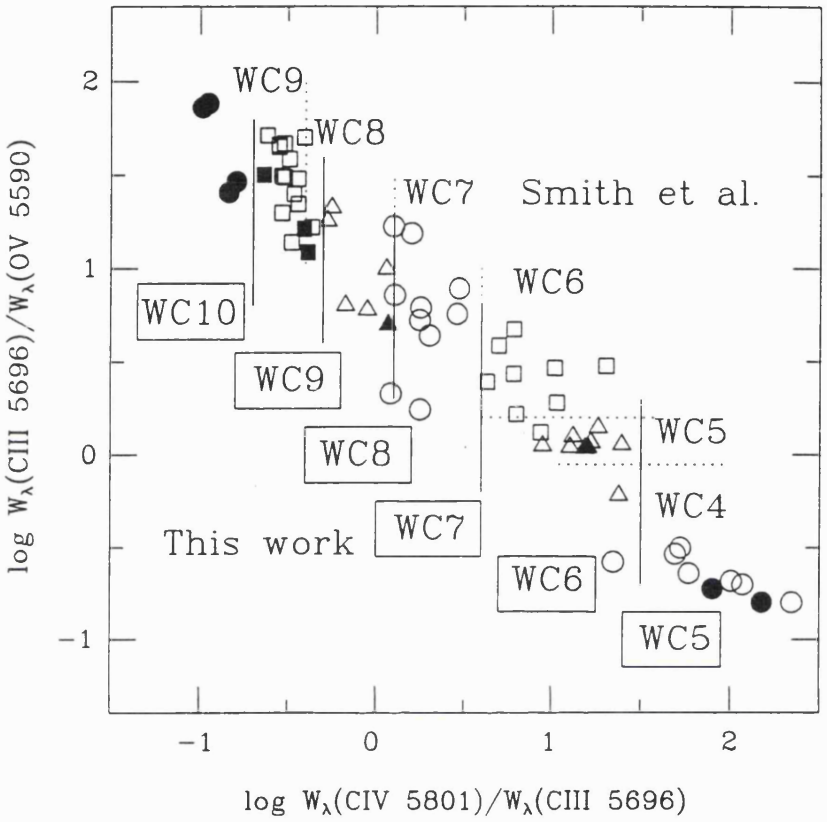

Figure 4.6: Emission line equivalent width ratios for both Galactic and LMC massive WC stars (open), and WC-type CSPN (filled). We follow the principal classification criteria for WCE stars according to Smith et al. (1990), namely C III λ5696/C IV $\lambda\lambda$5801–12 versus C III λ5696/O V λ5590. Boundaries of the existing Smith et al. (1990) spectral classification are shown (dotted lines) together with our revisions (solid lines, boxed spectral types)

then dredged up to the surface when the H–shell is ejected. Observed O/C ratios are critically dependent on the temperature and density of the He–burning zone. If O/C line ratios are similar in Population I and CSPN stars, we may expect similar conditions in their formation zones. Differences are however expected in values of (C+O)/He, with CSPN anticipated to possess significantly higher helium contents. We might therefore expect lower values of (C+O)/He in CSPN, relative to their massive counterparts.

From the ordinate axis of Fig. 4.4, it is apparent that O/C ratios do not show systematic differences between the two groups of stars, suggesting that these are comparable. We attempted to compare C/He ratios for the two groups of stars, using C IV λ5471/He II λ5412, since both these recombination lines are sensitive to abundance. However, the extremely high wind velocities, and weak emission lines of many stars, prohibited this comparison. Instead, in Fig. 4.5 we compare equivalent width line ratios of C IV $\lambda\lambda$5801–12/He II λ5412 versus and O V λ5590/He II λ5412, to seek information on potential C/He and O/He differences. Contrary to expectation, we find no systematic differences C/He between the two groups of star, although ionization effects produce weak C IV λ5808 in some ultra–high excitation CSPN. Our results support abundances recently derived from non-LTE analyses. Koesterke and Hamann (1995) obtained number fractions of C/He=0.08–0.4 for several massive WCE stars, while Koesterke and Hamann (1997) derived similar ratios of C/He=0.13–0.2 for two WCE–type CSPN, NGC6751 and Sand 3. Unfortunately, oxygen contents for massive WCE stars remain poorly determined. Therefore, there appears to be no clear discriminator between WCE/WO Population I stars and WC2–4 CSPN, indicating that a unified classification scheme is appropriate.

4.3.3 A Revised Spectral Classification for WCE and WO Stars

We now proceed to the decision of nomenclature – should we follow the existing WC or WO scheme for high excitation Wolf–Rayet stars? Spectral types should be chosen according to the dominance of features in their optical spectra. WN and WC stars can readily be distinguished by the prominence of nitrogen or carbon features, which is as a

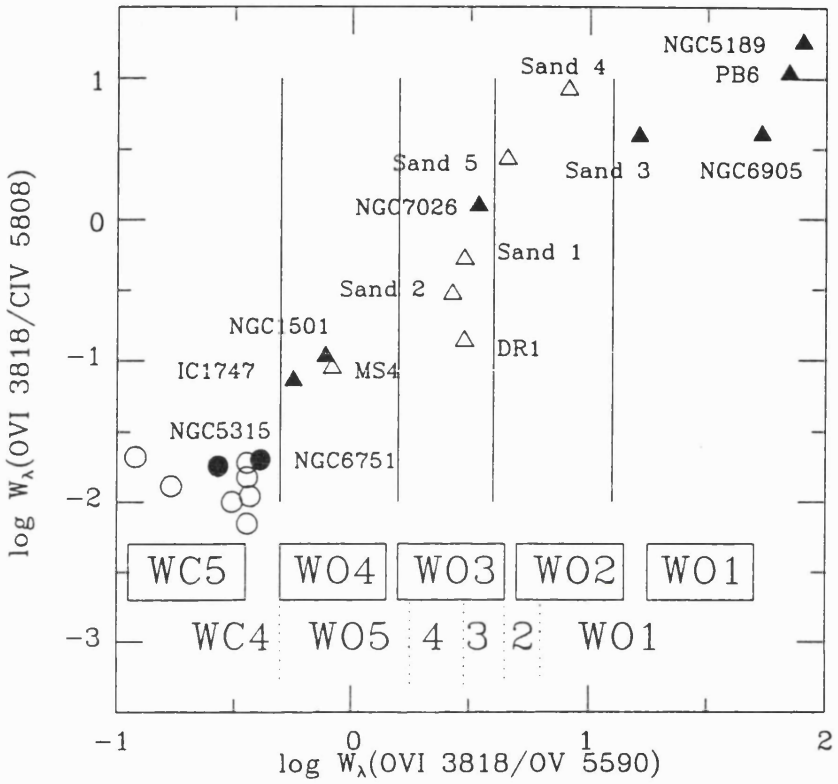

Figure 4.7: Emission line equivalent width ratios for massive WO stars (open), and WO–type CSPN (filled) using the principal classification criteria for WO stars from Kingsburgh et al. (1995). Boundaries of existing spectral types are shown (dotted lines), together with our revisions (solid lines, boxed spectral types)

result of a dramatic change in chemistry, caused by the rapid conversion of nitrogen to carbon. However, there appears to be no such dramatic change between massive WC and WO stars. Kingsburgh et al. (1995) demonstrated that there was no discontinuity in (C+O)/He ratios between WC and WO stars, although WO metal abundances were at the upper end of previous determination for WC stars. In contrast, significantly higher (C+O)/He ratios are anticipated in WO stars from massive star evolutionary models (Smith and Maeder 1991).

Therefore, it appears that the dominance of oxygen spectral features in WO stars is primarily as a result of ionization effects, rather than a dramatic abundance change relative to WC stars. We therefore favour the adoption of WO subclasses for high excitation stars, with spectral types chosen to provide a smooth ionization sequence from WC to WO. At present, high excitation WC spectral types are defined up to WC4 (Smith et al. 1990) or WC2 (Méndez and Niemela 1982), with low excitation WO spectral types defined from WO5 (Kingsburgh et al. 1995). We feel a smooth ionization transition from WC to WO would be more appropriate. This is accomplished in two ways.

Let us first re–examine the definition of early-WC stars according to Smith et al. (1990). From their quantification of the WC classification scheme, Smith et al. used W_λ(C IV $\lambda\lambda$5801–12)/W_λ(C III λ5696) as their primary ionization indicator, which provided a well defined division between subclasses, except between WC5 and WC6 for which a secondary diagnostic was required, namely W_λ(C III λ5696)/ W_λ(O V λ5590). Following the suggestion of Lindsey Smith (private communication), we propose that the existing WC5 and WC6 subclasses are merged into a single WC6 class, since their ionization strengths are comparable. This allows existing WC4 stars to be re–defined as WC5 stars. Our revisions are illustrated in Fig. 4.6, where we compare the equivalent width ratios of these lines for Galactic and LMC massive WC stars, updated from Figure 3 of Smith et al. (1990) to include our programme CSPN. From this figure, differences in the WC populations between the two groups of star are apparent (see Section 4.4). Our complete WC spectral classification definitions are indicated in Table 4.3.

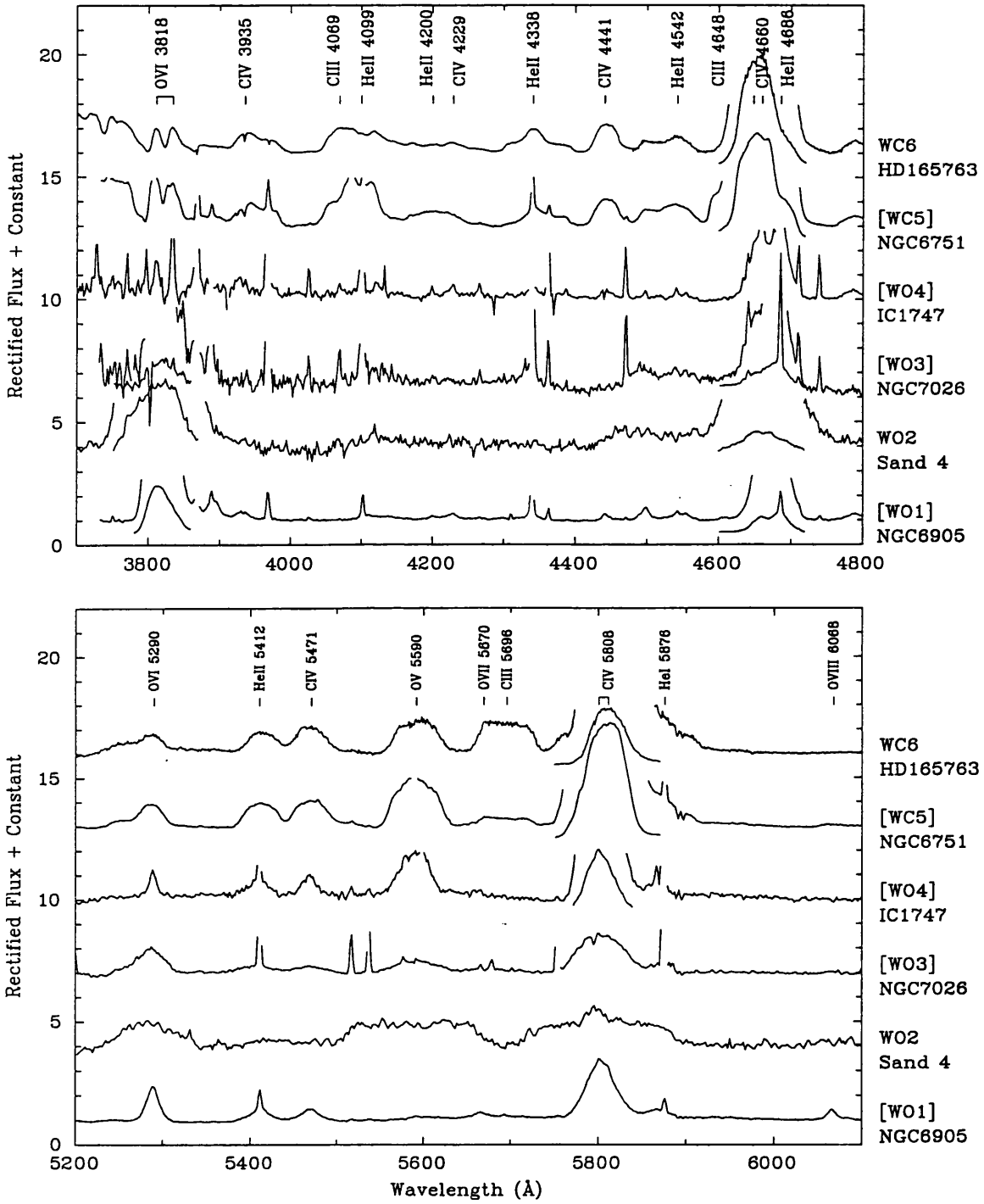

Figure 4.8: Spectral comparison of WO1–4..WC5–6 stars between $\lambda\lambda$3700–4800 and $\lambda\lambda$5200–6100, sorted by spectral type, demonstrating the change in ionization. Sharp emission lines are of nebular origin and include He II λ5412, Cl III λ5538 and He I λ5876. Spectra are rectified, separated by 3 continuum units, with very strong lines shown divided by a factor of five (ten for C IV λ5808 profiles for WC5–6 stars), offset by 0.5 continuum units, for clarity

We now re–examine the existing definitions of WO stars, according to Kingsburgh et al. (1990). An appropriate division between WC and WO subclasses appears to be the presence or absence of C III λ5696, as proposed by Kingsburgh et al. (1995). In Fig. 4.7 we present the primary and secondary equivalent width ratios from Kingsburgh et al. (1995), for those stars introduced in Fig. 4.4. Although both their criteria readily discriminate between existing WO stars, their primary indicator, W_λ(O VI $\lambda\lambda$3811-34)/ W_λ(C IV $\lambda\lambda$5801-12), fails to separate WO stars from higher ionization stars such as NGC 6905, and could be affected by O/C variations. We find that their secondary indicator, W_λ(O VI $\lambda\lambda$3811-34)/ W_λ(O V λ5590), provides a more suitable spectral type indicator, since it is based on a single element. From the motivation of minimising reddenings, we searched for suitable indicators in the yellow–red part of the spectrum (e.g. O VI λ5290), but found that O VI $\lambda\lambda$3811-34 was indispensible. Nevertheless, W_λ(O VI λ5290)/W_λ(O V λ5590) in excess of unity appear to be exclusive to ultra–high excitation WO–type CSPN.

In Fig. 4.7 we include the existing W_λ(O VI $\lambda\lambda$3811-34)/ W_λ(O V λ5590) divisions between WO subclasses according to Kingsburgh et al. (1995). Unfortunately their scheme suffers from the following deficiencies: (i) individual WO subclasses are defined over a very small range, $\sim$0.2 dex, in this equivalent width ratio at present, leading to very small numbers of stars in each spectral class; (ii) nothing distinguishes between Sand 4 and the higher excitation star NGC 6905; (iii) current subclass names fail to indicate that WO5 stars are of equal or higher ionization than WC4 stars. in contrast with the original WO definition by Barlow and Hummer (1982). We therefore feel it is more useful to re-define the existing WO boundaries, commencing with WO4 at the low excitation end, in order to smoothly connect with the WC subclass, with WO1 for the highest excitation stars. Although alternatives were carefully considered, such as introducing a WOE and WOL for early and late WO stars, the nomenclature scheme defined here is the most intuitive and physically meaningful.

Boundaries between WO spectral types have been chosen to follow the presence or absence of other oxygen ionization stages. Although WO subclasses are defined according

to their W_λ(O VI $\lambda\lambda$3811-34)/ W_λ(O V λ5590) ratio, as summarised in Table 4.3, secondary criteria are as follows: WO4 stars show W_λ(O VI $\lambda\lambda$3811–34) $\ll$ W_λ(C IV λ5801–12); WO3 stars have $0.1 \leq W_\lambda$(O VI/C IV)≤ 1.5; with O VIII λ5670 weak or absent; WO2 stars have W_λ(O VI/C IV)≥ 1.5 and W_λ(O VII λ5670/O V λ5590)≤ 1, and finally WO1 stars have W_λ(O VII λ5670/O V λ5590)≥ 1, plus the presence of O VIII λ6068.

In Table 4.4 we present a comparison between spectral types derived here for all programme CSPN together with previous classifications from the literature. Similar comparisons are made for massive WC stars in Table 4.5. In Fig. 4.8, we present rectified spectra of our programme WC5 and WO1–4 CSPN. For comparison, we include HD 165763 (WR111) from Crowther, Smith and Willis (1995b) newly classified here as a WC6 star, and Sand 4 (WR102), from Kingsburgh et al. (1995), newly classified as a WO2 star. NGC 6751 ([WC5]) is unique among our sample of high excitation CSPN in that it closely resembles the very strong emission profiles of massive WCE stars. Nevertheless, other WCE–type CSPN are known to exhibit similar characteristics (e.g. NGC 5315, Hamann 1996), so, a general spectroscopic distinction between CSPN and Population I WCE stars is not available (see Section 4.3.4 for WO stars). Nevertheless, from Fig. 4.7, our scheme confirms a genuine absence of massive WO stars with spectral type earlier than WO2. Ultra–high ionization WO1 stars, the so–called 'O VIII sequence' (Feibelman 1996), are found only in CSPN.

Additional criteria are necessary to distinguish between WCE or WO stars and other emission stars. In particular, example, C IV $\lambda\lambda$5801–12 emission is not restricted to WC or WO–type CSPN. C IV $\lambda\lambda$5801–12, O VI $\lambda\lambda$3811–34 and λ5290 emission is observed in Abell 78 (PN G081.2−14.9, Smith and Aller 1969). This star currently possesses a variety of spectral classifications, namely Of-WR(C) (following Mendez et al. 1991), [WC]–PG1159 (Hamann 1996) or 'weak emission line' (Tylenda et al. 1993). Although optical emission features in this star are extremely weak (W_λ(C IV λ5808)$\leq$15Å), a [WO1] spectral type is obtained for Abell 78 from our primary criteria presented in Table 4.3, although O VII–VIII are weak/absent. We therefore propose to restrict *bona fide* WCE or

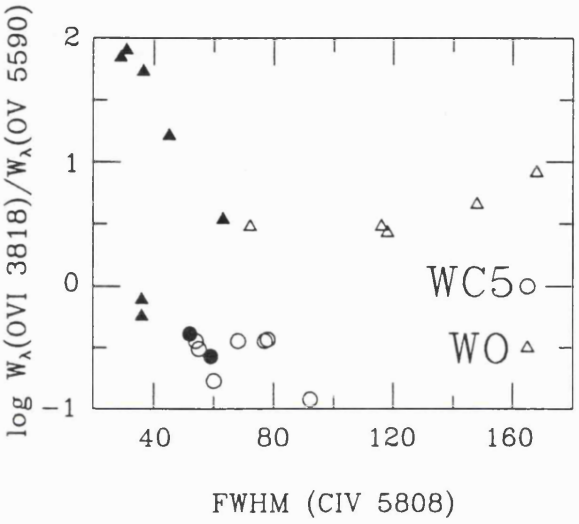

Figure 4.9: Comparison between the FWHM(C IV $\lambda\lambda$5801-12) versus our primary WO spectral diagnostic W_λ(O VI λ3811-34)/W_λ(O V λ5590) for massive WO and WC5 stars (open), and their CSPN counterparts (filled). This shows that we are unable to distinguish between massive WO and WC5 stars on the basis of FWHM(C IV $\lambda\lambda$5801-12) alone. However, all massive WO stars show a reasonable separation from CSPN from their FWHM (C IV $\lambda\lambda$5801-12).

Table 4.4: Revised spectral classifications for WC and WO-type CSPN, including several stars from previously published spectroscopy. We include subtypes from the literature – Smith and Aller (1969, SA69), Hu and Bibo (1990, HB90), Tylenda et al. (1993, T93) including revisions in Acker et al. (1996), plus Méndez and Niemela (1982) for WCE stars, Méndez et al. (1991) for SwSt1, Cohen and Jones (1987) for IRAS 21282+5050, and Menzies and Wolstencroft (1990) for IRAS 07027–7934

Star	SA69	HB90	T93	Others	This work
NGC 5189			WC2		WO1
PB6			WC3		WO1
NGC 6905			WC3	WC3	WO1
Sand 3			WC3		WO1
NGC 7026			WC3/4	WC3	WO3
IC 1747			WC4	WC4	WO4
NGC 1501			WC4	WC4	WO4
NGC 5315			WC4		WC5
NGC 6751			WC4	WC4	WC5
M1–25			WC6		WC6
NGC 40	WC8		WC8		WC8
BD+30°3639	WC9		WC9		WC9
He 2–459			WC9		WC9
He 2–99	WC9		WC9		WC9
SwSt1	WR-Of	WC10	*wel*	Of-WR(C)	WC9pec
IRAS 17514–1555		WC11			WC10
M4–18		WC11	WC11		WC10
He 2–113		WC11	WC11		WC10
CPD–56°8032		WC11	WC11		WC10
IRAS 07027–7934			WC11	WC11	WC10
K2–16			WC11		WC11
IRAS 21282+5050				WC11	O9–9.5

Table 4.5: Spectral classifications for massive WC and WO stars, including those stars revised relative to Smith et al. (1990) and Kingsburgh et al. (1995). We include many stars from previously published spectroscopy (Torres and Massey 1987), and compare with subtypes from the literature – van der Hucht et al. (1988, vdH88), Smith et al. (1990, SSM90), Kingsburgh et al. (1995, KBS95). All existing LMC WC4 stars are re-classified to WC5

WR	Star	vdH88	SSM90	KBS95	This work
4	HD 16523	WC5	WC5		WC6
9	HD 63099	WC5+a	WC5+O7		WC6+O7
17	HD 88500	WC5	WC5		WC6
19	LS3	WC4	WC4		WC5
29a	MS4	WC4+a	WO4+O4	WO5+O4	WO4+O4
32	MS5	WC5	WC5		WC6
33	HD 95435	WC5	WC5		WC6
52	HD 115473	WC5	WC4		WC5
53	HD 117297	WC8	WC8		WC9
102	Sand 4	WO1	WO1	WO1	WO2
111	HD 165763	WC5	WC5		WC6
114	HD 169810	WC5	WC5		WC6
142	Sand 5	WO2	WO2	WO2	WO2
143	HD 195177	WC4	WC5		WC6
144	MR110	WC4	WC4		WC5
150	ST5	WC5	WC5		WC4
Br93	Sand 2			WO4	WO3
AB8	Sand 1			WO4	WO3

WO spectral classifications for those stars showing sufficiently strong emission lines, in particular W_λ(C IV $\lambda\lambda$5801–12)$\gg$10Å. Clearly the present classification system for stars with a weak emission line spectrum is far from satisfactory at present. Since Abell 78 shows several charactistics in common with both WO stars and PG1159 stars (high temperature, high gravity, pre–white dwarfs), we tentatively propose a hybrid [WO1]-PG1159 classification for this star. Any further revisions are beyond the scope of the present work.

4.3.4 Can Line Widths Distinguish Between WC and WO Stars?

Since O VI $\lambda\lambda$3811-34 may be unavailable in heavily reddened objects, are alternative criteria available to distinguish between our new WO and WC5 stars? Smith et al. (1990) and Smith and Maeder (1991) proposed that since the Sanduleak (1971) WO stars show extremely broad emission lines relative to WC stars, FWHM (C IV $\lambda\lambda$5801–12)=90Å represented a suitable division between the two sequences. However, Willis et al. (1992) found that this represented a poor discriminator, at least for WR stars in M33, since line widths were observed to be metallicity dependent. In Fig. 4.9 we compare the FWHM(C IV $\lambda\lambda$5801–12) with our primary WO diagnostic for massive WC5 and WO stars in our Galaxy, the Magellanic Clouds and IC 1613, plus CSPN counterparts. Although the Sanduleak WO stars show extremely broad spectral features (FWHM$\sim$140$\pm$25Å), DR1 in IC 1613 shows a relatively normal line width (FWHM$\sim$72Å) relative to WC5 stars (FWHM$\sim60^{+30}_{-20}$Å). We therefore support the results of Willis et al. (1992), that it is not possible to cleanly distinguish between WO and new WC5 stars in the optical without spectroscopic observations at O VI $\lambda\lambda$3811–34. However, we note that the WO–type CSPN under investigation here do show systematically lower line widths than massive WO stars, with FWHM(C IV $\lambda\lambda$5801–12)$\sim$70Å representing an approximate division. More definite conclusions await comparisons with a more complete sample of WO–type CSPN.

4.4 Summary

We have presented new observations of WC and WO–type central stars of Planetary Nebulae and classical Wolf–Rayet stars, their more massive counterparts. A unified classification scheme has been developed, allowing an unambiguous definition of spectral type for all stars. In increasing order of excitation, our spectral classes range from WC11 to WC5 for Wolf–Rayet stars with a dominant carbon line spectrum, and subsequently from WO4 to WO1 for those with oxygen lines. The continuation in spectral sequence from WC to WO is used to indicate that the sequence is due primarily to excitation, rather than abundance.

Our unified scheme provides an objective method of comparing the massive Wolf–Rayet populations with CSPN. Our results support previous suggestions for an absence of WC–type CSPN at intermediate excitation (Tylenda et al. 1993). This is beautifully illustrated in Fig. 4.6, where WC6–8 CSPN are almost completely absent. From our sample of 51 massive WC stars, 61% are of spectral type WC6–8. Meanwhile, only 17% of WC–type CSPN (2 out of 12 stars) lie within this excitation range, i.e. the majority of WC–type CSPN are either of extremely low (WC9–11) or high (WC5) spectral type. WC10–11 stars are exclusive to CSPN. From our comparisons between the observed WO populations, narrow–lined, ultra–high excitation WO1 stars are also exclusive to CSPN (Fig. 4.7).

Our new classification scheme should allow greater progress to be made relating to the evolutionary sequence of WC and WO–type CSPN – specifically whether the sparsity of WC6–8 CSPN indicates either a rapid evolution between WCE and WCL CSPN, or alternative evolutionary states for WCE and WCL stars. Detailed physical and abundance studies are keenly sought, in order to verify our suggestions of comparable chemical abundances in both massive and CSPN WC–type stars.

Chapter 5

The WC10 Central Stars CPD–56°8032 and He 2–113: Distances and Nebular Parameters

CPD–56°8032 and He 2–113 are the two brightest members of a class of cool WR central stars of PN of which there are only six confirmed examples at present (M 4–18, K 2–16, IRAS 17514–1555 (PM 1–188) and IRAS 07027–7934). These WC10 stars have no hydrogen and may be the precursors to the hot non–radially pulsating PG1159 stars (Barlow and Storey 1993; Leuenhagen, Heber and Jeffery 1994). This link can be confirmed if one can show that the He, C and O abundances in their winds are the same as have been derived for the photospheres of PG1159 stars. They may also be the precursors of the H–deficient DB white dwarfs.

The wind expansion velocities of these WC10 stars (200 km s^{-1}) are much lower than those of most WR stars (> 1000 km s^{-1}). The reduced line blending means that elemental abundances can be derived more accurately than for other WR stars. We show that the wind electron temperatures can even be derived, using dielectronic lines – allowing the first direct measurement of the temperature of a hot star wind (Chapter 7).

The planetary nebulae around these two stars are two of the brightest IR emitters

known amongst PN (as revealed by the near infrared photometry of Webster and Glass (1974) and the mid infrared photometry of Cohen and Barlow (1980)). The rich mid infrared UIR–band spectrum of both objects was revealed by the spectrophotometry of Aitken et al. (1980) and Cohen et al. (1989). Very strong UIR–bands are normally attributed to aromatic hydrocarbons such as PAHs. They are correlated with a high C/O ratio and indicate a carbon–rich dust to be predominant (Barlow 1983, Cohen et al. 1989). Cohen et al. (1986, 1989) found that the ratio of UIR–band flux to total IR flux was the highest in their sample. Together with the other objects in their sample, they showed a strong correlation between the UIR flux ratio and nebular C/O ratio, and Cohen et al. (1989) noted that a determination of the nebular C/O ratio for CPD–56°8032 and He 2–113, expected to be high, was important for confirming the correlation and for throwing light on the origin of the UIR bands. We have determined the accurate nebular C/O ratios that are needed. The analysis of IUE spectrophotometry has shown CPD–56°8032 to possess an abnormal ultraviolet reddening law, with an unusually weak 2200 Å extinction feature (Rao, Giridhar and Nandy 1990; Jeffery 1995), consistent with a significant fraction of the extinction to the star arising from circumstellar dust.

CPD–56°8032 was first recognised as a cool carbon Wolf–Rayet star by Bidelman et al. (1968), while He 2–113 was found to be an emission–line star by Henize (1967); the spectrum was later discussed by Carlson and Henize 1979). Cowley and Hiltner (1969) described an intermediate dispersion spectrum of the blue spectral region of CPD–56°8032 and found weak nebular hydrogen and forbidden lines which were much narrower than the stellar He I, C II, C III and O II emission lines. They measured V = 11.04 and estimated an E(B–V) of 0.44. Thackeray (1977) described the red region of CPD–56°8032's spectrum, observed at intermediate resolution. Both stars are classified in Chapter 4 as [WC10].

The nebular properties of CPD–56°8032 were investigated by Houziaux and Heck (1982), who derived the nebular carbon abundance, while Rao (1987) derived abundances of nitrogen, oxygen and sulphur for both CPD–56°8032 and He 2–113.

Pollacco et al. (1992) discovered CPD–56°8032 to be a variable star, showing two

symmetric minima in its lightcurve about a year apart, both with a duration of about ten days. Lawson and Jones (1992) published further photometry of the star, covering a time span of about 1600 days. They found that the decline time from the mean visual magnitude of 11.1 to the minimum magnitude of 12.4 was about 80 days, with the initial fade occurring particularly quickly, in about ten days. They estimated the typical recovery time to be about 400 days. The deep minima exhibited by CPD–56°8032 suggest parallels with the hydrogen–deficient R CrB stars, whose deep declines are attributed to obscuration events by ejected dust clumps (e.g. Clayton 1996). However, He 2–113 (a spectroscopic twin to CPD–56°8032) has been monitored at visual wavelengths over a period of five years by Lawson and Jones (private communication) and was found not to vary within the observational uncertainties of ±0.1 magnitudes. The lightcurves of both objects are presented in Appendix A.

In Section 5.1, the nebular Balmer lines ratios are discussed and reddenings, broad-band stellar magnitudes, and the radial and expansion velocities of the nebulae are derived. In Section 5.2, the distances to the objects are estimated. In Section 5.3, pre–COSTAR *HST* Hβ images of the nebulae around the two stars are analysed for the first time. In Section 5.4, electron temperatures and densities are determined for both nebulae, together with nebular abundances for carbon, oxygen, nitrogen and sulphur, relative to hydrogen. Finally, in Section 5.5, we draw some conclusions. The two echelle spectra are displayed in Appendix C, together with complete line identifications.

5.1 Apparent Magnitudes, Radial Velocities and Reddenings

5.1.1 Apparent Magnitudes

We convolved our observed spectra of CPD–56°8032 and He 2–113 with broad–band V and B filter profiles (kindly made available to us by Dr. J. R. Deacon) to obtain an estimate of the apparent V and B magnitudes of the stars. For CPD–56°8032, the V magnitude

in May 1993 was found to be 10.9±0.1, indicating that the star was at maximum light and in agreement with the estimate of W. Lawson and A. Jones (private communication; see Appendix A) of 11.0±0.1 for the same epoch. The B magnitude derived from our 1993 spectrophotometry is 11.25±0.1. Lawson and Jones' lightcurve for CPD–56°8032, sampled between JD2447200 (early 1988) and JD2450300 (October 1996), indicated that during this period the star had two declines, each followed by a recovery to maximum light (V∼11.0): one starting in March 1990 and one in August 1994. The star took about 400 days to fully recover from the first minimum, which had an initial depth of about 1.3 magnitudes. From our 1981 spectrum of CPD–56°8032 we derive a V magnitude of 11.01±0.1 and a B magnitude of 11.38±0.1, again indicating that the star was at maximum light. For He 2–113, we derive V = 11.7±0.1 and B = 12.3±0.1 in May 1993. W. Lawson and A. Jones (private communication) found that He 2–113 never varied from a mean magnitude of V = 12.0±0.1 since late September 1990 (Appendix A).

5.1.2 The Nebular Balmer Lines in the Spectra of CPD–56°8032 and He 2–113

The Hα and Hβ lines observed in the spectra of both CPD–56°8032 and He 2–113 have shapes that cannot be perfectly fitted with a single Gaussian. This could either indicate the presence of an underlying stellar component or that the nebula has an irregular velocity structure.

The main argument in favour of a nebular origin for the entire flux in the Balmer lines comes from a comparison of the Hα line profiles with those of the nebular [O I] line at 6300 Å (see Fig. 5.1). As can be seen, the widths and the overall shapes of the wings of the lines are very similar. A comparison of the Hβ profiles with those of the circum–nebular sodium D–lines seen in absorption in the spectra of both stars also supports a nebular origin for the broad wings (see Section 5.1.4 and Fig. 5.2). The lack of evidence for Balmer line emission from the stellar winds is discussed further in Chapter 6. The observed Hα and Hβ line fluxes from both nebulae are presented in Table 5.2.

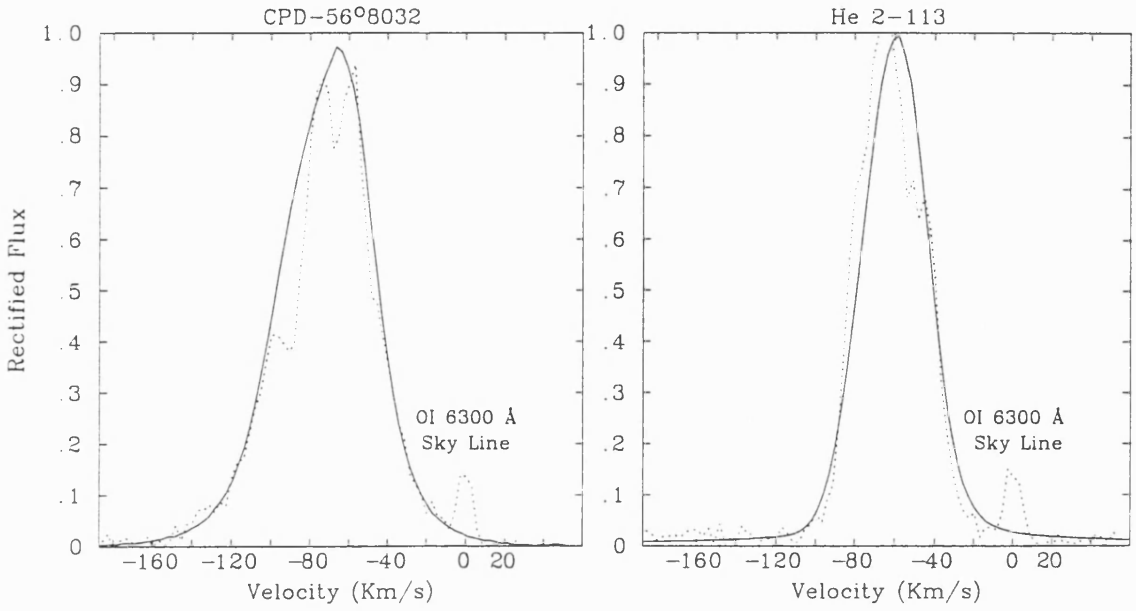

Figure 5.1: Comparison of the Hα line profile (solid) with that of the nebular [O I] line at 6300 Å (dotted), for CPD–56°8032 (left) and He 2–113 (right)

5.1.3 Nebular Radial Velocities and Expansion Velocities from the Balmer Lines

Radial velocities for the nebulae were obtained by determining the wavelength shifts of the nebular Balmer lines (the Hα and Hβ lines were used, since Hγ and Hδ were blended with stellar features, but a check using Hγ and Hδ did not show any serious discrepancies). The shift was determined by fitting a single Gaussian to each of the Hα and Hβ lines. Although a single Gaussian did not fit the profiles very well, it was felt that it was the best way to locate the overall centre of weight of the line, without introducing biases due to the asymmetry of the nebular lines. Mean heliocentric radial velocities of -59.4 ± 3.0 km s^{-1} and -57.3 ± 3.0 km s^{-1} were found for CPD–56°8032 and He 2–113, respectively, corresponding to LSR radial velocities of -59.6 km s^{-1} and -58.4 km s^{-1} respectively. These radial velocities are listed in Table 5.1, together with the nebular expansion velocities, which were assumed to be given by the mean half width at half maximum of the Hα and Hβ line profiles. Sahai et al. (1993) have measured the LSR radial velocity of

Table 5.1: Radial velocities derived for the components of the Na D line velocity components. The nebular expansion velocities are derived from an average of half the FWHM of the Hα and Hβ lines

Star's Name	LSR radial velocity (km s^{-1})	Nebular expansion velocity (km s^{-1})	LSR R.V. of components (km s^{-1})	D (kpc) (rotation curve)	$\|z\|$ (pc)	D (kpc) (IR flux)
CPD–56°8032	–59.6 ± 3.0	30 ± 4	–124 –110 –93 –20 –15 –7	1.6 ± 0.2	275	1.35 ± 0.3
He 2–113	–58.4 ± 3.0	19 ± 1	–97 –85 –68 –28 –19 0 +4	1.9 ± 0.2	132	1.50 ± 0.3

Table 5.2: Fluxes measured for the nebular hydrogen lines

Star	Line	1993 Flux (ergs cm^{-2} s^{-1})	1981 Flux (ergs cm^{-2} s^{-1})	1978/79 Flux (Aitken et al., 1980) (ergs cm^{-2} s^{-1})
CPD–56°8032	Hα	3.98×10^{-12}	5.38×10^{-12}	6.31×10^{-12}
	Hβ	9.60×10^{-13}	9.23×10^{-13}	1.12×10^{-12}
He 2–113	Hα	1.75×10^{-11}	–	–
	Hβ	2.16×10^{-12}	–	1.51×10^{-12}

CPD–56°8032 in the CO J = 2–1 and 1–0 lines and list a value of –57 km s^{-1} for both CO lines (no uncertainty quoted), which agrees with the value of (–59.6 ± 3.0) km s^{-1} found here from the nebular Balmer lines. Sahai et al. (1993) also determined a FWHM of 50 km s^{-1} for the J = 1–0 and 2–1 CO lines, in reasonable agreement with the mean FWHM of 60 km s^{-1} derived here for the Hα and Hβ lines, which we assume to be equal to twice the nebular expansion velocity.

5.1.4 High Velocity Components in the Circumstellar Neutral Gas

In Section 5.2.2 the sodium D lines are used to obtain an estimate of the distance to CPD–56°8032 and He 2–113. There we argue that some of the Na D line radial velocity components are of nebular origin. However a question which remains to be addressed is the origin of the highest velocity components of the sodium D lines. If their origin is nebular,

Table 5.3: Reddenings derived from Balmer lines ratios and from the radio to Hβ ratio

Star	Ratio	E(B–V) (1993)	E(B–V) (1981)	1978 E(B–V) (Aitken et al. 1980)
CPD–56°8032	Hα/Hβ	0.34	0.68	0.60
	radio/Hβ	0.68	0.69	0.60
He 2–113	Hα/Hβ	1.02	–	–
	radio/Hβ	0.98	–	1.10

we would expect to find the absorption features at a velocity corresponding to the radial velocity of the star minus the nebular expansion velocity. From the nebular LSR radial velocities and expansion velocities listed in Table 5.1, we would then expect a velocity component at –90 km s^{-1} for CPD–56°8032 and at –77 km s^{-1} for He 2–113. We identify these with the Na I components observed at –93 km s^{-1} (i.e. –33 km s^{-1} relative to the nebular central velocity) for CPD–56°8032 and at –85 km s^{-1} (i.e. –27 km s^{-1} relative to the nebular central velocity) for He 2–113 (Fig. 5.2; the combined error on the LSR radial velocity and on the nebular expansion velocity, together with the likely error on the velocity shift of the Na D line components, ±5 km s^{-1}, can explain the differences). In addition, each nebula shows further Na I absorption components with even greater blue–shifts, at LSR velocities of –110 and –124 km s^{-1} in the case of CPD–56°8032 (i.e. at –50 and –74 km s^{-1} in the nebular velocity frame) and at –97 km s^{-1} in the case of He 2–113 (–39 km s^{-1} in the nebular velocity frame).

An alternative way to look for a confirmation of the presence of high velocity nebular components is to look at the structure of nebular lines that should be formed in a similar region to the neutral sodium. Lines with this characteristic are, for instance, the [O I] $\lambda\lambda$6300.3,6363.8 doublet (the higher energy of the upper level of the 5577 Å line makes it more difficult to excite and only the sky counterpart was present in the spectrum). In Fig. 5.2, the profile of [O I] λ6300 is plotted, along with that of the sodium D2 line. On the y–axis we plot the rectified profiles, offset by arbitrary constants. On the x–axis, the zero–point corresponds to the nebular radial velocity. If we ignore anything with a velocity

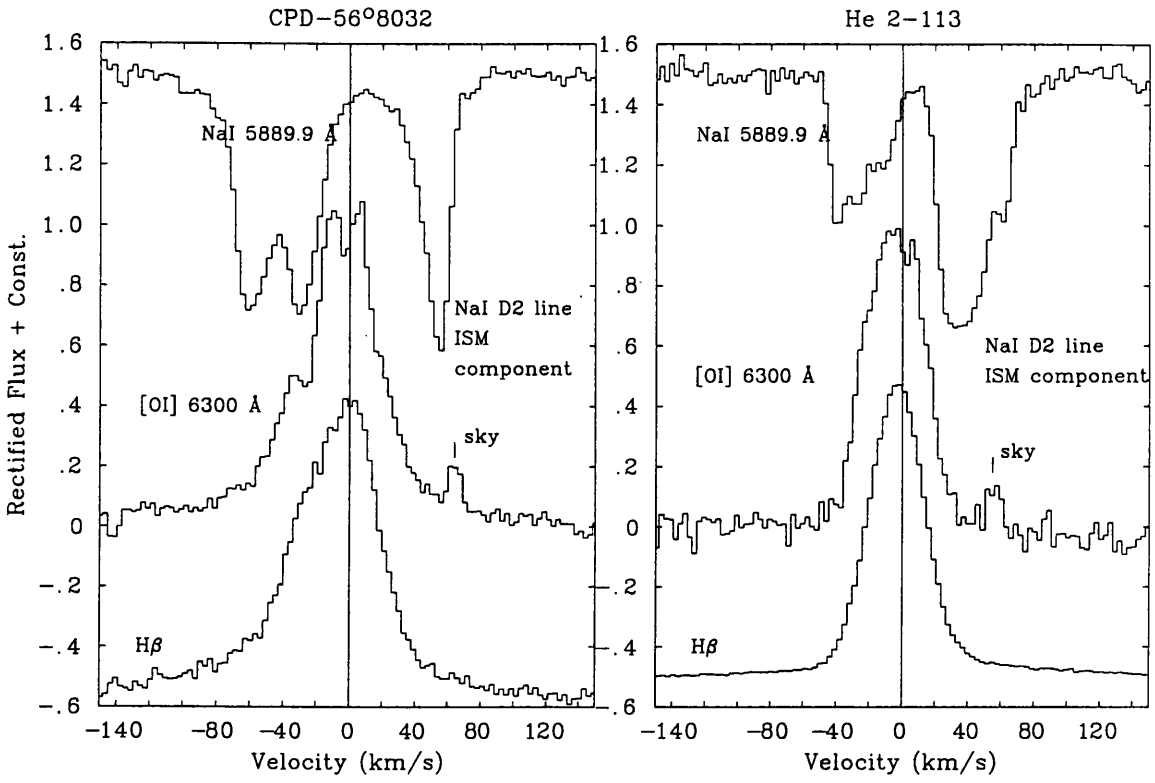

Figure 5.2: Comparison of the Na D2 line profile (upper), the nebular [O I] line profile at 6300.3 Å (middle) and the Hβ line profile (lower) for CPD–56°8032 (left) and He 2–113 (right). All velocities are corrected to zero–points corresponding to the radial velocities of the nebulae

more positive than the nebular velocity (i.e. the interstellar component of the sodium D2 line, the sky component of the [O I] 6300 Å line, and the nebular [O I] emission coming from the part of the nebula receding from the observer – for obvious reasons the latter would not have a sodium absorption counterpart), we notice a certain correspondence: for CPD–56°8032 the well defined troughs of the blue–shifted Na I D2 components correspond to the extended blue wing in the [O I] line profile. We underline that the slight mismatch in Fig. 5.2 between the bluest [O I] component and the velocity of the Na I absorption component nearest to it, is only 3.2 km s^{-1}, within the uncertainties in the respective wavelength calibrations. The same applies to He 2–113, although the most blue–shifted part of the Na D2 line component does not find a match in the [O I] line profile.

We also measured the width of the [C I] λ8727 line, which could also originate from the nebula. This line was observed in the echelle spectra of both CPD–56°8032 and He 2–113. Its FWHM, 48 km s^{-1} for CPD–56°8032 and 30 km s^{-1} for He 2–113, was somewhat smaller than the FWHM of the nebular [O I] lines.

We note that not only do the widths of the Hβ lines match the widths of the respective [O I] lines (as already demonstrated in Fig. 5.1, using Hα), but that this allows us to finally explain the asymmetry in the oxygen lines, which could not be explained by the presence of a stellar wind component (the lack of stellar hydrogen is also argued in Chapter 6).

5.1.5 Reddenings

The reddening to each object can be derived by comparing the fluxes in the nebular Hα and Hβ lines (see Table 5.2); the weaker Hγ and Hδ lines were too blended to measure their fluxes reliably. Using the Case B hydrogen recombination coefficients of Storey and Hummer (1995) for a nebula with electron density $N_e = 10^4$ cm^{-3} and electron temperature $T_e = 10^4$ K and the galactic reddening law of Howarth (1983), values of E(B–V) were derived which are given in Table 5.3. The radio observations of CPD–56°8032 and He 2–113 by Purton et al. (1982) indicate an optically thin free–free spectrum between 2.7 and 14.7 GHz for CPD–56°8032, with a 5.0 GHz flux of 26 $\pm$ 4 mJy, and an optically thin

free–free spectrum above about 9.0 GHz for He 2–113, with a 14.7 GHz flux of 160 ± 10 mJy. Reddenings were therefore also derived from a comparison of the radio and Hβ fluxes, using the method of Milne and Aller (1975) – the derived values of E(B–V) are listed in Table 5.3. In Tables 5.2 and 5.3 we also list the fluxes and reddenings obtained by Aitken et al. (1980) from observations carried out in 1978 and 1979.

5.1.5.1 CPD–56°8032

The 1993 Hα–Hβ baseline yielded an E(B–V) of 0.34 mags (c(Hβ)=0.49), much lower than the radio–Hβ value of 0.68 mags (c(Hβ)=0.99). The 1993 spectrum of CPD–56°8032 was considered optimal in terms of resolution but, bearing in mind that the blue part was not obtained in photometric conditions and had to be rescaled as described in Chapter 3, it was decided that the Hα–Hβ baseline was more susceptible to error, while the longer radio–Hβ baseline should smear out better the possible errors in the corrected Hβ flux. This reasoning was supported by measurements of the 1981 spectrum that yielded an E(B–V) of 0.68 from the Hα–Hβ baseline and a radio–Hβ value for E(B–V) of 0.69 (c(Hβ)=0.99). We finally adopted E(B–V) = 0.68 (c(Hβ)=0.99), as given by three out of four of our 1993 and 1981 ratios. We have not used the method of nulling the 2175 Å interstellar extinction feature to estimate a value of E(B–V), since the UV reddening law towards CPD–56°8032 has already been shown to be abnormal (Rao, Giridhar and Nandy 1990; Jeffery 1995; see also Section 5.4.1, where He 2–113 is also found to have an abnormal ultraviolet reddening law).

5.1.5.2 He 2–113

The same methods as above were used to obtain E(B–V) for He 2–113. The radio–Hβ baseline yielded E(B–V) = 1.02 (c(Hβ)=1.47), while the Hα–Hβ baseline yielded E(B–V) = 0.98 (c(Hβ)=1.41). The better agreement between the two baselines can be ascribed to the fact that, for this star, the entire optical spectrum was obtained in photometric conditions and no corrections were necessary. We finally adopted a value of E(B–V) = 1.00

(c(Hβ)=1.44) for He 2–113.

5.2 Distances

5.2.1 Distances from a Magellanic Cloud Luminosity Calibration

The distance to each star was estimated using two different methods. The first method uses the fact that effectively all the bolometric luminosity of CPD–56°8032 and He 2–113 is reradiated in the infrared by cool dust (Aitken et al. 1980). To obtain the bolometric luminosities we made use of the 1–3.5-μm photometry of Webster and Glass (1974), the 3.5–20-μm photometry of Cohen and Barlow (1980), the mean 7–22-μm IRAS LRS spectrum and the (colour-corrected) IRAS Point Source Catalogue 12–100-μm fluxes. We derived an infrared bolometric luminosity of 2820 D^2 $L_\odot$ for CPD–56°8032 and 2290 D^2 $L_\odot$ for He 2–113 (where D is the distance in kpc), using the measured integrated infrared fluxes of 9.01 x 10^{-15} W cm^{-2} and 7.32 x 10^{-15} W cm^{-2}, respectively.

We can estimate the distances to the stars by using Wolf–Rayet central stars of Magellanic Cloud Planetary Nebulae as calibrators, since they have known distances. Dr. X-W. Liu (private communication) analysed five Magellanic Cloud PNe having Wolf–Rayet nuclei and obtained a mean central star mass of 0.62 $\pm$ 0.02 $M_\odot$, from a comparison of the derived effective temperatures and luminosities with Vassiliadis & Wood (1994) helium–burning evolutionary tracks. This mean mass was assumed for our two stars (since neither star has any hydrogen in its envelope they must both be on helium–burning tracks). The Vassiliadis and Wood (1994) helium–burning tracks were then applied to predict the luminosity for central stars of this mean mass having effective temperatures of 29 400 K and 30 000 K (derived in Chapter 6 for CPD–56°8032 and He 2–113, respectively [1]). The predicted luminosity is 5100 $L_\odot$ for both stars (because the tracks were calculated only for stars of mass 0.600 $M_\odot$ or 0.634 $M_\odot$, we interpolated to obtain the luminosities cor-

[1]The effective temperatures were derived from our modelling of the stellar winds using the codes written by D.J. Hillier (1990) – see Chapter 6. We note that a change of 10,000 K in the adopted effective temperature only changes the derived distance by 5 %.

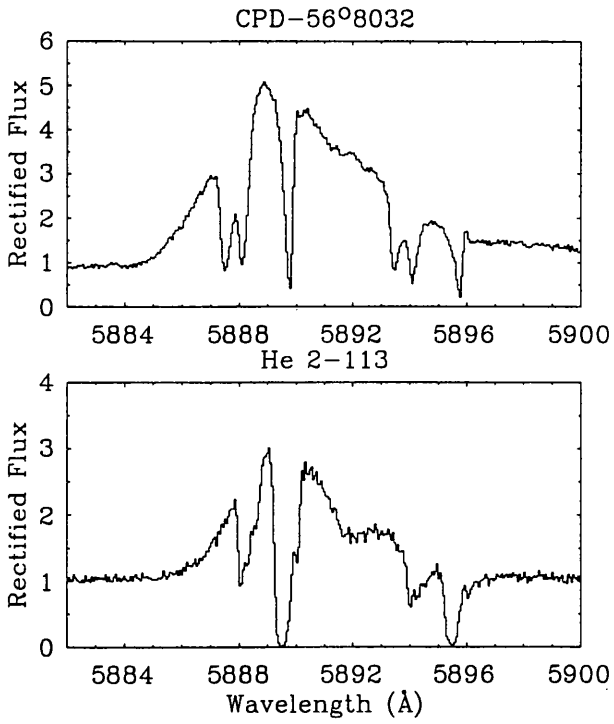

Figure 5.3: The Na D region in the spectra of CPD–56°8032 (upper) and He 2–113 (lower). The emission is due to C II multiplet 5 while the absorption lines are due to the Na D1 and D2 lines at 5895.924 and 5889.950 Å, which exhibit a number of radial velocity components

responding to 0.62 $M_{\odot}$). The distance established in this way for CPD–56°8032 was 1.35 kpc, while for He 2–113 we derived a distance of 1.50 kpc. Our error estimate of ±0.3 kpc is based on two factors; firstly, uncertainties in the IR flux estimate arise from the fact that, longwards of 20 μm, only three IRAS points are available and so the interpolation is affected by a corresponding uncertainty. Secondly, errors may be associated with using helium–burning tracks calculated for stars with hydrogen–rich envelopes and assuming them to apply to WR central stars which lack any hydrogen.

5.2.2 Galactic Rotation Curve Distances

An independent estimate for the distance to each of the stars comes from the Na I D interstellar absorption lines. Fig. 5.2.2 shows the wavelength range between 5880–5900 Å, dominated by emission due to the 3d ^{2}D - 4p ^{2}P^o Multiplet 5 of C II. Superimposed on

this feature is absorption due to the sodium D1 and D2 lines corresponding to a number of radial velocity components: some of interstellar origin, some related to the material around the stars (see below). LSR radial velocities of these absorption components were measured for both of the D lines and are tabulated in Table 5.1, along with the LSR radial velocity of the nebulae obtained from the Balmer lines. The Na I measurements were carried out by fitting a multiple cloud model to the data (where the number of components, their internal velocity dispersions and the column densities were free parameters), after the C II emission profile was rectified. The rectification was achieved by fitting two Gaussians to the emission lines. Fits with more than two Gaussians did not rectify the profiles satisfactorily, although we recognise the possibility of other weaker emission lines being present in the region. We fitted the Na D2 absorption line (see Fig. 5.4), which has the better signal to noise ratio, and then the D1 line with the same cloud parameters, to make sure that the components matched. The D1 fits are not as good as the D2 fits, mainly because of imperfect rectification of the emission profiles, but it is apparent that the positions of the velocity components match.

If interstellar sodium were homogeneously distributed, we would expect to find a wide Na I absorption feature extending from zero radial velocity up to the LSR radial velocity of material near to the star. Use of the galactic rotation curve for a particular line of sight would then allow us to derive the distance to the star. The obvious limitations of this method are the inhomogeneity of the interstellar medium, so that we cannot be sure that absorbing material extends all the way to the star (this means that we will really only measure a lower limit to the distance) and uncertainties associated with the adopted rotation curve. Moreover, in the case of planetary nebulae, there is the further problem that Na I may be present within the neutral envelope surrounding the nebula, causing absorption features at radial velocities corresponding to the nebular expansion velocity (e.g. Dinerstein, Sneden and Uglum 1995; see Section 5.1.4).

We adopted the rotation curve of Brand & Blitz (1993) with R_0 = 8.5 kpc and θ_0 = 220 km s^{-1}, which yields almost identical results to that of Fich et al. (1989). The

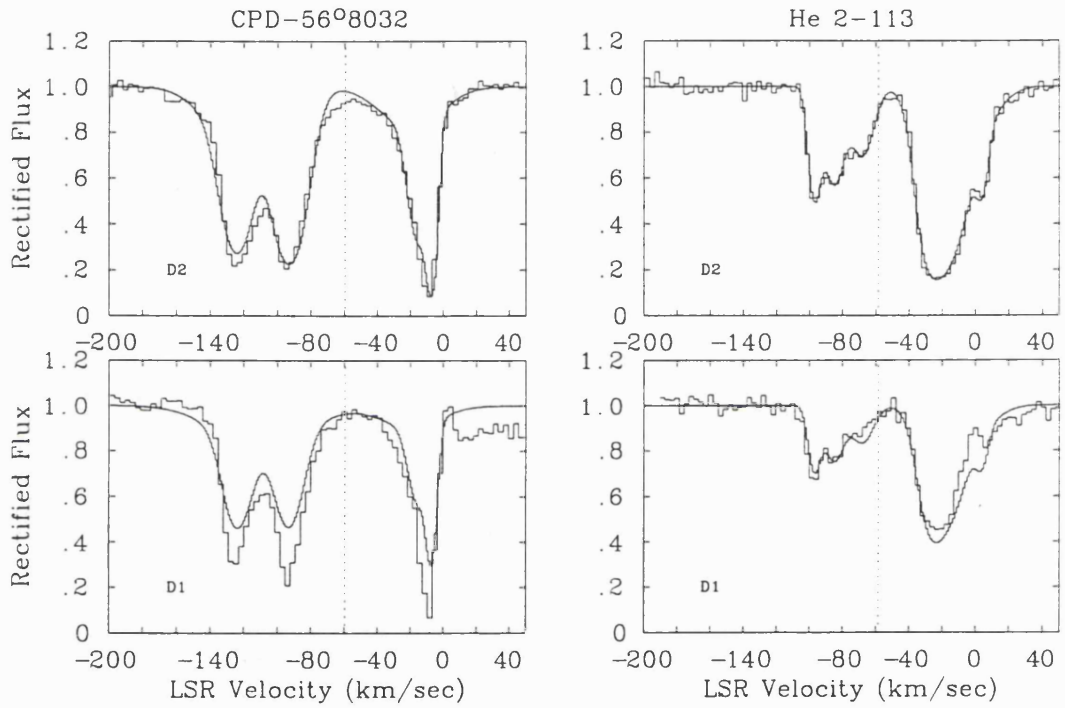

Figure 5.4: The rectified Na I D line profiles for CPD–56°8032 and He 2–113. The LSR radial velocity of each star is marked by the vertical dotted line.

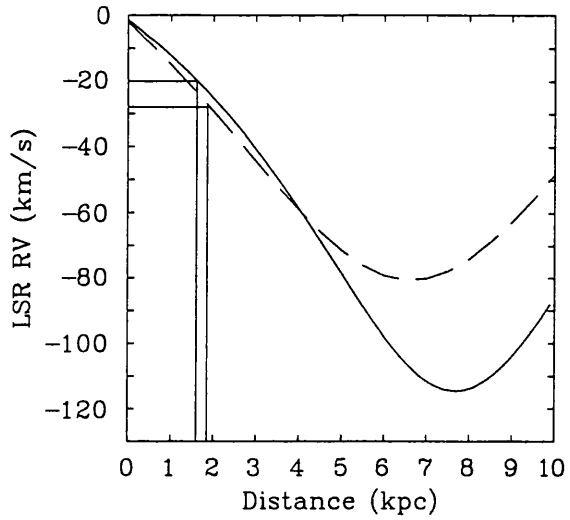

Figure 5.5: Galactic rotation curves for the directions towards CPD–56°8032 (solid) and He 2–113 (dashed), as predicted by the model of Brand and Blitz (1993).

galactic rotation curves corresponding to the directions towards CPD–56°8032 (l = 332.92, b = -9.91) and He 2–113 (l = 321.05, b = 3.99) are plotted in Fig. 5.5.

We cannot assume that all of the velocity components in Fig. 5.4 are of interstellar origin. Interstellar gas in the line of sight should move towards us at velocities more positive than -80 km s^{-1} for He 2–113 and more positive than -110 km s^{-1} for CPD–56°8032 (cf. Fig. 5.5). In addition, for both sightlines we should not expect to find *interstellar* material at velocities more negative then the object's radial velocity. In Fig. 5.4 the nebular radial velocities (derived from the Balmer lines) are marked by the vertical dotted lines. We interpret velocity components which are at more negative velocities than these as arising from expanding circumnebular neutral gas in front of the stars. If we confine our attention to less negative velocities than the nebular radial velocity, then for CPD–56°8032 the most negative (interstellar) velocity component is at -20 km s^{-1}, while for He 2–113 the most negative component is at -28 km s^{-1}. From Fig. 5.5, these velocities imply distances of 1.6±0.2 for CPD–56°8032 and 1.9±0.2 kpc for He 2–113. These values agree, within the relative uncertainties, with the respective distances of 1.35±0.3 and 1.50±0.3 kpc obtained from the Magellanic Cloud [WC] star luminosity calibration.

If we assume that the scale height of interstellar Na I is closely related to that of neutral hydrogen (144 ± 80 pc, Shull & Van Steenberg 1985; 197 ± 28 pc, De Marco 1993), then the rotation curve distance of 1.9 kpc for He 2–113 would put it at a height of 132 pc above the galactic plane, comfortably within a H I scale height, while for CPD–56°8032 the implied distance of 1.6 kpc would put it 275 pc below the plane, a little below the 197 pc that determine the H I scale height found by De Marco (1993). Both distance methods comfortably position both nebulae within the Sagittarius arm of the Galaxy (Lynds 1980; Humphreys 1987).

We adopt distances of 1.35 kpc and 1.50 kpc for CPD–56°8032 and He 2–113 respectively (Table 5.1), as found using the infrared bolometric luminosity method described in Section 5.2.1, and consider the rotation curve distances of 1.6 kpc (CPD–56°8032) and 1.9 kpc (He 2–113) as confirmation that the distance to both stars is indeed between 1 and 2 kpc, and not as large as the value of 2.36 kpc obtained for CPD–56°8032 by Rao et al. (1990) using a relation between dust temperature and nebular radius, or the value of 3.5 kpc determined for He 2–113 by Le Bertre et al. (1989) from kinematical considerations.

5.3 *HST* Images of CPD–56°8032 and He 2–113

The nebulae of CPD–56°8032 and He 2–113 are revealed by narrow emission lines superimposed on the central star spectra, with the latter's nebular lines showing much higher contrast against the stellar spectrum. However, the nebulae are too small to have had their structures resolved in any ground–based image. The only published dimensions for either of the two nebulae are by Kohoutek (1996) who quotes a size for the nebulosity around CPD–56°8032 of 1.3×1.2 arcsec, from a ground based image taken in Hα, and by Roche, Allen and Bailey (1986) who quote the 3.28–μm spatial extent of CPD–56°8032 to be 1.3 arcsec. The latter also noted the extent of the ionized region to be similar to the the extent of the region producing the 3.28–μm feature.

A search of the *HST* archive revealed that four exposures had been taken for each

Table 5.4: Log of *HST* WF/PC exposures of the nebulae around CPD–56°8032 (upper) and He 2–113 (lower)(PI: Bobrowsky).

Exposure	Filter	Exposure Time(s)	Date
w11s8p01t	F487N	140	02/10/92
w11s8q01t	F487N	140	10/10/92
w11s8r01t	F502N	35	02/04/93
w11s8s01t	F502N	35	10/10/92
w11s8d01t	F487N	120	01/02/93
w11s8e01t	F487N	120	01/02/93
w11s8f01t	F502N	30	03/03/93
w11s8g01t	F502N	30	03/03/93

nebula, two each in the Hβ and [O III] 5007 Å lines, with the WF/PC in PC configuration (800×800 pixels ×4chips, yielding a 66×66 arcsec field of view with 0.043 arcsec per pixel). These images were retrieved from the archive and analysed. Details of the exposures are given in Table 5.4.

These eight pre-COSTAR images were already calibrated by the pipeline process (for details see the *HST* Data Handbook, 1995, p. 427). In particular, the calibrated WF/PC images flagged the static and saturated bad pixels, the analogue to digital conversion, bias level determination and removal, pre-flash application, dark correction and flat–fielding. However, because of the *HST* spherical aberration, the images did need to be deconvolved.

The deconvolution process was carried out using both a theoretical and an observational point spread function (PSF). The theoretical PSF was generated by the program Tiny Tim (V4.0)[2]. This is used to model the PSF of the *HST* and is usually employed for image deconvolution and other applications. The PSFs generated in this way are easy to produce, noiseless, linear and computable for a given instrument and filter. However, due to the high frequency structure caused by the large number of optical components, the simulations never match ring for ring the observed PSF.

[2]Tiny Tim is supported by the Space Telescope Science Institute. All the documentation is available from http://www.stsci.edu/ftp/software/tinytim/

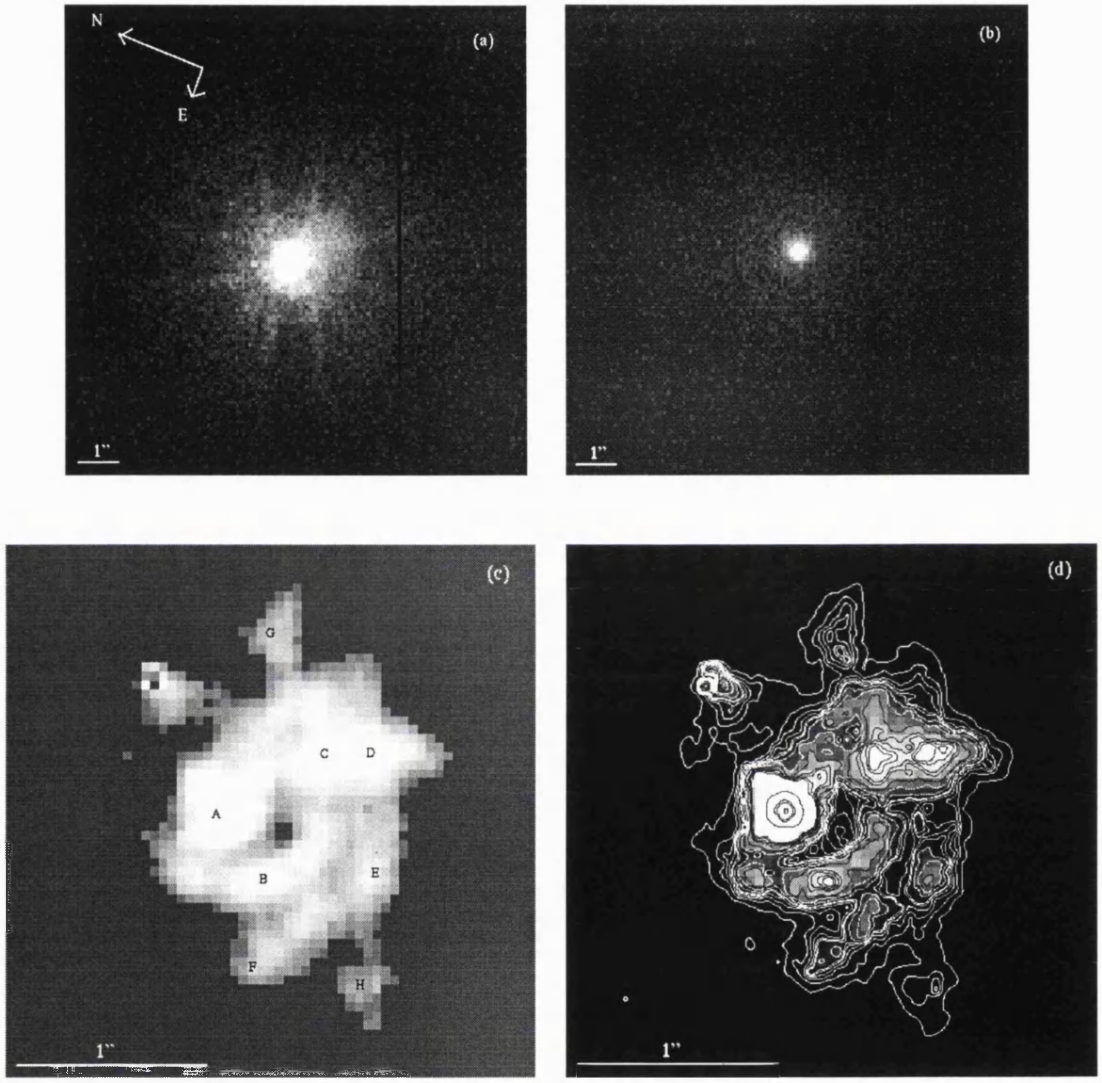

Figure 5.6: *HST* images of CPD–56°8032. a) The average of the two raw Hβ images; b) the average of the two raw [O III] images; c) the deconvolved Hβ image obtained using the [O III] image for the point spread function; d) a contour map of (c); the first white contour corresponds to a level of 1 count, the last black contour corresponds to a level of 16000 counts. The parts of the nebula labeled A–H in (c) are discussed in the text. The orientation of the images is shown in (a)

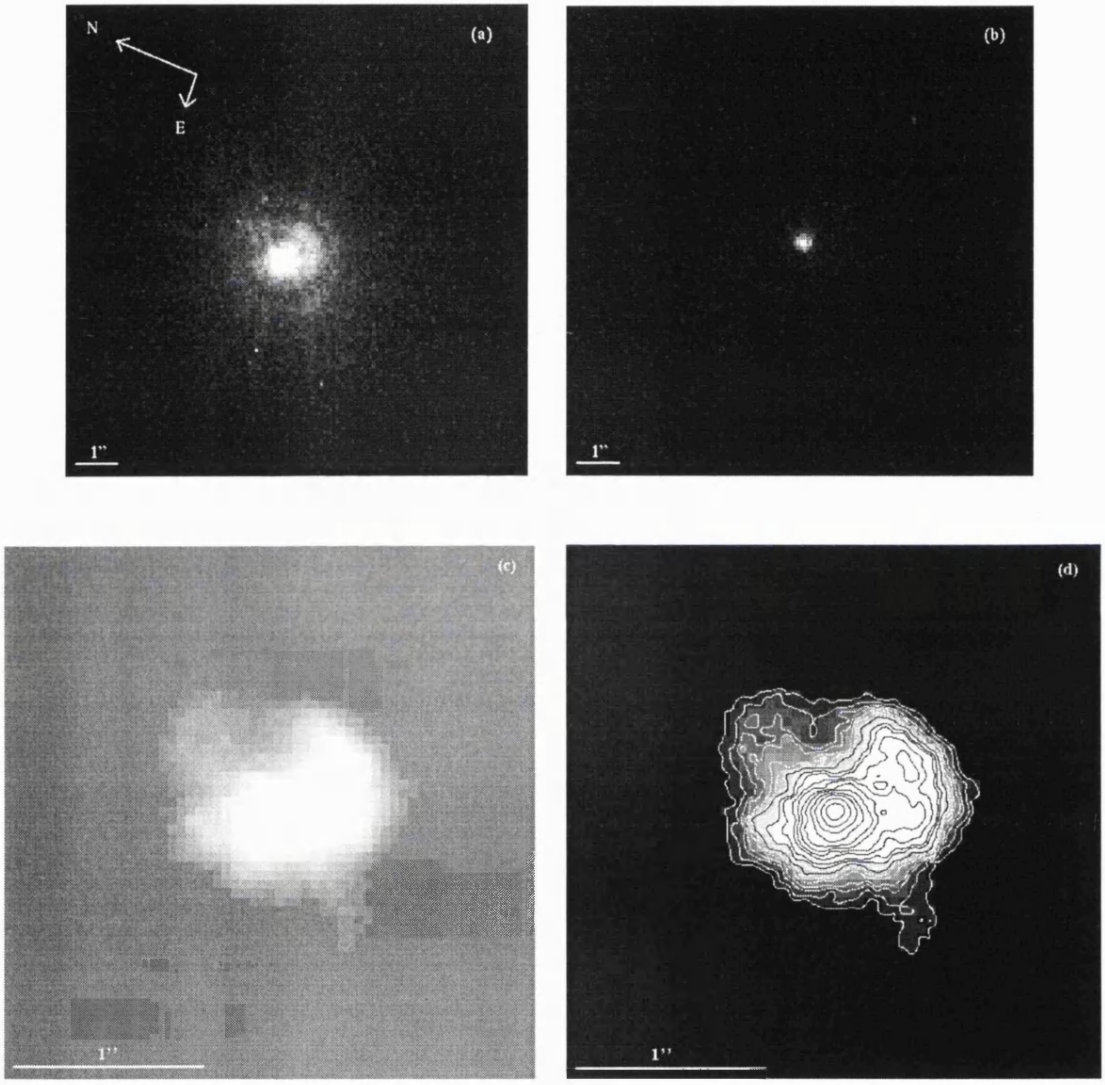

Figure 5.7: *HST* images of He 2–113. a) The average of the two raw Hβ images; b) the average of the two raw [O III] images; c) the deconvolved Hβ image obtained using the [O III] image for the point spread function; d) a contour map of (c): the first white contour corresponds to a level of 1 count, the last black contour corresponds to a level of 7000 counts. The orientation of the images is shown in (a)

For this reason, the images deconvolved in this way, despite showing all the nebular features, always displayed ghosts caused by the theoretical PSF. We therefore decided to use an observed PSF to deconvolve our images. The procedure followed was to clean cosmic rays from chip 6 (the part of the image that contained the object of interest) in all eight images, using both an automatic algorithm and a manual one. Next, the field of view was further reduced to 200×200 pixels centered on the star to speed up the deconvolution process.

The deconvolution was carried out using the Richardson-Lucy algorithm (R–L; see Snyder 1990), using the averaged 5007 Å images to give the PSF. The very low excitation nebulae around CPD–56°8032 and He 2–113 show no emission in the [O III] line at 5007 Å and consequently the 5007 Å images show only the star, while the Hβ images show both star and nebula. The R-L algorithm demands that the read-out-noise and the gain be specified. This is in order to model the noise characteristics of the image properly. It is important to account for read–out–noise so that low–level noise spikes are not construed as significant features and so that negative–noise deviations do not cause the iteration to diverge. For a single WF/PC exposure the canonical values for the two parameters are 13.0 (read-out-noise) and 7.5 (gain)(in the case of averaging N equal exposures, the read–out–noise should be multiplied by $\sqrt{N}$). In the next two Sections, we discuss the resulting images in more detail.

5.3.1 The Nebula around CPD–56°8032

Fig. 5.6 (c) shows a grey–scale plot of the nebula around CPD–56°8032. The image was obtained by averaging the two Hβ exposures (Fig. 5.6 (a)) and deconvolving the result with a PSF obtained from the average of the two [O III] exposures (Fig. 5.6 (b)). Deconvolutions were also tried using all the exposures independently; the result remained the same. The 60×60 pixel Hβ image of CPD–56°8032 in Fig. 5.6 (c) shows an irregular nebula of approximate dimensions 1.65 arcsec by 2.06 arcsec on the sky. The image exhibits a central 'blob', within which the star is located (A). It also shows a ring–like structure

Table 5.5: Observed (F) and dereddened (I) nebular line intensities for CPD–56°8032, from the 1993 UCLES spectrum and from the 1981 RGO Spectrograph spectrum. The adopted reddening is E(B–V) = 0.68. The dereddened Hβ flux as measured from the 1993 spectrum is 9.33×10^{-12} erg cm^{-2} s^{-1}; from the 1981 spectrum we find 8.97×10^{-12} erg cm^{-2} s^{-1}. Errors were assigned according to the difficulty in measuring fluxes. The unusually high FWHM of the [O I] lines are discussed in Section 5.1.4. The [N II] 5754.64 Å line has a low measured FWHM: this could be due to the fact that the line lies on top of a broad stellar feature (C II multiplet 21 and C III multiplet 3), making its FWHM difficult to measure accurately

	CPD–56°8032 - 1993					CPD–56°8032 - 1981		
Ion	λ (Å)	FWHM (km s^{-1})	F (ergs cm^{-2} s^{-1})	100×I /I(Hβ)	Errors (%)	F (ergs cm^{-2} s^{-1})	100×I /I(Hβ)	Errors (%)
[O II]	3726.0	–	4.38×10^{-13}	81.8	20	3.26×10^{-13}	63.3	40
[O II]	3728.8	–	–	–	–	2.52×10^{-13}	48.9	50
Hβ	4861.3	67	9.60×10^{-13}	100	10	9.23×10^{-13}	100	5
[N II]	5754.6	45	8.61×10^{-14}	5.1	10	1.44×10^{-13}	10.0	10
[O I]	6300.3	92	3.81×10^{-13}	21.3	10	4.42×10^{-13}	25.3	10
[O I]	6363.8	80	–	–	20	–	–	–
[N II]	6548.0	67	1.26×10^{-12}	61.9	10	1.67×10^{-12}	87.8	5
Hα	6562.8	55	3.98×10^{-12}	200.4	10	5.38×10^{-12}	281.5	5
[S II]	6716.5	69	2.02×10^{-13}	9.8	10	2.03×10^{-13}	10.1	35
[S II]	6730.8	–	4.56×10^{-13}	13.9	20	5.02×10^{-13}	24.90	20
[O II]	7320	–	6.75×10^{-13}	27.6	15	7.85×10^{-13}	32.9	5
[O II]	7330	–	3.44×10^{-13}	13.9	15	6.46×10^{-13}	27.0	5
O I	8445	53	7.43×10^{-14}	2.3	10	–	–	–
[S III]	9068.9	60	8.25×10^{-14}	2.3	15	–	–	–

peaking in intensity south and east of the star (B). It is possible to trace this ring to the north of the star, where it is much fainter. At points C and D (better shown in the contour plot in Fig. 5.6 (d)) there are two intensity peaks. Between points E and F there is an almost continuous line of emission, possibly part of a larger ring. Points G and H seem isolated from the rest of the structure. The majority of the emission originates from the southern side, possibly due to dust obscuration on the northern side. Similar spatial variations in the dust obscuration are seen across the face of NGC 7027 (Walton et al. 1988). This tempts us into speculation: the nebular hydrogen lines exhibit a 'haunch' on the blue side. This means that more nebular ionised gas is observed coming towards us. If the material positioned to the north–east of the nebula (Fig. 5.6 (c)) is receding and more heavily reddened, while material to the south–west of the nebula is approaching and less heavily reddened, this would result in the red part of the nebular lines being depressed with respect to the blue part.

Inspection of Fig. 5.6 (c) indicates that the ring BC seems to be elongated along a north-south axis. Measurements of the radius proceeded by identifying the centre of the ring emission at different locations. The radii thus obtained were averaged to obtain major and a minor radii of 0.49 arcsec and 0.38 arcsec ($\pm$ 0.05 arcsec) respectively. Kohoutek (1996) reported the nebular diameter to be 1.3×1.2 arcsec from a ground–based ESO 3.6 m telescope Hα image, with the major axis oriented north–south, in reasonable agreement with the present results. If an average of the major and minor radii of the ring is taken and a distance of 1.35 kpc adopted, together with a uniform expansion velocity of 30 km s^{-1}, we can calculate a dynamical age of about 100 years.

Dynamical ages obtained from *outer* nebular radii are not usually reliable and they only indicate a lower limit to the real nebular age since the majority of the nebula is still neutral. Mm–Wave imaging in CO, or in the continuum, would be required in order to obtain a more realistic estimate. However inner nebular radii may give an indication of the dynamical age since leaving the AGB since they don't suffer from this 'boundary' problem. For CPD–56°8032's nebula it is possible to obtain such an inner radius by measuring the

distance between the star and the ring–like structure. Using a value for the inner radius of 0.6 arcsec, a dynamical age of approximately 100 years is obtained.

5.3.2 The Nebula around He 2–113

The deconvolved Hβ image of this nebula is shown in Fig. 5.7 (c), on the same scale as CPD–56°8032. Apart from enhanced emission on the western side and, possibly, ansae along a north–south axis, very little structure is apparent in the deconvolved nebular image. We measured the nebular diameter to be about 1.4 arcsec north–south and 1.1 arcsec east–west. This, together with a distance of 1.5 kpc and an expansion velocity of 19 km s^{-1} results in a dynamical age of about 220 years. However for the same reasons given in Section 5.3.1, this can only be a lower limit to the age of the nebula.

5.4 Nebular Abundance Analysis

5.4.1 Nebular Line Fluxes

The spectroscopic analysis of the nebulae around CPD–56°8032 and He 2–113 is rendered difficult by the blending of nebular and stellar features. In previous analyses, Houziaux and Heck (1982) estimated the carbon abundance for CPD–56°8032's nebula, while Cohen et al. (1989) estimated both carbon and oxygen abundances for it (both used IUE data). Rao (1987) determined N/H, S/H and O/H ratios for the nebulae of CPD–56°8032 and He 2–113, using optical spectra.

In order to distinguish the nebular lines from the stellar lines, we scanned our echelle spectra for lines whose widths were systematically lower than the average FWHM values for the stellar wind lines (250 km s^{-1} for CPD–56°8032 and 160 km s^{-1} for He 2–113) and close to the FWHM widths of the nebular Balmer lines (60 and 40 km s^{-1}, respectively). Once the nebular lines were identified, their fluxes were measured using the DIPSO package (Howarth and Murray 1991). The measurements were carried out on the narrow–slit spectra (for best resolution) after they had been scaled up to the wide–slit flux levels, as

Table 5.6: Observed (F) and dereddened (I) nebular line intensities for He 2–113. The adopted reddening is E(B–V) = 1.00. The dereddened Hβ flux is 6.12×10^{-11} erg cm^{-2} s^{-1}

He 2–113					
Ion	λ (Å)	FWHM (km s^{-1})	F (ergs cm^{-2} s^{-1})	100×I /I(Hβ)	Errors (%)
[O II]	3726.0	44	3.26×10^{-13}	15.1	20
[O II]	3728.8	47	1.42×10^{-13}	14.8	20
Hβ	4861.3	39	2.16×10^{-12}	100	10
[N II]	5754.6	40	2.42×10^{-13}	5.8	10
[O I]	6300.3	79	2.87×10^{-13}	5.2	10
[O I]	6363.8	69	1.02×10^{-13}	1.8	20
[N II]	6548.0	36	2.54×10^{-12}	40.5	10
Hα	6562.8	39	1.77×10^{-11}	281.1	10
[S II]	6716.5	42	1.78×10^{-13}	2.6	10
[S II]	6730.8	43	3.76×10^{-13}	5.5	20
[O II]	7320	–	1.43×10^{-12}	16.3	15
[O II]	7330	–	1.26×10^{-12}	14.3	15
O I	8445.5	39	3.04×10^{-13}	2.4	10
[Cl II]	8578.7	32	1.49×10^{-13}	1.1	10
[S III]	9068.9	29	1.02×10^{-12}	6.7	30

Table 5.7: Log of the IUE observations used to measure the intensity of the C II] 2326 Å and C III 1909 Å lines

Star	Frame	Exposure Time (min)
CPD–56°	LWP11203L	30
	LWP21065L	15
	LWP21076L	25
	LWR5733L	10
	LWR7700L	25
	SWP36663L	60
	SWP42316L	60
	SWP6718L	20
	SWP8947L	55
He 2–113	LWP21075L	90
	SWP8950L	40
	SWP42315L	180

described in Chapter 3. The line fluxes were checked against measurements of unblended nebular lines (e.g. [S II] λ6717) in the photometric wide–slit spectra. For the lines that were blended with stellar features, de–blending was attempted and the line flux assigned an error that would reflect the uncertainty in its measurement. For lines that were either too heavily blended or had low signal to noise ratios, the measurement was not attempted. In Tables 5.5 and 5.6 we present the the nebular line fluxes for all the lines that were measured. Table 5.5 presents, along with measurements from the 1993 UCLES spectrum, measurements from our 1981 RGO Spectrograph spectrum of CPD–56°8032. However, line widths are not presented for the 1981 spectrum because the instrumental profile dominated over the intrinsic Doppler widths of the nebular lines. Table 5.6 presents the line fluxes measured from our 1993 UCLES observations of He 2–113.

To obtain the nebular carbon abundance we used the intensities of the C II] line at 2326 Å and of the C III] line at 1909 Å, measured from *IUE* spectra. Table 5.7 summarises the *IUE* images that were used. For CPD–56°8032, five different LWP frames (spectral range 1900–3200 Å) were averaged to improve the signal to noise ratio, while for He 2–113 only one LWP frame was found in the *IUE* archive. Four SWP frames (spectral range

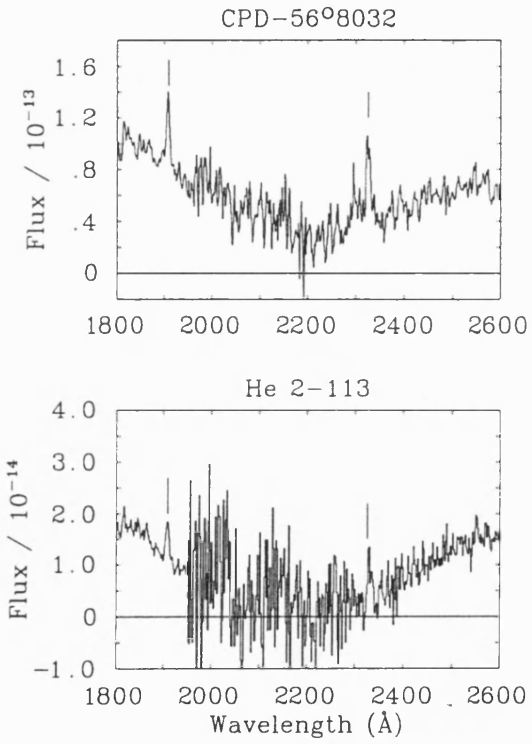

Figure 5.8: The C III] line at 1909 Å and the C II] line at 2326 Å, for CPD−56°8032 (upper) and He 2−113 (lower). Fluxes are in ergs cm^{-2} s^{-1} $Å^{-1}$

1200–2000 Å) were used for CPD–56°8032, while two were used for He 2–113. The region between 1800 Å and 2600 Å is displayed in Fig. 5.8 for both objects. As can be seen, the presence of the 2200 Å extinction feature does not allow us to locate the continuum accurately on the blue side of the 2326 Å feature, while it is somewhat easier to locate the continuum on both sides of the 1909 Å line. Due to the low signal–to–noise ratios, the flux and equivalent width measurements are affected by substantial uncertainties.

In order to account for the stellar wind component contributing to the lines, we made use of the stellar wind equivalent widths predicted for the C II] λ2326 and C III] λ1909 features by our models (Chapter 6). For the λ2326 line, we obtained the equivalent width of the nebular component by subtracting the model prediction for the stellar wind equivalent width (21.1 Å for CPD–56°8032 and 5.0 Å for He 2–113) from the total equivalent width of the 2326 Å feature as measured from the merged *IUE* spectra (35 Å for CPD–56°8032 and 36 Å for He 2–113, respectively). We then scaled the model stellar continuum flux to the dereddened observed continuum flux at 5610 Å and measured this normalised model continuum flux at 2326 Å (9.99×10^{-12} and 2.04×10^{-11} ergs cm^{-2} s^{-1}Å^{-1} for CPD–56°8032 and He 2–113), finally multiplying the derived nebular equivalent widths of 14 Å and 31 Å by these values. The result is equivalent to the dereddened flux arising from the nebular part of the λ2326 feature and was found to be 1.40×10^{-10} ergs cm^{-2} s^{-1} for CPD–56°8032 and 6.32×10^{-10} ergs cm^{-2} s^{-1} for He 2–113. For the C III] λ1909 feature, the measured equivalent widths of 6.8 Å for CPD–56°8032 and 7.0 Å for He 2–113, are slightly smaller than (CPD–56°8032) or equal to (He 2–113), the equivalent width predicted by the respective stellar wind model alone. We therefore conclude that there is no evidence for a significant nebular contribution to the observed C III] 1909 Å feature for either object.

The reason for using the stellar model continuum flux at 2326 Å and not the dereddened IUE continuum flux is that the accuracy of the latter is dependent on using the correct reddening law. The reddening law towards CPD–56°8032 has previously been shown to be abnormal (Rao et al. 1990; Jeffery 1995) in the sense that the 2200 Å extinction feature

is weak relative to the optical extinction. Confirming this, we found that dereddening the IUE spectra using the standard reddening law of Seaton (1979), with E(B–V) = 0.68 and 1.0 for CPD–56°8032 and He 2–113, respectively, led to an overcorrection of the interstellar 2200 Å extinction feature. This can be attributed to part of the reddening to each object being circumstellar. Since the C–rich dust around these objects may not have the same reddening law as ISM dust, and since the ultraviolet is the region most sensitive to reddening law variations, we therefore preferred to use our model stellar spectra, normalised to the dereddened optical spectra at 5610 Å, to estimate the dereddened stellar continuum flux at 2326 Å.

5.4.2 Nebular Temperatures and Densities

For both these objects, a nebular analysis is seriously hampered by the blending of stellar and nebular lines. Due to the fact that both nebulae are very compact, it was not possible to extract a clean nebular spectrum from the regions adjacent to the stellar spectrum.

Due to the richness of the stellar spectra, most nebular diagnostic lines are severely blended. The nebular [S II] λ6731 line is blended with a stellar wind C II Multiplet 21 component (at 6731.1 Å) and with a stellar wind C III Multiplet 3 component (at 6728.7 Å); the nebular [O II] 3726,3729 Å doublet is blended with a stellar wind O II Multiplet 3 component (at 3727.3 Å); while the [N II] nebular line at 5755 Å is partly blended with an O II Multiplet 31.03 wind component at 5753.8 Å. This made it difficult to diagnose the nebular temperature and density in the usual way.

Due to the blending problem affecting the temperature–sensitive [N II] λ5755 line, we have chosen to use the four [O II] lines at 7318.8, 7319.9, 7329.6 and 7330.6 Å to estimate the nebular electron temperature in the following manner. The $^2P^o_{3/2}$ and $^2P^o_{1/2}$ levels from which the lines originate have high critical densities (between 4×10^6 cm^{-3} and 6×10^6 cm^{-3}; Rubin 1989), so that their intensities are relatively insensitive to the nebular electron density, but their relatively high excitation energies make the lines temperature–sensitive.

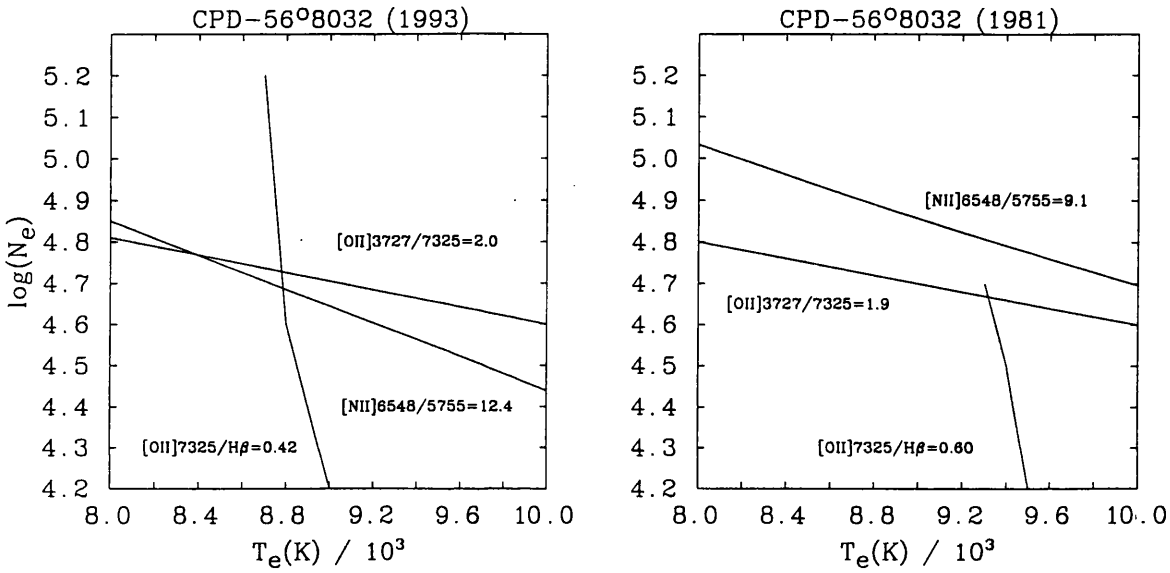

Figure 5.9: Diagnostic diagrams, $\log(N_e)$ vs T_e, for CPD–56°8032 (1993) (left) and CPD–56°8032 (1981) (right). The curves are based on the observed intensity ratios for [N II] 6548/5755; [O II] 3727/7325; and [O II] 7325/Hβ with the condition that the nebular O^+/H^+ ratio be equal to the mean PN O/H value of 4.8×10^{-4} found by Kingsburgh and Barlow (1994)

The abundance of oxygen in planetary nebulae has been found to be not significantly altered by nucleosynthetic processes during the evolution of the precursor star, as shown by a comparison with H II region oxygen abundances (Kingsburgh and Barlow 1994). We therefore adopted the mean O/H ratio of $(4.8\pm1.6)\times10^{-4}$ derived by Kingsburgh and Barlow for a sample of 80 galactic PN as appropriate for the nebulae of CPD–56°8032 and He 2–113 as well. Since there is no doubly ionized oxygen in either nebulae, we have that $O^+/H^+ = O/H$. Using the collision strengths and transition probabilities of Pradhan (1976) and Zeippen (1982), the dereddened [O II] $\lambda\lambda$7320,7330/Hβ flux ratios in Tables 5.5 and 5.6 imply electron temperatures of 8800 K and 9300 K for CPD–56°8032 (from our 1993 and 1981 spectra respectively) and 8400 K for He 2–113.

To estimate the errors on the derived temperatures, we calculated the temperatures corresponding to the limits on the mean PN O/H abundance stated by Kingsburgh and Barlow (1994): $O/H = (4.8\pm1.6)\times10^{-4}$. In this way we found the nebular temperature limits of CPD–56°8032 to be 8800^{+600}_{-400} K (from our 1993 spectrum) and 9300^{+400}_{-600} K (from our 1981 spectrum), while for He 2–113 we obtained 8400^{+500}_{-300} K. We finally rounded the errors to ±500 K for CPD–56°8032 and ±400 K for He 2–113.

The discrepancy between the temperatures derived from the two different observations of CPD–56°8032 is due to the intensities, relative to Hβ, for the [O II] 7320,7330 Å lines being greater in the 1981 observations than in the 1993 observations. The 1981 spectra had a lower resolution and so measurements carried out on its blended 7320,7330 Å lines are not as reliable as those carried out on the unblended features that appear in the 1993 spectrum. However, direct comparison of the 7300–7360 wavelength regions in the 1981 and 1993 spectra shows that, blending aside, the [O II] 7320,7330 Å lines did appear to be stronger in 1981 than in 1993. In order not to exclude the possibility of changes having occurred in the intervening 12 years in the physical conditions of the nebula, we adopt the temperatures stated above to derive independent densities and abundances (see below and Section 5.4.3) from these two independent observations of CPD–56°8032.

To estimate the nebular electron densities, we have used the flux ratio of [O II]

Table 5.8: The electron temperatures and densities derived for the nebulae of CPD–56°8032 and He 2–113.

Star	T_e(K)	log(N_e[cm^{-3}])
CPD–56°8032 (1993)	8800±500	4.8±0.1
CPD–56°8032 (1981)	9300±500	4.8±0.1
He 2–113	8400±400	4.8±0.1

$\lambda\lambda$3726,3729 to [O II] $\lambda\lambda$7320,7330. The λ3726.0 and λ3728.8 lines, originating from the $^2D^o_{5/2}$ and $^2D^o_{3/2}$ levels, have critical densities between 1×10^3 cm^{-3} and 4×10^3 cm^{-3} (Rubin 1989). Thus for electron densities lying between several thousand cm^{-3} and several million cm^{-3} (the latter being the critical densities of the $^2P^o$ levels from which the $\lambda\lambda$7320,7330 lines originate), the [O II] λ3727/λ7325 flux ratio will be a sensitive density diagnostic. As shown in Figs. 5.9 and 5.10, the 3727/7325 ratio does have a weak sensitivity to the nebular electron temperature, but is primarily sensitive to the electron density within the observed range.

In the case of CPD–56°8032, the [O II] $\lambda\lambda$3726,3729 complex was heavily blended with the stellar wind O II 3727.3 Å line, while for He 2–113 the narrower and weaker stellar wind line left the nebular [O II] lines uncontaminated. The O II 3727.3 Å line is the intermediate strength component of a triplet whose other components are at 3712.7 and 3749.5 Å. In order to determine the flux due to the nebular lines alone, we measured the equivalent widths of the P Cygni emission and absorptions components of the O II stellar wind lines at 3712.7 and 3749.5 Å and took an average of the sum of these emission and absorption equivalent widths to predict the O II λ3727.3 net emission contribution. We then measured the total equivalent width of the blend due to the nebular [O II] lines and the stellar wind O II line, and subtracted from it the predicted net stellar wind O II emission contribution. The nebular lines are estimated to contribute 70% of the total flux in the blend. This procedure was followed with the 1993 spectrum of CPD–56°8032. However, for the 1981 spectrum the entire spectral region (3700–3750 Å) was crowded with emission lines and the lower resolution could not distinguish the O II stellar wind features at 3712.7 Å and

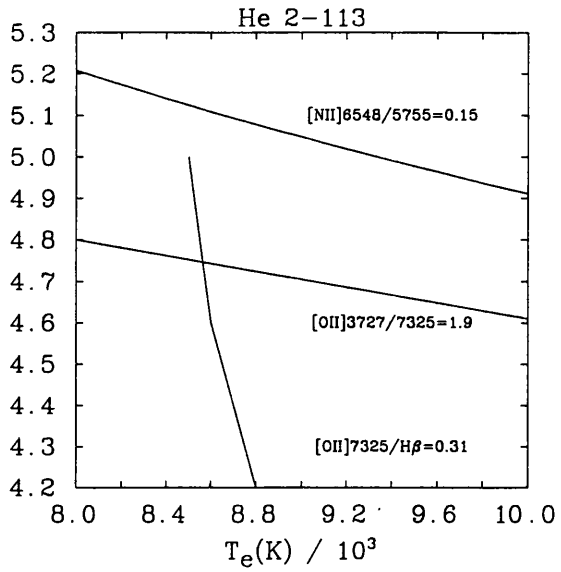

Figure 5.10: Diagnostic diagram, log(N_e) vs T_e, for He 2–113. The curves are based on the observed intensity ratios for [N II] 6548/5755; [O II] 3727/7325; and [O II] 7325/Hβ with the condition that the nebular O^+/H^+ ratio be equal to the mean PN O/H value of 4.8×10^{-4} found by Kingsburgh and Barlow (1994)

3749.5 Å. This may be the main reason why the [O II] $\lambda\lambda$3726,3729 fluxes from the 1981 spectrum are higher than from the 1993 spectrum. However, if we use our 1993 result, i.e. that the nebular lines contribute 70% to the blend, we obtain a nebular density which is less than 0.1 dex higher than obtained by assuming that all of the flux is due to [O II]. This is within the error estimate and would only increase the resulting abundances by small amounts, well within the relative uncertainties.

The nebular electron densities derived from the dereddened [O II] 3727/7325 ratios (from Tables 5.5 and 5.6) are found to be $\log(N_e/cm^{-3}) = 4.8\pm0.1$ for both the 1993 observation of CPD–56°8032, using $T_e = 8800\pm500$ K, and for the 1981 observation, using $T_e = 9300\pm500$ K. For He 2–113, we also obtained $\log(N_e/cm^{-3}) = 4.8\pm0.1$ using $T_e = 8400\pm400$ K. The loci of the [O II] 7325/Hβ and [O II] 7325/3727 ratios in the $\log(N_e)$ vs. T_e plane are plotted in Fig. 5.9 for CPD–56°8032 (1993; left) and CPD–56°8032 (1981; right) and in Fig. 5.10 for He 2–113. Also plotted for each nebula are the loci corresponding to the dereddened [N II] 6548/5755 ratios. These were calculated using the collision strengths and transition probabilities of Stafford et al. (1994) and Nussbaumer and Rusca (1979). In the case of the 1993 observation of CPD–56°8032, the [N II] ratio shows good consistency with the values of N_e and T_e given by the 7325/Hβ and 3727/7325 ratios, while for the 1981 observation, the [N II] ratio implies a density that is about 0.1 dex higher than given by the 3727/7325 ratio; in the case of He 2–113 the [N II] ratio implies an electron density which is 0.3 dex higher than given by the [O II] 3727/7325 ratio. Since, as mentioned above, the [N II] λ5755 line is potentially affected by serious line blending problems, we prefer to use the [O II] 7325/Hβ and [O II] 3727/7325 ratios as the electron temperature and density diagnostics. Overall, we prefer to base our conclusions about the nebula of CPD–56°8032 on the 1993 observations, because of their superior resolution.

The electron temperatures previously assumed for CPD–56°8032 were 10^4 K (Houziaux and Heck 1982: 'from the general appearance of the spectrum'); this was later adopted by Cohen et al. (1986); and 11,000 K (Rao 1987, who quotes the figure as an upper limit

based on the presence of the [S III] lines at 9069 and 9532 Å). For He 2–113, Rao (1987) quotes 8800 K (from a comparison with a nebular analysis of SwSt1 by Flower, Goharji and Cohen (1984), on the grounds that the nebulae are very similar). The nebular electron density for CPD–56°8032 was previously estimated to be 2×10^4 cm^{-3} (Rao 1987; from the ratio of the [N II] lines at 5755 and 6548 Å); Cohen at al. (1986) assumed it to be 1×10^4 cm^{-3}, from measurements on the similar nebula M 4–18 by Goodrich and Dahari (1985). For He 2–113, Rao (1987) found 1×10^5 cm^{-3} from the [C I] $\lambda\lambda$8727,9850 lines and a comparison with the spectrum of SwSt 1 (Flower, Goharji and Cohen 1984). Our own nebular temperatures and densities are summarised in Table 5.8.

5.4.3 Nebular Abundances

We have derived the nebular abundances of carbon, nitrogen and sulphur relative to hydrogen. The atomic collision strengths and transition probabilities for oxygen and nitrogen were discussed in Section 5.4.2. For S^+ we used collision strengths from Keenan et al. (1996) and transition probabilities from Mendoza and Zeippen (1982). For S^{2+} the collision strengths were taken from Mendoza (1983), while the transition probabilities were taken from Mendoza and Zeippen (1982). For C^+, we used collision strengths from Hayes and Nussbaumer (1984) and transition probabilities from Nussbaumer and Storey (1984).

As discussed in the previous Section, oxygen was assumed to have the same abundance as the mean PN value of $(4.8\pm0.16)\times10^{-4}$ found by Kingsburgh and Barlow (1994), in order to derive the electron temperature in the nebulae.

The nitrogen abundance was derived from the [N II] lines. The absence of the easily excited [O III] 4959,5007 lines in the spectra of these nebulae indicates the complete absence of O^{2+} ions. Although N^+ has a somewhat lower ionization potential than O^+ (29.6 eV vs. 35.1 eV) we do not expect a significant abundance of N^{2+} ions to be present in the nebulae. We find that $N^+/H^+=1.0\times10^{-4}$ and 6.6×10^{-5} for CPD–56°8032 and He 2–113, respectively. Both these values are below the mean PN value of 2.2×10^{-4} but similar to the solar abundance of nitrogen derived from H II regions (Table 5.9). Due to his adoption

Table 5.9: Nebular abundances for CPD–56°8032 and He 2–113. The abundances are by number The lines used to derive the abundances are indicated in the header. Where more than one line is indicated a weighted average was taken. The C II] line flux was measured from IUE spectra (see Section 5.4.1). The high uncertainty in its measured flux is reflected in the C/H uncertainty. The mean PN abundances are from Kingsburgh and Barlow (1994); The solar O/H and S/H values are from Grevesse and Anders (1989); the solar N/H ratio is from Grevesse et al. (1990); and the solar C/II ratio is from Grevesse et al. (1991)

	C/II	O/II	N/II	S^+/II^+	S^{++}/II^+	S/II	C/O
	C II]	[O II]	[N II]	[S II]	[S III]		
λ (Å)	2326	7320,30	6548,5755	6717,6731	9068		
CPD–56°8032 (1993)	6.3±3.0(-3)*	4.8(-4)	8.3±0.8(-5)	1.0±0.1(-5)	3.9±1.0(-7)	1.0±0.1(-5)	13.1
CPD–56°8032 (1981)	7.2±3.0(-3)	4.7(-4)	1.0±0.1(-4)	1.3±0.1(-5)	–	1.3±0.1(-5)	15.3
He 2–113	5.0±3.0(-3)	4.8(-4)	6.6±0.7(-5)	2.6±0.3(-6)	1.3±0.1(-6)	3.9±0.5(-6)	10.4
Mean PN value	5.5±3.0(-4)	4.8±1.0(-4)	2.2±1.0(-4)	–	–	8.3±4.2(-6)	1.15
Solar	4.0±0.5(-4)	8.5±0.1(-4)	1.0±0.1(-4)	–	–	1.7±0.2(-5)	0.47

* 6.3±3.0(-3)=(6.3±3.0)× 10^{-3}

of a high electron temperature of 11 000 K, Rao (1987) found lower values of N^+/H^+ for CPD–56°8032 (1.4×10^{-5} and 5.2×10^{-5}, using the [N II] lines at 6548 Å and 5755 Å respectively).

S^+ has a lower ionization potential than either O^+ or N^+, and [S III] lines are observed in the spectra, at 3722 Å, 9069 Å and 9532 Å. Only the 9069 Å line was measured, as it was inferred not to be significantly affected by water vapour absorption in the Earth's atmosphere. The rest wavelength of the [S III] 9069 Å line is 9068.9 Å (Osterbrock et al. 1992), while the only water vapour line that could affect the feature has a rest wavelength of 9069.126 Å. For both nebulae, the [S III] feature is blue–shifted by approximately 1.8 Å, corresponding to the nebular radial velocities of 60 km s^{-1}. Thus the nebular [S III] λ9069 line is shifted away from the water vapour line and its flux should not be depleted. For CPD–56°8032 we obtain $S/H = 1.2\times10^{-5}$ from the sum of the S^+ and S^{2+} abundances (Table 5.9), while for He 2–113 we obtain $S/H = 3.8\times10^{-6}$. These sulphur abundances agree with the mean PN value of 8.3×10^{-6} within the uncertainties (see Table 5.9).

The nebular carbon abundance is given directly by the abundance of C^+ since, as explained in Section 5.4.1, we consider the C III] line at 1909 Å to have a stellar wind origin. We obtain $C/H = 6.3\times10^{-3}$ for CPD–56°8032 and 5.0×10^{-3} for He 2–113. These carbon abundances are much higher than the mean PN value of 5.5×10^{-4} found by Kingsburgh and Barlow (1994), which may indicate that the inner (ionized) nebulae of these two objects have been contaminated by the C–rich stellar winds.

For CPD–56°8032 we can reconcile our C^+/H^+ ratio with the lower ratios derived by Houziaux and Heck (1982) and Cohen et al. (1989), on the grounds of our higher $I(\lambda2326)/I(H\beta)$ and of our lower electron temperaure (8800 K vs. their adopted 10 000 K).

No nebular He^+ recombination lines are detected in our spectra. Our claim that the He I lines in the spectra of CPD–56°8032 and He 2–113 are entirely of stellar origin is based on their profiles. However the P Cygni nature of the stellar wind He I lines could make it extremely difficult to detect a weak nebular component added to the stellar feature, so

that we cannot exclude the presence of some He^+ in the nebula. Table 5.9 summarizes our derived nebular abundances for both objects.

5.5 Discussion

The very high C/O number ratios derived from the ionized zone around CPD–56°8032 and He 2–113 (13 and 10, respectively; Table 5.9) confirms the strong correlation found by Cohen et al. (1989) between the C/O ratio and the ratio of UIR–band flux to total IR flux – these two objects had by far the highest ratios of UIR to total IR flux in their sample. Although their C/O ratios are very much higher than usually found for galactic PN, they are not unprecedented – the PN K648 in the globular cluster M15 has C/O=8 (Howard, Henry and McCartney 1997), while the galactic halo PN H 4–1 and BB–1 have C/O ratios of 10 and 13, respectively (Clegg 1989, Howard et al. 1997).

It has been suggested that [WCL] stars evolve into [WCE] stars and subsequently become PG1159–type white dwarfs (e.g. Barlow and Storey 1993; Leuenhagen et al. 1994). According to what we shall call the 'standard scenario' the [WC] central stars originate from AGB giants with their hydrogen deficiency being caused by the almost complete removal of their hydrogen envelopes, perhaps due to a thermal pulse at the end of the AGB phase.

In the alternative *born–again* scenario (Schönberner 1979; Iben et al. 1983; see Chapter 1), a H–burning central star returns to the top of the AGB to complete another excursion, this time as a helium–burner, with a H–deficient atmosphere and with a new, hydrogen–deficient PN around it. This latter scenario resolved some discrepancies in the abundances seen in PN such as Abell 30 and Abell 78 (which have WR/*wel* central stars) and is always maintained as a possibility for the evolution of H–deficient and WR central stars.

However, the hydrogen–rich outer nebulae around A 30 and A 78 have very low electron densities and surface brightnesses, consistent with having been ejected a considerable time ago, whereas their inner nebular knots, attributed by Iben et al. (1983) to ejecta from a

final helium–shell flash on the white dwarf track that caused the stars to briefly return to the AGB, are helium–rich and lack any hydrogen (Hazard et al. 1980). By contrast, the high electron densities of the hydrogen–rich nebulae around CPD–56°8032 and He 2–113 (6×10^4 cm^{-3}) appear consistent with both objects having recently left the AGB and transited to the PN phase according to the standard scenario. Although the inner nebulosity carbon abundances are enhanced with respect to the mean PN value, this could, however, be the result of contamination of the nebular material by the WR wind.

Since the material around both the objects considered in this paper is unlikely to be fully ionized, due to the low effective temperatures of the stars (the strong observed CO emission supports this interpretation), we cannot conclude anything as to the overall outer dimensions and dynamical ages of the circumstellar material from the *HST* observations (what we see in Figs. 5.6 and 5.7, is only the ionised part of the nebulae – neutral gas could be present outside that region extending up to several times the ionised regions). However, the apparent expansion age of CPD–56°8032's inner ring of nebular emission is only 100 years, which could give us some idea as to when the nebular ejection *terminated.*

In conclusion, we can say that these two stars are most likely to be objects that have evolved from the AGB according to the standard scenario. A few questions remain, which will have to await resolved nebular spectroscopy and deeper images.

Chapter 6

The WC10 Central Stars CPD–56° 8032 and He 2–113: Model Analysis and Comparison with Nebular Properties

In this Chapter we present a detailed model atmospheric analysis of the two [WC10] central stars of planetary nebulae, CPD–56°8032 and He 2–113. Our study is based on high resolution AAT–UCLES spectroscopy spanning $\lambda\lambda$3500–9200 (see Chapter 3 for a log of the observations and details of the data reduction) and the non–LTE iterative scheme of Hillier (1990; described in Chapter 2 and Section 6.1). Spectroscopic similarities are reflected in comparable physical properties: for both stars we obtain $T_{\rm eff}\sim$30kK and $\log L/L_{\odot}$=3.7; $\log(\dot{M}/M_{\odot}{\rm yr}^{-1})$=−5.4 for CPD–56° 8032 and $\log(\dot{M}/M_{\odot}{\rm yr}^{-1})$=−6.1 for He 2–113, while v_{∞}=225 and 160 km s^{-1} for CPD–56° 8032 and He 2–113, respectively.

The derived stellar properties are fairly consistent with the recent study of Leuenhagen et al. (1996), when adjusted for the different distances adopted, while we find excellent agreement between our C^{2+} wind temperature and the independent determination carried out in Chapter 7, supporting our assumption of radiative equilibrium. Both stars are

Table 6.1: Selected observational results for our programme stars (from Chapter 5 except for distance and absolute V magnitude)

Star	Distance	Visual Magnitude	Interstellar Reddening	Radial Velocity	Absolute Magnitude
	Kpc	V	E(B–V)	km s^{-1}	M_V
CPD–56° 8032	1.53	11.1	0.68	−58.7	−1.9
He 2–113	1.23	11.9	1.00	−57.4	−1.8

highly enriched in carbon and oxygen in reasonable agreement with Leuenhagen et al. (1996), although we obtain a zero stellar hydrogen content for He 2–113 (as in Chapter 5).

Finally, we confront our model flux distributions with observed nebular properties using Zanstra and photoionization techniques and identify a major discrepancy between the observed and predicted nebular properties for these PN. The hydrogen ionizing fluxes predicted by our WR non–LTE models greatly exceed those implied by nebular observations. The lack of heavy element line blanketing in our wind models could be responsible. However, the geometry and high nebular densities of these PN indicate that they represent poor probes of the Lyman continuum flux of their central stars.

We describe our observations and non–LTE spectroscopic technique (Hillier 1990) in Section 6.1. Results are presented in Section 6.2 and compared with previous investigations, notably those from the recent study by Leuenhagen et al. (1996 – hereafter LHJ) which included our programme stars. We undertake Zanstra and photoionization modelling in Section 6.3 to test the validity of current model atmosphere fluxes for WR stars and discuss our results in Section 6.4.

6.1 Spectroscopic Analysis

In this Section we summarise the high spectral resolution AAT observations of CPD–56° 8032 and He 2–113 used for our quantitative study, together with observational results taken from Chapter 5. We also describe our non–LTE model atmosphere code, including its main assumptions, and outline the method followed for the determination of stellar

properties.

6.1.1 Observations

Table 6.1 lists various observational results for our programme stars, which are taken mostly from Chapter 5. Observed visual magnitudes are taken from our spectrophotometry which are within 0.1 mag of near–simultaneous V–band photometry obtained by W.A. Lawson and A. Jones (private communication). We take a slightly different approach to that in Chapter 5 for the determination of distances. Following Chapter 5, we assume core masses of $0.62\,M_{\odot}$ which was obtained by X. W. Liu (private communication) for five LMC Wolf–Rayet CSPN, and applied the Vassiliadis and Wood (1994) tracks to obtain stellar luminosities of $5250\,L_{\odot}$. We then utilised interstellar reddenings obtained from Chapter 5 (using nebular line fluxes) and bolometric corrections obtained in this work to derive distances of 1.53 (1.35) kpc for CPD–56° 8032 and 1.23 (1.50) kpc for He 2–113, with distances in parenthesis obtained in Chapter 5. Our distances are within the errors quoted in Chapter 5, though rely on our theoretical bolometric correction being reliable (see Section 6.3). Bolometric corrections depend on our derived stellar properties, and are extremely temperature sensitive, ranging from −3.0 mag at $T_{\rm eff}$=30kK to −4.5 mag at $T_{\rm eff}$=50kK for O stars according to Vacca et al. (1996). The main deficiency in our analysis is the neglect of line blanketing (see Section 6.2.1), the incorporation of which may lead to systematic errors of up to 0.1 mag in bolometric corrections based on initial test calculations.

Our attempts to verify the interstellar reddenings to CPD–56° 8032 and He 2–113 using model atmosphere continuum distributions were hampered by their variable nature (e.g. Pollacco et al. 1992). Nevertheless, in Fig. 6.1, reddened ultraviolet to near–IR continuum flux distributions (obtained in Sect. 6.2), are compared with observations. Leuenhagen et al. (1996) obtained a similar level of continuum fitting to observations. The flux distributions are relatively well reproduced using our previously derived reddening of E(B–V)=1.00 mag for He 2–113, except in the far–UV. In the case of CPD–56° 8032, its

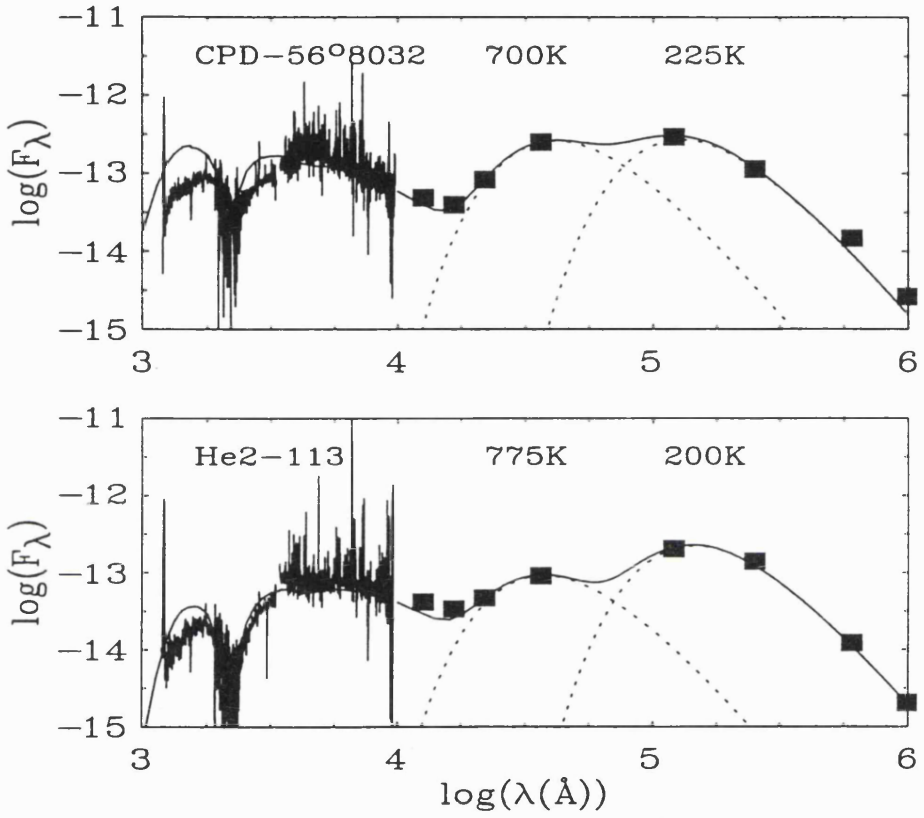

Figure 6.1: Theoretical continuum energy distributions (solid lines) for CPD–56° 8032 (reddened by E(B–V)=0.68) and He 2–113 (reddened by E(B–V)=1.00) compared to IUE and AAT spectrophotometry, optical to near-IR broad band photometry (Webster & Glass 1974) and IRAS colour–corrected fluxes. We include two–component blackbody fits (dotted lines) to their IR excesses, caused by dust from their PNe. Fluxes are shown in erg cm^{-2} s^{-1} $Å^{-1}$

Table 6.2: Physical properties of [WC10] stars from spectral synthesis. We include wind performance numbers, $[(\dot{M}v_\infty)/(L_*/c)]$, and Lyman ionizing photons, Q_0, while abundance ratios are by number

Star	T_* (kK)	R_* ($R_\odot$)	$T_{\rm eff}$ (kK)	$R_{2/3}$ (R_*)	log L_* ($L_\odot$)	log $\dot{M}$ ($M_\odot$/yr)	v_∞ (km s^{-1})	$\dot{M}v_\infty$ (L_*/c)	H	C	O	log Q_0 (s^{-1})	(B−V)$_0$ (mag)	M_V (mag)
									He	He	He			
CPD−56°[a]	34.5	2.0	30.0	1.32	3.72	−5.4	225	9.7	0.0	0.50	0.10	47.26	−0.21	−1.9
He 2–113	31.2	2.5	30.9	1.02	3.72	−6.1	160	1.2	0.0	0.55	0.10	47.19	−0.34	−2.3

[a]CPD−56°8032.

observed UV spectrum falls below model predictions, reddened by E(B–V)=0.68 using the standard extinction curve of Howarth (1983). The poor match may result from variability[1], from a non–standard extinction curve along this line–of–sight as deduced by Rao, Giridhar and Nandy (1990), Jeffery (1995) and in Chapter 5, or from a higher interstellar extinction than is implied from nebular observations.

In Fig. 6.1 we have included blackbody fits to the IR excesses for both stars (dotted lines), which represent the warm dust contribution from their PNe. Our inability to fit both near and far infrared fluxes with a single blackbody curve, indicates the presence of warm and cool dust. Characteristic dust temperatures are similar for both stars, namely $T_{\rm dust}\approx$700 K and 225 K for CPD–56° 8032 and $T_{\rm dust}\approx$775 K and 200 K for He 2–113.

6.1.2 Model Technique

Model calculations are based on the iterative technique of Hillier (1990) which solves the transfer equation in the co-moving frame subject to statistical and radiative equilibrium, assuming an expanding, spherically–symmetric, homogeneous and static atmosphere (a description of the Standard Model for WR stars and of the Hillier modelling code is presented in Chapter 2, although some of the more model–specific choices are described below). In summary, for a given mass–loss rate $\dot{M}$, the density ρ and velocity field $v(r)$ are

[1]IUE spectrophotometry was obtained in August 1991, when the star was recovering from a minimum that had brought it 1.3 mag below maximum (W.A. Lawson, private communication)

related via the equation of continuity ($\dot{M} = 4\pi r^2 \rho(r) v(r)$). The velocity law is assumed to be of the form $v(r) = v_\infty(1 - R_*/r)^\beta$, for the supersonic part. We assume a standard β=1 velocity law here, reproducing approximate line profile shapes. The stellar radius (R_*) is defined as the inner boundary of the model atmosphere and is located at a Rosseland optical depth of 20. The temperature stratification is determined from the assumption of radiative equilibrium with the temperature parameter (T_*) defined by the usual Stefan-Boltzmann relation. Similarly, the effective temperature ($T_{\rm eff}$) relates to the radius ($R_{2/3}$) at which the Rosseland optical depth equals 2/3.

For the present application, the adopted model atom consists of hydrogen (H I), helium (He I-II), carbon (C II-IV) and oxygen (O II-VI) with He I-II, C II-III and O II treated in detail. In total 210 bound–bound levels (835 non–LTE transitions) were considered. Collisional and radiative excitation and ionization processes are also incorporated, with Opacity Project radiative data used for most non–hydrogenic ions (Berrington et al. 1987), except for C III for which special calculations were performed by P.J. Storey, including core polarization. Low temperature dielectronic lines are included for C II-III and O II-III although the most recent C II coefficients are not yet implemented. Our selection of atomic data is identical to that used by Crowther et al. (1995c) for WN/C stars (see also Chapter 2).

The spectral synthesis proceeded as follows (see additionally Crowther et al. 1995a). Stellar parameters result from line profile fits to diagnostic He I-II, C II-IV, O II-III lines together with the absolute visual magnitude (Table 6.1). In the absence of high resolution ultraviolet observations of either star, we measured stellar terminal wind velocities from optical He I P–Cygni profiles, resulting in 225±20 km s^{-1} for CPD–56° 8032 and 160±15 km s^{-1} for He 2–113. Ideally, line profile diagnostics were chosen to be well isolated, with a known line formation mechanism. Our first task was to match the He I λ4471 and He II λ4686 emission line strengths, plus the absolute visual magnitude $M_{\rm V}$, by adjusting R_*, L_* and $\dot{M}$ and assuming carbon and oxygen contents from Barlow and Storey (1993). We next adjusted the C/He and O/He ratios in order to reproduce the chosen line profile diagnostics: C II λ4267, λ4802, C III λ4516 and C IV λ5801–12 for car-

bon, O II λ4591–96 and O III λ5592 for oxygen. Finally, since the metal content produces significant changes in the temperature distribution and thus in the overall ionization state, stellar parameters and abundances were re–adjusted in order to reproduce all diagnostics simultaneously.

Before discussing the results for the individual stars, we first consider some of our assumptions. Spherical symmetry and homogeneity are important assumptions though their reliability for [WCL] stars are largely unknown. While no evidence for clumping is apparent for the programme stars under investigation, Balick et al. (1996) and Acker et al. (1997) have recently shown that NGC 40 ([WC8]) and BD+30 3639 ([WC9]) show line profile variability reminiscent of classical WCL stars (Robert 1994), which is attributed to the presence of clumped material. The presence of clumping in the region where the optical line profiles of [WC10] stars be formed could lead to us overestimating mass–loss rates by about a factor of 3–4 (Hillier 1991; Schmutz 1997).

6.2 Results and Comparison with Previous Investigations

We now present the results of our spectroscopic investigation, including a discussion of the reliability of model assumptions, e.g. the neglect of heavy–metal line blanketing. We compare our results with the recent analysis of LHJ, who analysed a large sample of [WCL] stars. The overall agreement is very good, except for our derived elemental abundances. We also compare our derived electron temperature in the C^{2+} line formation region with results from a dielectronic line analysis (Chapter 7) and for the first time confirm the validity of radiative equilibrium in massive stellar winds.

6.2.1 Spectroscopic Results

In Figs. 6.2 and 6.3 we present a comparison of selected observed line profiles (solid) with our synthetic spectra (dotted) for CPD–56° 8032 and He 2–113, respectively. Overall, our profile fits successfully reproduce the strength and width of many emission profiles covering a wide range in excitation and ionization. Further, the observed ionization stratification

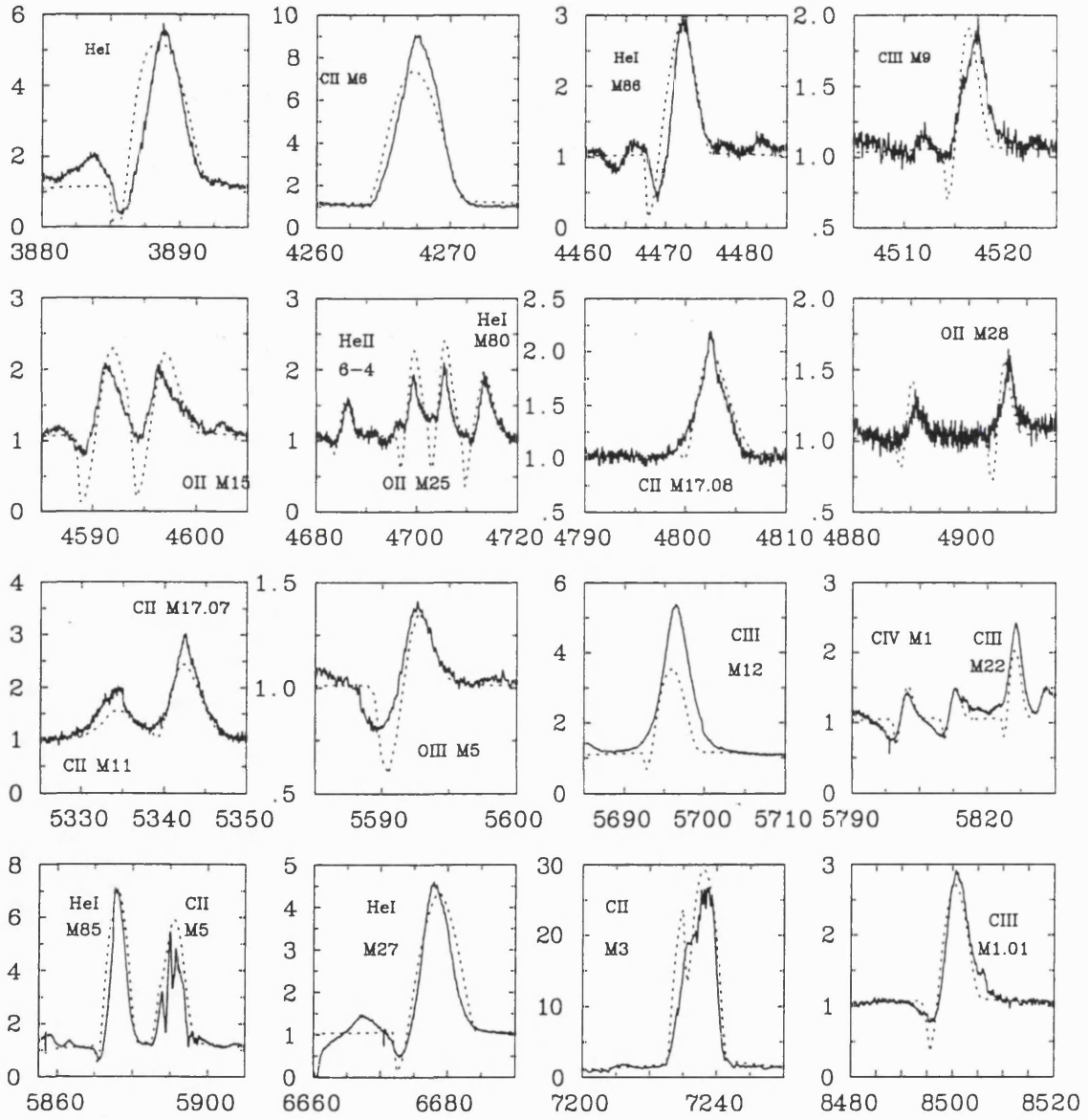

Figure 6.2: A comparison between our synthetic spectrum of CPD–56° 8032 (dotted line) and AAT+UCLES observations (solid line)

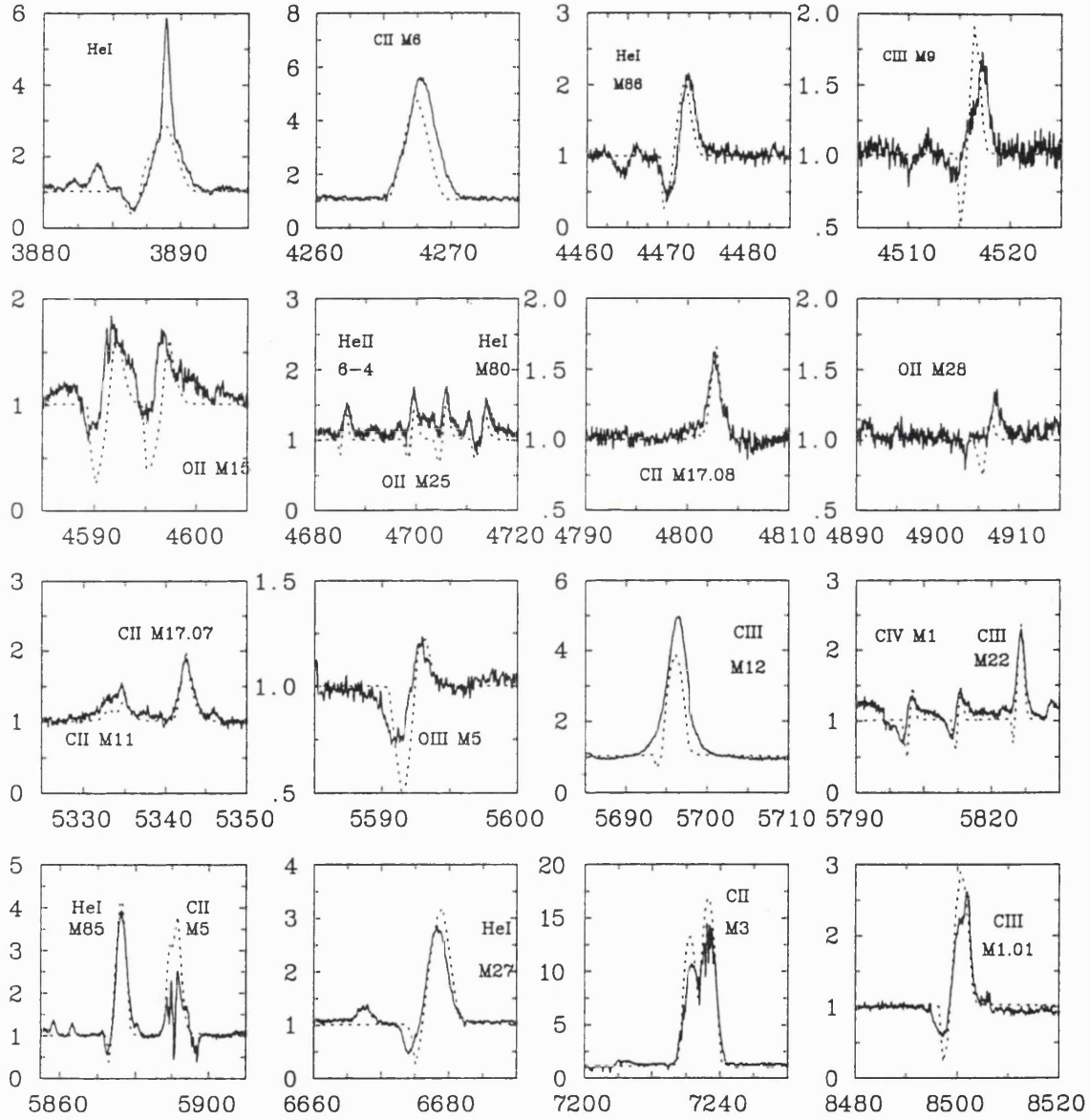

Figure 6.3: A comparison between our synthetic spectrum of He 2–113 (dotted line) and AAT+UCLES observations (solid line)

is well reproduced, as inferred from an inspection of line profile widths for different ions (e.g. compare He II to C II). However, some important differences remain. In common with previous comparable studies of WN and WC stars (Crowther et al. 1995b, Hillier 1989), the theoretical profiles overestimate the strengths of absorption lines for He I, C III and O II profiles. In addition, poor agreement is found between theoretical and observed emission line strengths of some non–diagnostic lines, of which the most notable example is the WC classification line C III λ5696, despite the use of sophisticated atomic data for C III.

We present a summary of our derived stellar parameters in Table 6.2. Overall, as reflected in their spectra, the stellar properties and chemistries derived for CPD–56° 8032 and He 2–113 are very similar. The stellar wind of CPD–56° 8032 is faster, denser, and consequently more extended, while the carbon content in He 2–113 is marginally greater. Our final abundance determinations indicate H:He:C:O mass fractions (in %) of 0:34:52:14 for CPD–56° 8032 and 0:34:53:13 for He 2–113.

We include values of the wind performance number, $\dot{M}\, v_\infty /(L/c)$, a commonly used indicator of wind density which indicates the efficiency at which radiation momentum is imparted to the wind, and is equal to unity in the 'single scattering limit' (i.e. scattering of each photon once in a single line). As with most other WR–type stars, the wind performance values of these [WC10] stars are in excess of unity, causing difficulties for radiatively driven wind theory (e.g. Kudridzki et al. 1989) unless multiple scattering is efficient. Lucy and Abbott (1993) have demonstrated how the ionization stratification of Wolf–Rayet stars may help solve this long established problem.

In Fig. 6.4 we present various inferred wind properties, including T_e, N_e and the ionization balance versus Rosseland optical depth ($\tau_{\rm Ross}$). This demonstrates the wide range of physical properties throughout the winds of each star. Overall, the two winds are very similar, though He^+, C^{2+} (and O^{2+}) remain the dominant ionization stages over a greater part of the wind of He 2–113 than of CPD–56° 8032, because of its lower stellar temperature and wind density. Line formation regions of selected diagnostics are also

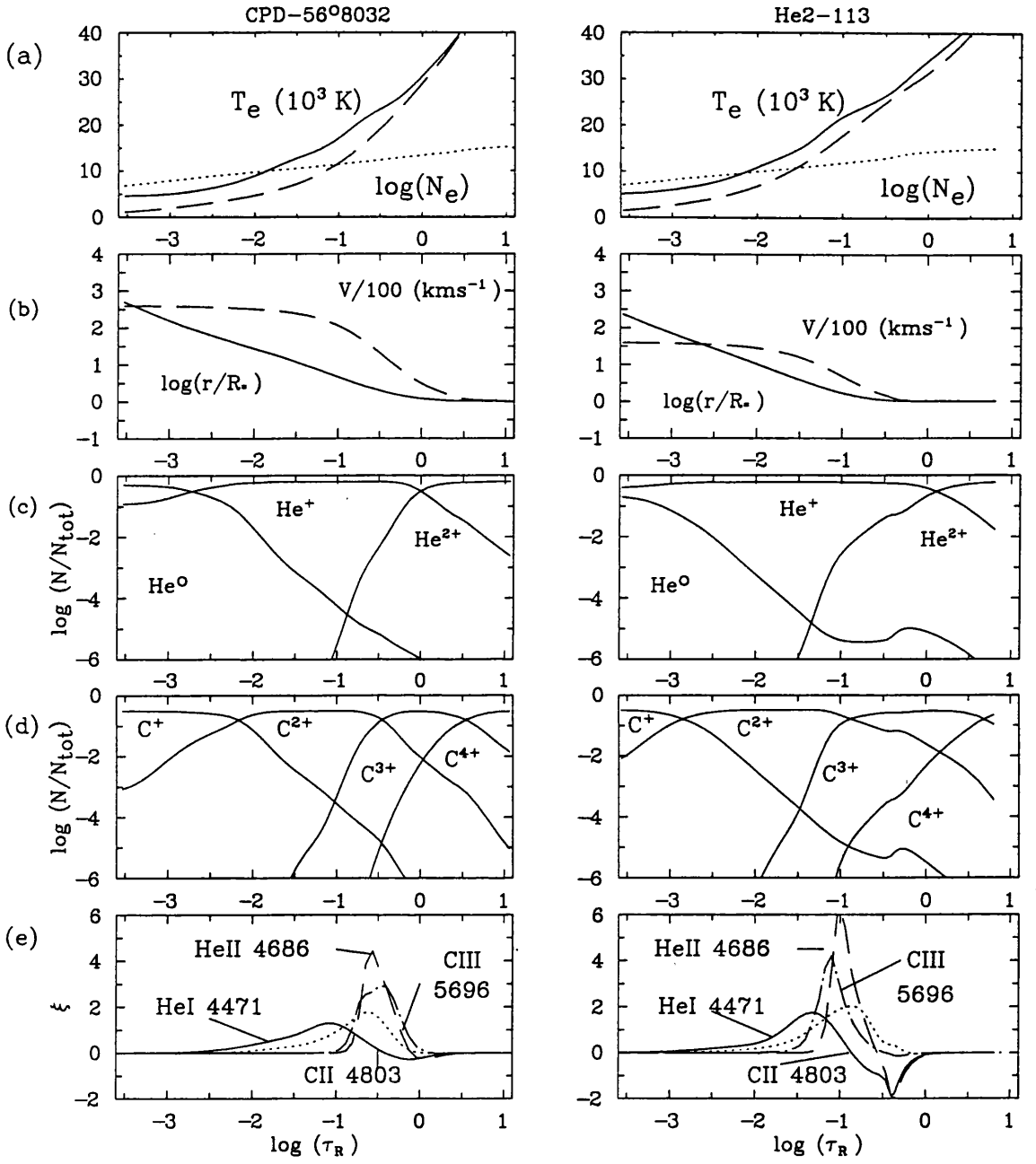

Figure 6.4: Stellar wind parameters for CPD–56° 8032 (left column) and He 2–113 (right column) as a function of Rosseland optical depth ($\tau_{\rm Ross}$). (a) Wind electron temperatures (solid lines) and densities (dotted lines), where the dashed line represents the grey distribution. (b) Stellar radii (solid lines) and our assumed velocity distributions (dashed lines). Variation of helium (c) and carbon (d) ionization stages. (e) Line formation regions for selected diagnostics. The meaning of ξ is discussed in the text

Table 6.3: Comparison of our derived stellar parameters with those of Leuenhagen et al. (1996, LHJ), plus those of Leuenhagen et al., scaled to our assumed distance (LHJ2)

Analysis	T_* (kK)	R_* ($R_\odot$)	$T_{\rm eff}$ (kK)	$\log L_*$ ($L_\odot$)	$\log \dot{M}$ ($M_\odot {\rm yr}^{-1}$)	v_∞ (km s^{-1})	D (kpc)
			CPD–56° 8032				
LHJ	32.0	3.4	30.0	4.06	−5.6	240	2.36
LHJ2	···	2.2	···	3.68	−5.9	240	1.53
This Work	34.5	2.0	30.0	3.72	−5.4	225	1.53
			He 2-113				
LHJ	30.0	6.5	29.0	4.51	−5.5	200	3.50
LHJ2	···	2.3	···	3.60	−6.2	200	1.23
This work	31.2	2.5	30.2	3.72	−6.1	160	1.23

presented in Fig. 6.4(e), where ξ (Hillier 1989), plotted on the ordinate axis is given by:

$$\xi = \alpha r^3 \int_{-1}^{+1} N_u \beta(\mu)(1.0 - I(\mu)\chi_L/\eta_L) \exp(-\tau_c(\mu)) d\mu$$

where I(μ) is the local specific intensity, χ_L is the line opacity, η_L is the line emissivity, $\tau_c(\mu)$ is the thermal continuum optical depth to the boundary, α is a constant depending on the line under consideration, and β_μ is the angle dependent Sobolev escape probability (Castor 1970).

Our current modelling technique neglects the effect of heavy element line blanketing, which would lead to a higher ionization in the inner regions (through backwarming) but a lower wind ionization (by flux blocking) in the outer regions. The effect of blanketing on stellar properties is related to excitation and wind density. From our experience we expect that blanketing will have only a minor effect on the derived stellar parameters of [WC10] stars (except perhaps bolometric corrections), although it is expected to have a major effect on the theoretical UV energy distribution.

We anticipate that the effect of heavy element line blanketing on the stellar parameters of [WC10] stars is not critical for the following reasons: while opacities due to Fe and Ni provide a dramatic effect for hot stars composed of principally helium or hydrogen (Hubeny 1996), the carbon opacities included here have a dominant effect in WC stars (Hillier and

Miller 1997). Secondly, Crowther et al. (1995a) found that the effect of line blanketing in WNL stars with T_*~30kK did not introduce significant uncertainties into the derived stellar parameters. Finally, the inability to reproduce all observed ionization stages is frequently attributed to the neglect of blanketing (e.g. Crowther et al. 1995b) while no such inability is found here for our programme stars.

6.2.2 Comparison of Stellar Properties with Previous Studies

We now turn to a comparison of the stellar properties derived for our programme stars with those published previously. Up until very recently, studies of WC–type CSPN have been restricted to very simplified techniques inappropriate for stars with highly extended atmospheres. The only comparable study has recently been carried out by LHJ who included CPD–56° 8032 and He 2–113 in their sample of [WCL] CSPN. While their study used an independent code, the same assumptions of spherical symmetry and homogeneity were made.

LHJ used significantly higher distances than we have obtained here for both CPD–56° 8032 (2.36kpc from Rao et al. 1990) and He 2–113 (3.5kpc from Le Bertre et al. 1989). We compare stellar parameters obtained here with those derived by LHJ in Table 6.3, and have also scaled their results to our derived distances for the purpose of comparison. Overall, we find (surprisingly) good agreement between the two analyses, given the inherent difficulties involved in such studies, the use of independent codes and different optical datasets. However, LHJ adopt slightly higher terminal velocities and their scaled mass–loss rates are 0.2–0.5dex lower than our value.

Although comparable profile fits are obtained for many lines over the spectral region in common with their study, namely $\lambda\lambda$4050–4900 (and note improved profile fits to He II λ4686 and C III λ4516), we suggest that our results are more reliable for the following reasons: (i) our higher resolution observations span a much greater range, $\lambda\lambda$3500–9200 allowing detailed fits to additional ionization and abundance diagnostics. Further, our observations include ions not covered by LHJ, including C IV and O III. LHJ claimed that

Table 6.4: Comparison of abundances (by number) for CPD–56° 8032 and He 2–113 derived here with the non–LTE study of Leuenhagen et al. (1996, LHJ)

Analysis	H/He	C/He	O/He
	CPD–56° 8032		
LHJ	$\leq$0.05	0.40±0.05	0.05±0.01
This work	$\lesssim$0.02	0.50±0.10	0.10±0.05
	He 2–113		
LHJ	$\leq$ 0.64	0.37±0.05	0.03±0.01
This work	$\lesssim$ 0.02	0.55±0.15	0.10±0.05

C IV $\lambda\lambda$5801,11 emission is not expected in the spectrum of either star, on the grounds that they did not observe these features in the spectra of either M 4–18 nor K 2–16. We would like to point out however, that the C IV features *are* present in the spectra of M 4–18 (as they are present in the spectra of CPD–56° 8032 and He 2–113 – cf. Appendices C and D) and that they did not observe them due to the lower resolution of theis spectra (2.7 Å). (ii) The stellar luminosities resulting from the distances adopted by LHJ would indicate current core masses of 0.69 $M_{\odot}$ and 0.94 $M_{\odot}$ for CPD–56° 8032 and He 2–113, respectively, the latter of which whould be highly peculiar for a low mass progenitor, according to recent evolutionary models (Vassiliadis and Wood 1994).

In Chapter 7, we will use C II dielectronic lines to derive electron temperatures of 20±1.5kK and 17±1.5kK for CPD–56° 8032 and He 2–113, respectively. Unfortunately, it is not straightforward to directly compare with our results since in Fig. 6.4 we can see the temperature variation across the line formation region of each line. Nevertheless, the peak of the line formation region for C II lines (e.g. λ4802) corresponds to ~20kK for both objects, in good agreement with Chapter 7. *This provides the first independent confirmation of the assumption of radiative equilibrium in WR atmosphere studies.*

6.2.3 Stellar Abundances

We present our derived atmospheric abundances for CPD–56° 8032 and He 2–113 in Table 6.4, together with the determinations from LHJ. Since we have at our disposal many

C II and He I recombination lines, formed through similar processes in a comparable part of the stellar wind, we anticipate that the derived C/He ratios are reliable. In contrast, more uncertainty in our derived O/He abundance ratios needs to be admitted since the number of suitable oxygen lines (principally O II) is far fewer, and their line formation mechanisms are more complex.

Comparing our derived abundances with LHJ, we find somewhat higher carbon and oxygen abundances, which fall outside their claimed uncertainties. Given the limited number and variable quality of fits obtained by both LHJ, and in this study, we feel higher uncertainties need to be admitted, especially for oxygen, and demonstrate the scale of conflicting results from studies based on very similar codes and observational datasets.

Regarding hydrogen, re–iterating our conclusions from Chapter 5, we attribute the broad pedestal in the Balmer profiles of He 2–113 to a nebular origin from comparision with the purely nebular [O I] lines at 6300 and 6363 Å. In contrast, LHJ obtained H/He$\leq$0.64 (by number) for He 2–113 from fitting the broad Balmer emission assuming a stellar origin. Our calculations including hydrogen confirm that the wings of the Hβ emission feature can be reproduced with a similar stellar H/He ratio, however we were unable to simultaneously reproduce the wings of the stronger Hα line using an identical abundance.

LHJ suggested that an observed feature in the spectrum of He 2–113 at λ4634 was due to N III, and proposed that this indicated material from a previous H–burning phase is still mixed into the atmosphere. While our observations confirm the presence of this λ4634 feature it may not be due to nitrogen – should nitrogen be present, other N III lines at $\lambda\lambda$4097,4103 and $\lambda\lambda$5324,50 would be expected which are not observed.

6.3 Comparison of Stellar Flux Distributions with Nebular Properties

In this Section we compare the model atmosphere flux distributions with observed nebular properties, by carrying out a Zanstra analysis and photoionization modelling of the

PN using, in addition to our own WR model fluxes, blackbody and LTE Kurucz model distributions.

6.3.1 Zanstra Analysis

The hydrogen Zanstra analysis relies on the assumption that the nebula is optically thick to hydrogen Lyman continuum photons. If this assumption is valid, as should be the case for the young, high density PN of CPD–56° 8032 and He 2–113, the dereddened Hβ flux, together with the appropriate recombination coefficients, should give a reliable estimate of the number of photons (Q_0) emitted shortwards of 912 Å by the star.

From the Hβ nebular observations (Chapter 5) and our adopted distances from Table 6.1, we obtain log $Q_0(s^{-1})$=45.74 for CPD–56° 8032 and log $Q_0(s^{-1})$=45.26 (D=1.23 kpc) for He 2–113. The numbers of ionizing photons predicted by our model corresponds to log $Q_0(s^{-1})$=47.23 and 46.51 for CPD–56° 8032 and He 2–113 respctively, exceeding those inferred from the nebulae, by factors of 30 and 80 for CPD–56° 8032 and He 2–113, respectively. Therefore, either the Zanstra assumptions are not met for these nebulae, or the Lyman ionizing fluxes predicted are far too strong (see Sect. 6.3.2).

We have also carried out Zanstra analyses using both blackbody and line blanketed LTE Kurucz ATLAS9 energy distributions, obtaining temperatures corresponding to the observed ionizing fluxes and V–band magnitudes. With regard to CSPN, Kurucz ATLAS9 flux distributions have one major advantage over our derived energy distributions that impacts heavily on the nebular properties, namely the extremely thorough line blanketing in the far and extreme ultraviolet. However, let us recall that for extended atmospheres, the assumption of LTE in Kurucz models completely breaks down, while we have also shown that the assumed solar chemical composition of the Kurucz atmosphere is invalid.

By imposing the ionizing capabilities of these flux distributions, the resulting stellar luminosities are significantly *lower* than those derived in the present analysis, up to a factor of 3.5 for the Zanstra analysis of CPD–56° 8032 using a blackbody. We obtain blackbody temperatures of 18 000 K and 22 000 K for CPD–56° 8032 and He 2–113, respectively.

ATLAS9 flux distributions yield effective temperatures of 25 000 K for CPD–56° 8032 and 29 000 K for He 2–113, which are very smilar to determinations by Aitken et al. (1980) using earlier LTE model atmospheres. For the 25 000 K Kurucz model, we adopt log g=3.0, while at 29 000 K we adopt log g=3.5 since this reppresents the lowest gravity model calculated at this temperaiure.

While the 'effective temperatures' obtained in our non–LTE wind model study, 30 000 and 31 000 K for CPD–56° 8032 and He 2–113 respectively, are quite similar to the Kurucz (1991) Zanstra fits to the observed nebular Balmer lines, the differences in their ionizing capabilities are apparent (see Figs. 6.5 and 6.6), illustrating the problems encountered when dealing with effective temperatures for stars with very extended atmospheres.

6.3.2 Photoionization Modelling

As demonstrated in the previous subsection, blackbody and Kurucz energy distributions can be chosen to reproduce the observed *nebular* ionizing fluxes, although these bear no relation to the observed *stellar* spectrum. We now carry out a more sophisticated study of the nebular spectrum predicted by our non–LTE model flux distribution, plus the blackbody and Kurucz distributions, using photoionization modelling of Harrington et al. (1982). We assume that the nebula can be represented by a hollow, spherical shell of uniform density which is ionized and heated solely by the UV radiation of the central star (see Section 2.2.5 for a description of the code).

The WR non–LTE models luminosities and distances were maintained at the values listed in Tables 6.1, 6.5 and 6.6, while for the blackbody and Kurucz model atmospheres, the luminosities were scaled to the adopted distance in order to reproduce the dereddened V magnitude.

The electron densities were fixed at their empirically derived values of 63 000 cm^{-3} for both CPD–56° 8032 and He 2–113 (Chapter 5). The inner nebular radii (Tables 6.5 and 6.6) were fixed at the value derived from the HST observations (Chapter 5), scaled to the adopted distances. The outer radii were chosen so as to include the Strömgren sphere

Table 6.5: Comparison of results from photoionization models for CPD–56° 8032 with observations (I(Hβ)=100), using non–LTE, blackbody and Kurucz energy distributions, demonstrating the failure of all fluxes

Parameter	Observed	non–LTE	Blackbody	Kurucz
T_{eff}(kK)	–	29	18	25
$\log(L/L_{\odot})$	–	3.72	3.18	3.56
R($R_{\odot}$)	–	2.0	4.0	3.2
log $Q_0(s^{-1})$	45.74	47.23	45.74	45.74
log(I(Hβ))	–11.03	–9.52	–11.03	–10.95
ϵ	–	0.1	1	1
R_{inner}(pc)	0.004	0.004	0.004	0.004
R_{outer}(pc)	0.008	0.022	0.005	0.005
C/H$\times10^3$	6.3	6.3	6.3	6.3
N/H$\times10^5$	8.3	8.3	21	8.3
O/H$\times10^4$	4.8	4.8	22	4.8
S/H$\times10^5$	1.0	1.0	2.2	1.0
$M_{PN}(M_{\odot})$	–	0.020	0.00064	0.0041
1909 C III]	0	0.0	0.0	0.0
2326 C II]	1500	423	79	310
3727 [O II]	82	27	41	23
5007 [O III]	0.0	0.0	0.0	0.0
5755 [N II]	5.1	1.9	1.3	1.4
6300 [O I]	21	1.9	4.3	1.7
6548 [N II]	62	33	43	29
6717 [S II]	9.8	1.7	5.2	3.5
7325 [O II]	41	12	12	9.3
9069 [S III]	2.3	33	8.5	14
S^{2+}/S^{+}	0.038	2.80	0.16	0.47
T_e(K)	8800	7400	6200	7100

Table 6.6: Comparison of results from photoionization models for He 2–113 with observations (I(Hβ)=100), using non–LTE, blackbody and Kurucz energy distributions, demonstrating the failure of all fluxes

Parameter	Observed	non–LTE	Blackbody	Kurucz
T_{eff}(kK)	...	30	22	29
$\log(L/L_{\odot})$	...	3.72	3.32	3.60
R($R_{\odot}$)	–	2.5	2.5	2.7
log $Q_0(s^{-1})$	45.26	46.51	45.26	45.26
log(I(Hβ))	–10.21	–9.49	–10.21	–10.14
ϵ	–	0.1	1	1
R_{inner}(pc)	0.002	0.002	0.002	0.002
R_{outer}(pc)	0.008	0.020	0.008	0.006
C/H$\times10^3$	5.3	5.3	5.3	5.3
N/H$\times10^5$	6.6	6.6	6.6	6.6
O/H$\times10^4$	4.8	4.8	4.8	4.8
S/H$\times10^5$	3.9	3.9	3.9	3.9
$M_{PN}(M_{\odot})$	–	0.014	0.0011	0.0069
1909 C III]	0	0.0	5.7	0.9
2326 C II]	1032	397	50	489
3727 [O II]	30	32	26	37
5007 [O III]	0	0.0	0.7	0.0
5755 [N II]	5.8	1.7	1.4	2.0
6300 [O I]	5.2	1.9	0.4	0.6
6548 [N II]	40	29	25	31
6717 [S II]	2.6	2.8	0.6	0.3
7325 [O II]	31	15	11	18
9069 [S III]	6.7	44	10	15
S^{2+}/S^{+}	0.5	2.4	0.81	6.7
T_e(K)	8400	7600	7300	7800

and are also shown in Tables 6.5 and 6.6. The clumping filling factor was maintained at its default value of unity for a completely filled nebula, unless the Hβ flux was grossly overestimated, in which case the vacuum filling factor (1-ϵ) was increased.

As a starting point we adopted the empirically derived nebular abundances (Chapter 5, see Tables 6.5 and 6.6, column 2). For the abundance of neon, we assumed the mean PN value of Ne/H=1.2×10^{-4} (Kingsburgh and Barlow 1994). Since helium is expected to be mostly neutral in these nebulae we assumed He/H$\sim$0.1 for each PN, though the precise choice is not critical. In principle, lines of carbon and oxygen could then be fitted by changing the corresponding abundances. In practice, there was no way of fitting line fluxes and nebular electron temperatures simultaneously, and the abundances were fixed at their empirically derived values, apart from one instance which was used as a demonstration (see below). In Tables 6.5 and 6.6 we compare theoretical predictions with dereddened nebular observations.

For both PN, the WR non–LTE flux distributions fail to predict the observed nebular line strengths and electron temperatures despite the vacuum filling factor having been set to the unrealistically high value of 0.9. In both cases, the predicted electron temperatures are too low, while the nebular ionization balance is poorly predicted (witness the S^{2+}/S^{+} ratios). However, the blackbody and Kurucz (1991) model atmospheres perform no better, with equally poor T_e and ionization balance, despite being chosen to reproduce the observed hydrogen Lyman continuum flux! In the case of our blackbody modelling of CPD–56° 8032, we investigated the effect of artificially increasing the nitrogen and oxygen abundances, in order to increase the [O II] and [N II] fluxes. However, this proved unsuccessful *and* further reduced the nebular electron temperature, due to the greater cooling. In conclusion, we were unable to find a satisfactory combination of parameters which could reproduce the observed nebular properties of CPD–56° 8032 and He 2–113.

From looking at Figs. 6.5 and 6.6, we might suspect that the lack of heavy element line blanketing in our WR non–LTE model could be to blame for the apparent excess of ionizing photons. However this cannot be the sole cause of the problem, since we

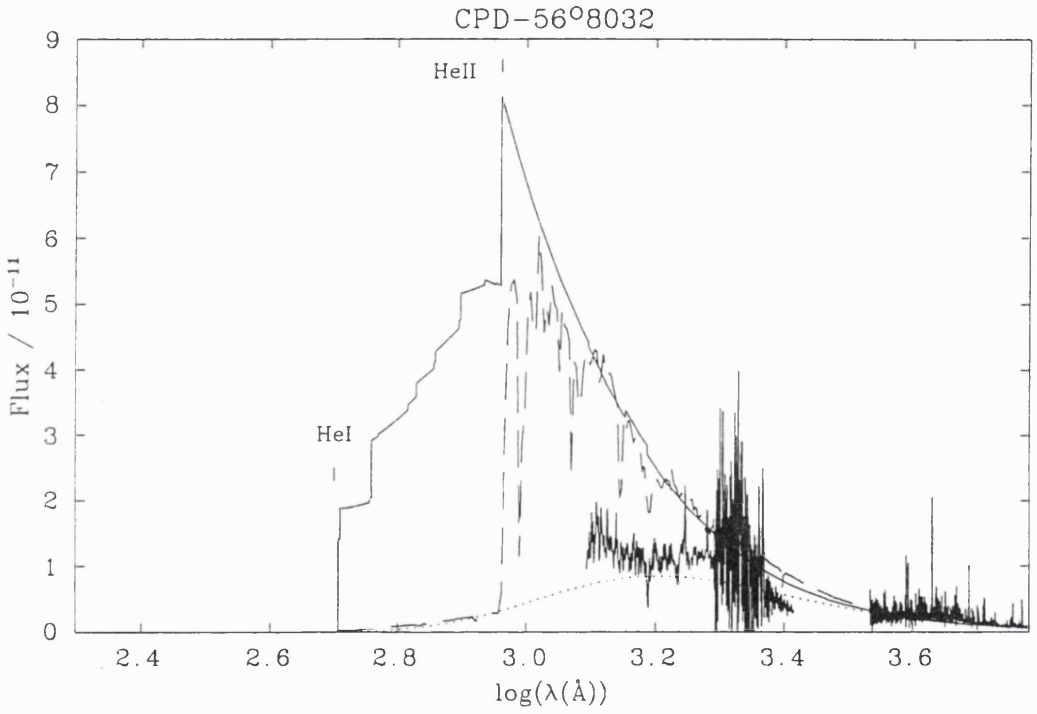

Figure 6.5: The optical and UV spectrum of CPD–56°8032 compared with a 18 000 K blackbody flux distribution (dotted line), a 25 000 K, log(g)=3.0 plane–parallel Kurucz model atmosphere (dashed line) and a 34 000 K WR non–LTE model atmosphere (solid line). The H I and He I ionization edges are marked

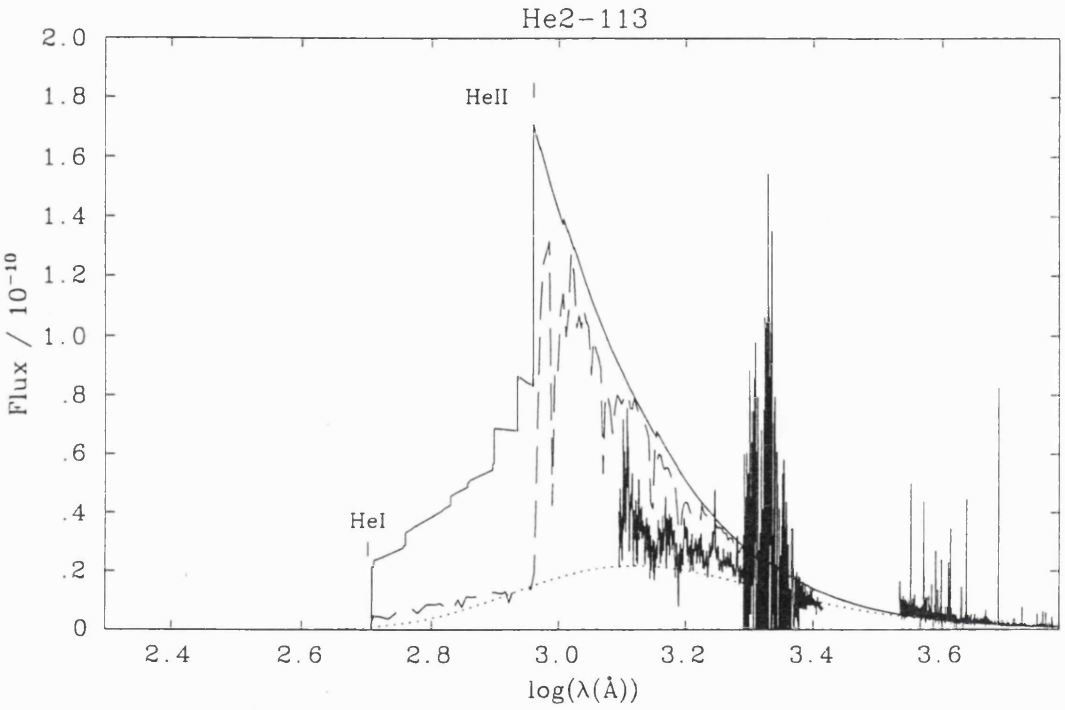

Figure 6.6: The optical and UV spectrum of He 2–113 compared with a 22 000 K blackbody flux distribution (dotted line), a 29 000 K, log(g)=3.5 plane–parallel Kurucz model atmosphere (dashed line) and a 30 500 K WR non–LTE model atmosphere (solid line). The H I and He I ionization edges are marked

would otherwise expect a similar problem to arise in the case of the PN of M 4–18 (which has a WC10 central star whose spectrum is almost identical to the one of He 2–113; Chapter 8). Another reason for the discrepancy might be sought in the irregular shapes of these two young, high density PN, which are far from being hollow spheres with well defined boundaries. Once again, however, we see that the similarly irregular and high density PN of SwSt 1 (which has a [WC9pec] central star, Chapter 4) can be modelled well using different flux distributions (Chapter 8).

Given the above considerations, we propose that the high nebular density of CPD–56° 8032 and He 2–113 is playing a role. Barlow (1983) showed that the dust optical depth inside the ionized zone of a PN may exceed unity when the electron density exceeds a few 1×10^5 cm^{-3}. Therefore dust may be complicating the situation for CPD–56° 8032 and He 2–113 by competing with the gas in absorbing stellar UV radiation. We recall that both these PN have very high infrared excesses relative to normal PN. *Therefore these two PN may represent poor probes of the stellar Lyman continuum flux distribution.*

6.4 Discussion

Our model results for the [WC10] central stars CPD–56° 8032 and He 2–113 compare remarkably well with the results obtained by Leuenhagen et al. (1996) despite the independent nature of the two codes. However, some differences are obtained, the most important of which for evolutionary considerations is that neither star contains hydrogen – as demonstrated in Chapter 5, the Balmer profiles of He 2–113 are of nebular origin.

We also differ from Leuenhagen et al. (1996) who claimed that nitrogen was detected in the wind of He 2–113. Although we confirm the presence of this feature (λ4634), it lies in a very crowded part of the optical spectrum and need not be due to nitrogen. If N III is responsible for this feature, other strong nitrogen lines would be expected (e.g., N II $\lambda\lambda$5667–5730, N III $\lambda\lambda$4097–4103), which are absent from the spectrum of He 2–113. In the presence of hydrogen, nitrogen could have been interpreted as the normal product of hydrogen-burning. Without hydrogen, nitrogen would have to be produced by conversion

of dredged-up carbon. However, this process only happens at the base of the envelopes of the most massive post–AGB stars, invoking a high mass for He 2–113.

We have demonstrated that current non–LTE model atmospheres are very *successful* in reproducing the observed optical spectra of CPD–56° 8032 and He 2–113. However, predicted flux distributions are equally *unsuccessful* in simultaneously reproducing their observed nebular properties. Although theoretical models could be at fault, it appears that the high densities of these two PN may allow dust to compete with the gas in absorbing UV radiation from the central star. Nevertheless, nebulae in general certainly represent useful indirect probes of the EUV flux distribution of hot stars in general (Esteban et al. 1993; Crowther et al. 1998b). Therefore other WC–type CSPN should be investigated using the technique outlined here to provide a more conclusive test of theoretical models.

Chapter 7

Wind Electron Temperatures and Abundances for [WCL] Stars

In this Chapter we present a method for the direct determination of the wind electron temperature of [WCL] central stars CPD–56°8032, He 2–113, M 4–18, IRAS 17514–1555 and K 2–16. In a previous effort to determine the wind electron temperature of [WC10] stars, Barlow and Storey (1993) analysed a spectrum of CPD–56° 8032 taken with the AAT RGO Spectrograph at a resolution of 1.0 and 0.50 Å in first and second order (see Chapter 3). The higher resolution UCLES spectra used here (also described in Chapter 3), allow much more reliable deblending of the components of the C II dielectronic multiplets. We have also extended the sample from one to five stars.

By using the derived electron temperatures we determine the abundances of carbon and oxygen with respect to helium for CPD–56°8032, He 2–113 and M 4–18. Abundance determinations have received much attention in the past due to a major caveat that could seriously affect results: if the lines used to obtain abundances are optically thick, a fraction of the line flux would not be observed and consequently abundances would be underestimated. High optical depth would also bias the electron temperature determination. For this reason we dedicate Section 7.7 to the study of optical thickness for a group of carbon and helium lines with the aim of assessing the quality of our results.

7.1 Theory of Dielectronic Line Formation

A great number of the lines in the spectra of WC stars are excited primarily by recombination processes. Of these some are due to the process of low temperature dielectronic recombination (Storey 1981, Nussbaumer and Storey 1984). Such lines arise from quasi–bound autoionizing states lying at energies above the ionization limit of the ion in question. These states are formed by dielectronic capture from the continuum and decay either by radiative transitions to other states (autoionizing or bound) or by radiationless transitions back to the continuum (autoionization). The latter process usually dominates and the population of the states is given by the Saha equation. We are here concerned with dielectronic lines that arise from transitions directly from autoionizing states.

The emissivity of a line per unit volume per unit time is:

$$\varepsilon(\lambda) = N_i \Gamma_\lambda^R h\nu, \tag{7.1}$$

where N_i is the population of level i (the upper level of the transition in question), Γ_λ^R is the Einstein A coefficient (i.e. the transition probability), h is the Planck constant and ν is the transition's frequency. To obtain an expression for the population of an autoionizing level i, we consider that, in Thermodynamic Equilibrium (TE), the rate of autoionization per unit volume per unit time must equal the rate of dielectronic capture per unit volume per unit time, i.e.:

$$N_i^S \Gamma_i^A = N_e N_+^S \alpha_c, \tag{7.2}$$

where Γ_i^A is the autoionization probability of level i, N_e and N_+ are the electron and ion densities, α_c is the rate coefficient for dielectronic capture and where we use the superscript S to indicate the TE (Saha) population. If the level is not in TE with the continuum, one must include a term which accounts for the depopulation of the level via downwards transitions. This translates into the expression:

$$N_i \Gamma_i^A + N_i \Gamma_i^R = N_e N_+ \alpha_c, \tag{7.3}$$

where Γ_i^R is the total downwards probability from level i, assumed to be due to radiative processes. The recombination coefficient α_c, however, is an intrinsic atomic property,

independent of whether the level is in TE with the continuum. Hence, from Eq. 7.2:

$$\alpha_c = \left(\frac{N_i}{N_e N_+}\right)_S \Gamma_i^A. \tag{7.4}$$

Substituting Eq. 7.4 in Eq. 7.3 we obtain:

$$N_i(\Gamma_i^A + \Gamma_i^R) = \left(\frac{N_i}{N_e N_+}\right)_S N_e N_+ \Gamma_i^A. \tag{7.5}$$

Let's now parameterise the departure of the level from TE with the departure coefficient b_i so that:

$$\left(\frac{N_i}{N_e N_+}\right) = b_i \left(\frac{N_i}{N_e N_+}\right)_S, \tag{7.6}$$

from Eqs. 7.5 and 7.6 it follows that:

$$b_i = \frac{\Gamma_i^A}{\Gamma_i^A + \Gamma_i^R}, \tag{7.7}$$

and

$$\frac{N_i}{N_e N_+} = \left(\frac{N_i}{N_e N_+}\right)_S \frac{\Gamma_i^A}{\Gamma_i^A + \Gamma_i^R}. \tag{7.8}$$

But from the Saha equation we know that:

$$\left(\frac{N_i}{N_e N_+}\right)_S = \frac{\omega_i}{2\omega_+} \left(\frac{h^2}{2\pi m k T}\right)^{\frac{3}{2}} e^{-E_i/kT}, \tag{7.9}$$

where ω_i and ω_+ are the statistical weights of the upper (autoionizing) state and of the recombining ion ground state ($C^{2+}\ ^1S$, $w_+ = 1$) respectively, m is the electronic mass, k is the Boltzmann constant, T is the electron temperature of the line forming region and E_i is the energy of the autoionizing state with respect to the $C^{2+}\ ^1S$ ground level. From Eqs. 7.8 and 7.9 we obtain the expression for the level population:

$$N_i = N_e N_+ \frac{\Gamma_i^A}{\Gamma_i^A + \Gamma_i^R} \frac{\omega_i}{2\omega_+} \left(\frac{h^2}{2\pi m k T}\right)^{\frac{3}{2}} e^{-E_i/kT}. \tag{7.10}$$

Substituting Eq. 7.10 in Eq. 7.1 we obtain an expression for the emissivity of the transition as a function of electron temperature and density and ionic density in the plasma where the transition occurs:

$$\varepsilon(\lambda) = N_e N_+ \frac{\omega_i}{2\omega_+} \left(\frac{h^2}{2\pi m k T}\right)^{\frac{3}{2}} e^{-E_i/kT} b_i \Gamma_\lambda^R h\nu. \tag{7.11}$$

The line flux received at the Earth is given by:

$$F(\lambda) = \frac{1}{4\pi D^2} \int_V \varepsilon_\lambda dV, \tag{7.12}$$

where V is the emitting volume and D the distance to the source. By comparing the fluxes in lines of sufficiently different E_i we can determine the electron temperature directly. By combining Eqs. 7.10, 7.11, and 7.12 we have:

$$F(\lambda, T_e) = Q(\lambda, T_e) \times \frac{1}{4\pi D^2} \int N_e N_+ dV, \tag{7.13}$$

where

$$Q(\lambda, T_e) = \frac{\omega_i}{2\omega_+} \left(\frac{h^2}{2\pi m_e k T_e} \right)^{\frac{3}{2}} e^{-\frac{E_i}{kT_e}} \frac{\Gamma_i^A \Gamma_\lambda^R}{\Gamma_i^R + \Gamma_i^A} h\nu. \tag{7.14}$$

We now define:

$$X(\lambda, T_e) = \frac{I(\lambda)}{Q(\lambda, T_e)} \tag{7.15}$$

where $I(\lambda)$ is the measured de–reddened flux in the line of wavelength λ. If the electron temperature for the region of formation of C II recombination lines is assumed to be constant, their relative intensities can be used as a tool to determine the wind electron temperature of their formation region. The intensities of the dielectronic lines are determined by fitting the region of the spectrum containing them (details of the fits are given in Section 7.3).

If our stated assumption were correct and the flux measurements were free of error we would obtain the same value of $X(\lambda, T_e)$ from each of the four transitions at the electron temperature of the emitting region. Since the data have errors we calculate a weighted mean, $\bar{X}(T_e)$, from the four transitions, making use of the uncertainties in the observed fluxes. We then vary T_e to minimise

$$\chi^2 = \sum_{i=1}^{4} \left(\frac{X(\lambda_i, T_e) - \bar{X}}{\sigma_i} \right)^2 \tag{7.16}$$

where σ_i is the error on $X(\lambda_i)$. In this way we obtain an estimate of the electron temperature consistent with the fluxes and errors of all four transitions. We also obtain an estimate of the error on the temperature by determining those temperatures for which χ^2 changes by unity from its minimum value.

Table 7.1: Summary of the atomic data used to analyse dielectronic lines. E is the energy of the upper state measured from the ground level of C III

λ (Mult.) (Å)	E (cm^{-1})	Γ_u^A (s^{-1})	Γ_l^A (s^{-1})	FWHM (km s^{-1})	Γ_u^R (s^{-1})	Γ_{ul}^R (s^{-1})	Configuration
5113.69 (50)	25065.2	8.263(10)[a]	1.901(11)	17	2.101(8)	6.94(7)	$4f'(^2D_{5/2})$–$3d'(^2P^o_{3/2})$
4619.24 (51)	24961.0	1.623(9)	1.488(12)	110	2.564(8)	1.84(8)	$4f'(^2G_{9/2})$–$3d'(^2F^o_{7/2})$
4964.73 (25)	5515.1	1.901(11)	–	15	2.005(9)	2.89(7)	$3d'(^2P^o_{3/2})$–$3p'(^2P_{3/2})$
8793.80 (28.01)	3318.5	1.488(12)	–	210	2.480(9)	1.99(7)	$3d'(^2F^o_{7/2})$–$3p'(^2D_{5/2})$

[a] $8.263(10)=8.263\times10^{10}$

7.2 Atomic Data

The four C II multiplets of interest are shown in the Grotrian diagram in Fig. 7.1. The fine structure of the initial and final terms separates each multiplet into three components for multiplets 50, 51 and 28.01 and four components for multiplet 25, whose separations are approximately comparable to the WC10 line widths. We fit the fine structure components and any other line that may lie in the same spectral region to obtain the flux in each component. The flux in the strongest component of each multiplet is then used in the temperature determination. The atomic data required for the analysis are given in Table 7.1.

The energies relative to the ionization limit are taken from Moore (1970). The autoionization and radiative lifetimes needed to calculate b_u are given in Table 7.1. The autoionization probabilities were derived from a $C^{2+} + e^-$ scattering calculation by Davey (1995) in which the autoionizing states appear as resonances in the calculated photoionization cross–section. The probabilities Γ_u^A were obtained by fitting these resonances to Fano profiles. The calculation by Davey (1995) was carried out in LS–coupling and neglects all relativistic energy shifts and fine–structure interactions (spin–orbit etc.). This is a good approximation for the $3d'\ ^2P^o$ and $^2F^o$ terms, but not for the $4f'$ terms, where these interactions are stronger. We have therefore carried out an atomic structure calculation using the program SUPERSTRUCTURE (Eissner, Jones and Nussbaumer 1974,

Nussbaumer and Storey 1978) which incorporates these effects. The calculation, which includes all terms of the two electron configuration 2s2p3d and 2s2p4f, incorporates the spin–orbit interaction and the two–body fine–structures interactions described by Eissner et al. (1974). The electron radial wavefunctions are calculated in scaled Thomas–Fermi–Dirac potentials, with the scaling parameters being determined by making the statistically weighted sum of all the term energies a minimum. The electrostatic Hamiltonian matrix was corrected empirically to ensure that the term separations match the experimental values as closely as possible.

From this calculation we obtained the radiative transition probabilities for the 4f′–3d′ transitions given in Table 7.1. We also obtained the transformation matrix between LS and intermediate coupling which enables us to derive autoionization probabilities in intermediate coupling from those given by Davey (1995) for LS–coupling. These are also given in Table 7.1. Leuenhagen and Hamann (1994) argue that selection rules forbid autoionization for doublet and quartet states of the 2s2p(^{3}P)nl series. This is not the case. In LS coupling it is only necessary that S, L and parity be conserved in autoionization to the $2s^2(^1S)+e^-$ continuum. Thus autoionization is allowed for the doublet series of the correct parity. In intermediate coupling only J and parity need to be conserved and quartet levels may also autoionize, albeit more weakly. Leuenhagen and Hamann also expect that autoionizing levels would be too broad for the resulting lines to be observable. From Table 7.1 we see that the autoionizing probabilities, although generally much larger then the corresponding total radiative decay probabilities, are not so large as to make the lines too broad to detect. The largest autoionization probability, 1.49×10^{12} s^{-1} for the 3d′($^2F^o_{7/2}$) state, corresponds to a FWHM of only $\sim$ 210 km s^{-1}. Below we present a summary of the quantum theory involved in determining the values of the above–mentioned probabilities for intermediate coupling.

In intermediate coupling, including the effect of two–body fine structure interactions (spin–orbit, spin–spin, etc.), only J and parity are 'good' quantum numbers. So, for example, the wavefunction of the $^4G_{7/2}$ level can be expanded in terms of the two LS–

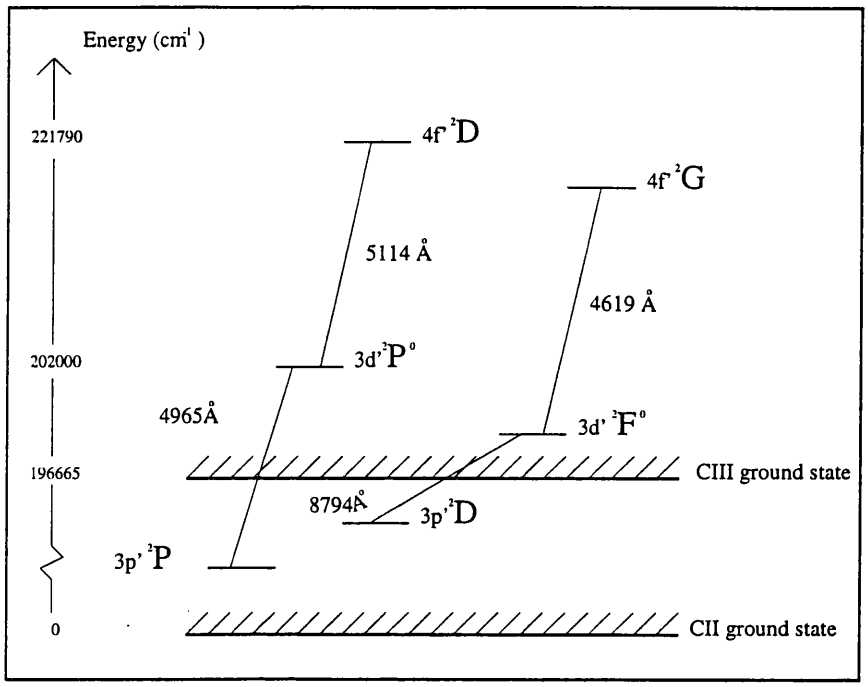

Figure 7.1: Grotrian diagram of the energy levels of the C II autoionizing lines

coupled ${}^4\underline{G}_{7/2}$ and ${}^2\underline{G}_{7/2}$ states, where we use underlining to indicate an LS–coupled state.

$$\Psi({}^4G_{7/2}) = \alpha\Psi({}^4\underline{G}) + \beta\Psi({}^2\underline{G}). \tag{7.17}$$

The autoionization for such a state depends on the matrix element of an operator 'o' between the state and the continuum.

$$\Gamma^A({}^4G_{7/2}) = \left|\langle\Psi({}^4G_{7/2})\,|o|\,\Psi(continuum)\rangle\right|^2. \tag{7.18}$$

Substituting Eq. 7.17 into Eq. 7.18 we obtain:

$$\Gamma^A({}^4G_{7/2}) = \left|\langle\alpha\Psi({}^4\underline{G})\,|o|\,.\Psi(continuum)\rangle + \langle\beta\Psi({}^2\underline{G})\,|o|\,\Psi(continuum)\rangle\right|^2 \tag{7.19}$$

Now, since quartet states are forbidden to autoionize in LS coupling, the first term in Eq. 7.19 is null. This leaves us with:

$$\Gamma^A({}^4G_{7/2}) = \beta^2\left|\langle\Psi({}^2\underline{G})\,|o|\,\Psi(continuum)\rangle\right|^2 \tag{7.20}$$

and hence

$$\Gamma^A({}^4G_{7/2}) = \beta^2\Gamma^A({}^2\underline{G}), \tag{7.21}$$

Table 7.2: Intermediate coupling auto–ionising probabilities (Γ_i^A) for the 4f′ states of C^{2+} (in units of s^{-1})

$\Gamma^A(^2F_{5/2}) = (0.0346)^2\ \Gamma^A(^2\underline{D}) = 1.806\times\ 10^8$	
$\Gamma^A(^4F_{3/2}) = (0.0296)^2\ \Gamma^A(^2\underline{D}) = 1.322\times\ 10^8$	
$\Gamma^A(^2F_{7/2}) = (0.0489)^2\ \Gamma^A(^2\underline{G}) = 4.300\times\ 10^6$	
$\Gamma^A(^4F_{5/2}) = (0.0333)^2\ \Gamma^A(^2\underline{D}) = 1.673\times\ 10^8$	
$\Gamma^A(^4F_{7/2}) = (0.0151)^2\ \Gamma^A(^2\underline{G}) = 4.100\times\ 10^5$	
$\Gamma^A(^4F_{9/2}) = (0.0296)^2\ \Gamma^A(^2\underline{G}) = 1.576\times\ 10^6$	
$\Gamma^A(^4G_{5/2}) = (0.0161)^2\ \Gamma^A(^2\underline{D}) = 3.911\times\ 10^7$	
$\Gamma^A(^4G_{7/2}) = (0.4401)^2\ \Gamma^A(^2\underline{G}) = 3.483\times\ 10^8$	
$\Gamma^A(^4G_{9/2}) = (0.3097)^2\ \Gamma^A(^2\underline{G}) = 1.724\times\ 10^8$	
$\Gamma^A(^2G_{7/2}) = (0.8963)^2\ \Gamma^A(^2\underline{G}) = 1.445\times\ 10^9$	
$\Gamma^A(^4G_{11/2}) = (1.0000)^2\ \Gamma^A(^4\underline{G}) = 0.0$	
$\Gamma^A(^2G_{9/2}) = (0.9504)^2\ \Gamma^A(^2\underline{G}) = 1.623\times\ 10^9$	
$\Gamma^A(^4D_{7/2}) = (0.0164)^2\ \Gamma^A(^2\underline{G}) = 4.837\times\ 10^5$	
$\Gamma^A(^4D_{5/2}) = (0.6707)^2\ \Gamma^A(^2\underline{D}) = 6.788\times\ 10^{10}$	
$\Gamma^A(^4D_{3/2}) = (0.3912)^2\ \Gamma^A(^2\underline{D}) = 2.309\times\ 10^{10}$	
$\Gamma^A(^2D_{5/2}) = (0.7400)^2\ \Gamma^A(^2\underline{D}) = 8.263\times\ 10^{10}$	
$\Gamma^A(^4D_{1/2}) = (1.0000)^2\ \Gamma^A(^4\underline{D}) = 0.0$	
$\Gamma^A(^2D_{3/2}) = (0.9189)^2\ \Gamma^A(^2\underline{D}) = 1.276\times\ 10^{11}$	

which is valid as long as there is only one significant interaction between the $^4G_{7/2}$ and a doublet state as in Eq. 7.17 The β values are obtained from the SUPERSTRUCTURE calculation described above.

In Table 7.2 we list the intermediate coupling Γ^A for the 4f levels, while Table 7.3 lists the Γ_i^R values also calculated in intermediate coupling. For reasons of space not all the 4f′–3d′ transitions are included in Table 7.3, but only the transitions whose wavelengths are close to the dielectronic lines of interest are listed. In this way the intermediate coupling information could be used in fitting the dielectronic line components more reliably.

7.3 Line Fitting: CPD–56°8032, He 2–113 and M 4–18

Once a multiplet was chosen for fitting, lines lying in the same wavelength region were identified and their positions, constrained to the relative values obtained from reference tables (Moore 1970 for C II, Martin, Kaufman and Musgrove 1993 for O II), were given

Table 7.3: Intermediate coupling transition probabilities (Γ_λ^R) for the 4f' states of C^{2+}

Air Wavelength (Å)	Γ_λ^R (s^{-1})
4627.60	2.910×10^4
4636.58	5.126×10^2
5162.53	2.940×10^4
4625.64	3.745×10^7
4634.61	1.360×10^6
4629.97	1.902×10^7
4618.56	1.572×10^8
4627.50	7.136×10^6
4619.25	1.843×10^8
4594.92	5.159×10^4
4603.77	3.560×10^4
4592.97	2.766×10^1
4601.81	4.143×10^5
5119.46	5.609×10^7
4588.34	1.455×10^5
5113.71	3.202×10^6
5120.17	1.586×10^7
4588.29	1.235×10^4
4597.11	5.454×10^5
5113.65	6.939×10^7
5110.28	4.126×10^1
5116.73	7.461×10^1
5107.81	1.818×10^7
5114.25	8.908×10^7

to the fitting routine as a free parameter. The relative intensities of multiplets are then calculated using LS (for O II and for the 3d' ^{2}P and ^{2}F states of C II) or intermediate coupling (for the 4f' ^{2}G and ^{2}D states of C II) as described in Section 7.2.

If the dielectronic multiplet is suspected of blending with other recombination lines, it is necessary to be able to estimate the intensity of the contaminating line, in order for the fit to determine the residual flux in the dielectronic lines. The intensity of the blended recombination line can be estimated by knowing the theoretical ratio of its flux to the flux of an unblended line residing outside the fitted region and whose flux can be measured. This could be done thanks to newly calculated effective recombination coefficients (Davey 1995) and the following relation:

$$I = N_e N_+ \alpha_{eff(ul)} h\nu \tag{7.22}$$

where all the symbols were previously defined and $\alpha_{eff(ul)}$ is the effective recombination coefficient.

Until now, due to the lower resolution of the spectra, [WC10] stellar wind lines have been fitted with Gaussian profiles. However with the higher resolution achieved by the UCLES or the UES echelle configurations, the spectral line profiles were observed to be very non–Gaussian (see Fig. 7.2). This is due to the velocity structure of the wind and to the optical depth of the lines.

For this reason, the C II line at 4802 Å was used as a template profile to fit all the other lines. For CPD–56° 8032, the 4802 Å line appears as a clean, unblended profile, while for the spectra of He 2–113 and M 4–18, with their narrower line profiles, the continuum on the blue and red sides of the 4802 Å line is not level. A blend with another stellar wind line was disregarded due both to the difficulty of fitting two Gaussians of similar widths to the feature at 4802 Å and to the fact that no suitable candidate line could be identified at that wavelength (see Fig. 7.2). The possibility of a blend of stellar and nebular components for the same transition was also excluded: although for CPD–56° 8032 the line at 4802 Å could be fitted well with two components, hinting at such a blend, no other C II recombination line could be fitted as well using the same method. Moreover,

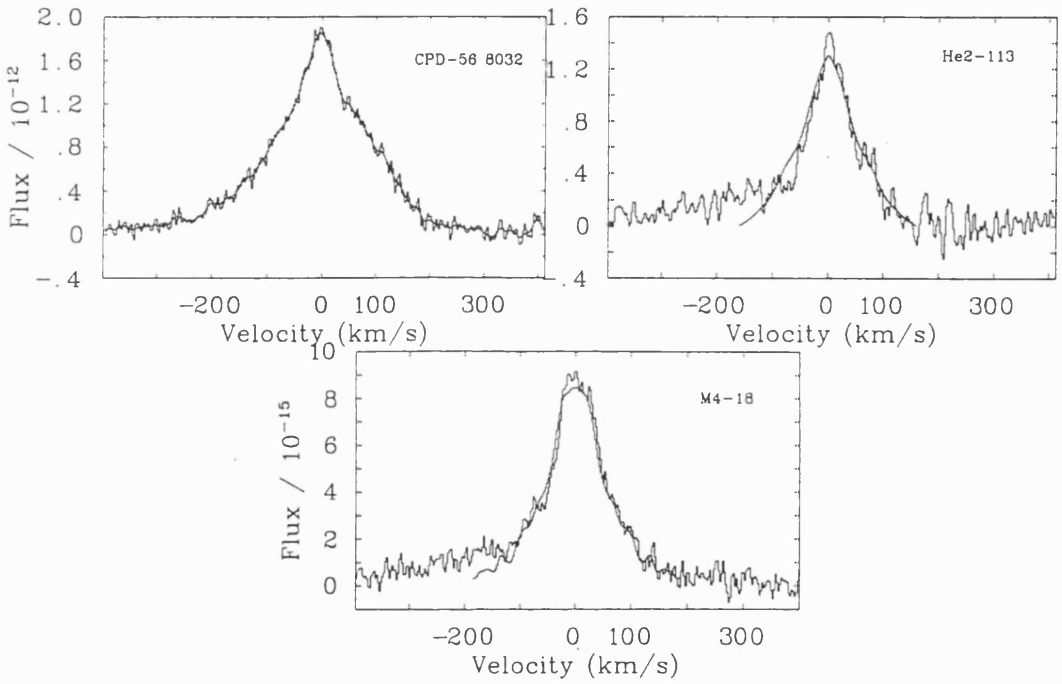

Figure 7.2: The C II line at 4802 Å which was used as a template profile to fit all other lines (CPD–56° 8032 and He 2–113 are shown at the top, M 4–18 at the bottom. Overlaid is the smoothed profile that was used in the fits

one would expect the effect of a nebular component to the C II line to be more evident in the spectra of He 2–113 and M 4–18 (which exhibit an overall stronger nebular spectrum – Chapter 5 and Appendix C), but this was not the case. Additionally, one would not expect a significant abundance of C^{2+} ions (which give the C II recombination spectrum) in such low excitation nebulae (only very weak [O III] $\lambda\lambda$4959,5007 lines are observed in the spectra of these nebulae).

For He 2–113 and M 4–18 the 4802 Å profiles are smoothed and the red side was reflected onto the blue about the center of the line. The profile obtained in this way was then used as the template to fit the dielectronic lines. Overall in the case for He 2–113, the shape of the smoothed profile was broader then the original (see Fig. 7.2). As a result, all the fits to the dielectronic lines for this star are slightly too broad (Fig. 7.4). However this was believed to be the best option, since no other suitable line could be found to be used as an unblended template. The unblended C II lines at 4267 Å or 6461 Å have broader profiles than that of the λ4802 line, possibly due to higher optical depth (see Section 7.7 for an explanation of the relationship between FWHM and optical depth). Using these lines as template profiles returned extremely poor fits.

7.3.1 C II Multiplet 51, λ5114

The fit to C II Multiplet 51 is shown in Figs. 7.3, 7.4 and 7.5 (a). Seven lines were identified between 5100 and 5130 Å. The autoionising Multiplet 51 (solid line) is composed of three components, with tabulated wavelengths (Moore 1970) of 5107.8, 5113.7 and 5114.3 Å. These were accompanied by C II multiplet 16.06 (one line at 5122.15 Å), three lines of C II at 5113.7, 5119.5 and 5120.2 Å, arising from configuration $3d'^2P^o$–$4f'^4D$ (these lines, forbidden by L–S coupling rules, were identified when carrying out the intermediate coupling calculations mentioned in Section 7.2) and one unidentified line that was left free as an input parameter of the fit (Table 7.4, row 8). The intensities of the dielectronic lines and of the other three lines calculated in intermediate coupling are listed in Table 7.4, while the intensities of the Multiplet 16.06 and of the unidentified lines were left

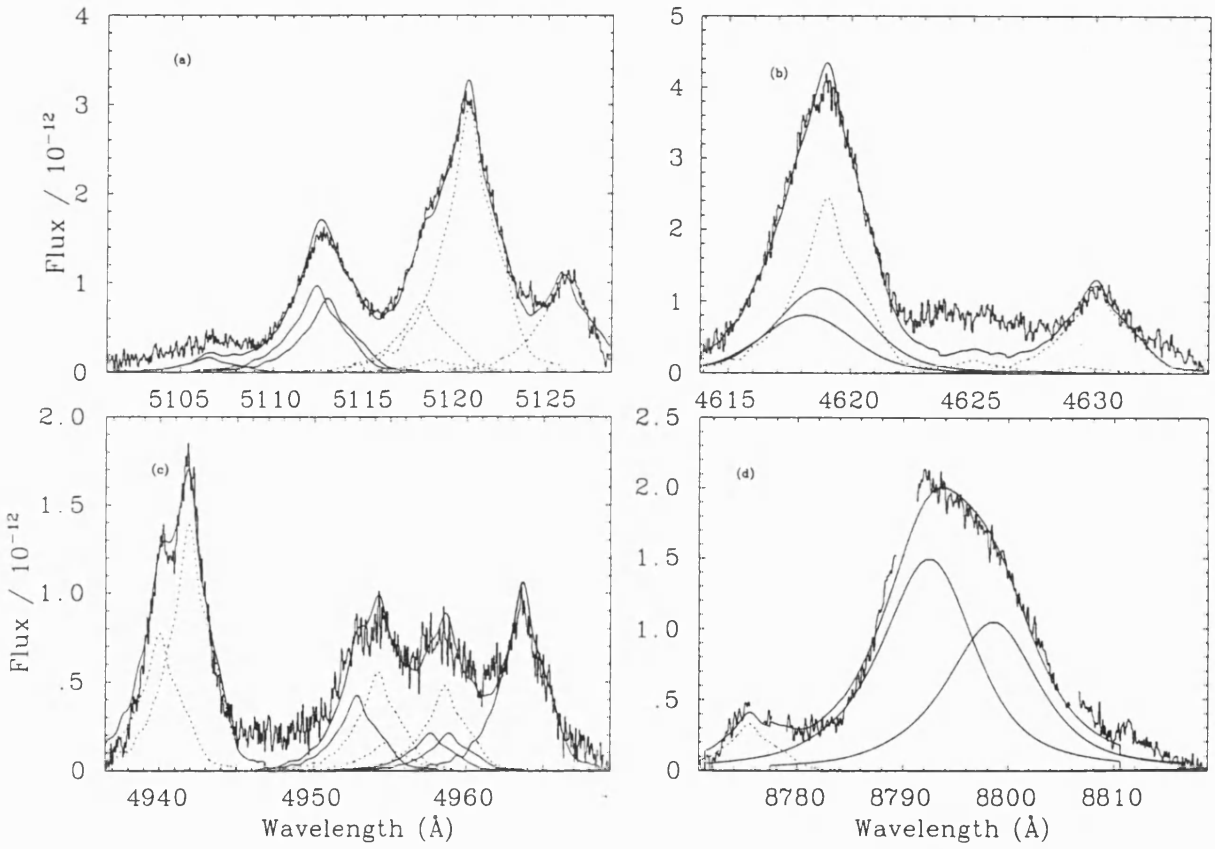

Figure 7.3: CPD-56° 8032: fits to four dielectronic multiplets of C II (a to d). Solid lines are used for the autoionising lines, while dashed lines are used for the other components in the fit which arise from recombinations to bound states

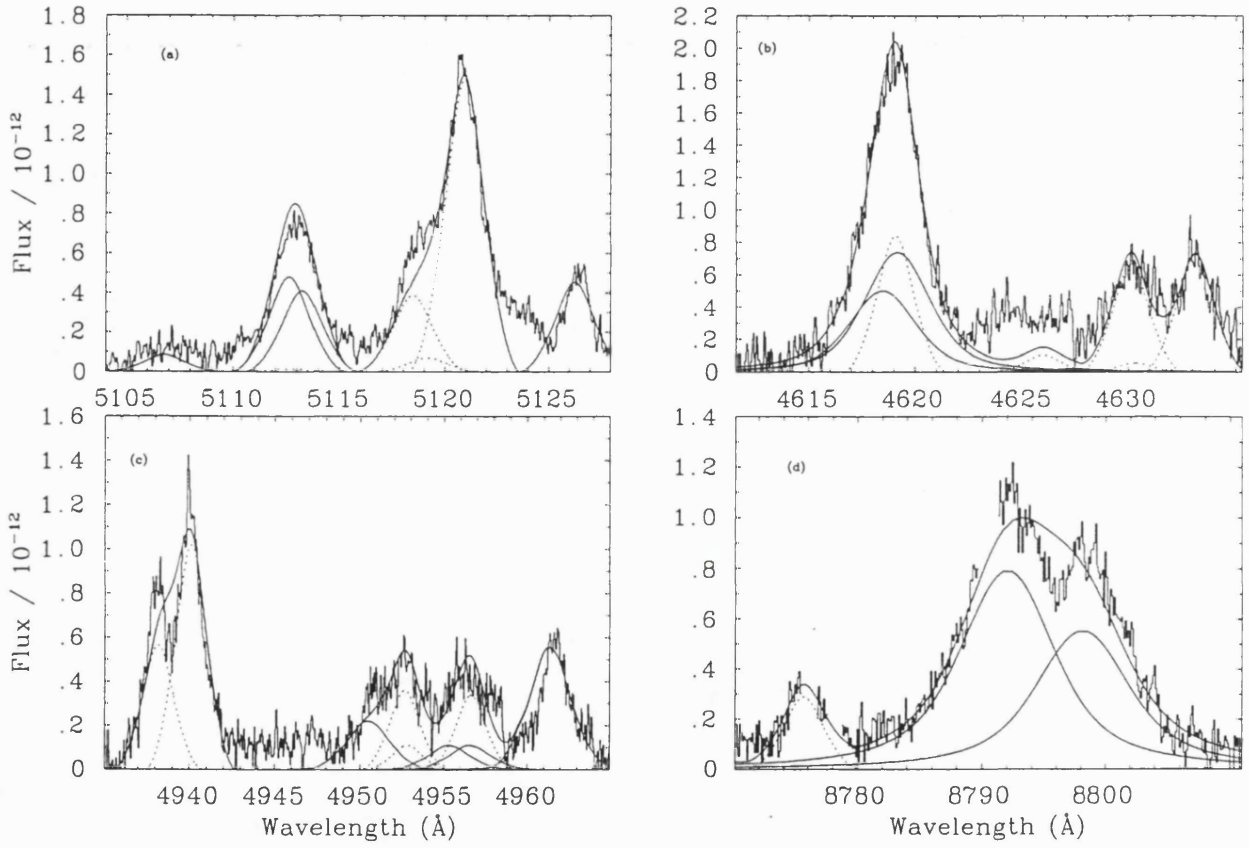

Figure 7.4: He 2–113: fits to four dielectronic multiplets of C II (a to d). Solid lines are used for the autoionising lines, while dashed lines are used for the other components in the fit which arise from recombinations to bound states

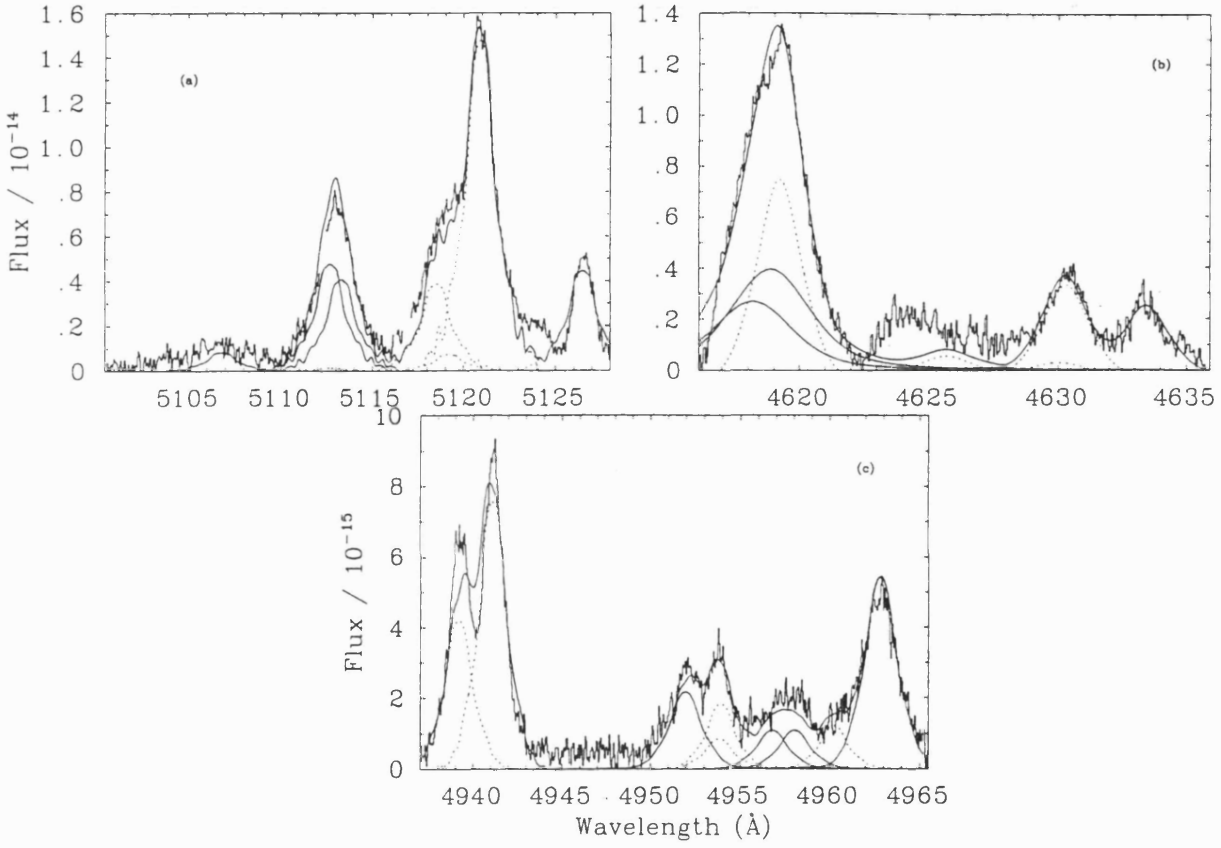

Figure 7.5: M 4–18: fits to three of the four dielectronic multiplets of C II (a to c). Solid lines are used for the autoionising lines, while dashed lines are used for the other components in the fit which arise from recombinations to bound states

Table 7.4: Fitted parameters for the C II Multiplet 51. Observed wavelengths are not corrected for the heliocentric radial velocities of the stars: −59.4 km s^{-1} for CPD−56° 8032, −57.3 km s^{-1} for He 2−113 and −51.6 km s^{-1} for M 4−18

				CPD−56° 8032		He 2−113		M 4−18	
No.	Ion and Mult. No.	λ_{rest} (Å)	Int. (norm.)	λ_{obs} (Å)	I (erg cm^{-2} s^{-1})	λ_{obs} (Å)	I (erg cm^{-2} s^{-1})	λ_{obs} (Å)	I (erg cm^{-2} s^{-1})
1	C II M16.06	5122.15	–	5120.34	1.037×10^{-11}	5120.92	3.445×10^{-12}	5120.90	1.53×10^{-13}
2	C II M51	5107.97	1	5106.17	5.906×10^{-13}	5106.79	1.973×10^{-13}	5106.82	8.63×10^{-15}
3	C II M51	5113.69	5.73	5112.01	3.384×10^{-12}	5112.63	1.130×10^{-12}	5112.66	4.93×10^{-14}
4	C II M51	5114.26	4.89	5112.62	2.888×10^{-12}	5113.24	9.646×10^{-13}	5113.27	4.21×10^{-14}
5	C II	5113.69	0.18	5112.07	1.063×10^{-13}	5112.69	3.551×10^{-14}	5112.72	1.55×10^{-15}
6	C II	5119.45	4.64	5117.82	2.740×10^{-12}	5118.45	9.153×10^{-13}	5118.48	3.99×10^{-14}
7	C II	5120.10	0.87	5118.53	5.138×10^{-13}	5119.15	1.716×10^{-13}	5119.18	7.47×10^{-15}
8	?	?	–	5125.07	3.803×10^{-12}	5126.23	1.081×10^{-12}	5126.45	4.58×10^{-14}

free. The wavelengths of the dielectronic lines and of the three 3d′−4f′ lines were tied to each other (making use of tabulated theoretical values) but left free to shift together as a block. The wavelengths of the λ5122.15 line and of the unidentified line were left for the fit determine. The relative intensities of the M51 dielectronic lines were calculated in intermediate coupling and fixed relative to one another, as were those of the 3d′−4f′ components. Multiplet 12 of C II is also present in this wavelength region, but its inclusion did not return a satisfactory fit and it was not retained.

7.3.2 C II Multiplet 50, λ4619

To determine the strength of the dielectronic lines components of Multiplet 50 (Figs. 7.3, 7.4 and 7.5 (b)), the theoretical relative intensities of the autoionising triplet (solid lines) were calculated in intermediate coupling (see Table 7.5). In addition, three line components arising from $4f'^4G$–$3d'^2F^o$ transition were identified (from intermediate coupling calculations) at 4625.6 Å, 4634.6 Å and 4630.0 Å and their relative intensities calculated (0.15:0.05:0.8 of the line at 4619.3 Å, for the lines in rows 4 to 7 in Table 7.5). A systematic search of lines from high states of C II indicates, however, that the λ4619 feature is

also blended with the 8f–4d transition. The energy of the 8f state is not known experimentally, but can be estimated using the known positions of the 4f, 5f, 6f, 7f states. Our technique for making this estimate is described in the Appendix B. The air wavelength of the 8f–4d transition is calculated to be 4620.7Å, and it is therefore completely blended with the dielectronic features of interest. An estimate of the contribution to the λ4619 feature from the 8f–4d transition can be made by comparison with the apparently unblended C II 8g–4f transition at λ4802. We assume that the departures from LTE for the 8g and 8f states are the same. This should be a good approximation, since heavy particle collisions can be expected to equalize departure coefficients for states of the same n but different l. Using hydrogenic transition probabilities for the two transitions (Storey and Hummer 1991), we obtain a relation between the intensities which is I(λ4620.7) = 1.03 I(λ4802). The dereddened flux for the λ4802 transition is 5.60×10^{-12} erg s^{-1} cm^{-2} for CPD–56°8032, 2.48×10^{-12} erg s^{-1} cm^{-2} for He 2–113 and 8.43×10^{-14} erg s^{-1} cm^{-2} for M 4–18. We finally make a least squares fit to the λ4619 feature, including a line of fixed intensity and corresponding to the expected flux of the 8f–4d transition.

From Table 7.5 we notice that the fluxes in the output for the line at 4620.7 A, do not quite correspond exactly to 1.03 times the fluxes in the 4802 Å line for each star, however this does not imply a significant enough change in the overall flux of the M50 dielectronic multiplet to make a difference to the temperature determination.

Another uncertainty in the determination of the flux of M50 λ4621 is the level of the continuum. The local apparent continuum in this wavelength region (between 4622 and 4628 Å in Figs. 7.3, 7.4 and 7.5 (b)) is about 20% higher than what is estimated to be the correct continuum level. Support for the correctness of our continuum placement can be gained by considering two weak O II lines, $\lambda\lambda$4602.11, 4609.42, belonging to the 4f^{2}F^o–3d^{2}D multiplet. The theoretical intensity ratio is 1.43, and the measured value using our overall blackbody continuum placement, is 1.47. If the elevated pseudo–continuum due to the blend of weak lines was used instead, the relative intensity ratio would be 2.35, in disagreement with theory. This phenomenon is also displayed by other WC10 stars such

Table 7.5: Fitted parameters for C II Multiplet 50. The intensity of profile 7 is fixed at 1.03×I(λ4802) as described in the text. The observed wavelengths are not corrected for the heliocentric radial velocities of the stars: −59.4 km s^{-1} for CPD−56° 8032, −57.3 km s^{-1} for He 2–113 and −51.6 km s^{-1} for M 4–18

				CPD−56° 8032		He 2–113		M 4–18	
No.	Ion and Mult. No.	λ_o (Å)	Int. (norm.)	λ_{obs} (Å)	I (erg cm^{-2} s^{-1})	λ_{obs} (Å)	I (erg cm^{-2} s^{-1})	λ_{obs} (Å)	I (erg cm^{-2} s^{-1})
1	C II M50	4619.23	1	4618.34	6.17×10^{-12}	4619.33	3.34×10^{-12}	4619.29	9.78×10^{-14}
2	C II M50	4627.63	0.03	4626.60	1.85×10^{-13}	4627.60	1.00×10^{-13}	4627.55	2.92×10^{-15}
3	C II M50	4618.73	0.68	4617.65	4.19×10^{-12}	4618.45	2.27×10^{-12}	4618.60	6.65×10^{-14}
4	C II	4625.63	0.15	4624.73	6.00×10^{-13}	4625.73	2.21×10^{-13}	4625.68	6.44×10^{-15}
5	C II	4634.60	0.05	4633.70	2.00×10^{-14}	4634.70	7.35×10^{-15}	4634.65	2.14×10^{-16}
6	C II	4629.96	0.80	4629.06	3.20×10^{-13}	4630.06	1.18×10^{-13}	4630.01	3.43×10^{-15}
7	C II8f–4d	4620.7	–	4621.28	7.72×10^{-12}	4619.21	1.75×10^{-12}	4619.21	8.51×10^{-14}
8	Si IV M6	4631.20	–	4629.73	3.84×10^{-12}	4630.14	1.39×10^{-12}	4630.29	3.77×10^{-14}
9	?	?	–	–	–	4633.10	1.51×10^{-12}	4633.42	2.78×10^{-14}

as K 2–16 and the WC12/R Cor Bor star V348 Sgr (Leuenhagen, Heber and Jeffery 1994). In an effort to identify the lines responsible for raising the local continuum, we found three lines (from the intermediate coupling calculation described in Section 7.2 – rows 4 to 7 in Table 7.5), but as can be seen from Figs. 7.3, 7.4 and 7.5 (b), there is still surplus flux.

For dielectronic Multiplet 50, if the lines are fitted using the template profiles derived from the 4802 Å line, the feature is under-fitted. If, on the other hand, the template profile is convolved with a Lorentzian profile of appropriate width (see Table 7.1 – in accordance with the lifetime of the lower state of the transition, which is much shorter than the lifetime of the upper state and hence determins the width of the line), the fit is very good. This is probably the explanation for the "unclear broadening mechanism" encountered by Leuenhagen Heber and Jeffery (1994) for the 4619 Å line in the star V 348 Sgr. The line broadening mechanism is discussed further in Section 7.3.4.

The feature at ~4631 Å is possibly due to Si IV Multiplet 6. In the spectra of He 2–113 and M 4–18 a second peak is visible (Figs. 7.4 and 7.5 (b)) at about 4633 Å. This has been attributed to N III (Leuenhagen Hamann and Jeffery 1996), but we argue that if that were

Table 7.6: Fitted parameters for C II Multiplet 25. The observed wavelengths are not corrected for the heliocentric radial velocities of the stars: –59.4 km s^{-1} for CPD–56° 8032, –57.3 km s^{-1} for He 2–113 and -51.6 km s^{-1} for M 4–18

				CPD–56° 8032		He 2–113		M 4–18	
No.	Ion and Mult. No.	λ_o (Å)	Int. (norm.)	λ_{obs} (Å)	I (erg cm^{-2} s^{-1})	λ_{obs} (Å)	I (erg cm^{-2} s^{-1})	λ_{obs} (Å)	I (erg cm^{-2} s^{-1})
1	C II M25	4964.73	1	4963.32	3.59×10^{-12}	4963.82	1.78×10^{-12}	4963.84	6.16×10^{-14}
2	C II M25	4959.92	0.20[a]	4958.52	7.18×10^{-13}	4959.01	3.57×10^{-13}	4959.03	1.23×10^{-14}
3	C II M25	4958.67	0.20[a]	4957.33	7.18×10^{-13}	4957.77	3.57×10^{-13}	4957.78	1.23×10^{-14}
4	C II M25	4953.85	0.40[a]	4952.52	1.44×10^{-12}	4952.94	7.14×10^{-13}	4952.96	2.47×10^{-14}
5	O II M33	4941.07	1	4939.68	2.61×10^{-12}	4940.16	1.26×10^{-12}	4940.19	4.28×10^{-14}
6	O II M33	4943.00	0.55[b]	4941.59	4.70×10^{-12}	4942.09	2.27×10^{-12}	4942.11	7.69×10^{-14}
7	O II M33	4955.71	0.11[b]	4954.32	5.22×10^{-13}	4954.80	2.53×10^{-13}	4954.82	8.51×10^{-15}
8	?	–	–	4959.54	1.62×10^{-12}	4958.63	7.61×10^{-13}	4961.21	1.22×10^{-14}
9	?	–	–	4955.34	1.87×10^{-12}	4954.65	8.10×10^{-13}	4954.90	1.84×10^{-14}

[a]Intensities normalised to the C II line λ4964.73

[b]Intensities normalised to the O II line λ4941.069

the case then we should be able to observe the principal lines of N III (e.g. λλ4097,4103 and λλ5324,50) and N II (e.g. λλ4447,3995,5686), and this is not the case. We fit the features with lines whose wavelengths are left free, and the fitted line centre wavelengths and intensities are tabulated in Table 7.5, rows 8 and 9.

7.3.3 C II Multiplet 25, λ4965

Besides the autoionizing Multiplet 25 (four components – see Figs. 7.3, 7.4 and 7.5 (c), LS coupling intensities are shown in Table 7.6) , we could identify only three lines belonging to O II M33 (λλ4943,4941,4956, with LS coupling relative intensities also listed in Table 7.6). However, the fit to the region then fell noticeably below the data. We therefore introduced two unidentified lines, with free wavelengths and intensities. This was not considered to interfere with the derived dielectronic line fluxes, due to the strongest dielectronic line being mostly unblended and therefore constraining the intensities of the M25 quartet components to the same values regardless of the two unidentified lines. Here, as was the

case for M50 (Section 7.3.2), a short region of elevated continuum (at ~4946 Å in Figs. 7.3, 7.4 and 7.5 (c)) remained unexplained.

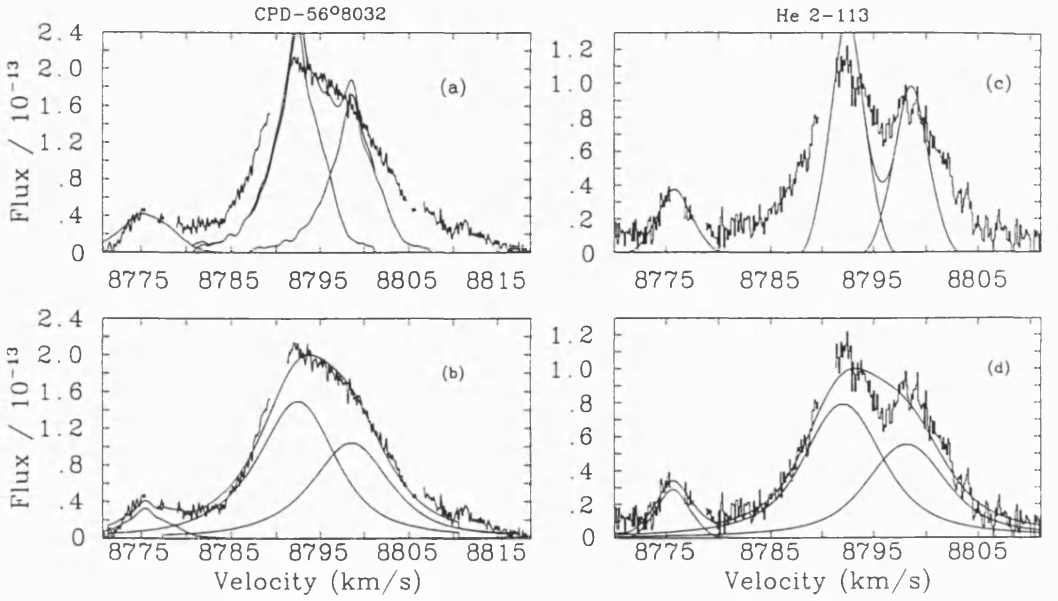

Figure 7.6: Comparison between fits to the 8794 Å multiplet components before (a and b) and after (c and d) convolving the template profile with a Lorentzian of width corresponding to the autoionization lifetimes of the two states of the transition

7.3.4 C II Multiplet 18.01, λ8794

C II Multiplet 18.01, in the far red of the spectral region, was affected by telluric lines which were removed before fitting (Figs. 7.3 (d) and 7.4 (d)). Moreover, it came from a different echelle setting to the other dielectronic multiplets and hence it might be affected by errors in the absolute flux calibration. The UES spectrum of M 4–18 was taken in the range 4200–5850 Å and Multiplet 18.01 was not included.

As was the case for the dielectronic Multiplet 50 (Section 7.3.2), the 8794 Å triplet (the LS coupling relative intensities are listed in Table 7.7) had to be fitted with a profile obtained by convolving the 4802 Å template with a Lorentzian profile whose width corresponded to the predicted lifetime of the upper state of the transition (the lower level of this transition is bound and its lifetime is much shorter than the lifetime of any auto–

Table 7.7: Fitted parameters for C II Multiplet 28.01. Observed wavelengths are not corrected for the heliocentric radial velocities of the stars: −59.4 km s^{-1} for CPD−56° 8032 and −57.3 km s^{-1} for He 2–113

				CPD−56° 8032		He 2–113	
No.	Ion and Mult. No.	λ_o (Å)	Int. (norm.)	λ_{obs} (Å)	I (erg cm^{-2} s^{-1})	λ_{obs} (Å)	I (erg cm^{-2} s^{-1})
1	C II M28.01	8799.9	1	8797.90	1.347×10^{-12}	8798.92	6.533×10^{-13}
2	C II M28.01	8828.98	0.07	8826.98	9.426×10^{-14}	8828.00	4.573×10^{-14}
3	C II M28.01	8792.8	1.43	8791.80	1.926×10^{-12}	8792.84	9.342×10^{-13}
4	?	?	–	8774.84	1.965×10^{-13}	8775.84	1.145×10^{-13}

ionising level). A comparison of the fit before and after this convolution was carried out is displayed in Fig. 7.6; as can be seen, the improvement is obvious.

7.4 Wind Electron Temperatures

As already described in Section 7.1, electron temperatures were derived by minimising the difference between the ratios of measured and computed fluxes for the autoionising lines. This minimisation was carried out by calculating all the line theoretical intensities prior to iterating to minimise χ^2. The dereddened fluxes derived for the strongest dielectronic line in each multiplet are summarised in Table 7.8, along with the associated errors. Errors are gauged at 15% for multiplets 51 and 25 of CPD−56°8032 and 10% for the less blended He 2–113 and M4–18. For multiplets 50 and 28.01, the uncertainty was determined to be about 30% due to blending with the line at 4620.7 Å, in the case of M50, and to being located in a different echelle setting, in the case of M28.01.

If all the lines are used, and errors chosen based on the confidence in the fits, the derived electron temperatures are (18 900±2400) K for CPD−56° 8032, (17 000±1300) K for He 2–113 and (16 700±1400) K for M 4–18.

If only the two most optically thin lines are used (optical depths are calculated in Section 7.7) the wind electron temperature is (21 300±2000) K for CPD−56°8032, (16 400±1600) K for He 2–113 and (19 000±2000) K for M 4–18. To calculate the parameters needed

Table 7.8: Summary of the dereddened fluxes measured for the strongest component of each dielectronic multiplet for CPD–56°8032, He 2–113 and M 4–18, together with associated error estimates

Mult.	Wavelength (Å)	I(CPD–56° 8032) (ergs cm^{-2} s^{-1}) E(B–V)=0.68	Error (%)	I(He 2-113) (ergs cm^{-2} s^{-1}) E(B–V)=1.0	Error (%)	I(M 4–18) (ergs cm^{-2} s^{-1}) E(B–V)=0.45	Error (%)
51	5113.7	3.38×10^{-12}	15	1.13×10^{-12}	10	4.49×10^{-14}	10
50	4619.2	6.17×10^{-12}	30	3.34×10^{-12}	30	8.79×10^{-14}	20
25	4964.7	3.59×10^{-12}	15	1.79×10^{-12}	10	5.58×10^{-14}	10
28.01	8793.8	1.93×10^{-12}	30	1.00×10^{-12}	30	–	–

for the determination of the wind abundances, we will adopt an electron temperature of 20 000 K for CPD–56°8032, 17 000 K for He 2–113 and 19 000 K for M 4–18.

The electron temperature derived here for the wind of CPD–56° 8032 is higher than the value of 12 800 K derived by Barlow and Storey (1993) who used Gaussian fits to the flux in the entire multiplets in their lower (0.5 Å) resolution spectrum.

7.5 Wind Electron Temperatures for IRAS 17514–1555 and K 2–16

IRAS 17514–1555 is a [WC10] with a spectrum very similar to that of CPD–56°8032, while K 2–16, with a slightly lower–ionization spectrum is classified as a [WC11] (Chapter 4). Spectra for both objects were obtained at the INT in July 1996 (see Chapter 3 for details of the observations and data reduction), at a resolution of about 1 Å. The spectral range includes three out of four of the dielectronic lines so that the same analysis could be carried out. The high resolution spectroscopy of CPD–56°8032, He 2–113 and M 4–18 had given us a clear indication of what lines resided in the dielectronic lines' wavelength regions, so that despite the lower resolution of the INT spectra, a detailed analysis could still be carried out using fine structure components. The reddening to IRAS 17514–1555

was determined from the Hα–Hβ decrement to be E(B–V)=0.32. Pollacco and Hill (1994) determined E(B–V)=0.83, while from the stellar colours (Chapter 4, Table 4.1) we obtain E(B–V)=1.05. The measurements of the fluxes in the nebular Hα and Hβ lines, carried out on our own intermediate resolution spectra, might have been affected by a substantial error, overall due to blending with the stellar features. Moreover the Hα profile seems to exhibit a broad pedestal, and appers to be considerably weaker than the [N II] line at 6583 Å. These peculiarities, and the fair agreement of the Pollacco and Hill reddening with that derived from the stellar colours, induced us to adopt E(B–V)=0.83. We note however that the temperature determination obtained using E(B–V)=0.32 only varies within the uncertainty. For K 2–16 no previous determination of the reddening exists. Moreover the nebular spectrum is very feeble and even Hα is extremely weak. We therefore derived electron temperatures using a reddening of E(B–V)=0.6 but tried the analysis also using values of E(B–V)=0.1 and 1.0: the temperature determination only varied within the error bars.

Gaussian lines were used for the fits (see Fig. 7.7), since the intrinsic profile shapes were not resolved. To fit the IRAS 17514–1555 C II Multiplet 50 lines, we defined a wider range (5105–5165 Å) than for the other stars, since its stellar lines are broader (FWHM=310 km s^{-1}, as measured from the unblended line at 4803 Å – the instrumental width is only $\sim$90 km s^{-1}), and the long–wavelength side of the fitting region was blended with several other lines. The fit is presented in Fig. 7.7; the fluxes in the extra fitted lines are not listed in Table 7.9. Moreover, in the spectral region containing C II Multiplet 25 we note for this star the presence of the nebular [O III] λ4959 line.

The fitted C II line intensisites are listed in Table 7.9. Dielectronic Multiplet 50 was excluded from the temperature determination. As already discussed in Section 7.3.2, that multiplet is affected by severe blending and only through an indirect method were we able to de–blend that feature. This method is deemed to be good enough for high resolution spectroscopy, but in the case of low resolution spectra the errors on the measured fluxes would be higher. Moreover, as will be discussed in Section 7.7, the best lines for

Table 7.9: Fitted parameters for the C II multiplets 51 and 25 for the stars IRAS 17514–1555 (for E(B–V)=0.83) and K 2–16 (for E(B–V)=0.6)

				IRAS 17514-1555		K 2-16	
No.	Ion and Mult. No.	λ_0 (Å)	Int. (norm.)	λ_{obs} (Å)	I (erg cm^{-2} s^{-1})	λ_{obs} (Å)	I (erg cm^{-2} s^{-1})
1	C II M16.06	5122.15	–	5122.21	8.77×10^{-14}	5122.2300	0.283×10^{-12}
2	C II M51	5107.97	1	5108.74	6.14×10^{-15}	5108.3730	0.257×10^{-13}
3	C II M51	5113.69	5.73	5114.44	3.51×10^{-14}	5114.0730	0.147×10^{-12}
4	C II M51	5114.26	4.89	5115.04	2.99×10^{-14}	5114.6730	0.125×10^{-12}
5	C II	5113.69	0.18	5114.44	1.10×10^{-15}	5114.0730	0.461×10^{-14}
6	C II	5119.45	4.64	5120.24	2.83×10^{-14}	5119.8730	0.119×10^{-12}
7	C II	5120.10	0.87	5120.84	5.30×10^{-15}	5120.4730	0.222×10^{-13}
8	?	?	–	5127.54	5.82×10^{-14}	5126.3130	0.966×10^{-13}
1	C II M25	4964.73	1	4965.70	3.82×10^{-14}	4965.2110	0.155×10^{-12}
2	C II M25	4959.92	0.20[a]	4960.90	7.66×10^{-15}	4960.4120	0.312×10^{-13}
3	C II M25	4958.67	0.20[a]	4959.60	7.67×10^{-15}	4959.1110	0.312×10^{-13}
4	C II M25	4953.85	0.40[a]	4954.80	1.54×10^{-14}	4954.3120	0.625×10^{-13}
5	O II M33	4941.07	1	4942.00	1.76×10^{-14}	4941.5110	0.571×10^{-13}
6	O II M33	4954.32	0.55[b]	4944.00	3.17×10^{-14}	4943.5110	0.103×10^{-12}
7	O II M33	4959.54	0.11[b]	4956.70	3.49×10^{-15}	4956.2110	0.113×10^{-13}
8	?	?	–	4950.68	5.58×10^{-15}	4960.0440	0.416×10^{-13}
9	?	?	–	4959.33	1.67×10^{-14}	4956.3020	0.571×10^{-13}
10	?	?	–	4971.75	6.49×10^{-14}	4970.6950	0.243×10^{-13}

[a]Intensitied normalised to the C II line λ4964.73

[b]Intensitied normalised to the O II line λ4941.069

the temperature determination are those at 4965 and 5114 Å, due to their lower and mutually comparable optical depth. The inputs for these fits were the same as the inputs for the other objects. The electron temperature for IRAS 17514–1555 was found to be (20 700±2000) K, while for K 2–16 we obtained (21 400±2000) K.

7.6 Stellar Wind Abundances from Recombination Lines

To determine the relative abundances of He^+, He^{2+}, C^{2+}, C^{3+} and O^{2+} in the stellar winds, we used recombination lines from a number of multiplets belonging to these ions, assuming that the winds are optically thin to the chosen lines. For M 4–18 the spectral range of the high resolution echelle (UES) spectrum (4200–5850 Å) did not include all the lines used to determine the abundances of CPD–56°8032 and He 2–113. Lines residing outside

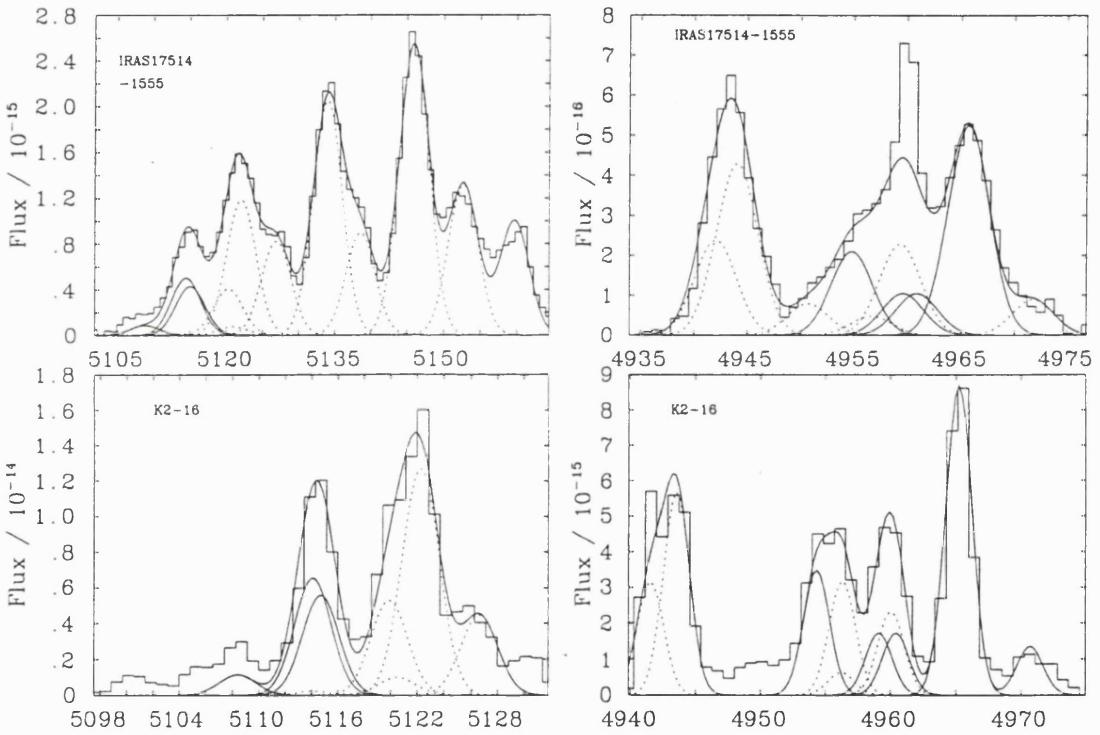

Figure 7.7: IRAS 17514–1555 and K 2–16: fits to dielectronic multiplets 51 (top) and 25 (bottom). Solid lines are used for the autoionising lines, while dashed lines are used for the other components in the fit which arise from recombinations to bound states

this range were instead measured on the lower resolution long–slit (IDS) spectrum (see Chapter 3). For this purpose the continuum level of the IDS spectrum was scaled to the UES spectrum continuum level[1], so that the common parts of the two spectra overlapped to a very good degree of accuracy (<10%). Fluxes measured on the IDS spectrum were however considered less reliable (also due to the lower resolution) and the weights for these measurements were reduced (column 7, Table 7.11).

Since effective recombination coefficients and collisional rates are temperature dependent, the wind electron temperatures derived in the previous Section are used to calculate the emission measures. The C^{2+} ion is the dominant ion stage of carbon in the winds and this method diagnoses the temperature in the C^{2+} line formation region. We assumed that the O II and C II lines originate in similar regions, together with the He I lines (although O^{2+}, with a higher ionization potential than C^{2+}, might extend deeper into the wind, where the electron temperature is higher). We will also discuss the use of the C II dielectronic lines as abundance diagnostics, along with the C II radiative recombination lines.

The abundance of an ionic species is determined from Eq. 7.13, where the expression for Q for the dielectronic lines can be found in Eq. 7.14 for the dielectronic lines, while for ordinary bound–bound recombination lines we obtain:

$$Q(\lambda, T_e) = h\nu\alpha_{eff}. \tag{7.23}$$

Integrating over the volume of emission,

$$\frac{I}{Q} = \frac{1}{4\pi D^2}[N_i], \tag{7.24}$$

where $[N_i]$ represents the product of the ionic and electron densities integrated over the emitting volume. The ratio of the emission measures of two ionic species can thus be

[1] As already pointed out in Chapter 3, the IDS spectrum was believed to be photometric, while the UES one, obtained during a service night, was not necessarilly so. However since abundances are obtained by comparing fluxes, the absolute level of the flux is irrelevant.

obtained in a straightforward manner

$$\frac{[N_i]}{[N_j]} = \frac{I_i/Q_i}{I_j/Q_j}. \tag{7.25}$$

To obtain the relative abundances for a pair of elements, one takes the ratio of the total emission measure for each of the elements, after summing over all the observed ionization stages. Thus for element X and Y, with number densities N_X and N_Y,

$$\frac{N_X}{N_Y} = \frac{\Sigma_p[N_X^{+p}]}{\Sigma_q[N_Y^{+q}]}. \tag{7.26}$$

In the case of He^0 transitions, allowance had to be made for collisional population of the upper levels from the 2^3S metastable state. For the ratios, C/R, of the rates of collisional to radiative recombination population, collisional rates were obtained from Kingdon and Ferland (1995) for the He I lines at 4471.5, 5875.7, 7065.3 and 6678.1 Å. In the Kingdon and Ferland expression for C/R, the total He I recombination coefficient and the line effective recombination coefficient, are calculated for low ($\sim 10^6$ cm^{-3}) electron density. However, since they appear in both the numerator and denominator, the effect of density cancels out to a first approximation. For the He I lines at 4713.2 and 5047.7 Å, we used the results of Clegg (1987 – which compare quite well with the result of Kingdon and Ferland for the lines at 4471.5 Å, 5875.7 Å, 7065.3 Åand 6678.1 Å), but with the above-mentioned values for the effective recombination coefficients and with collisional rates from the 29-state R-matrix calculation of Sawey and Berrington (1993). A density of 10^{11} cm^{-3} and temperatures of 20 000 K, 17 000 K and 19 000 K were used for CPD–56°8032, He 2–113 and M 4–18, respectively.

High density (10^{11} cm^{-3}) recombination coefficients were also available (Davey 1995) for the C II lines at 4493 Å [2] (9g–4f), 4802 Å (8g–4f), 5340 Å (7g–4f) and 6461 Å (6g–4f), which were observed unblended in the spectra of both stars. For the C II lines at 4267 Å, high density effective recombination coefficients were also obtained from Davey, although they were only tabulated for a temperature of 12 800 K. To scale them to the

[2]The energies of the nf and ng series are known experimentally up to $n = 7$ (f series) and $n = 8$ (g series). See Appendix B for the energies of higher members of these series.

right temperatures, scaling factors of 1.56 (CPD–56°8032 and M 4–18) and 1.32 (He 2–113) were calculated by comparing hydrogenic effective recombination coefficients (Storey and Hummer 1995) for a density of 10^{11} cm^{-3} and for temperatures of 12 800 K, 20 000 K and 17 000 K.

For the C^{3+} ion, hydrogenic recombination coefficients were obtained from Storey and Hummer (1995). The C III lines used for the abundance determination originated from high transitions and the hydrogenic approximation was considered to provide sufficient accuracy.

For the He^{2+} ion, only the 4–3 λ4686 line was used and its recombination coefficient was taken from Hummer and Storey (1991) but for a rather low density of 10^4 cm $^{-3}$; this should not have a serious effect on the total abundance determination since He^{2+} is found to be a factor of 200 less abundant than He^+.

For the O II ion, new O II recombination coefficients at low electron densities have been tabulated by Liu et al. (1995). These new intermediate coupling recombination coefficients are expected to be more accurate than any currently in the literature. Case B was assumed to prevail, in the sense that all radiative transitions to the ground term $2s^22p^3\ ^4S^o$ are assumed to be optically thick. This assumption was found by Liu et al. to be necessary to obtain agreement between the O^{2+} abundances derived from different multiplets in the nebular spectrum of NGC 7009. In particular, the 3d–3p and 4f–3d doublet transitions give O^{2+} abundances which differ by an order of magnitude from the others, if Case B is not assumed. These recombination coefficients were calculated for a density of 10^6 cm^{-3} and not for a density of 10^{11} cm^{-3} more appropriate to the WC10 wind emission regions. For higher densities, the recombination coefficient increases, making the I/Q ratios smaller and hence the derived O^{2+} abundance lower. For this reason we consider our O/He abundance ratios (of 0.36 for both objects) to be upper limits. However, to give an indication of the effect of a higher electron density, a scaling factor was calculated by comparing the effective recombination coefficients for low and high density for C II transitions with the same configuration as the O II transitions used (3d–3p and 4f–3d). Recombination coefficients

for C^{2+} were calculated at 13 000K by Davey (1995) for densities of 10^4 and 10^{11} cm^{-3}. O/He abundance ratios obtained applying these factors (1.45 for the 3d–3p transition and 1.34 for the 4f–3d transition) are also listed in Table 7.12, along with the uncorrected values.

The dereddened line fluxes are listed in Tables 7.10 and 7.11. The errors associated with the flux measurements were about 10% for the C II lines (although for the weaker 9g–4f lines at 4493 Å they might have been slightly higher) and about 15% for the weaker O II and C III lines. The He I lines, despite being stronger and easier to measure, always had P Cygni profiles, so that the red side had to be projected onto the blue side about the centre of the line, with the uncertainties involved gauged at about 20%. We estimate an uncertainty of 10% for the flux of the He II λ4686 line.

In selecting the O II lines to use as diagnostics, we looked for unblended lines or blends whose components belonged to the same multiplet. Beside the lines listed in Table 7.10 (for which a detailed description follows) we found three other candidates, M53.03 at 4237.93 Å, M26 at 4395.97 Å and M33 at 4941.09,43.02 Å. For all of these, however, the I/Q ratios were one order of magnitude higher than for the four O II multiplets listed in Tables 7.10 and 7.11. We therefore decided to disregard them on the grounds that if the I/Q ratio for a line is too high, it can mean that its flux was overestimated due, for instance, to blending.

We finally used the following O II lines: Multiplet 28, which has three components (4890.8, 4906.8 and 4924.5 Å). Two of these were measured and their fluxes are given in Table 7.10. Multiplet 20 contains 7 components, some of which are blended together. For CPD–56°8032, we measured the flux corresponding to the blend of $\lambda\lambda$4103.0,4105.0,4104.7 (three of the seven components of Multiplet 20), while for He 2–113 the weak λ4103.0 component was resolved and was not included in the measurement. These M20 fluxes are tabulated in Table 7.10, in the row corresponding to O II 4105 Å. What is tabulated as λ4277.0 in Table 7.10 is in fact the sum of the four components of O II Multiplet 67. For M 4–18 the O II line at 4105 Å was excluded since it resided outside the range covered by

Table 7.10: Dereddened fluxes and I/Q values determined for unblended stellar features in the spectra of CPD–56°8032 and He 2–113. Most of the O II lines were blends of several components. Details of which components were used are given in the text. C/R correction factors are given for He I and the tabulated I/Q values for this ion are already corrected using these factors

		CPD–56°8032					He 2–113				
Ion(Mult.)	λ (Å)	I (cgs units)	I (norm.)	C/R	I/Q	Wt.	I (cgs units)	I (norm.)	C/R	I/Q	Wt.
C II(28.01)	8793.8	1.99×10^{-12}	0.35	–	4.32×10^{13}	0.8	9.95×10^{-13}	0.40	–	1.73×10^{13}	0.8
C II(25)	4964.7	3.56×10^{-12}	0.63	–	7.90×10^{13}	1.0	2.19×10^{-12}	0.88	–	3.74×10^{13}	1.0
C II(50)	4619.2	9.81×10^{-12}	1.75	–	5.90×10^{13}	0.7	3.58×10^{-12}	1.44	–	4.24×10^{13}	0.7
C II(51)	5113.69	3.38×10^{-12}	0.60	–	8.71×10^{13}	1.0	1.14×10^{-12}	0.46	–	3.87×10^{13}	1.0
C II(6)	4267.2	6.22×10^{-11}	11.11	–	7.41×10^{13}	1.0	2.95×10^{-11}	11.89	–	2.97×10^{13}	1.0
C II(17.04)	6461.9	7.37×10^{-12}	1.32	–	9.24×10^{13}	1.0	4.59×10^{-12}	1.85	–	4.80×10^{13}	1.0
C II(17.06)	5342.4	7.33×10^{-12}	1.31	–	1.73×10^{14}	1.0	2.53×10^{-12}	1.02	–	4.96×10^{13}	1.0
C II(17.08)	4802.7	5.60×10^{-12}	1	–	1.93×10^{14}	1.0	2.48×10^{-12}	1	–	7.13×10^{13}	1.0
C II(–)	4492.8	4.33×10^{-12}	0.77	–	2.62×10^{14}	0.7	1.45×10^{-12}	0.58	–	5.93×10^{13}	0.7
Mean C^{2+}					$(1.16\pm0.80)\times10^{14}$					$(4.37\pm0.40)\times10^{13}$	
C III(46)	5305.1	2.37×10^{-12}		–	1.93×10^{11}	1.0	1.19×10^{-12}		–	9.35×10^{10}	1.0
C III(46)	8664.4	1.39×10^{-12}		–	9.26×10^{10}	0.5	1.21×10^{-12}		–	7.19×10^{10}	1.0
Mean C^{3+}					$(1.59\pm0.38)\times10^{11}$					$(8.27\pm2.60)\times10^{10}$	
O II(28)	4890.8	1.00×10^{-12}		–	1.28×10^{14}	0.9	5.53×10^{-13}		–	5.27×10^{13}	0.9
O II(28)	4906.8	1.88×10^{-12}		–	1.13×10^{14}	1.0	9.48×10^{-13}		–	4.22×10^{13}	1.0
O II(20)	4105	3.21×10^{-12}		–	5.55×10^{13}	0.5	2.25×10^{-12}		–	4.23×10^{13}	0.5
O II(67)	4277.0	2.91×10^{-12}		–	1.71×10^{14}	0.7	3.02×10^{-12}		–	1.23×10^{14}	0.7
Mean O^{2+}					$(1.21\pm0.24)\times10^{14}$					$(6.34\pm1.27)\times10^{13}$	
He I(86)	4471.5	1.13×10^{-11}	2.02	1.33	1.06×10^{14}	1.0	6.16×10^{-12}	2.48	0.90	5.86×10^{13}	1.0
He I(85)	5875.7	2.15×10^{-11}	3.83	1.52	9.46×10^{13}	1.0	1.67×10^{-11}	6.73	1.09	7.26×10^{13}	1.0
He I(79)	7065.3	9.08×10^{-12}	1.62	3.35	1.59×10^{14}	0.3	6.34×10^{-12}	2.56	3.05	1.06×10^{14}	0.3
He I(27)	6678.1	8.76×10^{-12}	1.56	0.48	2.17×10^{14}	0.9	5.55×10^{-12}	2.24	0.38	1.20×10^{14}	0.9
He I(80)	4713.2	7.10×10^{-12}	1.27	1.27	6.44×10^{14}	0.9	2.02×10^{-12}	0.61	1.12	1.74×10^{14}	0.9
He I(22)	5047.7	1.95×10^{-12}	0.35	1.10	6.95×10^{14}	1.0	1.46×10^{-12}	0.59	0.97	4.69×10^{14}	1.0
Mean He^{+}					$(3.37\pm0.97)\times10^{14}$					$(1.76\pm0.37)\times10^{14}$	
He II	4686.0	1.85×10^{-12}		–	2.47×10^{12}	1.0	2.21×10^{-12}		–	2.08×10^{12}	1.0

Table 7.11: As Table 7.10 but for M 4–18

Ion(Mult.)	λ (Å)	I (cgs units)	I (norm.)	C/R	I/Q	Wt.
C II (25)	4964.7	5.58×10^{-14}	0.66	–	1.17×10^{12}	1.0
C II (50)	4619.2	8.79×10^{-14}	1.04	–	5.38×10^{11}	1.0
C II (51)	5113.7	4.49×10^{-14}	0.53	–	1.18×10^{12}	0.7
C II (6)	4267.2	9.93×10^{-13}	11.78	–	1.11×10^{12}	1.0
C II (17.04)	6461.9	1.54×10^{-13}[a]	0.18	–	1.87×10^{12}	0.8
C II (17.06)	5342.4	1.25×10^{-13}	1.48	–	2.80×10^{12}	1.0
C II (17.08)	4802.7	8.43×10^{-14}	1	–	2.76×10^{12}	1.0
C II (–)	4492.8	4.64×10^{-14}	0.55	–	2.17×10^{12}	0.7
Mean C^{2+}					$(1.65\pm0.80)\times10^{12}$	
C III (46)	5305.1	4.95×10^{-14}		–	4.03×10^{9}	1.0
O II (28)	4890.8	1.37×10^{-14}		–	1.69×10^{12}	0.9
O II (28)	4906.8	2.37×10^{-14}		–	1.36×10^{12}	1.0
Mean O^{2+}					$(1.52\pm0.15)\times10^{12}$	
He I (86)	4471.5	1.44×10^{-13}	1.71	1.19	1.36×10^{12}	1.0
He I (85)	5875.7	4.24×10^{-13}[a]	5.03	1.38	1.70×10^{12}	0.8
He I (27)	6678.1	1.24×10^{-13}[a]	1.47	0.45	3.20×10^{12}	0.7
He I (80)	4713.2	5.07×10^{-14}	0.60	1.23	4.51×10^{12}	0.9
He I (22)	5047.7	3.89×10^{-14}	0.46	1.07	1.34×10^{13}	1.0
Mean He^{+}					$(5.09\pm3.00)\times10^{12}$	
He II	4686.0	4.94×10^{-14}		–	6.59×10^{10}	1.0

[a]Fluxes measured from the scaled INT–IDS spectrum

Table 7.12: Elemental abundance ratios, by number, for the winds of CPD–56°8032, He 2–113 and M 4–18

Ratio	CPD–56°8032	He 2–113	M 4–18
C/He (dielectronic)	0.20	0.20	0.18
C/He (bound–bound)	0.45	0.29	0.41
C/He (all)	0.34	0.25	0.33
O/He (before correction)	0.36	0.36	0.29
O/He (after correction)	0.25	0.26	0.20

the echelle spectroscopy and on the IDS spectrum the severe blending did not allow the measurement to be carried out. The line at 4277 Å was also left out due to its weakness.

Four of the nine C II lines that were used are the dielectronic lines that were used in the wind electron temperature determination. The remaining five lines form as a result of the ng–4f (n=6 to 9) transitions already discussed, plus the 4f–3d 4267 Å transition. This line is usually thought to be much more optically thick and not to be suitable for abundance determinations. However, we believe this not to be necessarily the case and introduce it here; its optical depth will be analysed in Section 7.7.

C III lines were chosen with upper levels as high above the ground state as possible and with orbital quantum numbers as large as possible, so as to make the hydrogenic approximation, used in deriving the effective recombination coefficients, as realistic as possible. We chose the lines at 5305.1 Å (M46, $5f^3F^o$–$7g^3G$) and at $\lambda\lambda$8665.2,8663.6 Å (M45, $6g^3G$–$5f^3F^o$). The measurement was slightly more difficult in the case of He 2–113 and M 4–18 than for CPD–56°8032, due to the 8665.2,63.6 Å lines being blended with the nebular hydrogen Paschen series line (n = 14–3, 8665.02 Å), while the 5305.1 Å line had a mild P Cygni profile. Despite the difficulties encountered, it can be seen from Table 7.10 that the I/Q values derived from the two lines are in agreement. An error of 30% is quoted, which includes a 15% uncertainty in the line flux measurements and a 15% uncertainty in the effective recombination coefficients. In conclusion, for all our objects the C^{3+} abundance is found to be about 500 times smaller then the C^{2+} abundance.

Table 7.13: Comparison of abundances (by number) for CPD–56° 8032, He 2–113 and M 4–18 derived here using exclusively recombination lines from bound–bound transitions, with abundances derived by bulk non–LTE modelling of the stellar atmosphere (only for CPD–56° 8032 and He 2–113; Chapter 6) and the non–LTE study of Leuenhagen et al. (1996; LHJ)

Analysis	H/He	C/He	O/He
	CPD–56° 8032		
LHJ	$\lesssim$0.05	0.40±0.05	0.05±0.01
Modelling	$\lesssim$0.02	0.50±0.10	0.10±0.05
Recombination	–	0.45±0.10	0.25±0.10
	He 2–113		
LHJ	$\lesssim$0.64	0.37±0.05	0.03±0.01
Modelling	$\lesssim$0.02	0.55±0.15	0.10±0.05
Recombination	–	0.29±0.10	0.26±0.10
	M 4–18		
LHJ	$\lesssim$0.5	0.37±0.05	0.02±0.01
Modelling	–	–	–
Recombination	–	0.41±0.10	0.20±0.10

After the He I lines had been corrected for collisional effects, the corrected fluxes were used to obtain the emission measures listed in Tables 7.10 and 7.11. The I/Q values for all the ions were then averaged using the weights for each line listed in columns 6 and 10 of Table 7.10 and column 6 of Table 7.11. The weights are based on the confidence in the I/Q ratio once all the sources of uncertainty were taken into consideration. The averaged I/Q values of different ionization stages of the same element were then summed, with the summed I/Q values from the carbon, oxygen and helium ions yielding the final abundance ratios listed in Table 7.12. The weights given to the I/Q values in Tables 7.10 and 7.11 are purely based on the measurement uncertainty and do not take into account optical depth.

In Table 7.13 we compare the stellar wind abundance results derived from our recombination line analysis with those of Leuenhagen et al. (1996), who constructed non–LTE models for these and other [WCL] stars, and with our own non–LTE wind modelling (Chapter 6). We find values of C/He comparable within a 2σ uncertainty, while the cor-

rected O/He ratios obtained here compare within the uncertainties with the values derived in Chapter 6, but are 5 to 10 times higher than the values obtained by Leuenhagen et al. (1996).

Contrary to Leuenhagen at al., we find that CPD–56°8032 and He 2–113 have no detectable hydrogen in their winds (see Chapters 5 and 6). This restores these [WCL] stars to their former status as hydrogen–free WR stars. For M 4–18 we will have to await higher resolution spectroscopy of a wider spectral range to carry out the same kind of comparison between the hydrogen lines and nebular forbidden lines described in Chapter 5. Only in this way once can solve the nature of the asymmetric Hβ line profiles described in Chapter 8.

7.7 Optical Depth Effects

In the abundance determinations in Section 7.6, we have made use of lines between low-lying states of He, O and C which might reasonably be expected to have different and not insignificant optical depths. In addition, the wind temperature determinations have tacitly assumed that the dielectronic lines are optically thin. In this Section, we discuss the effect of line optical depth on our conclusions.

The wind parameters used to carry out this optical depth analysis are mainly taken from the stellar wind modelling presented in Chapter 6. Although we have argued in Chapter 8 that the stellar wind model for He 2–113 is suitable also for the wind of M 4–18, we nonetheless limit this analysis to CPD–56°8032 and He 2–113 for which a dedicated model exists.

The optical thickness of the wind in a given transition depends, amongst other things, upon the population of the lower state of the transition and the oscillator strength for that transition. For a series of transitions terminating in a common lower state, the oscillator strength falls as n^{-3}, where n is the principal quantum number of the upper state, while the population of the lower state decreases as its energy increases. The decline in optical thickness with increasing upper state principal quantum number is illustrated by the ng–4f

series in C II ($6 \leq n \leq 9$) which are visible in our spectra. These lines, which display no P–Cygni structure, show a decreasing FWHM as n increases (see Table 7.15). This effect, which has also been described in massive Wolf–Rayet stars by Schulte–Ladbeck, Eenes and Davis (1995), is attributable to the decline in optical thickness, since the emission from the inner, low–velocity part of the wind is relatively stronger for less optically thick lines while the emission from the outer higher velocity part is approximately unchanged, leading to an apparent narrowing of the line. On the basis of the empirical evidence from line FWHM, the winds of the two stars are optically thick to many of the lines used in the abundance analysis. Nonetheless, the abundances derived from the various lines of apparently different optical depths are in broad agreement, although there is a tendency for the abundances derived from the dielectronic lines to be lower than from the C II bound–bound transitions. The optical thickness of the C II dielectronic lines cannot be assessed empirically from their FWHM due to blending and the additional autoionization broadening that some of the lines exhibit. They certainly arise from energetically high-lying atomic states, but being 3p–3d and 3d–4f transitions, they have relatively large oscillator strengths. In addition, the wind models described in Chapter 6 do not include the temperature diagnostic dielectronic lines, so we have carried out an escape probability analysis of these, and other lines to determine their optical thickness.

We use the escape–probability formalism of Castor (1970) for an expanding spherically symmetric atmosphere, in which an optical depth $\tau(z,r)$ is defined by

$$\tau(z,r) = \frac{\pi e^2}{mc} \times (gf)_{u,l} \times \frac{\left(\frac{N_l}{g_l} - \frac{N_u}{g_u}\right) \times r}{\nu_o v r/c} \times \frac{1}{1 + z^2/r^2(\mathrm{dln}v/\mathrm{dln}r - 1)} \qquad (7.27)$$

where r is the distance from the centre of the star, z is the distance from the centre of the star projected in the direction to the observer, f is the oscillator strength for the level, ν_o is the frequency at the line centre and the velocity field has the (assumed) form:

$$v(r) = v_\infty (1 - \frac{R_c}{r})^\gamma \qquad (7.28)$$

where v_∞ is the terminal velocity of the wind and R_c is the radius of the star (defined from the centre to the base of the wind), and γ, which defines the degree of acceleration

Table 7.14: Continuum opacities (τ_c) and departure coefficients for all the levels used, as a function of $log(R/R_*)$ The stellar radius for CPD–56°8032 was 2.2 $R_\odot$, while for He 2–113 was 2.5 $R_\odot$

CPD–56°8032										
log(R/R$_*$)	0.0	0.0203	0.085	0.183	0.378	0.606	0.866	1.094	1.354	1.549
log(τ_c)	1.05	0.56	0.11	−0.25	−0.56	−0.88	−1.19	−1.5	−1.81	−2.13
b(3d)	1.00	0.993	0.983	1.063	1.726	1.637	0.444	0.050	0.0033	0.00040
b(4f)	1.00	1.00	1.00	1.00	1.28	1.06	0.161	0.045	0.003	0.0005
b(6g)	1.00	1.00	1.00	1.00	1.00	0.45	0.073	0.035	0.024	0.013
b(7g)	1.00	1.00	1.00	1.00	0.94	0.40	0.12	0.073	0.051	0.029
b(8g)	1.00	1.00	1.00	1.00	0.94	0.45	0.28	0.23	0.18	0.12
b(9g)	1.01	1.02	1.03	1.0	0.92	0.73	0.49	0.37	0.26	0.18
He 2–113										
log(R/R$_\odot$)	0.0	0.0049	0.019	0.158	0.450	0.826	1.236	1.660	2.087	2.496
log(τ_c)	1.320	−0.239	−0.473	−0.873	−1.335	−1.791	−2.264	−2.776	−3.275	−3.712
b(3d)	1.00	0.84	0.62	0.73	0.51	0.19	0.025	0.0015	0.0002	0.0001
b(4f)	1.00	0.97	0.79	0.90	0.30	0.011	0.0020	0.0003	0.00007	0.00004
b(6g)	1.00	0.99	0.86	0.80	0.40	0.12	0.032	0.0073	0.0028	0.0024
b(7g)	1.00	0.99	0.89	0.70	0.20	0.072	0.036	0.017	0.0097	0.0077
b(8g)	1.00	0.99	0.90	0.72	0.37	0.27	0.16	0.084	0.054	0.058
b(9g)	1.00	0.99	0.90	0.72	0.37	0.27	0.16	0.084	0.054	0.058

of the wind, is usually taken to be 1. With this velocity law, the logarithmic derivative of v with respect to r is $R_c\ v_\infty\ /rv(r)$.

For each star a grid was established of 10 points that spanned the depth of the wind. Grid points were equally spaced in log(τ_{Ross}) (where τ_{Ross} is the Rosseland optical depth). For each grid point we extracted the physical radius, the electron temperature and density, the fraction of C^{2+} and H^+ (see Fig. 6.4 in Chapter 6), the continuum optical depth (at 5000 Å) and the departure coefficients for the upper and lower levels of each transition (see Table 7.14). These last two quantities were obtained from the models described in Chapter 6, but are not explicitly given there. For the dielectronic transitions we calculated b values from Eq. 7.7 and Table 7.1 for states above the ionization limit, while for lower levels the b values were set to unity. The wind model of Chapter 6 did not include the 9g level – its departure coefficients were set to the same values as the 8g level.

In the model, we neglect the stellar continuum and its absorption by the lines, obtaining the flux emitted in the lines as a function of radius and of velocity. We obtain predicted relative fluxes for all the dielectronic lines of C II and for the bound–bound transitions of C II and neutral helium. The optical depth in the lines can also be monitored throughout the wind.

7.7.1 Results of the Escape Probability Model

In Table 7.15 we present a summary of the predicted fluxes, on an arbitrary scale, optical depths and observed FWHM of the line sample. The optical depths are calculated at a point with $z = 0$ at a radius corresponding to the peak of the line formation region which was determined to be 3.0 R_* for CPD–56°8032 and 2.5 R_* for He 2–113. We use the tabulated optical depth values only for comparison purposes.

We observe, first of all, that the trend in optical depths of the bound–bound lines confirms the trends outlined above, that the more optically thick lines come from lower levels and that the optical depth falls when progressing up a series with a common lower state (4f–6g, λ6450; 4f–7g, λ5340; 4f–8g λ4802). Also, the model relative fluxes in Table 7.15 correspond reasonably well with those in Table 7.10, for both bound–bound and dielectronic lines, suggesting that the relatively low I/Q values obtained from the dielectronic lines must be explained by atomic physics and opacity rather than uncertain measurement. Table 7.15 also confirms that some lines between low-lying states (e.g. λ4267 4f–3d of C II or λ5876 triplet of He I) which give reasonable abundances have very high optical depths. It appears that the line fluxes predicted by the theory of recombination in an optically thin medium also approximately describe the emission from lines of high optical thickness, with the exception of the dielectronic lines, where relatively modest optical depths significantly affect the derived abundances. In the next Section we seek to explain these observations.

Table 7.15: Predicted normalised fluxes, optical depths and observed FWHM for a sample of carbon and helium lines used in the derivation of abundances (T stands for triplet)

λ (Å)	Trans.	Flux (arbitrary)	$\tau^{\dagger}_{r'}$	FWHM (km s^{-1})
		CPD–56°3082		
4965	3d′–3p′	1.08	0.52	–
4619	4f′–3d′	1.81	2.08	–
5114	4f′–3d′	0.83	0.52	–
4267	4f–3d	5.66	241	226
6450	6g–4f	1.06	12.31	228
5340	7g–4f	0.96	3.54	184
4802	8g–4f	1.0	1.49	162
4493	9g–4f	0.95	0.76	<160
4471	4d–2pT	3.18	14.1	–
5876	3d–2pT	4.52	80.5	–
7065	3s–2pT	3.08	8.80	–
		He 2–113		
4965	3d′–3p′	0.92	0.066	–
4619	4f′–3d′	1.71	0.22	–
5114	4f′–3d′	0.75	0.053	–
4267	4f–3d	5.63	19.8	160
6450	6g–4f	2.55	0.48	150
5340	7g–4f	1.07	0.16	125
4802	8g–4f	1.0	0.066	<95
4493	9g–4f	0.70	0.031	<95
4471	4d–2pT	2.22	3.9	–
5876	3d–2pT	4.52	27.6	–
7065	3s–2pT	2.05	3.8	

$^{\dagger}r'$=3.0R_* for CPD–56°8032

$^{\dagger}r'$=2.5R_* for He 2–113

7.7.2 A Two-Level Atom

Consider a 2–level atom in which the populations are determined solely by radiative processes, both bound–free and bound–bound (although we will neglect photoionization). The population of the upper level (N_2) is given by

$$N_e N_+ \alpha_2 = N_2 \Gamma^R_{21} \beta_{21} \tag{7.29}$$

where Γ^R_{21} is an Einstein A-coefficient, α_2 is a recombination coefficient, and β_{21} is the single–flight escape probability for photons in the transition, which decreases as the optical depth increases. The emissivity in the transition is just $N_2 \Gamma^R_{21} \beta_{21} h\nu = N_e N_+ \alpha_2 h\nu$, which is the same as in the optically thin case, no matter how great the optical depth in the line. As the optical depth increases, the population of the upper state rises so that the flux in the line is preserved. The abundance derived from such a transition using optically thin recombination theory will be independent of optical depth effects.

Consider now an ideal dielectronic line where the two states are embedded in the continuum, their populations are given by the Saha equation and are independent of the optical depth. The emissivity $N_2 \Gamma^R_{21} \beta_{21} h\nu$, will fall as the optical depth increases due to the fall in the escape probability and the abundance derived from the transition will fall as the optical depth rises.

In practice all states are coupled to each other and the continuum by collisional processes, so the purely radiative case described above is never realised in practice, but the λ4267 4f–3d transition in C II might be expected to be a reasonable approximation. Both states are low–lying, so that collisional processes are relatively unimportant, and as in the model two–level atom, there is no alternative decay route from the 4f state once the transition becomes optically thick.

To illustrate these effects for a transition $u \rightarrow$l, we define an effective recombination coefficient α'_{ul} by

$$N_e N_+ \alpha'_{ul} = N_u \Gamma^R_{ul} \beta_{ul} h\nu, \tag{7.30}$$

so that α' is a measure of the emissivity in a particular transition allowing for the effects of

optical depth. In Fig. 7.8 we show the behaviour of this quantity as a function of radius in the wind of CPD–56°8032. In each plot, the horizontal line segment shows the value of the effective recombination coefficient for that particular transition taken from optically thin recombination theory at the temperature of maximum emission in the wind. The length of the segment represents the width of the line forming region as indicated by Fig. 6.4 (e) in Chapter 6. These are the values that were used to determine the abundances in Table 7.10. The vertical line shows the approximate radius of maximum emission in the recombination lines. This is taken to be at 3 R_* for the peak of the C II line forming region and at 5 R_* for the peak of the He I line forming region. We note that the values of α' at the radius of maximum emission generally lie within about a factor of three of the optically thin theory, even though the optical depths in the lines range from about 0.5 to 241. We note also that the values of α' for the three dielectronic lines ($\lambda\lambda 4619, 4965, 5114$) are all smaller than the corresponding optically thin values, as expected.

We have not included the recombination lines of O II in this analysis, but some general points can be made by comparing O II with C II. Due to the ^3P parentage of the O II configurations, a particular valence electron configuration of O II results in many more states than the corresponding C II configuration. For example the two O II lines of Multiplet 28 listed in Table 8, correspond to transitions to the 3p($^4S^o_{3/2}$) state. This state, with a statistical weight of 4, have a population approximately 4/54 of the whole (^3P)3p configuration. If all other factors were equal (elemental abundance, distribution in the wind, oscillator strengths and energies of states), the optical depth of the O II lines would be lower than that of the corresponding C II transitions by the same factor. We conclude the the O II lines used in the abundance analysis are likely to have low optical depths and be correspondingly more reliable as abundance indicators, although other problems with these lines have been discussed above.

We would like to underline that the above arguments are only qualitative in nature. Only a complete modelling of the whole envelope can give us any assurance of a correct treatment of the opacity. However from this limited exercise we conclude that low–lying

bound–bound transitions can be combined with optically thin recombination theory to obtain indicative abundances. As a result we prefer to use bound–bound rather then dielectronic transitions for our abundance determination.

As far as the wind electron temperature is concerned, we see from Fig. 7.9 that the escape probabilities for the $\lambda\lambda$5114,4965 lines are very similar throughout the wind (while the escape probability for the C II λ4619 line is much lower), implying that the two lines will be equally attenuated by the wind and their ratio therefore preserved. This gives renewed confidence in using these two lines to determine the wind electron temperature.

7.8 Summary

We have demonstrated the use of low temperature dielectronic recombination lines for the determination of the wind electron temperature of [WC10] central stars of PN. This is the first direct spectroscopic determination of such a quantity in a WR star. Stellar wind abundances have also been derived for carbon and oxygen relative to helium. Carbon abundances are derived using bound–bound transitions, not the dielectronic recombination lines, since these systematically underestimate the abundance due to optical depth effects. This is due to their upper levels being in LTE with the continuum and not being able to compensate for optical depth by increasing their upper level populations.

Oxygen abundances, derived using low density effective recombination coefficients can only be considered as upper limits. A scaling factor to simulate the effect of using higher density effective recombination coefficients was calculated. Although this cannot be considered an exact method, the abundances derived after the application of such scaling factor compare quite well with values obtained from bulk modelling of the wind carried out in Chapter 6. The oxygen lines used all arise from bound–bound transitions. Moreover the opacity of such lines is lower, due to the different atomic structure of the O II ion.

Optical depth effects are *not* thought to influence the electron temperature determination since the escape probabilities of the two most optically thin dielectronic lines are almost identical throughout the wind.

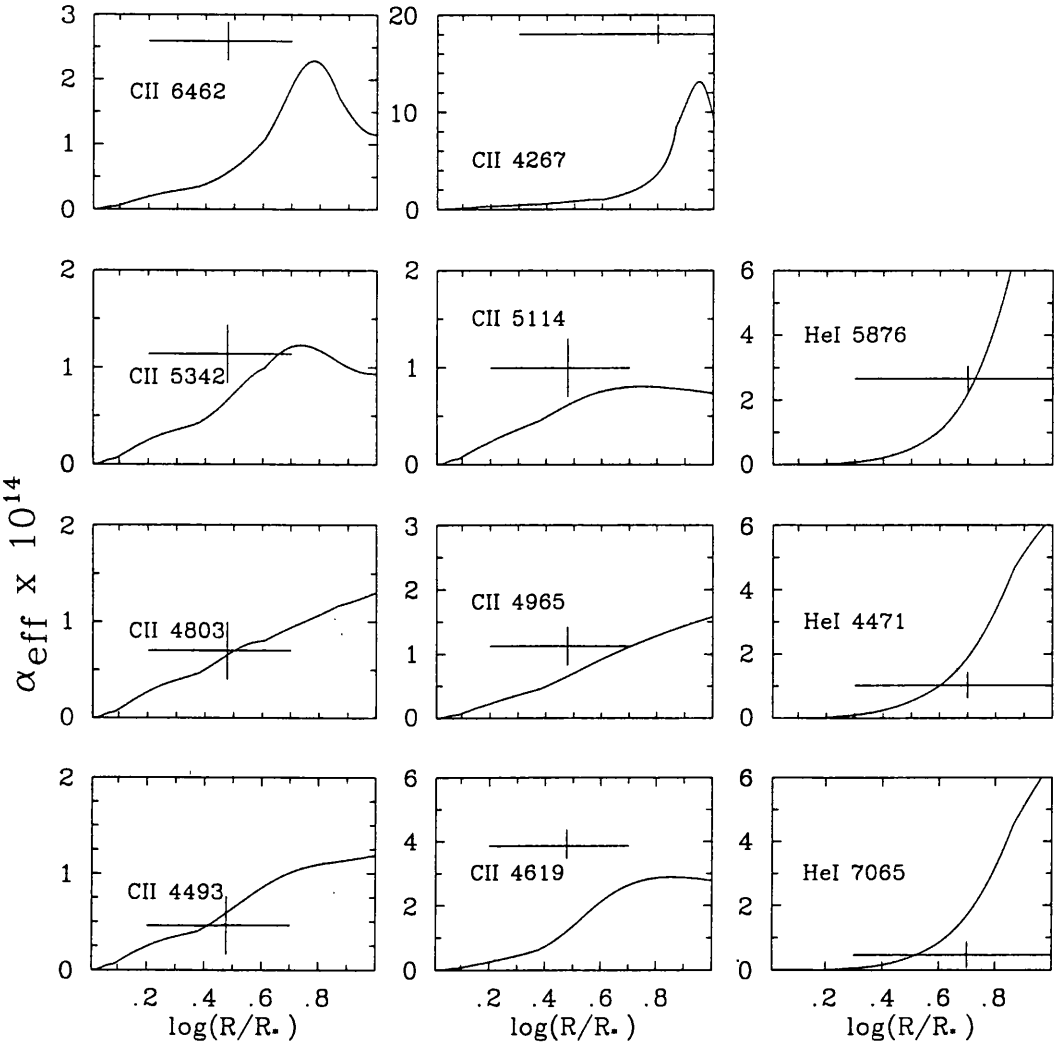

Figure 7.8: Effective recombination coefficients in the optically thin case (line segments) and allowing for optical depth effects as defined in Eq. 7.30 (curves) for selected lines of C II and He I. The length of the horizontal segment indicates the approximate width of the emission region. The vertical segments indicate the radius of peak emission (3 R_* for C II lines, 5 R_* for He I lines and C II λ4267)

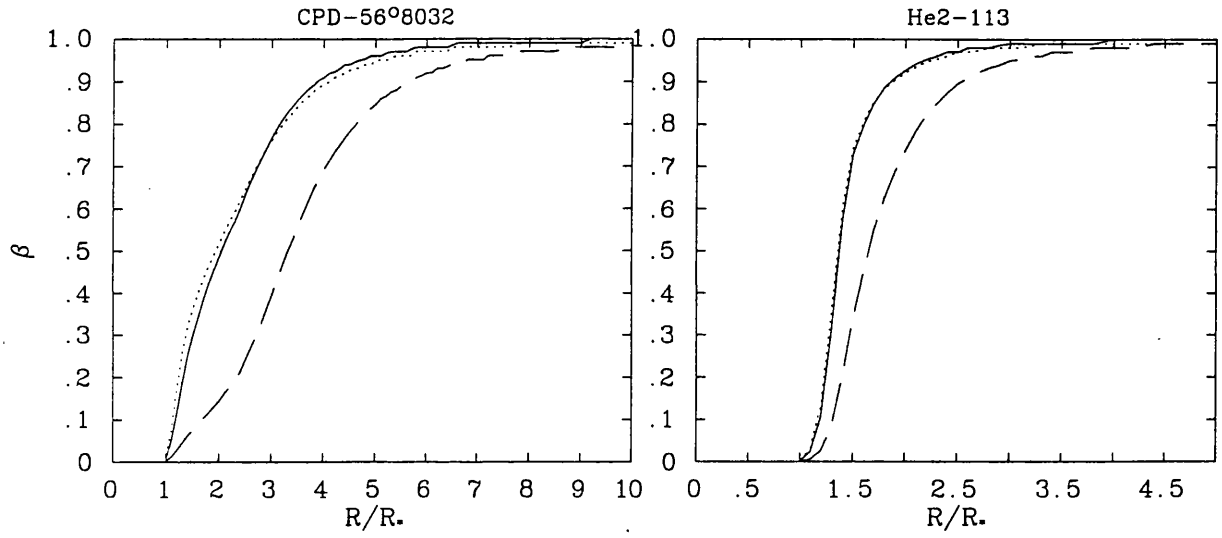

Figure 7.9: Escape probabilities for the dielectronic lines λ5114 (solid lines), λ4965 (dotted lines) and λ4619 (dashed lines)

Chapter 8

M 4–18 and SwSt 1: Distances and Nebular Parameters

In this Chapter we carry out a study of the PN around M 4–18 and SwSt 1. The techniques used (outlined in Chapter 2) are analogous to the ones applied to the PN of CPD–56°8032 and He 2–113 (Chapter 5).

M 4–18, the eighteenth object in Minkowski's unpublished fourth list (see Perek and Kohoutek 1967), was classified by Webster and Glass (1974) as having a WC10 central star, together with CPD–56°8032, He 2–113 and V 348 Sgr. Its classification then oscillated between WC10 and WC11 as different authors adopted different schemes. van der Hucht et al. (1981) classified it as WC11, as did Sabbadin and Bianchini (1979), although we have shown (Chapter 4) that if we adopt a scheme consistent with the quantitative classification of Smith, Shara and Moffat (1990), M 4–18 has to be classified as a WC10 star, like CPD–56°8032 and He 2–113.

Before 1985 only very limited studies existed of this star (e.g. Sabbadin and Bianchini 1979, Sabbadin 1980). Goodrich and Dahari (1985) derived quantitative nebular parameters and abundances from their low resolution optical spectroscopy and UV IUE spectra. They also carried out a limited stellar analysis, applying the energy balance method to determine an effective temperature, T_{eff}=22 000 K, and using a blackbody bolometric

correction and a distance of 3.5 kpc (obtained by applying the Cudworth (1974) distance scale method), they determined a luminosity of $2600L_{\odot}$. From these values and the post-AGB evolutionary tracks of (Schönberner 1981) they determined a stellar mass of 0.55 $M_{\odot}$. Surendiranath and Rao (1995) carried out the most extensive nebular analysis on M 4–18 to date along with nebular modelling, although their adopted distance of 1 kpc (based on a relationship between nebular radius and electron density – Pottasch 1984), is in clear contrast with observed evolutionary tracks. The central star was modelled by Leuenhagen, Hamann and Jeffery (1996) and was derived to have a stellar effective temperature of 31 000 K and a stellar wind terminal velocity of v_{∞}=350 km s $^{-1}$ (very similar properties to He 2–113). No CO emission is detected from M 4–18 (Huggins et al. 1996, Dayal and Beiging 1996). Thermal infrared emission (10 μm) reveals an asymmetrical 2" x 3" shell (Dayal and Bieging 1996). Ground-based optical imaging of M 4–18 is presented in the Morphological Catalogue of Northern Galactic PN (Manchado et al. 1996).

SwSt 1 was first discussed by Swings and Struve (1940, 1943). They showed the spectrum to be dominated by broad emission lines of stellar origin and by strong sharp forbidden lines which they attributed to the nebula. The star was classified as WC10 by Cohen (1975) and by Carlson and Henize (1979) from comparing C III λ4650 with C II $\lambda\lambda$3920,4267 lines. In Chapter 4 we noticed that the line ratios that we used as primary classification diagnostics positioned SwSt 1 closer to the WC9 group. However the peculiarity of this object prevents its being classified as a normal WC9 star. Carlson and Henize (1979) reported their spectrum to be similar to the spectrum shown by Swings and Struve, although they noted several changes in the appearence of stellar and nebular lines. We will discuss these changes in our conclusion (Section 8.9). The nebula itself has been detected at radio frequencies (e.g. Milne and Aller 1975, 1982) and VLA observations indicate an angular diameter of 0.8" (Kwok, Purton and Keenan 1981). Infrared observations (Aitken et al. 1979) show a 9.7 μm silicate emission feature, which is normally an indication of an oxygen-rich envelope. They also identify the presence of an additional, warm component that could be identified as graphite; Aitken and Roche (1982) also classified SwSt 1 as an

oxygen–rich PN, on the grounds that its 8–13 μm spectrum has emission features typical of the Trapezium region of Orion and the circumstellar shells of some oxygen–rich giants. The PN of SwSt 1 was analysed by Flower, Goharji and Cohen (1984) and by de Freitas Pacheco and Veliz (1987) who determined physical conditions and abundances. Both analyses found C/O ratios <1, confirming that the envelope is oxygen–rich. A Zanstra analysis to determine the effective temperature was carried out by de Freitas Pacheco and Veliz (1987). Dinerstein et al. (1995) detected nebular neutral sodium absorption and H_2 emission, but no CO is detected in the neutral envelope of SwSt 1 (Huggins et al. 1996). Modelling of the central star has been carried out by Leuenhagen and Hamann (1997), who determined T_{eff} ~T_* ~34 000 K, R_*=1.03 $R_\odot$, $\dot{M}$=1.2×10^{-7}$M_\odot$ yr^{-1} and L=1860 $L_\odot$ (D=1.4 kpc), with percentage abundances of H, He, C and O (by mass) of $\leq$10, 44, 53 and 3, respectively.

In the sections that follow we will determine apparent magnitudes, nebular radial and expansion velocities, reddenings and distances to the central stars; we will also carry out nebular abundance analyses and modelling and will present HST and ground–based images of each PN. We will finally draw some conclusions and compare our results to the ones already obtained for CPD–56°8032 and He 2–113 in Chapter 5.

8.1 Apparent Magnitudes

We convolved our observed central star wide slit spectrophotometry of M 4–18 and SwSt 1 with broad–band V and B filter profiles (kindly made available to us by Dr. J.R. Deacon) to obtain an estimate of the apparent V and B magnitudes of the stars. For M 4–18 we found V=14.11 and B=14.24. This star was observed on the 12th of December 1995 to brighten by about 0.03 mag during 7 hours of observations (Handler 1996) . The author considers, given the sensitivity of the instrument and the good photometric conditions, the variability of the star to be well established. Therefore, while we note the nature of the variability of CPD–56°8032 and M 4–18 to be very different, it is important to consider all types of light variation. Given the extreme uncertainty surrounding the variability

properties of these stars and the implications that the discovery of declines could have on the evolutionary conclusions that can be drawn from them, more photometry is desirable.

For SwSt 1 we derive V=11.48 and B=11.54. The V-band photometry of A. Jones reveals the star to vary between 11.1 and 10.2 mag. In Appendix A we show that the lightcurve of He 2–113 exhibits only a seasonal light variation equivalent to ~0.5 mag. In the case of SwSt 1, the seasonal light variation seems to be superimposed on another variation. This second variation is between 10.8 mag and 10.4 mag and does not seem to have a clear period. The photometry by A. Jones is estimated to have an uncertainty of ±0.1 mag, although under certain conditions and depending on the colours of the star, this uncertainty can be larger. Therefore it is at this time impossible to make any further speculation as to the nature of the variability. The lightcurve for SwSt 1 is also presented in Appendix A.

8.2 The Nebular Balmer Lines

Nebular Balmer lines are used to determine radial and nebular expansion velocities as well as reddenings. Moreover, from high resolution spectra we can also obtain information as to the nebular geometry from the line profiles. For M 4–18 the intrinsic profiles of nebular lines could not be obtained from the low resolution INT spectra. The WHT–UES echelle spectrum of this star only includes Hβ and the [N II] line at 5755 Å in its nebular line coverage. Hβ (see Fig. 8.1 (a)) seems to have a broad pedestal and a blue–shifted absorption (whose minimum intensity is registered at 3.0 Å or 185 km s^{-1} to the blue of the line's rest wavelength) but, due to the much weaker nature of [N II] λ5755, comparison of the two nebular lines does not allow one to reach a conclusion as to the origin of the pedestal.

For M 4–18, the flux in Hβ obtained from a one or a two Gaussian fit did not change substantially, however a double Gaussian fit was instructive as to the nature of the broad pedestal and of the apparent P–Cygni absorption displayed by the Hβ profile. If the two Gaussians' central wavelengths were fit independently (Fig. 8.1 (b)), their widths were

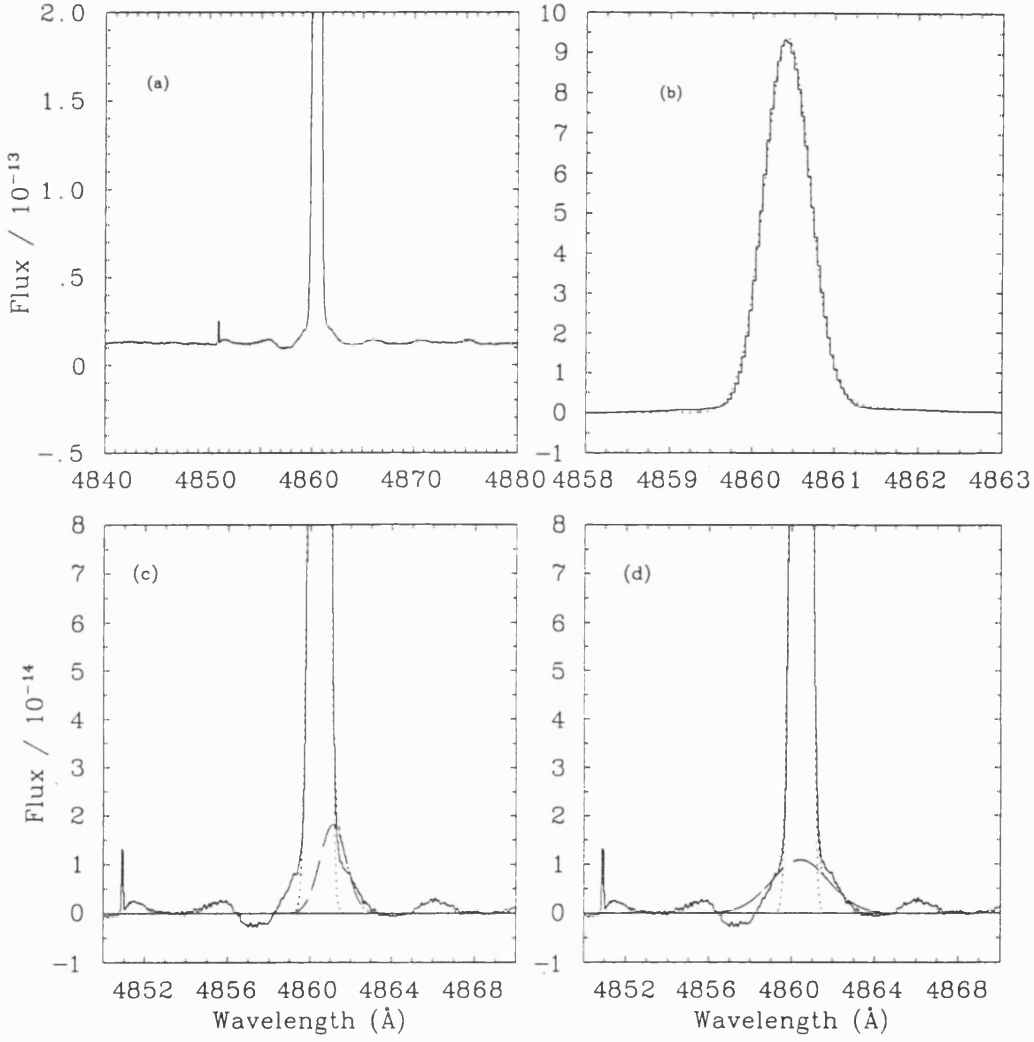

Figure 8.1: (a) Base of the Hβ line in the WHT–UES spectrum of M 4–18, revealing the presence of a broad pedestal and of a possible P–Cygni–type profile. (b) Double Gaussian fit (dotted line) to the continuum—subtracted Hβ profile (solid line; only the overall fit is plotted). (c) and (d) The two Gaussians (dotted and dashed lines) used in the fit to Hβ (solid line). A two Gaussian fit with either unconstrained line centers (c), or with centres constrained to have the same wavelength (d) does not reppresent the base of the Hβ profile satisfactorily (see text)

determined to be 40 and 93 km s^{-1} respectively, the broader Gaussian being displaced 0.7 Å to the red side of the narrower one. When the Gaussians were constrained to have the same central wavelength (Fig. 8.1 (c)), their widths were determined to be 40 and 200 km s^{-1} respectively. Neither of the two fits succesfully reppresented the base of the Hβ profile, due perhaps to the asymmetric structure of this feature. As was the case for He 2–113, this could hint at the possibility of a stellar component or to a nebular high velocity component. This cannot be verified until high resolution spectroscopy is obtained of a larger spectral range. Leuenhagen and Hamann (1997) determine an upper limit of H/He$\leq$10 (by mass) from fitting the base of Hβ with a synthetic profile generated by their non-LTE Wolf–Rayet code.

From the high resolution spectrum of SwSt 1 we notice that the Balmer lines appear remarkably regular with shapes closely approximating Gaussian curves. A comparison with the nebular forbidden lines reveals however that lines arising from singly ionised ions (e.g. [N II] λ6548 and [S II] λ6717), as well as lines coming from neutral ions (e.g. [O I] λ6300) are systematically broader (FWHM$\sim$45–60 km s^{-1}), while lines arising from doubly ionised ions (e.g. [O III] λ5007 and [Ar III] λ7750) have widths similar to the Balmer lines (FWHM(Hβ)=40.2 km s^{-1}) or narrower (FWHM$\sim$30–40 km s^{-1}; see Fig. 8.2). This is consistent with the lines arising from higher ionization stages being formed in an inner, slower part of the PN, with the lines from lower ionization stages being formed further out in an accelerating part of the flow. The Balmer emission, coming from the entire ionised region, might be expected to produce broader lines, however, it might be more intense in the inner, denser region of the PN, yielding narrower profiles.

Moreover, the iron forbidden lines display a slight asymmetry (Fig. 8.3); a double Gaussian fit shows that the blue–shifted sides emits about 20% less than the red–shifted sides. The two Gaussians are centered at –11.3 and +4.0 km s^{-1} for the [Fe III] line λ4701, at –11.2 and +10.8 km s^{-1} for the [Fe III] line λ4881, at –11.3 and +5.7 km s^{-1} for the [Fe III] line λ4733 and at –11.0 and +7.1 km s^{-1} for the [Fe III] line λ5270. The Hβ and [O III] images shown in Fig.8.12 (see Section 8.7.2), and the radio image of Kwok, Purton

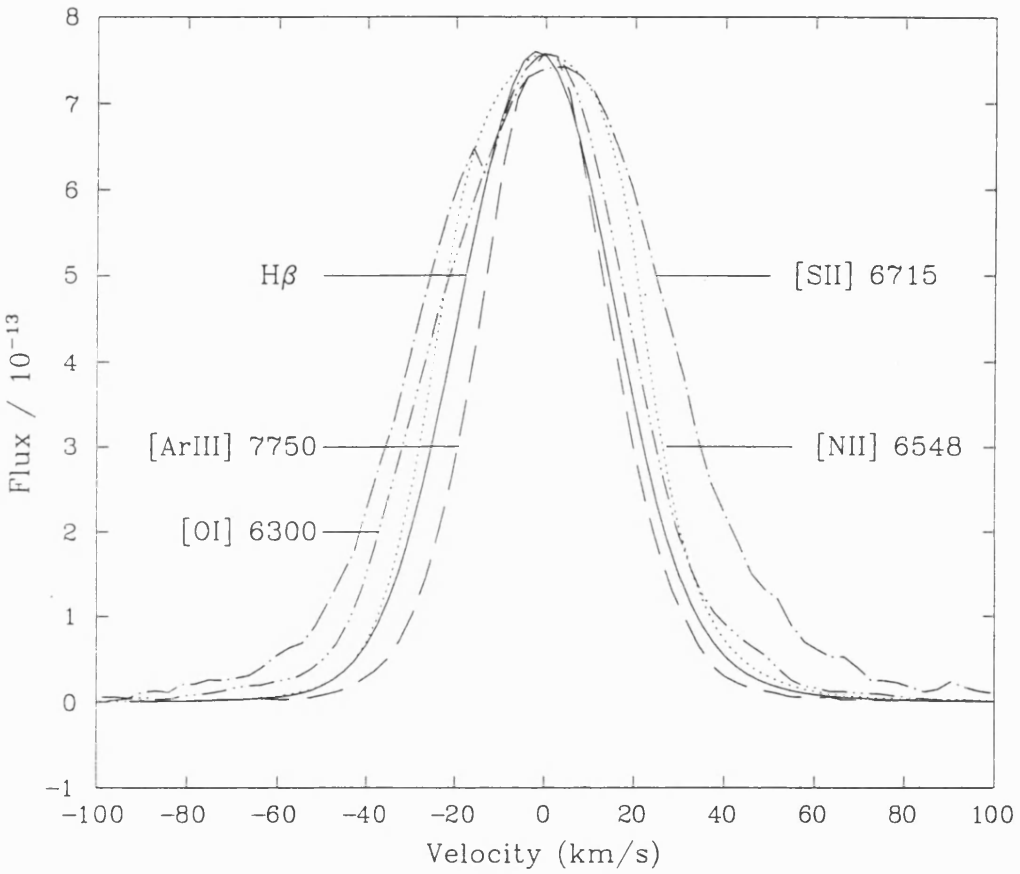

Figure 8.2: Comparison of selected nebular lines in the AAT–UCLES spectrum of SwSt 1. The lines are background subtracted and normalised to the peak intensity of the [Ar III] line λ7750 (8.0×10^{-13} ergs cm^{-2} s^{-1})

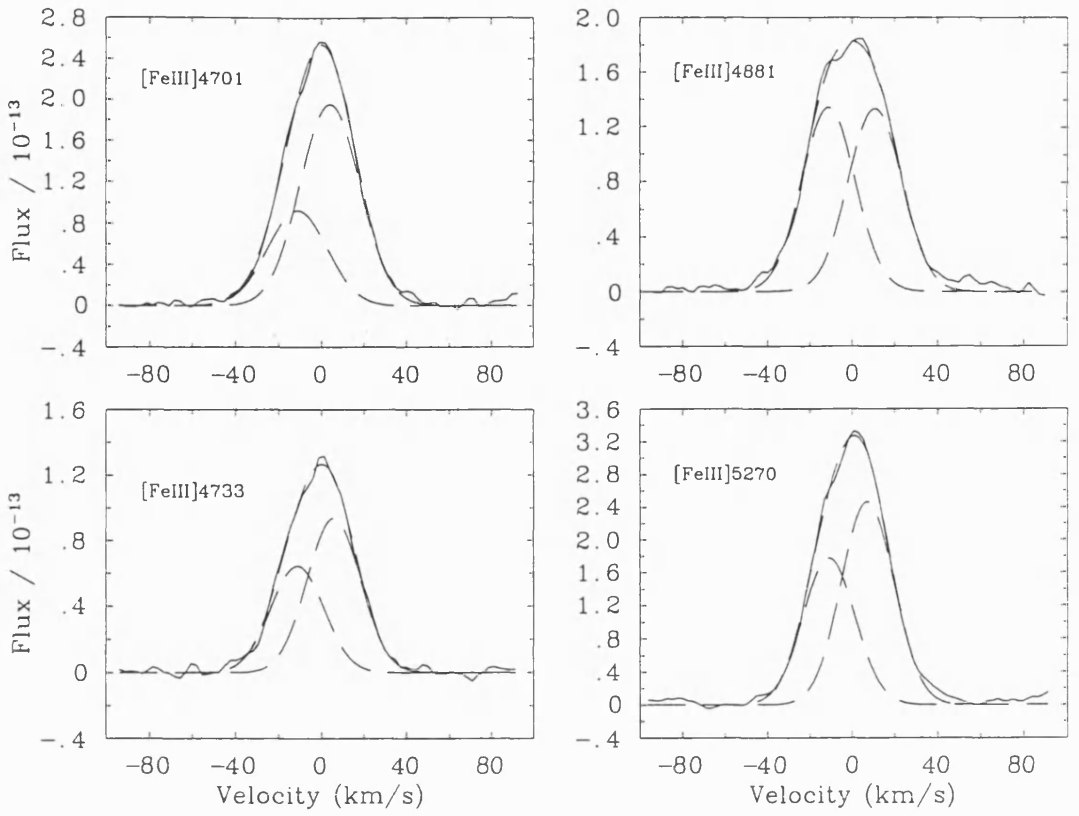

Figure 8.3: Selected [Fe III] lines for SwSt 1 fitted with a double Gaussian

and Keenan (1981) confirm an asymmetric morphology for this young PN.

The Hα and Hβ line fluxes observed for these two nebulae are presented in Tables 8.2 and 8.3, along with the photoelectric Hβ measurements of Carrasco et al. (1983) for M 4–18 and Perek (1971) for SwSt 1.

8.3 Nebular Radial Velocities and Expansion Velocities

Nebular radial velocities were obtained by determining the wavelength shifts of the nebular Balmer lines (for M 4–18 only the Hα and Hβ lines were used, since Hγ and Hδ were blended with stellar features, but a check using Hγ and Hδ did not show any serious discrepancies with the results obtained using the Hα and Hβ lines). The velocity was determined by fitting a single Gaussian to the Hα and Hβ lines and taking the average of the two values, then correcting to the heliocentric and LSR frames of reference. Even

when, as already discussed, a single Gaussian did not fit the data very well (as was the case for CPD–56°8032 and He 2–113), it was felt that this would be the best way to locate the overall center of the line without biases introduced by the asymmetry. A mean heliocentric radial velocity of –51.6 ± 1.0 km s^{-1} was derived for M 4–18 from an average of the Hβ and Hγ lines observed in the echelle spectrum, which corresponds to an LSR radial velocity of –50.8 ± 1.0 km s^{-1}. The INT spectrum was also used to derive a radial velocity, although the spectral resolution was comparable with the radial velocity shift and so the UES result should be preferred (RV(INT)=–46.1± 5.0 km s^{-1} (heliocentric) and –45.3 ± 5.0 km s^{-1} (LSR)). Most of the unblended stellar features in the echelle spectrum of M 4–18, on the other hand, had a less negative radial velocity shift than measured for the nebular lines ($RV_\odot$~–33 km s^{-1}) although for some lines (e.g. C II λ4802) it was more negative ($RV_\odot$=–65 km s^{-1}). This trend was confirmed by the INT spectrum.

The heliocentric radial velocity was measured for SwSt 1 to be –17.8 ± 1.0 km s^{-1} from an average of the Hβ, Hγ and Hδ lines (for SwSt 1 the nebular spectrum is easier to distinguish from the stellar one due to overall weaker stellar features); the LSR radial velocity was determined to be –8.1 ± 1.0 km s^{-1}. Radial velocities are listed in Table 8.1, together with nebular expansion velocities (again measured from averaging Hβ, Hγ and Hδ), assumed to be equal to the half width at half maximum of the Balmer lines.

8.4 Reddenings

The reddening to each object can be derived by comparing the relative fluxes in the nebular Hα and Hβ lines; the weaker Hγ and Hδ lines in the spectrum of M 4–18 were too blended to measure their fluxes reliably, but they could be reliably measured in the higher resolution spectrum of SwSt 1. Using the Case B hydrogen recombination coefficients of Storey and Hummer (1995) for a nebula with electron density $N_e = 10^4$ cm^{-3} and $T_e = 10^4$ K and the galactic reddening law of Howarth (1983), values of E(B–V) were derived. Reddenings were also derived from a comparison of the radio and Hβ fluxes, using the method of Milne and Aller (1975). Below we discuss in detail the individual stars, while in

Table 8.1: Radial and expansion velocities (Columns 2 and 3) for M 4–18 and SwSt 1 obtained from the Balmer emission lines. Radial velocities for the Na D absorption line components of SwSt 1 are also presented (Column 4). Finally, distances derived from different methods are presented in Columns 5 and 6

Name (spectrograph)	LSR Radial Velocity (km s^{-1})	Nebular Expansion Velocity (km s^{-1})	LSR RV of Na I Components (km s^{-1})	D^{method} (kpc)	D (IR Flux) (kpc)
M 4–18 (UES)	-50.8±1.0	20±1	–	–	–
M 4–18 (IDS)	-45.3±5.0	–	–	9.5[a]	–
SwSt 1(UCLES)	-8.1±1.0	21±2	-78,-38,+8	4.3–5.5[b]	3.96

[a]Distance derived from scaling the optical and UV flux of M 4–18 to He 2–113

[b]Distance derived from Na I D positive line components

Table 8.2: Wide–slit (8") fluxes (ergs cm^{-2} s^{-1}) measured for the nebular hydrogen lines of M 4–18, compared with values from the literature

Line	WHT–UES (1996)	INT–IDS (1996)	GD85	SR95	Carrasco et al. (1983)
Hα	–	2.69×10^{-12}	8.10×10^{-12}	4.85×10^{-12}	–
Hβ	6.61×10^{-13}	5.54×10^{-13}	1.04×10^{-12}	–	1.70×10^{-12}
Hγ	2.30×10^{-13}	–	4.10×10^{-13}	–	–
Hδ	–	–	4.50×10^{-13}	–	–

GD85 = Goodrich and Dahari (1985)

SR95 = Surendiranath and Rao (1995)

Table 8.3: Wide–slit (5") fluxes (ergs cm^{-2} s^{-1}) measured for the nebular hydrogen lines of SwSt 1, compared with values from the literature

Line	AAT–UCLES (1993)	Perek (1971)	FGC84	dFV87
Hβ	3.19×10^{-11}	1.66×10^{-11}	2.14×10^{-11}	1.82×10^{-11}
Hγ	1.20×10^{-11}	–	7.24×10^{-12}	–
Hδ	6.53×10^{-12}	–	–	–

FGC84 = Flower, Goharji and Cohen (1984)

dFV87 = de Freitas Pacheco and Veliz (1987)

Table 8.4: Reddenings for M 4–18 derived from Balmer lines ratios and from the radio–Hβ baseline method. In bold font are the values adopted by different authors

Ratio	E(B–V) INT (1996)	E(B–V) UES (1996)	E(B–V) GD85	E(B–V) SR95	E(B–V) CCS83
Hα/Hβ	**0.45**	–	**0.90**	–	–
Hβ/Hγ	–	0.61	0.41[a]	–	–
radio/Hβ	0.74	0.70	0.48	**0.48**	0.46[b]

GD85 = Goodrich and Dahari (1985)
SR95 = Surendiranath and Rao (1995)
CCS83 = Carrasco, Costero and Serrano (1983)
[a] Derived by us using their Hβ and Hγ fluxes
[b] Derived by us using their Hβ flux

Table 8.5: Reddenings derived from Balmer lines ratios and from the radio–Hβ baseline for SwSt 1. In bold font are the values adopted by the different authors

Ratio	E(B–V) AAT (1993)	E(B–V) FGC84	E(B–V) dFP87	E(B–V) P71
Hα/Hβ	–			
Hβ/Hγ	**0.51**[a]			
Hβ/Hδ	**0.41**[a]			
radio/Hβ	0.30	**0.34**	**0.41**	0.50[b]

FGC84 = Flower, Goharji and Cohen 1984
GD85 = Goodrich and Dahari 1985
dFV87 = de Freitas Pacheco and Veliz 1987
P71 = Perek 1971
[a] We adopted 0.45, the average of 0.51 and 0.41
[b] Derived by us using his Hβ flux

Tables 8.4 and 8.5 we list our results together with reddenings selected from the literature for comparison.

8.4.1 M 4–18

Our value for the Hβ flux, obtained from a wide–slit INT–IDS spectrum, is lower than the photometry by Carrasco Serrano and Costero (1983) , indicating that although the 5" slit should have included all the nebula, the poor seeing (ranging between 5" and 8") might have contributed to losing some nebular flux. The Hβ flux obtained from the WHT–UES spectrum cannot be considered absolute since the slit width was selected to maximise resolution and was only wide enough to include all the stellar flux (the seeing was 1"–2" during the night). The reddening derived from the Hα–Hβ baseline is E(B–V)=0.45. The radio flux of M 4–18 was measured by Aaquist and Kwok (1990) to be 22 mJy at 5 GHz and by Zijlstra, Pottasch and Bignell (1989) to be 15 mJy at 15 GHz (which would correspond to a 5 GHz flux of 17.3 mJy for optically thin free–free emission). If the photoelectric flux of Carrasco et al. is compared to the more recent radio flux of Aaquist and Kwok, we obtain E(B–V)=0.46 lending support to our Hα/Hβ estimate of 0.45 for E(B–V). This value also rectified the 2200 Å UV feature successfully in the IUE spectrum. We therefore adopt a value of E(B–V)=0.45 for the reddening towards M 4–18.

8.4.2 SwSt 1

For SwSt 1, considerable discrepancy exists between the Hβ flux measured for this thesis and those found in the literature. In Table 8.3 we see that our own value is about one third higher then the other values, although Acker, Stenholm and Tylenda (1989) measured an even higher Hβ flux (5.89×10^{-11} erg cm^{-2} s^{-1}). The possibility of a true variation in time was therefore investigated (since we recall the variability of the visual photometry, and since changes in the stellar and nebular emission lines were noticed between 1940 and 1969 (Carlson and Henize 1979), see also Section 8.9), but as no clear trend exists in either the Hβ fluxes or in the radio flux measurements we attribute the differences to calibration

and measurement errors.

From the Hβ–Hγ baseline in our UCLES 5" wide–slit spectrum, we determine E(B–V)=0.51, while from the Hβ–Hδ baseline we find E(B–V)=0.41. For SwSt 1, radio fluxes at 15 GHz have been measured by Kwok et al. (1981; 207 ± 11 mJy), Milne and Aller (1982; 240 ± 12 mJy) and Aaquist and Kwok (1990; 175 ± 17 mJy). The weighted average (211 ±17 mJy) corresponds to a 5 GHz flux of 243.0 mJy for optically thin free–free emission, which we adopted, together with our UCLES value for the Hβ flux, to derive E(B–V)=0.30. Comparison of the Perek (1971) photoelectric flux with this mean radio flux yields E(B–V)=0.50. We finally adopt E(B–V)=0.46, the mean obtained from the Hβ/Hγ and Hβ/Hδ ratios. This value is in good agreement with the radio determination of 0.50 for E(B–V) quoted above and, if applied to the UV spectrum, succeeded in smoothing the 2200 Å feature.

8.5 Luminosities and Distances

8.5.1 Distances from a Magellanic Cloud Luminosity Calibration

As already described in Chapter 5, Magellanic Cloud Wolf–Rayet central stars have been used to derive a mean central star mass for WC central stars of 0.62 $M_{\odot}$. This mass was then applied to derive luminosities for CPD–56°8032 and He 2–113 corresponding to their effective temperatures, which were in turn used, together with their integrated IR fluxes, to determine their distances. The PN of SwSt 1, with a high electron density, a small apparent radius and a significant IR excess was thought to be a good candidate to apply the same method. On the other hand, for the low electron density PN around M 4–18, the low IRAS fluxes (see Table 8.6) were believed to be an indication that the stellar luminosity was not entirely re-radiated in the infrared. Integration of the SwSt 1 fluxes between 1 μm and 100 μm (Table 8.6) resulted in a flux of 9.41×10^{-16} W cm^{-2} corresponding to an infrared bolometric luminosity of 290 D^2 $L_{\odot}$.

The predicted luminosity for CPD–56°8032 and He 2–113 was calculated to be 5100

Table 8.6: JHK and colour–corrected IRAS fluxes for M 4–18 and SwSt 1

Band	Wavelength (μm)	M 4–18 (erg cm^{-1} Å^{-1})	SwSt 1 (erg cm^{-1} Å^{-1})
J	1.25	–	7.59×10^{-14}
H	1.65	–	4.58×10^{-14}
K	2.2	–	7.59×10^{-15}
	12.0	9.41×10^{-16}	3.90×10^{-15}
	25.0	4.19×10^{-15}	3.19×10^{-14}
	60.0	2.92×10^{-16}	1.43×10^{-15}
	100.0	6.00×10^{-17}	1.56×10^{-19}

$L_\odot$ for effective temperatures of about 30 000 K. The higher excitation of the spectrum of SwSt 1 (Chapter 4) leads us to believe that its effective temperature should be higher. There are no models of this peculiar object, although its classification as a [WC9pec] (Chapter 4) would confine its temperature between 40 000 K and 50 000 K. We therefore adopt a temperature of 45 000 K, as obtained by Leuenhagen et al. (1996) for the [WC9] central star of He 2–99. For this temperature the helium–burning tracks of Vassiliadis and Wood (1994) predict a luminosity of 4600 $L_\odot$, where we interpolated between the tracks for 0.600 $M_\odot$ and 0.634 $M_\odot$ cores. The distance obtained in this way is 4.0 kpc [1]. The error associated with this determination is estimated to be $\pm$0.2 kpc, although it is healthy to remember that it only takes into account measurement errors and errors in the choice of temperature. It does not however take into account uncertainties associated with the key assumptions associated with this method.

8.5.2 Galactic Rotation Curve Distances

In the perpetual quest for a better distance estimate we applied the the sodium D line method described in Chapter 5 to the spectrum of SwSt 1. For M 4–18 the high resolution UES spectrum stops short of the Na D lines' wavelengths and the INT spectrum's

[1] If the luminosity of 5100 $L_\odot$ determined for CPD–56°8032 and He 2–113 is adopted for SwSt 1 a distance of 4.2 kpc is derived, showing the error associated with the temperature determination not to be large.

resolution is not sufficient to apply the method. Unluckily, while for M 4–18 the rotation curve is such that it would allow one to determine the distance to quite a good accuracy (i.e. likely errors in the determination of the radial velocity of the Na D line components only lead to small differences in the derived distance), for SwSt 1 this is not the case.

In Fig. 8.4(a) we show the spectral range containing the NaD lines, while in Fig. 8.4(c) we show Na D1 and D2 lines in their respective LSR rest frames. From Fig. 8.4(b) and (c) we see that the line of sight to SwSt 1 has a positive rotation curve, while most of the Na D line components have negative radial shifts. The underlying stellar emission lines (which were rectified away in the case of CPD–56°8032 and He 2–113) are much weaker than for CPD–56°8032 and He 2–113 and could not be rectified efficiently. Moreover we note the possibility of the Na I D lines having emission components (as already noticed by Dinerstein, Sneden and Uglum 1995): the stellar lines present in the range are C II $\lambda\lambda$5889,92, C III λ5894 and He II λ5897. The C III line is undoubtedly the most prominent. However the 'spike' of emission on the red side of the D2 absorption feature is taller than the peak of the C III emission, suggesting that, if due to the stellar C II line, such line would be stronger than C III λ5894. This is in disagreement with the rest of the spectrum where lines of C III dominate over C II (see Appendix E). In a similar manner, the emission 'spike' on the red side of the D1 absorption does nor conform with deriving either from the wing of the C III stellar line nor with the presence of the He II. Additionally both the D1 and D2 emission 'spikes' are centered at their heliocentric rest wavelengths. Due to the stellar lines and the possibility of Na emission components, we felt that in the case of SwSt 1 a multiple cloud fit would have over-interpreted the data and we limited ourselves to measuring the centers of the absorption components. The radial velocities of the troughs are measured to be -78 ± 5 km s^{-1}, -38 ± 2 km s^{-1} and $+8\pm2$ km s^{-1} (although this last component is not as well defined as the previous two and the measurement of its position is jeopardised by the possibility of circumstellar sodium emission described above). The only interstellar component is likely to be the one with positive velocity (see Fig. 8.4(c)). It corresponds to a distance of 4.9 ± 0.6 kpc, where the indicated uncertainty

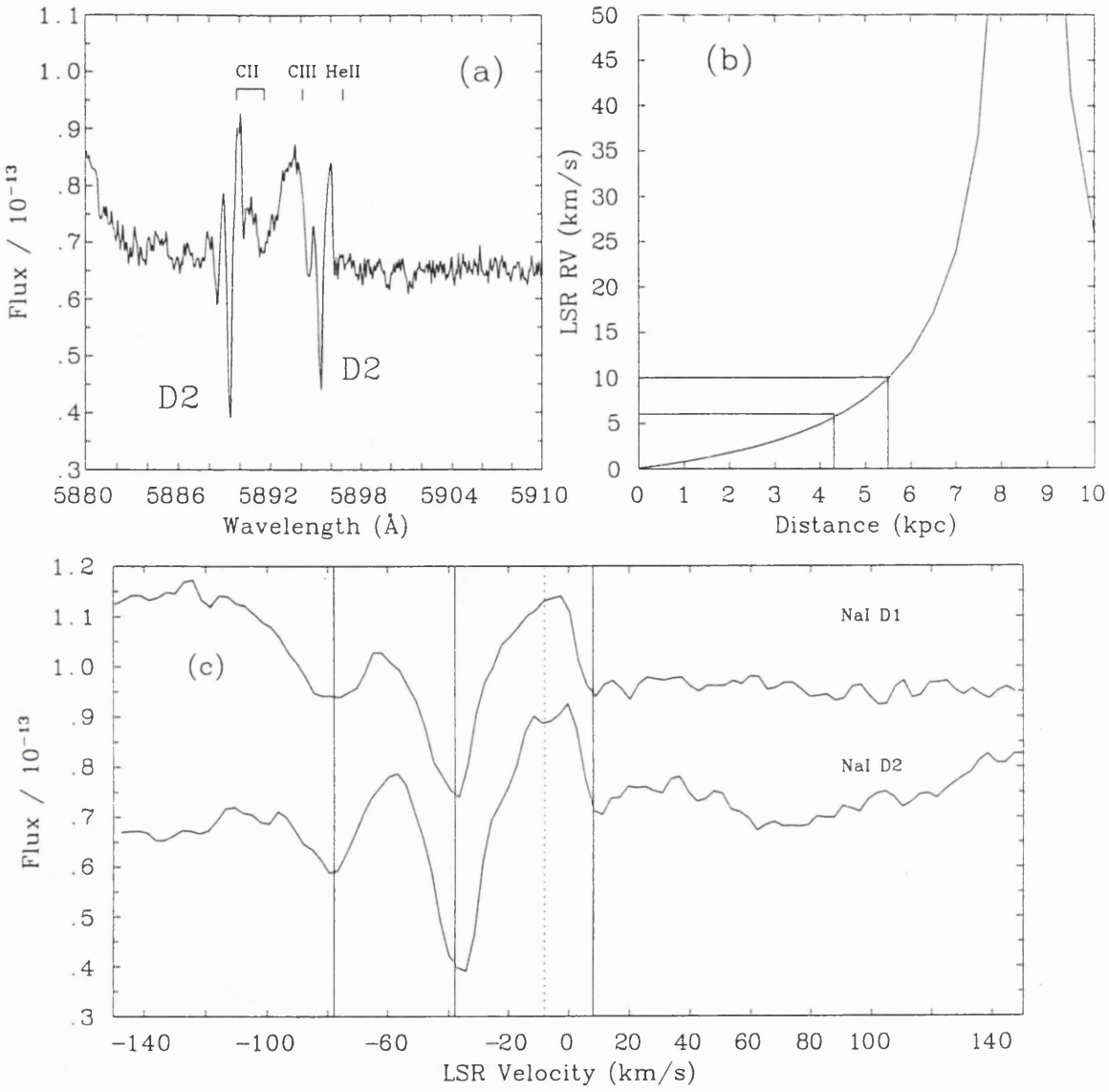

Figure 8.4: (a) The sodium D lines towards SwSt 1 (where the wavelength scale has been corrected for a heliocentric radial velocity of −17.8 km s^{-1} and where we have indicated the positions of C II Multiplet 5, C III Multiplet 20 and the He II λ5896.8 line. (b) The rotation curve for the direction of SwSt 1. The distances corresponding to LSR radial velocities of +6 and +10 km s^{-1} are 4.3 and 5.5 kpc. (c) The sodium D lines displayed in their LSR rest frame. The D1 line (lower) has its original flux units, while the D2 line has been displaced upwards by an additive factor of 3×10^{-14}. The dotted line marks the LSR radial velocity of the nebula, while the solid lines show the position of the three most prominent Na I absorption components

derives solely from locating the center of the trough, but does not take into account that the position the trough itself might not be reliable due to the stellar and Na emission lines. We therefore feel that this estimate cannot be considered reliable.

As already pointed out in Chapter 5, sodium is present in the envelope of the PN and can be a good tracer of velocity components. Our own measurements of the radial velocity components for the Na D lines of SwSt 1 are drawn as solid vertical lines in Fig. 8.4(c) along with the LSR radial velocity of the star. If corrected for the heliocentric radial velocity the emission lines lie at 0±4 km s^{-1}, while the two troughs are measured to be at −70±2 and −28±2 km s^{-1}. The nebular expansion velocity determined from half of the FWHM of the Balmer lines is 20 (± 1) km s^{-1}. Hence we would expect absorption components of the Na D lines associated with the nebular material to be found at a heliocentric radial velocity of about −20 km s^{-1}. The trough of the first component is at about −28 km s^{-1}, 8 km s^{-1} more negative than expected, although this discrepancy can be almost justified by the relative uncertainties. The component at −70 km s^{-1} has then to be explained by assuming that SwSt 1's PN has a velocity component moving at a higher velocity then the 'shell' measured by the Balmer lines. In the case of CPD−56°8032 and He 2−113 we had noticed a correspondence between the high velocity components of the Na D line troughs and the shape of the emission lines of [O I]. The same comparison in SwSt 1 reveals that fitting the [O I] lines with a double Gaussian (of which one is kept at a FWHM=40 km s^{-1}) cannot identify components with FWHM larger than 60 km s^{-1}. This would explain a Na D line component at about −30 km s^{-1} (like the observed component at −28 km s^{-1}) but not the trough at −70 km s^{-1}. So, in conclusion, the absorbing sodium must be associated with a different part of the nebula from the collisionally excited neutral oxygen.

Dinerstein, Sneden and Uglum (1995) also found evidence for circumstellar as well as interstellar components towards SwSt 1. They measured the emission component of the Na D lines to be at −7 km s^{-1}, while they determined the absorption component to be at −27 km s^{-1} (where their measurements are corrected for a heliocentric radial velocity of −20 km s^{-1}). These correspond within the uncertainties to our emission component at 0

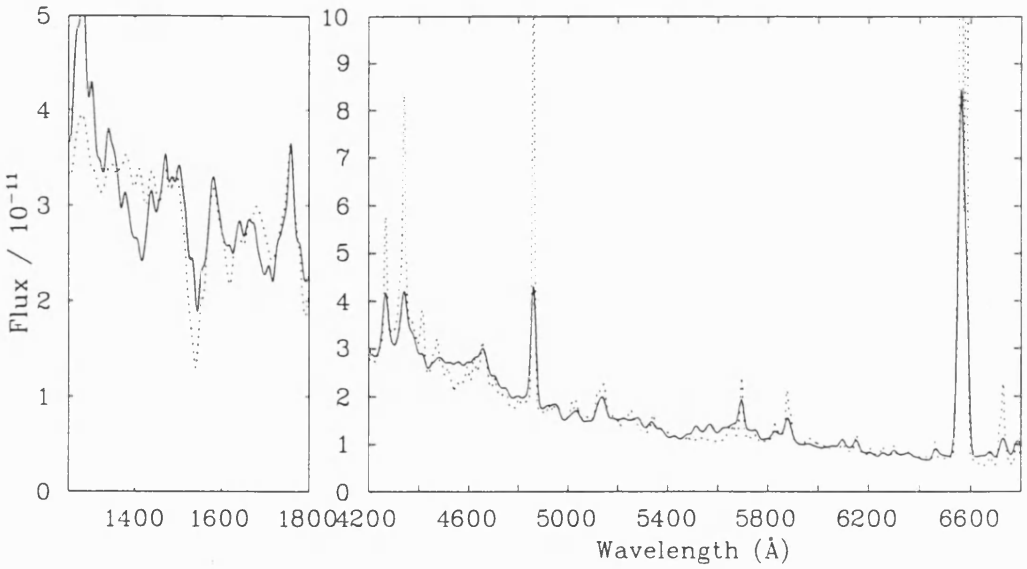

Figure 8.5: Comparison of the optical and UV spectra of He 2–113 (solid line) and M 4–18 (multiplied by 40, dotted line)

km s^{-1} and absorption component at –28 km s^{-1}. They do not find a double absorption as we do, and indeed their Fig. 2 is significantly different from our Fig. 8.4 (a), although their claimed resolution (0.20 Å) is similar to our own. It is not possible at present to compare the two spectra in order to resolve this discrepancy. Dinerstein at al. (1995) do not give particular importance to the high velocity Na D line absorption components found within their sample of 21 PN, which they attribute in most cases to measurement effects. However they do mention the possibility of the existence of higher velocity components in the PN envelope and they compare this effect to the fast low ionization outflows (FLIERs) described by Balick (1993, 1994).

8.5.3 The Distance to M 4–18

To obtain a distance to M 4–18 we scaled the apparent stellar V magnitude to the value obtained for He 2–113. In Fig. 8.5 we plot selected wavelength regions of the UV and optical dereddened spectrum of M 4–18 (for E(B–V)=0.46), multiplied by 40, along with the dereddened spectrum of He 2–113 (for E(B–V)=1.00). As can be seen, the two spectra

are almost identical between 1200 and 6800 Å. It was felt that this lends support to the similar nature of the two objects and reinforces the belief that the difference in the observed magnitudes is due to a difference in reddening and distance. From this scaling, M 4–18 would be 6.3 times further than He 2–113, positioning it at 9.5 kpc.

Before proceeding we would like to point out that it is feasible to have a star at 1.5 kpc with 3.1 mag of extinction (He 2–113), and another star at about 10 kpc with only 1.4 mag of extinction (M 4–18). In fact M 4–18 has l=146° and b=+7°. At 10 kpc and with an ISM scale height of ~200 pc (Chapter 5) we see that the sightline to M 4–18 only crosses about 1.6 kpc of ISM. For 0.6 mag of extinction per kpc (Whittet 1992, p. 11) it is not unfeasible that M 4–18 has only A_v=1.4.

Surendiranath and Rao (1995) adopt a distance of 1 kpc, mainly based on a relationship between the dust temperature and the PN radius (Pottasch et al. 1984). A literature search on the distance to M 4–18 reveals that most estimates position M 4–18 between 4 and 7 kpc. Moreover if we adopt for M 4–18 the same bolometric luminosity (L=5100$L_\odot$) and bolometric correction (BC=–2.8) as for He 2–113, at a distance of 10 kpc and with a reddening of 1.4 mag, we obtain a predicted apparent magnitude of 14.43 mag, not dissimilar from the magnitude of 14.11 derived in Section 8.1. The same reasoning based on the observed dereddened V magnitude and the distance of 1 kpc adopted by Surendiranath and Rao (1995) results in M 4–18 having L=72 $L_\odot$, making it a very different star from He 2–113. Even adopting M=0.54 $M_\odot$ and T_{eff}=23 000 K (Surendiranath and Rao 1995), the helium–burning tracks of Vassiliadis and Wood (1994) indicate a luminosity of 3000 $L_\odot$ (Surendiranath and Rao used the tracks of Schönberner and Weidemann (1981); however no post–AGB track to our knowledge predicts luminosities as low as 100 $L_\odot$). Lastly, a distance of 1 kpc and an optical radius of 2" would imply a very compact and young nebula, leaving us with the problem of justifying an electron density as low as 6300 cm^{-3} (cf. N_e(He 2–113)=63 100 cm^{-3}, Chapter 5).

8.6 Nebular Abundance Analysis

Spectroscopy of the PN around M 4–18 was carried out by Goodrich and Dahari (1985) and by Surendiranath and Rao (1995). Before 1985 the only existing analysis of this nebula had been carried out by Sabbadin (1980) who, with a 15 Å resolution spectrum, had derived a reddening constant of E(B–V)=0.7 from the Balmer decrement. Goodrich and Dahari applied low resolution spectroscopy (6 and 13 Å), together with IUE images from the archive, to the determination of the PN physical conditions and abundances. Surendiranath and Rao also carried out a nebular abundance analysis. The latter, moreover, applied their own nebular modelling code (incorporating provision for dust) to M 4–18 using optical and UV (IUE) spectra.

Previous analyses of SwSt 1's nebula were carried out by Flower, Goharji and Cohen (1984) on IUE observations and by de Freitas Pacheco and Veliz (1987), who determined conditions in the PN from their optical spectroscopy.

8.6.1 Nebular Line Fluxes

8.6.1.1 M 4–18

Our own analysis of the nebula around M 4–18 is entirely based on our INT spectrum (1.4 Å resolution in the range 3700–6800 Å). For this object the nebular spectrum is much stronger (relative to the star) than either the nebular spectra of CPD–56°8032 or He 2–113. However, due to the lower resolution of our INT spectrum, the stellar and nebular spectra are nonetheless heavily blended. For larger nebulae, long–slit spectroscopy gives the option of extracting the nebular spectrum off the star, however with a seeing of about 3" (at the time of the observations M 4–18 was rising at the end of the night which contributed to the poor seeing) and a nebular diameter of less then 4" (see Section 8.7.1), M 4–18 could not be treated in this way.

To determine the abundance of oxygen (as well as their use as a density diagnostic) we used the [O II] lines at 3726 and 3729 Å. As was the case for CPD–56°8032 and He 2–113,

they were blended with stellar lines, although this time we felt that contamination from the stellar O II M2 components was not significant (as the unblended components of M2 were particularly weak). However this doublet did reside at the end of our spectral range, where the sensitivity of the instrument drops sharply and the continuum did present 'wiggles'. We therefore assign a 30% error to our measurements. Neither Goodrich and Dahari nor Surendiranath and Rao noted the presence of [O III] in the spectrum of M 4–18. However inspection of our 4900–5100 Å region reveals that both the [OIII] lines at 5007 and 4959 Å are present[2]. A very weak λ5007 line is also noticed in the spectra of CPD–56°8032 and He 2–113.

If we believe the C III] λ1909 line to be entirely of stellar origin (as was the case for He 2–113, the spectroscopic twin of M 4–18), then the only transition from which to derive the nebular carbon abundance is the C II] λ2326 feature (a log of the IUE observations of M 4–18 is presented in Table 8.9). As can be seen from Fig. 8.6, this line is very weak indeed. Its equivalent width can be estimated to lie between 11 and 19 Å. We carried out the measurement on the dereddened IUE spectrum (whose 2200 Å feature is, as we have pointed out in Section 8.4.1, completely flattened by the adopted dereddening) and we feel confident that the value for the equivalent width can be gauged to be 15±4 Å. The model of the stellar spectrum of He 2–113 (Chapter 6) predicted the equivalent width of the stellar component of λ2326 feature to be 5 Å. Given the extreme similarity of the stellar spectra of these two objects we felt it appropriate to adopt this value for M 4–18. We therefore proceeded to subtract the stellar model's equivalent width from the measured one, finally obtaining a value of 10±4 Å for the nebular part of the λ2326 line.

The flux in the line was then obtained in two different ways. In the first instance we multiplied the nebular λ2326 line's equivalent width by the IUE dereddened continuum flux at 2326 Å (2.5×10^{-13} ergs cm^{-2} s^{-1} Å^{-1}). In the second instance we scaled He 2–

[2]The [OIII] line at 4959 Å is heavily blended with C II stellar components (i.e. the four components of the dielectronic Multiplet 25), but as we have fitted this region (see Chapter 7) it was easy to recognise its presence.

113's model continuum flux to M 4–18's dereddened continuum 5500 Å flux from our INT spectrum (2.58×10^{-14} ergs cm^{-2} s^{-1} Å^{-1}). We then measured the continuum level of the scaled model at 2326 Å to be 4.38×10^{-13} ergs cm^{-2} s^{-1} Å^{-1} and multiplied this by the nebular equivalent width, obtaining a flux for the nebular λ2326 line of 4.38×10^{-12} ergs cm^{-2} s^{-1} [3].

For sulphur the only lines that could be used were the [S II] $\lambda\lambda$6713,31 lines. The [S III] λ3722 line is blended with the [O II] $\lambda\lambda$3726,29 lines and the $\lambda\lambda$9069,9532 lines were outside our range. Only Surendiranath and Rao (1995) derived the abundance of S^{2+}/H^+ (see Section 8.6.2.1), although they did not explicitly state their flux measurement for $\lambda\lambda$9069,9532. For nitrogen we used the lines 5755 and 6548 Å, excluding the [N II] λ6584 line which is blended with the stellar C II line at 6578 Å.

8.6.1.2 SwSt 1

The strong nebular spectrum of SwSt 1 and the high resolution of our UCLES spectroscopy made it a pleasure to measure its nebular line fluxes! The nebular spectrum of SwSt 1 is much richer than the spectrum of any of the previously analysed late–WC PN. Stellar wind He I lines are observed, along with recombination lines of C^{2+}, O^+, Si^{2+} and Si^{3+}. Besides the lines we measured (listed in Table 8.8) we identify forbidden lines of Fe^+ (e.g. [Fe II] λ4606), Fe^{2+} (e.g. [Fe III] λ4881) and possibly Fe^{3+} (e.g. [Fe IV] λ5677). We also identify [Ne III] λ3868, [Ar III] λ5191,7136,7751 and [Cl III] $\lambda\lambda$5517,5537. A line list is presented in Appendix E.

Many nebular He I lines could be measured in the spectrum of SwSt 1. Amongst them we selected the ones at 4471.5, 5875.7, 6678.1 and 7065.2 Å. We later disregarded the line at 7065.2 Å due to its being mainly dominated by collisions and to the possibility of it being affected by telluric absorption. The [O II] line complex at 7325 Å is made up of 4 lines with wavelengths 7318.8, 7319.9, 7329.6, and 7330.6 Å. While in the spectra of

[3]The same procedure could be adopted by scaling the model to the dereddened continuum V flux of our UES spectrum (6.64×10^{-13} ergs cm^{-2} s^{-1} Å^{-1}), but as the conditions on the night of observation were not necessarily photometric we decided not to use this method.

CPD–56°8032 and He 2–113 the components form two compact blends at 7319 and 7330 Å, in the spectrum of SwSt 1 the individual components are blended but distinguishable. Unfortunately, the blend at 7319 Å was affected by an echelle order join which removed a part of the flux. In order to obtain a measurement of the flux in those lines we therefore snipped the section containing the join. The snipped line, despite missing the central part, still had clearly identifiable wings and could therefore be successfully fitted with ELF. We nonetheless decided to assign a 50% uncertainty to it and did not use it in any of the parameters determinations. The [O II] lines at 3726 and 3729 Å are resolved and completely unblended with any stellar feature. [O III] λ5007 was saturated so we used instead the [O III] lines at 4959 and 4363 Å.

All four [S II] nebular lines included in our wavelength range could be measured, namely the lines at 4068.6, 4076.3, 6716.5 and 6730.8 Å. The line at 4068.6 Å was found to lie on an order join, however since abundance results obtained with it or with the weaker lines at 4076.3 Å were very similar, we decided to treat it normally and only assign it a marginally higher uncertainty. To determine the abundance of S^{2+}, we used the four lines included in our spectrum: λ6312.1 λ9068.9 and λ9531.0. The telluric water vapour line at 9069.126 Å might be affecting the measurement of the [S III] line at 9068.9 Å. This suspicion was reinforced by the fact that the [S III] λ9069/λ6312 and the λ9531/λ6312 ratios determined inconsistent electron temperature and density combinations, with the former yielding the more discrepant values.

Three lines of singly ionised nitrogen reside in our spectral range, but as the [N II] ratio λ6583/λ6548 was equal to 1.4, instead of 2.90, we decided that the strong λ6583 line was saturated (as was Hα) and did not include it in any of our determinations. Together with the λ6548 line we used [N II] λ5755.

To derive the nebular C/H ratio we used both the semi-forbidden C III] λ1909 and the C II] λ2326 lines from IUE observations (Table 8.9). We believe the stellar contribution to these two features to be negligible since this star has a much weaker spectrum than either CPD–56°8032 or He 2–113. We also decided to include both C^{+} and C^{2+}, due to

Table 8.7: Observed (F) and dereddened (I; E(B–V)=0.46) nebular line intensities for M 4–18 from the 1996 INT spectrum. The dereddened Hβ flux is 2.59×10^{-12} erg cm^{-2} s^{-1}. Errors are indicated. The spectral resolution of 1.4 Å did not allow a determination of the intrinsic FWHM of the nebular lines

Ion	λ (Å)	F (ergs cm^{-2} s^{-1})	100×I /I(Hβ)	Errors %
[O II]	3726.0	5.69×10^{-13}	145.5	30
[O II]	3728.8	3.01×10^{-13}	76.8	30
Hβ	4861.3	5.75×10^{-13}	100	10
[N II]	5754.6	1.11×10^{-14}	1.4	10
[O I]	6300.3	2.15×10^{-14}	2.4	10
[O I]	6363.8	9.73×10^{-15}	1.1	10
[N II]	6548.0	4.44×10^{-13}	47.9	10
Hα	6562.8	2.70×10^{-12}	289.5	10
[N II]	6583.4	1.54×10^{-12}	164.4	20
[S II]	6716.5	7.19×10^{-14}	7.4	10
[S II]	6730.8	1.41×10^{-13}	14.6	20

the higher ionization nature of this PN. The UV IUE spectrum is displayed in Fig. 8.6.

8.6.2 Nebular Temperatures, Densities and Abundances

8.6.2.1 M 4–18

From Fig. 8.7 we determine log(N_e)=3.7 and T_e=8200 K for M 4–18. The electron density is adopted as a compromise between log(N_e)=3.5 as given by the [O II] doublet and log(N_e)=3.9 as given by the [S II] doublet. Goodrich and Dahari (1985) derived T_e=5600±1600 K and log(N_e)=4.0±0.1, while Sabbadin (1980) obtained T_e=8500 K from the [N II] lines. Surendiranath and Rao obtain log(N_e)=3.9 and T_e=8500 K from their spectroscopy, while from their nebular modelling they obtained log(N_e)=3.8 and T_e=6600 K (we will discuss their model in Section 8.8).

We observe that Surendiranath and Rao's (1995) abundance of S^{++}/H^+ is about one order of magnitude lower than their abundance of S^+/H^+. Our S^+/H^+ ratio should there-

Table 8.8: Observed (F) and dereddened (I; E(B–V)=0.45) nebular line intensities for SwSt 1 from the 1993 UCLES spectrum. The dereddened Hβ flux is 1.50×10^{-10} erg cm^{-2} s^{-1}. Errors are gauged at 10%. The lines' rest wavelengths are from Kaufman and Sugar 1986. The spectral resolution is indicated at the beginning of every section

Ion	λ_o (Å)	FWHM (km s^{-1})	F (ergs cm^{-2} s^{-1})	100×I /I(Hβ)
		Δv~900 km s^{-1}		
C II]	2326	–	1.28×10^{-10}	85.3
C III]	1909	–	1.06×10^{-10}	70.6
		Δv~30 km s^{-1}		
[O II]	3726.0	44	6.51×10^{-12}	30.00
[O II]	3728.8	46	2.55×10^{-12}	11.73
[S II]	4068.6	41	5.23×10^{-13}	2.17
[S II]	4076.3	41	2.05×10^{-13}	0.85
		Δv~10 km s^{-1}		
Hδ	4101.7	44	6.20×10^{-12}	24.7
Hγ	4340.5	41	1.19×10^{-11}	44.87
[O III]	4363.2	31	7.11×10^{-14}	0.27
He I	4471.5	38	6.96×10^{-13}	2.50
Hβ	4861.3	41	3.22×10^{-11}	100.00
[O III]	4958.9	34	3.80×10^{-12}	11.40
[O III]	5006.8	33	1.01×10^{-11}	29.53
[N I]	5197.9	77	4.80×10^{-14}	0.13
[N I]	5200.2	73	2.91×10^{-14}	0.08
		Δv~30 km s^{-1}		
[O I]	5577.3	30	7.83×10^{-14}	0.19
[N II]	5754.6	28	1.42×10^{-12}	3.26
He I	5875.7	42	3.17×10^{-12}	7.07
[O I]	6300.3	49	7.43×10^{-13}	1.49
[S III]	6312.1	39	1.30×10^{-12}	2.61
[O I]	6363	49	2.45×10^{-13}	0.49
[N II]	6548.0	46	1.64×10^{-11}	31.13
He I	6678.1	39	9.26×10^{-13}	1.71
[S II]	6716.5	62	3.91×10^{-13}	0.72
[S II]	6730.8	55	7.92×10^{-13}	1.45
He I	7065.2	39	2.11×10^{-12}	3.61
[O II]	7318.6	–	3.96×10^{-12}:	6.45
[O II]	7319.4	–	4.35×10^{-11}:	70.67
[O II]	7329.6	33	8.36×10^{-12}	13.60
[O II]	7330.7	35	8.62×10^{-12}	14.00
[S III]	9068.9	34	2.00×10^{-11}	25.27
[S III]	9531.0	38	7.53×10^{-11}	90.67

Table 8.9: Log of the IUE observations of M 4–18 and SwSt 1 used to measure the intensities of the C II] λ2326 and C III] λ1909 lines

Star	Frame	Exposure Time (min)
M 4–18	LWR21064L	166
	LWR8402L	166
	SWP42313L	333
	SWP9659L	300
SwSt 1	LWR10077L	12
	LWR4804L	92
	SWP5565L	60

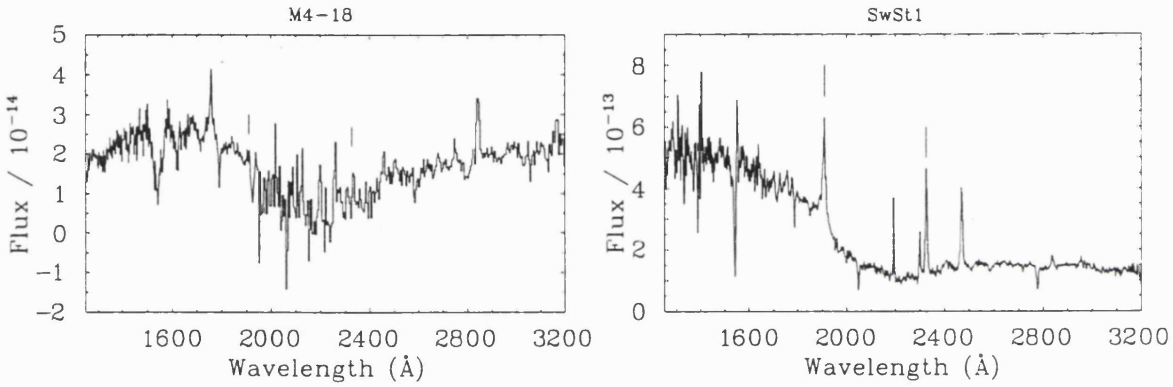

Figure 8.6: Observed IUE spectra of M 4–18 (left) and SwSt 1 (right). The positions of the 1909 Å C III] and 2326 Å C II] lines are marked by dashes

Table 8.10: Nebular logarithmic abundances (on a scale where log(N(H)=12.0), determined for M 4–18. The C/O number ratio is on a linear scale

Ratio	log(X/H)+12.0	Lines Used
C	8.90±0.03	C II] λ2326
N	7.65±0.04	[N II] $\lambda\lambda$6548,5755
O	8.59±0.01	[O II] $\lambda\lambda$3726,29
Ne	7.84±0.05	[Ne II] 12.8 μm[a]
S	6.21±0.06	[S II] $\lambda\lambda$6713,31
C/O	2.0±0.6	–

[a]line flux from Aitken and Roche 1982

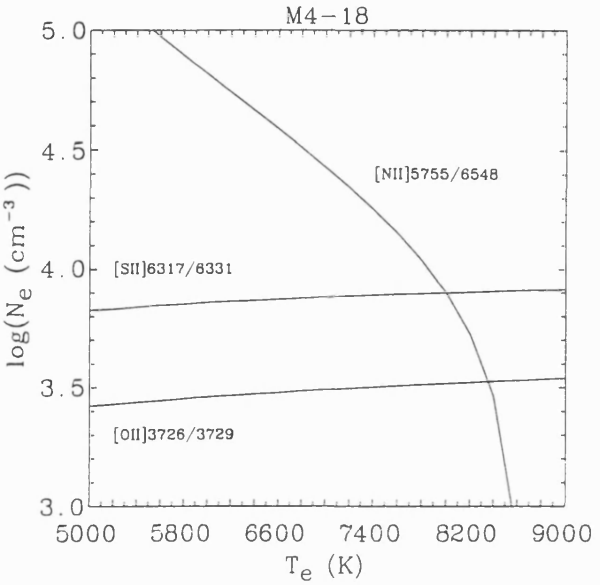

Figure 8.7: Diagnostic diagram, log(N_e) vs T_e, for M 4–18

fore be representative of S/H. For oxygen, nitrogen and carbon we believe the abundance of the singly ionised ions to be representative of the whole ionised populations since [O III] λ5007 and C III] 1909 are weak or absent.

We list the derived abundances in Table 8.10. Surendiranath and Rao (1995) derive abundances which agree with our own, apart from the case of oxygen, for which they derive a logarithmic abundance of 8.1 vs. our 8.59. Surendiranath and Rao used both the [O II] lines at 3727 *and* 7325 Å, the latter residing outside our range. However for the [O II] $\lambda\lambda$3727,29 lines we notice that we obtain dereddened fluxes almost 10 times higher than those of Surendiranath and Rao.

The abundances derived by Goodrich and Dahari (1985) are also in agreement with our own derived values once the different adopted reddening, electron temperature and density are taken into account. The C/O ratio derived by us for this PN (although affected by substantial uncertainty) is much lower then the ratios found for CPD–56°8032 and He 2–113 (Chapter 5).

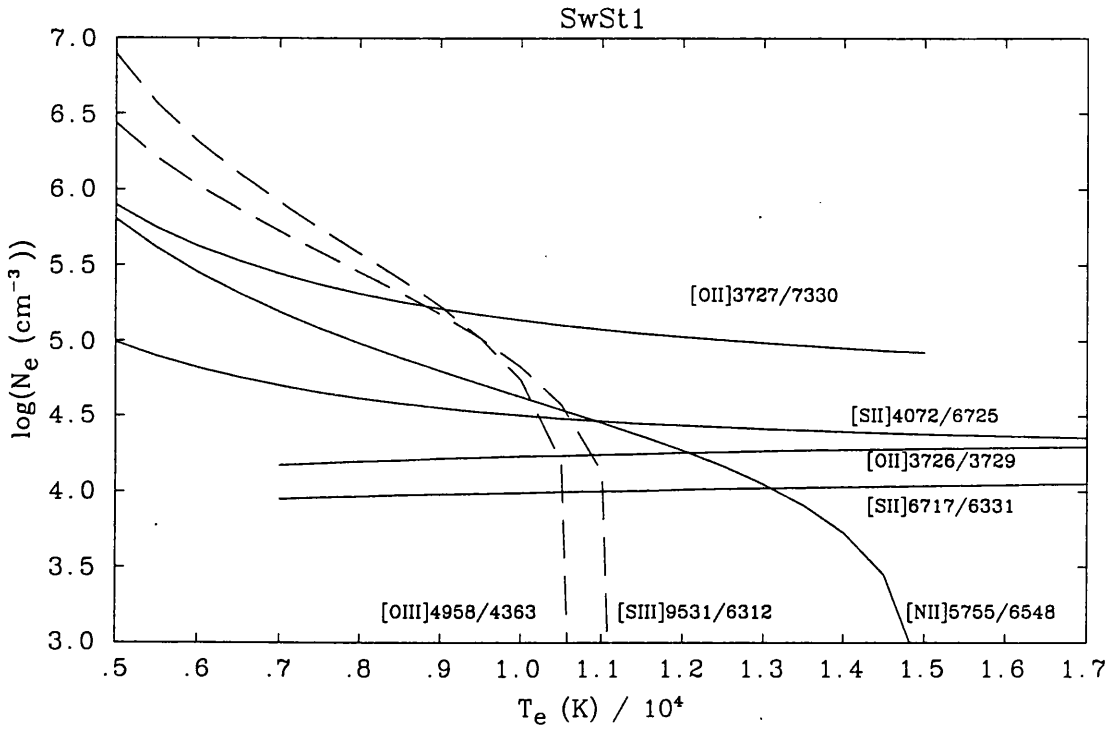

Figure 8.8: Diagnostic diagram, $\log(N_e)$ vs T_e, for SwSt 1. The solid lines are obtained from ratios of ions in the first stage of ionization, the dashed lines are for ions in the second ionization stage

8.6.2.2 SwSt 1

As can be seen from Fig. 8.8, different line ratios seem to yield different combinations of temperature and density for SwSt 1. The temperature–density combination derived from doubly ionised ions is 9600 K for $\log(N_e)= 5.0$ (we do not take into account the [S III] ratio $\lambda9069/\lambda6312$, for which $\lambda9069$ might be affected by water vapour lines).

Ratios of singly ionised elements seem to agree on a lower density ($4.0<\log(N_e)<4.5$), if we make an exception for the [O II] ratio $\lambda3727/\lambda7330$. This ratio uses lines from two different grating settings and therefore might be affected by errors in the flux calibration. However if this were the cause of the discrepancy we would also have to be wary of the [S III]$\lambda9531/\lambda6312$ ratio (which we have used above) and the [S II] $\lambda4068/\lambda6725$ ratios, although these employ the green and red settings and not the blue and red settings used by the [O II] $\lambda3727/\lambda7330$ ratio. From the three ratios, [O II] $\lambda3726/\lambda3729$, [S II] $\lambda6317/\lambda6731$ and [N II] $\lambda5755/\lambda6548$, one would have to choose T_e=12 500 K and $\log(N_e)$=4.2. SwSt 1 is a young and compact PN and we therefore feel unjustified in using different electron density and temperature combinations for the singly and doubly ionised regions, a choice that is more appropriate for more extended, higher ionization objects. We are therefore more inclined to attribute the scatter to measurement error and adopt mean values for the electron temperature and density of 10 500 K and 31 600 cm^{-3} ($\log(N_e)$=4.5), respectively. These are the values summarised in Table 8.11.

Flower, Goharji and Cohen (1984) derived $\log(N_e)$=5.0 for SwSt 1 from the C III] $\lambda1907/\lambda1909$ ratio, which they measured from their high resolution IUE spectroscopy. They also quoted an upper limit for the electron density of 2×10^4 cm^{-3}, derived from the [O II]$\lambda3729/\lambda3726$ ratio (which is almost identical to ours), however they argued that this ratio is too close to the high density limit to be reliable. Although their argument for adopting a high density does not seem incorrect, we cannot neglect the fact that so many of our diagnostic ratios are more consistent with a lower value of the density. Their temperature determination, using the [O III]$\lambda5007/\lambda4363$ ratio, was 8800 K (for E(B–V)=0.70), not inconsistent with our own value (although we employ a lower reddening,

Table 8.11: Nebular electron temperatures and densities adopted for SwSt 1 and M 4–18

Star	T_e (K)	$\log(N_e)$
M 4–18	8 200±200	3.7±0.2
SwSt 1	10 500± 500	4.5±0.2

the effect is not major over such a short baseline). However their determination using the [O III] λ5007/λ1663 ratio defines a higher electron temperature (15 000 K). If we ascribe the discrepancy to the fact of using two different spectra (IUE and optical) in the second determination, we can reconcile our own determinations of the temperature and density for the doubly ionised element with theirs.

de Freitas Pacheco and Veliz (1987) derived $\log(N_e)$=5.0 and T_e=11 400±500 for SwSt 1 from [S II]$\lambda\lambda$4068,76/$\lambda\lambda$6716,30, [O III]λ4363/(λ4959+λ5007) and [N II]λ5755/$\lambda\lambda$6548,84. Their diagnostic diagram is not inconsistent with our own.

Our derived abundances are listed in Table 8.12. The C/H number ratio of 2.51×10^{-4} is not particularly high (the mean PN value as determined by Kingsburgh and Barlow (1994) is 5.49×10^{-4}). However the C/O number ratio, at 0.98, is higher than previously determined (Flower Goharji and Cohen (1984) obtained 0.72, while de Freitas Pacheco and Veliz (1987) calculated 0.54). This number is very important as a C/O<1 would imply an oxygen–rich PN, very different from the majority of PN. To obtain the N/H number ratio we multiplied the N^+/H^+ ratio by a ionization correction factor of 1.05 obtained from the ration of the oxygen and the singly ionized oxygen abundances in accordance with the appendix Kingsburgh and Barlow (1994).

The different abundances derived by Flower, Goharji and Cohen (1984) and by de Freitas Pacheco and Veliz (1987) can be attributed to the different electron temperatures and densities adopted.

Table 8.12: Nebular abundances for SwSt 1, on a logarithmic scale where log(N(H)=12.0 for the elemental abundances and on a linear scale for the ionic and C/O ratios

Ratio	Abundance	Lines Used
He^+/H^+	0.044 ± 0.004	He I λλ4471,5876,6678,7065
C^+/H^+	1.21(-4)[a] ± 0.60(-4)	C II]λ2326
C^{2+}/H^+	1.30(-4) ± 0.64(-4)	C III]λ1909
C/H	8.40 ± 0.3	–
N^+/H^+	1.99(-5) ± 0.20(-5)	[S II]λλ5755,6548
N/H[b]	7.32 ± 0.1	–
O^+/H^+	2.44(-4) ± 0.24(-4)	[O II]λλ3726,3729,7330
O^{2+}/H^+	1.05(-5) ± 0.10(-5)	[O II]λ4959
O/H	8.41 ± 0.2	–
Ne/H	7.99 ± 0.05	[Ne II] 12.8 μm[c]
S^+/H^+	2.96(-7) ± 0.30(-7)	[S II]λλ6713,6731,4077,4069
S^{2+}/H^+	3.87(-6) ± 0.80(-6)	[S III]λλ6312,9072,9535
S/H	6.61 ± 0.1	–
C/O	0.98 ± 0.5	–

[a] $1.21(-4)=1.21\times10^{-4}$

[b] $ICF(N)=O/O^+=1.05$, $N/H=IFC(N)\times N^+/H^+$, following Kingsburgh and Barlow 1994

[c] line flux from Aitken and Roche 1982

Table 8.13: Log of the HST WF/PC exposures of M 4–18 and of the WF/PC2 exposures of SwSt 1 (SwSt 1, PI: Bobrowsky; M 4–18, PI: Sahai)

Exposure	Filter	Exposure Time (s)	Date
M 4–18			
u35t2401t	F656N	350	18/04/96
u35t2402t	F656N	350	18/04/96
SwSt 1			
w11s4l01t	F487N	3.5	14/02/93
w11s4m01t	F487N	3.5	18/02/93
w11s4n01t	F502N	12.0	18/02/93
w11s4o01t	F502N	12.0	18/02/93

8.7 Images of M 4–18 and SwSt 1

8.7.1 The Nebula around M 4–18

The M 4–18 nebula, with an optical diameter of 4" (Shaw 1985) and a radio diameter of 4" (Zijlstra et al. 1989), is reproduced below (from the IAC catalogue of northern sky PN, with permission of one of the authors [M. Guerrero]; see Fig. 8.9). The images were obtained with the 2.5 m Nordic Optical Telescope (La Palma); the CCD camera (1024x1024 pix^2) had a pixel size of 0.139". From the Hα image (Fig. 8.9, top panel) we measure a nebular diameter of 3.0"$\pm$0.5". From a comparison of the Hα and [N II] images (the 10 Å–bandpass filters were centered at 6562 and 6583 Å respectively), we note the the central star seems to be brighter in [N II] than in Hα. This is probably caused by the fact that while at Hα we only observe the stellar continuum, at 6583 Å we observe stellar emission in the strong C II line at 6578 Å. This difference is reflected in the contours of the normalised images (where we normalised to the peak stellar intensity), where we see that the contours gather closer to the center in the [N II] picture. As to the [O III] image (Fig. 8.9, bottom panel; the filter central wavelength is 5007 Å), although the emission might appear extended, its FWHM is 0.7", the same as measured by the authors for field stars. We therefore conclude (also recollecting the very weak [O III] $\lambda\lambda$5007,4959 lines) that the observed emission in the 5007 Å filter is caused by the stellar continuum.

The post–COSTAR WFPC2 Hα image from the HST archive did not need to be deconvolved. At 0.043"/pix the resolution of the image is 0.1". It shows a clear elongated ring (see Fig. 8.10) which peaks in intensity 1.28" north and south of the star and 0.8" east and west. The ring is embedded in a slightly larger more spherical shell with angular diameter of 3.2" ($\pm$0.20"), only marginally smaller than the Shaw (1985) optical image and the Zijlstra et al. (1989) radio image, and in good agreement with the 10 μm image of Dayal and Bieging 1996. This PN is suggestive of those morphologies that form as a result of a denser torus of material formed during the AGB, before the PN was ejected (the reason for asymmetric mass loss is not clear although it has been proposed that rotation

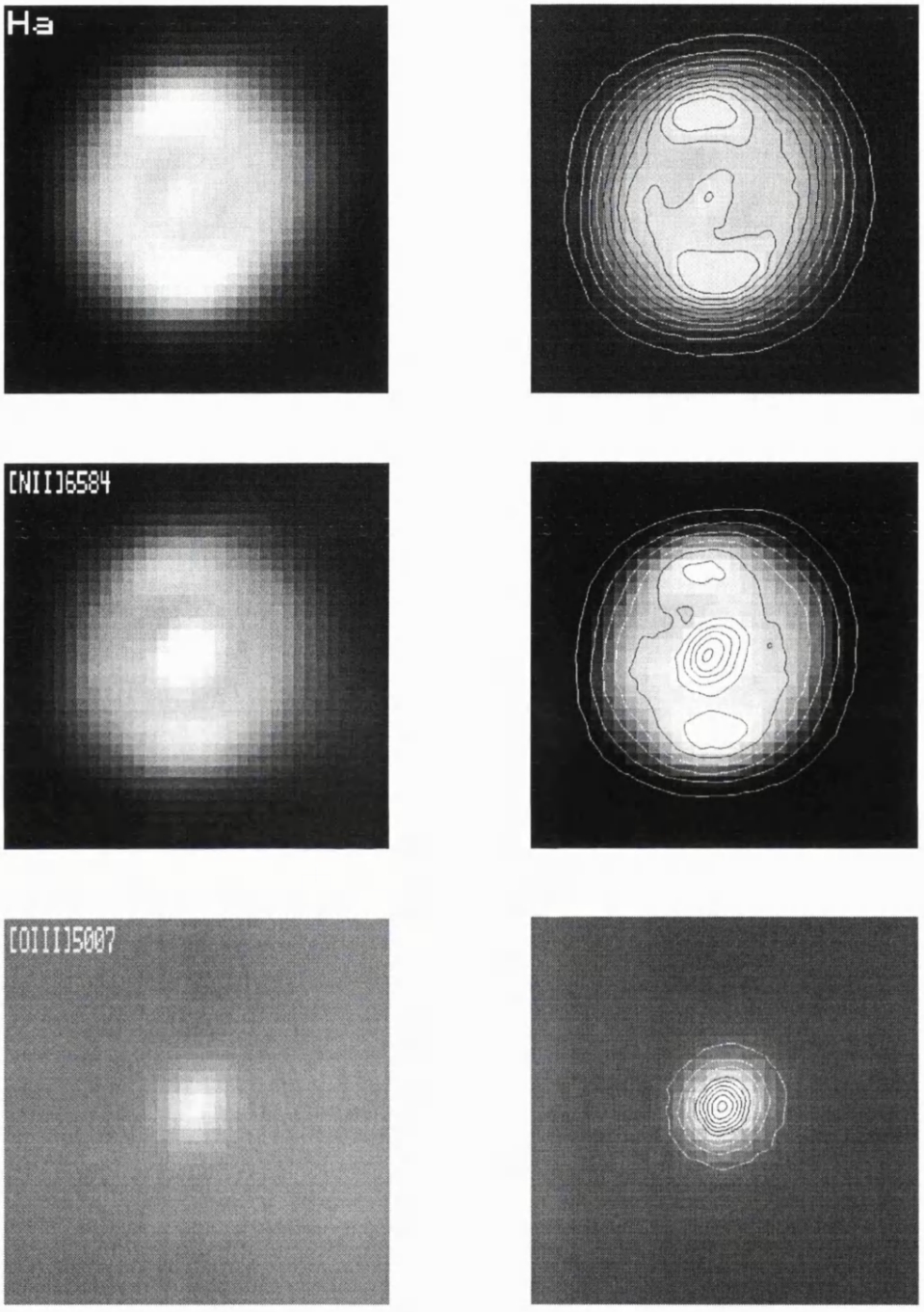

Figure 8.9: Ground–based images of M 4–18 taken with Hα, [N II] λ6584 and [O III]λ5007 filters (left–hand–side); the FOV is 4.8", north is to the top, east is to the left. The images on the right–hand–side have been normalised to the central star's peak intensity, 7900 counts, 6400 counts and 1700 counts for the Hα, [N II] and [O III] images respectively. The ten contours are linearly equally spaced between 1 and 0.1

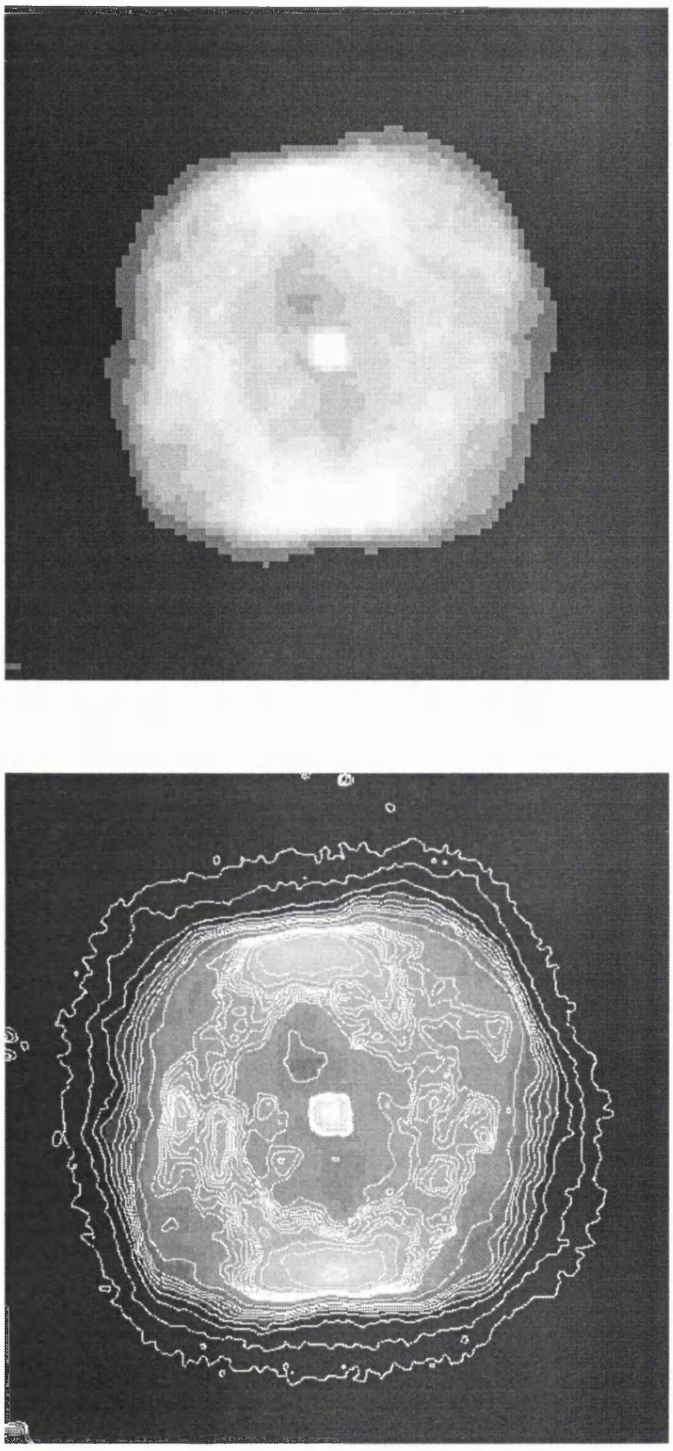

Figure 8.10: The HST WFPC2 Hα image of M 4–18, shown as a grey–scale plot (upper) and a contour plot (lower). North is towards the top, east to the left. The field of view is 4.5"

and/or binarity may be the cause (Soker and Livio 1989[4], Bond and Livio 1990) and/or magnetic fields (Pascoli 1992, Pascoli et al. 1992, Soker and Harpaz 1992[5]); when the PN overtakes the torus during its expansion, it encounters a differential resistance with the result of expanding faster at the poles than at the equator (this theory is a natural derivation of the interactive wind theory developed originally for spherical PN by Kwok Purton and Fitzgerald in 1978). It appears the M 4–18 ionization front has reached the torus and is now starting to 'bulge' out at the poles. The brighter regions north and south of the star are probably due to higher density. For a distance of 9.5 kpc and an angular radius of 1.6" M 4–18 would have a radius of 0.073 pc. We have already commented on the unreliability of using dynamical ages for PN and we are all aware of the great uncertainty associated with distance measurements, however, irrespective of that, little doubt can be cast upon the fact that the PN of M 4–18 is older than the high density, very compact PN of He 2–113. Now, M 4–18 has an almost identical stellar spectrum to He 2–113 therefore presumably has a very similar position on the T_{eff}–axis of the HR diagram. In order to justify a slower evolution since leaving the top of the AGB (that could give time for the PN to expand further), one should invoke a lower central star mass for M 4–18 than for He 2–113, hinting at an intrinsic difference between there two stars. We will not speculate further on the origin of this difference as there is at present no reliable method to determine either the masses nor the history of WR central stars. We only want to emphasize that from a purely dynamical point of view the PN of WC10 central stars are far from being a homogeneous group.

[4]These authors actually dispute the idea that a single AGB star can rotate fast enough to cause the axisymmetric mass loss.

[5]Although the first two articles claim that magnetic fields can produce axisymmetric mass loss, the third claims the magnetic fields in AGB stars are too weak to produce substantial asphericities unless the star is a rapid rotator, e.g. in a common envelope binary.

8.7.2 The Nebula around SwSt 1

For SwSt 1, Perek and Kohoutek (1967) quote an angular diameter of 5", while Aaquist and Kwok (1990) measured a 5 GHz radio diameter of only 1.3". No resolved optical image of SwSt 1 was found in the literature. The HST archive search showed that SwSt 1 was observed in 1992 in the Hβ and [O III] λ5007 lines by Bobrowsky, as part of his WF/PC snap–shot survey. Deconvolution of this image followed the same steps as already described in Chapter 5 for CPD–56°8032 and He 2–113. However the nebula around SwSt 1 is more highly ionised than the ones around CPD–56°8032 and He 2–113, as revealed by the prominent [O III] lines observed in our spectrum. Hence the [O III] image could not be used as a point spread function to deconvolve the Hβ image. We therefore used the program Tiny Tim (described in Chapter 5) to create theoretical PSFs for the Hβ and [O III] images (the theoretical Hβ PSF is shown in Fig. 8.11 together with the raw images).

The deconvolved images of SwSt 1 (Fig. 8.12) reveal a broken ring of diameter (1.3"x 0.9")$\pm$0.2", elongated in the east–west direction, in agreement with the radio image of Kwok, Purton and Keenan (1981) and Aaquist and Kwok 1990, but smaller then the 5" quoted by Perek and Kohoutek (1967). Although the images are of poor quality, this structure could be a ring whose plane is at about 30° from the line of sight. This asymmetry is confirmed by the radio picture presented by Kwok, Purton and Keenan (1981). The [O III] image confirms the ring structure, although, as expected, it appears smaller than the H β image (about 75% of the size), as can be seen from overlaying the normalised contours of the [O III] image on the grey–scale plot of the H β image (Fig. 8.13).

8.8 Nebular Modelling

8.8.1 Zanstra Temperatures

Following the formula of Milne and Aller (1975; Eq. 2.40), with a 5 GHz flux of 22 mJy for M 4–18 (Aaquist and Kwok 1990) and 243 mJy for SwSt 1 (the weighted average of Kwok et al. 1981, Milne and Aller 1982 and Aaquist and Kwok 1990, see Section 8.4.2),

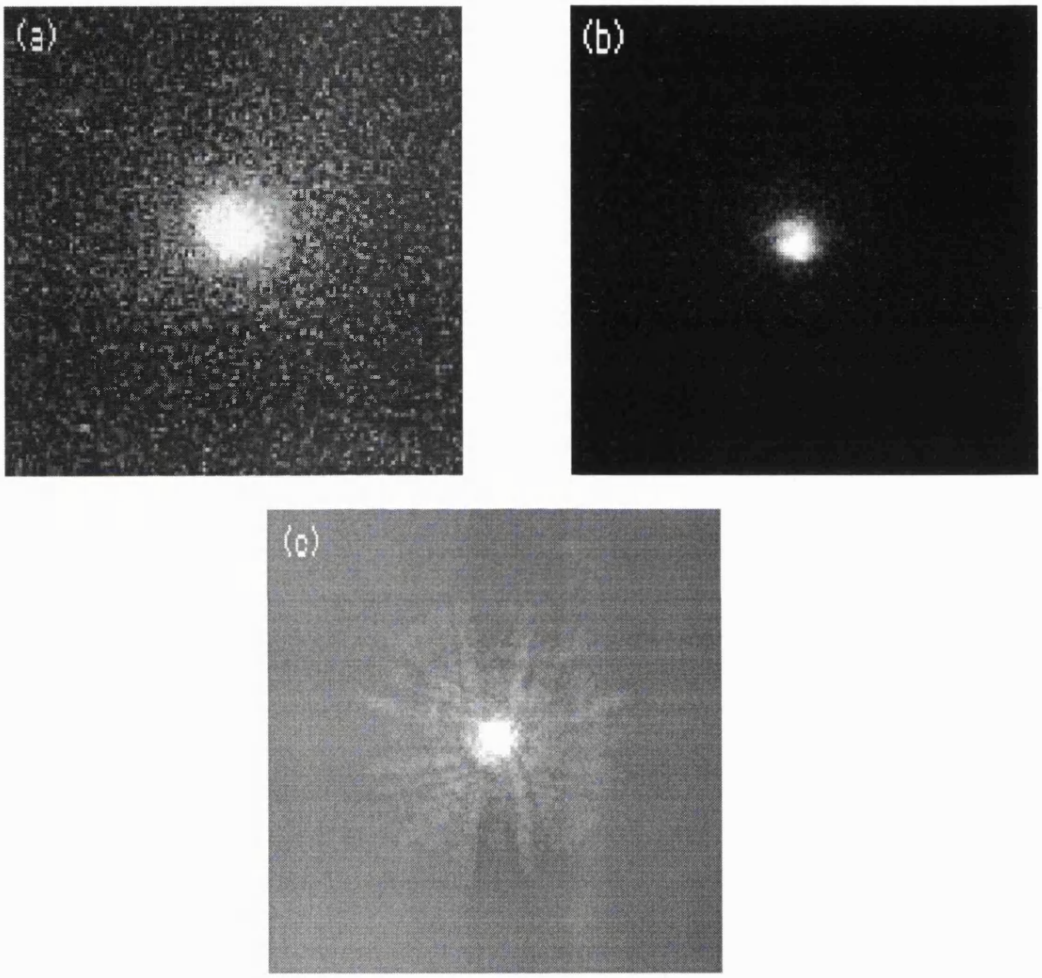

Figure 8.11: HST images of SwSt 1; a) The average of the two raw Hβ images; b) the average of the two raw [O III] images; c) the synthetic point spread function generated by the program Tiny Tim; the FOV is 6", north is towards the top, east to the left

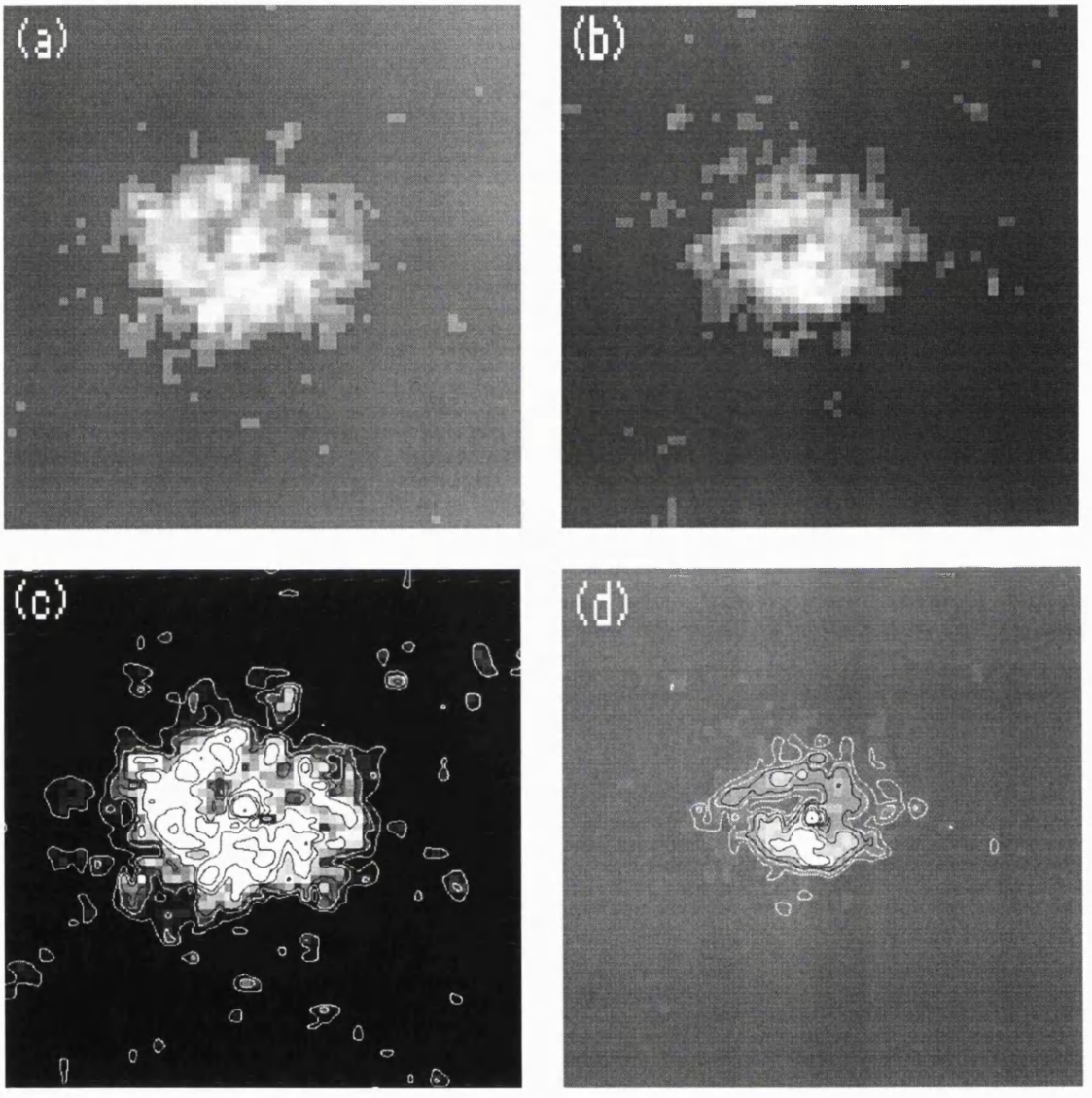

Figure 8.12: Deconvolved Hβ (a and c) and [O III] (b and d) HST images of SwSt 1; Images (a) and (b) are displayed on a log scale, while images (c) and (d) are normalised to the central star's peak counts (450 for Hβ and 270 for [O III]) and displayed linearly; contours are at levels of 1, 0.3, 0.2, 0.1, 0.06, 0.03, 0.02 and 0.01 counts; the FOV is 2.6", north is towards the top, east to the left

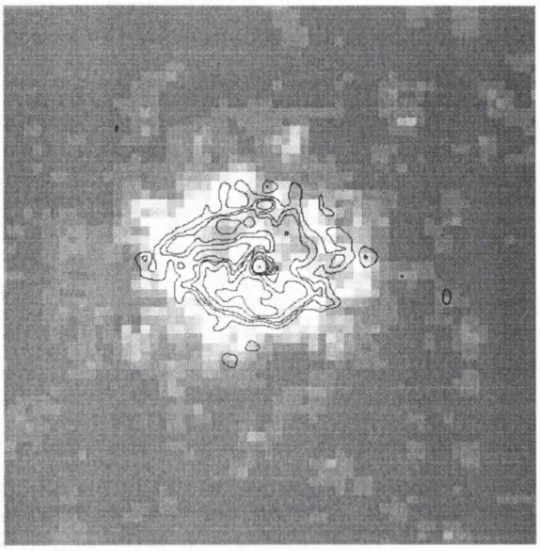

Figure 8.13: Deconvolved Hβ HST image of SwSt 1. Over-plotted are the contours from the [O III] image (Fig. 8.12)

we predict intrinsic Hβ fluxes of 7.97×10^{-12} ergs cm^{-2} s^{-1} for M 4–18 and 8.07×10^{-11} ergs cm^{-2} s^{-1} for SwSt 1. These Hβ fluxes agree within the uncertainties with the fluxes of Carrasco et al. (1983; for M 4–18) and Flower, Goharji and Cohen (1984; for SwSt 1) for the adopted reddenings of c(Hβ)=0.65 for M 4–18 and 0.68 for SwSt 1. From these dereddened Hβ fluxes and the distances of 9.5 kpc for M 4–18 and 4.0 kpc for SwSt 1 we derive a flux of hydrogen–ionizing photons corresponding to $\log(Q_o(s^{-1}))$=47.25 and $\log(Q_o(s^{-1}))$=47.51 for M 4–18 and SwSt 1, respectively.

The stellar model for He 2–113 (Chapter 6), with an effective temperature of 30 900 K, a luminosity of 5200 $L_\odot$ and a radius of 2.0 $R_\odot$, if scaled to the 5500 Å[6] flux of M 4–18, predicts $\log(Q_o)$=47.07. We carried out a Zanstra analysis of both objects using blackbody as well as Kurucz ATLAS9 (Kurucz 1991) model atmospheres with log(g)=4.0, the minimum gravity tabulated for atmospheres of the required effective temperatures. We derive blackbody H I Zanstra temperatures of 30 600 K and 30 300 K (±500 K) for for M 4–

[6]The nebular continuum fluxes were subtracted away from the stellar fluxes before normalising the theoretical stellar flux distributions to the continuum V magnitude, although the operation did not result in a substantial difference

18 and SwSt 1 respectively, while the ATLAS9 model grid yields effective temperatures of 34 000±500 K for both objects. The radii predicted for the scaled blackbodies are 2.6 and 3.7 $R_\odot$ for M 4–18 and SwSt 1 at the adopted distances, from which luminosities of 5380 (M 4–18) and 10 260 $L_\odot$ (SwSt 1) can be derived. A similar exercise for the Kurucz atmospheres yields radii of 2.6 and 3.5 $R_\odot$ for M 4–18 and SwSt 1 and luminosities of 7840 (M 4–18) and 14 960 $L_\odot$ (SwSt 1).

For SwSt 1 it was felt that the inferred luminosities were too high compared to the luminosity of 4600 $L_\odot$ derived from a comparison with LMC WR central stars. We therefore decided to adopt a luminosity of 5000 $L_\odot$ for the 30 300 K blackbody distribution, from which the distance was scaled to 2.8 kpc. At this distance the 34 000 K Kurucz model atmosphere yielded a luminosity of 7230 $L_\odot$. For M 4–18 the blackbody and Kurucz model atmosphere luminosities were satisfactory and no scaling was applied.

For M 4–18, Goodrich and Dahari (1985) derived a temperature of 22 000 K using the Stoy (1933) energy–balance method. Surendiranath and Rao (1995) derived the blackbody H I Zanstra temperature to be 26 000 K, while by fitting a blackbody to the optical and UV energy distribution they obtained a best fit of 23 000 K (the value they adopted for their nebular modelling). For SwSt 1, de Freitas Pacheco and Veliz (1987) derived a blackbody HI Zanstra temperature of 32 000 K. A comparison by Flower, Goharji and Cohen (1987) of the stellar ultraviolet and nebular free–free radio continuum fluxes yielded a blackbody H I Zanstra temperature of 36 000 K, although the authors found that a 30 000 K blackbody fitted their optical and UV data better.

8.8.2 The Modelling Strategy

Photoionization modelling of PN is the best way to test the internal consistency of empirical derivations. However since a perfect match between modelled quantities and observations is never reached, it has to be decided which observables to maintain as model inputs and which should be left free to change. The Harrington photoionization code used to model M 4–18 and SwSt 1 has already been described in Chapters 2 and 5.

The model and blackbody distribution luminosities and distances were fixed at the values derived above. The inner nebular radius was fixed at the value derived from the HST observations, scaled to the adopted distance. The clumping and vacuum filling factors were left at their default values of 1.0 and 0.0, as the Hβ fluxes were always reproduced using a completely filled nebula. The electron densities were also fixed at the empirically derived values. Lastly we made sure that the model reached far enough to include the edge of the Strömgren sphere. This was achieved by increasing the thickness of the PN shell until the electron temperature at the outer grid points registered a few hundred degrees kelvin. In this way we made sure that the model did not leave out any emission. The grid points at the outer edge of the ionized nebula were more tightly concentrated in order to sample the region of rapidly changing degree of ionization.

As a starting point we adopted the empirically derived abundances. Lines of oxygen and carbon were then fitted by changing their abundances. Carbon and oxygen are important coolants and changing the abundances does not only vary the line strengths, but also the electron temperatures. When a compromise was reached on the strength of these lines and on the electron temperatures, lines of sulphur, nitrogen and neon were fitted by varying those abundances. Other unobserved abundances were left at the mean PN value as determined by Kingsburgh and Barlow for a set of 80 southern PN, or at their solar values.

In Tables 8.14 and 8.15 we compare theoretical predictions with empirical observations.

8.8.2.1 M 4–18

To model the PN of M 4–18 we used 59 radial grid points. The mean model electron temperature listed in Table 8.14 is for the N^+ ion, although there was good agreement amongst the temperatures indicated by the model for the most prominent ions.

The non–LTE model's luminosity and temperature were maintained at the values determined by the stellar atmosphere model for He 2–113 described in Chapter 6, since, as already mentioned, the stellar spectra of M 4–18 and He 2–113 were extremely similar.

Table 8.14: Comparison of results from photoionization models for M 4–18 with observations (I(Hβ)=100), using WR non–LTE, blackbody and Kurucz plain–parallel energy distributions

Parameter	Observed	WR non-LTE	Blackbody	Kurucz
T_{eff}(kK)	–	30.5	30.6	34.0
$\log(L/L_{\odot})$	–	3.72	3.73	3.89
$R_*(R_{\odot})$	–	2.5	2.6	2.5
$\log Q_0(s^{-1})$	47.25	47.08	47.25	47.21
log(I(Hβ))	–11.1	–11.3	–11.1	–11.1
ϵ	–	1	1	1
R_{inner}(pc)	0.034	0.034	0.034	0.034
R_{outer}(pc)	0.048	0.051	0.061	0.062
$M_{PN}(M_{\odot})$	–	0.18	0.18	0.18
τ(H I)	–	>100	>100	>100
He/H	–	0.1	0.1	0.1
C/H$\times10^4$	7.9	7.9	5.5	3.8
N/H$\times10^5$	4.6	4.6	4.5	4.5
O/H$\times10^4$	4.3	4.3	3.0	2.5
Ne/H$\times10^5$	7.0	5.6	5.6	5.3
S/H$\times10^6$	1.8	1.8	6.6	7.5
1909 C III]	0	0.0	6.1	2.7
2326 C II]	97	103	92	108
3726 [O II]	146	155	145	162
3729 [O II]	77	74	69	78
5007 [O III]	0.2	0.0	29	2.0
5755 [N II]	1.4	1.2	2.0	2.3
6300 [O I]	2.4	1.9	0.9	0.9
6363 [O I]	1.1	0.6	0.3	0.3
6548 [N II]	48	42	43	56
6717 [S II]	7.4	7.8	7.1	7.0
6731 [S II]	14.6	14	13	13
7325 [O II]	14.4[a]	13	14	17
128 000 [Ne II]	45	44	44	44
S^{2+}/S^+	–	3.2	1.7	6.6
$T_e(N^+)$(K)	8200	8000	8600	9100

[a]From Goodrich and Dahari I(λ7325)=6.75$\times10^{-13}$ and I(Hβ)=4.68$\times10^{-12}$ ergs cm^{-2} s^{-1}, where we have used E(B–V)=0.45 to deredden their observed values.

The Hβ flux predicted by this distribution is 0.18 dex lower than observed. This is contrary to the results obtained for He 2–113, where the same model atmosphere predicted significantly *more* Hβ flux than observed, indicating that the effect of heavy element line blanketing probably does not play a key role in the atmospheres of the coolest WC stars and that the origin of the discrepancy for He 2–113 and CPD–56°8032 is astrophysical.

In all three cases, the nebula is optically thick[7] and possibly embedded in a considerable amount of neutral material. As already described, the inner nebular boundary was maintained constant at the observed value, while the outer boundary was chosen so that the last few grid points fell outside of the Strömgren sphere. Therefore the outer radius tabulated in Table 8.14 is the actual radius of the ionised region and, as we can see, for a distance of 9.5 kpc, compares very well with the outer nebular radius measured from the HST image for the WR non–LTE flux distribution, while it is 20% larger for the blackbody and Kurucz nebular models.

The observed nebular electron temperature and line ratios are reproduced within the uncertainties in the cases of the WR non–LTE model atmosphere and blackbody distributions, while for the Kurucz atmosphere the model's electron temperature is too high. The S^+/H^+ and S^{2+}/H^+ abundance ratios quoted by Surendiranath and Rao (1995) indicate that $S^{2+}/S^+ \sim 0.1$, although they do not list their measured fluxes and it is thus not possible to make a fair comparison. The ionization structure of sulfur seems in any case to be over–predicted in all three cases, the worst case being once again for the Kurucz model. However, the lines of [O III] and C III] are over–predicted by about a factor of 10, and by more than 100 in the case of [O III], for the Kurucz and blackbody atmospheres respectively, therefore in this instance the Kurucz distribution performs better then the blackbody model, but the WR model is better still. If we compare the three stellar flux distributions (Fig. 8.14) we can see that while the Kurucz atmosphere has got the highest number of photons just shortward of the ionization limit for S II (at $\log(\lambda)=2.9$), it is the

[7]The τ(HI) tabulated in Tables 8.14 and 8.15 is the hydrogen Lyman continuum optical depth at 912 Å.

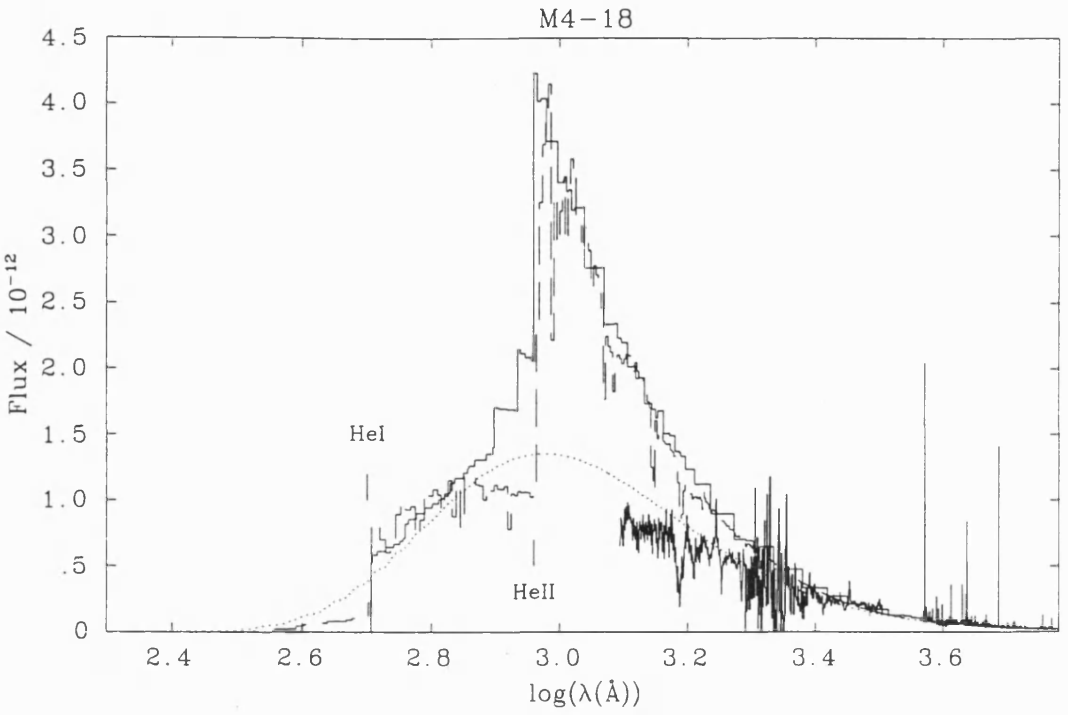

Figure 8.14: The optical and UV spectrum of M 4–18 compared with a 30 000 K blackbody flux distribution (dotted line), a 34 000 K, log(g)=4.0 plane–parallel Kurucz model atmosphere (dashed line) and a 30 000 K WR non–LTE model atmosphere (solid line). The H I and He I ionization edges are marked

blackbody distribution that has the highest number of photons capable of ionising O II (at log(λ)=2.7), therefore explaining the model results. Overall the WR non–LTE model atmosphere is the best for reproducing the line intensities (we note in particular there was no need to alter the abundances from their empirical values to obtain such fits).

Surendiranath and Rao (1995) ran their photoionization model of the M 4–18 PN adopting a different approach. They used a 22 000 K blackbody and kept the nebular electron density constant at 6620 cm^{-3}, allowing their abundances to vary. Our main criticism derives from their adopted distance of 0.9 kpc, which leads, if the observed magnitude is taken into account, to a luminosity of 72 $L_{\odot}$ (as already discussed in Section 8.5.3).

Table 8.15: Comparison of results from photoionization models for SwSt 1 with observations (I(Hβ)=100), using blackbody and Kurucz plain–parallel energy distributions

Parameter	Observed	Blackbody	Kurucz
T_{eff}(kK)	–	30.3	34.0
$\log(L/L_{\odot})$	–	3.70	3.86
R($R_{\odot}$)	–	2.5	3.5
log $Q_0(s^{-1})$	47.20	47.2	47.2
log(I(Hβ))	-10.1	-10.1	-10.1
ϵ	–	1	1
R_{inner}(pc)	0.0023	0.0023	0.0023
R_{outer}(pc)	0.0039	0.0173	0.0171
$M_{PN}(M_{\odot})$	–	0.048	0.026
τ(H I)	–	>100	>100
He/H	0.04	0.11	0.11
C/H$\times10^4$	2.51	2.51	2.51
N/H$\times10^5$	1.99	3.62	2.47
O/H$\times10^4$	2.57	1.12	0.78
S/H$\times10^6$	4.17	3.3	5.9
Ne/H$\times10^5$	9.8	9.0	7.8
1909 C III]	71	24	20
2326 C II]	85	135	233
3726 [O II]	30	41	40
3729 [O II]	18	15	15
4363 [O III]	0.3	0.4	0.1
4471 He I	2.5	1.8	0.7
5007 [O III]	29	48	7.0
5755 [N II]	3.2	3.8	3.8
5876 He I	7.1	5.1	2.1
6300 [O I]	1.5	0.9	0.4
6363 [O I]	0.5	0.3	0.1
6548 [N II]	31	41	37
6678 He I	1.7	1.5	0.6
6717 [S II]	0.7	0.9	1.2
6731 [S II]	1.4	2.1	2.3
7325 [O II]	28	24	25
9532 [S III]	91	62	129
128 000 [Ne II]	68	71	67
S^{2+}/S^{+}	22	8.0	13
$T_e(N^{+})$(K)	10 500	10 500	10 900

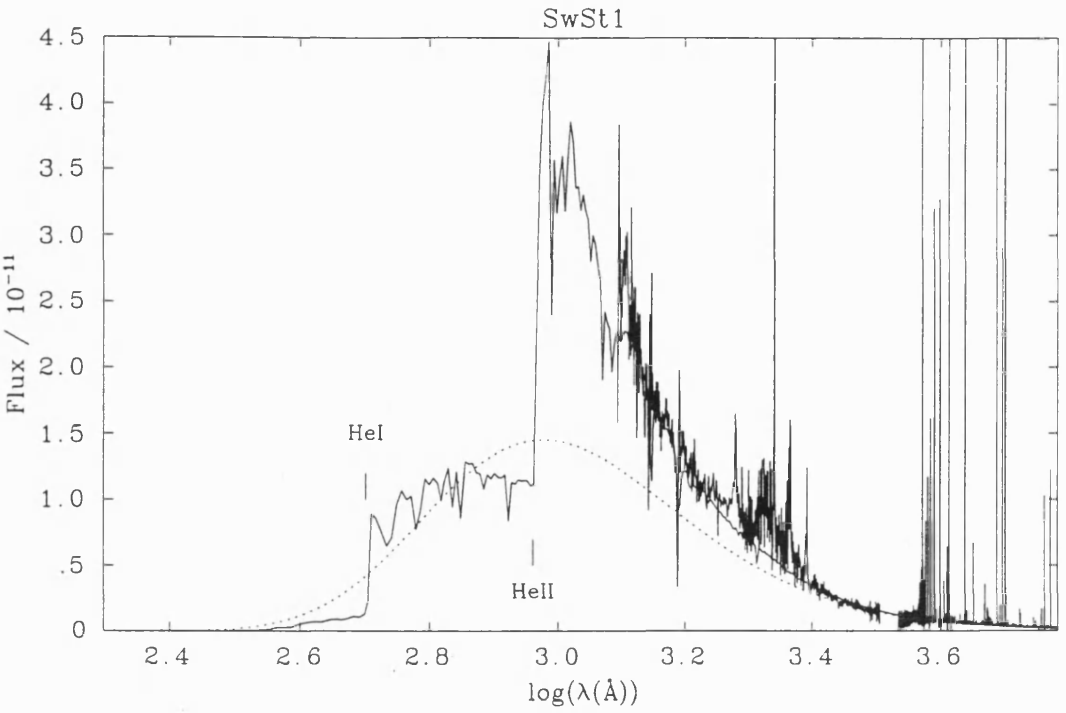

Figure 8.15: The optical and UV spectrum of SwSt 1 compared with a 30 300 K blackbody flux distribution (dotted line), and a 34 000 K, log(g)=4.0 plane–parallel Kurucz model atmosphere (solid line). The H I and He I ionization edges are marked

8.8.2.2 SwSt 1

38 radial grid points were used to sample SwSt 1's nebula. The nebular modelling results are presented in Table 8.15. For this model we did not have a WR non–LTE model atmosphere and we could only compare blackbody and plain–parallel Kurucz stellar fluxes. For SwSt 1, the blackbody stellar atmosphere reproduced the observed nebular results better than the Kurucz distribution although the dereddened stellar spectrum is more in agreement with the Kurucz model (Fig. 8.15). Both distributions underestimate the nebular C III] line flux (Table 8.15), although the blackbody model overestimates the [O III] λ5007 line flux (while the Kurucz model atmosphere underestimates it). The reverse is the case for the [S III] λ9532 line, although both distributions underestimate the overall ionization of sulfur.

8.9 Discussion

8.9.1 M 4–18

The central star of M 4–18 is a spectroscopic twin of the central star of He 2–113, with only marginally stronger stellar lines (although the relative line strengths are extremely similar). Based on this claim we might suppose the stellar masses, luminosities, evolutionary paths and the timescales since the ejection of the nebulae to be very similar. If we start with this assumption, the observed (dereddened) V magnitudes of the stars imply a distance for M 4–18, which is 7 times larger than that distance to He 2–113. If this is the case, and considering that the angular diameter of M 4–18 is about four times the angular diameter of He 2–113, we conclude that the linear diameter of the PN of M 4–18 should be 20 times the linear diameter of the PN of He 2–113. Since He 2–113 has a much higher electron density than M 4–18 (63000 vs. 5000 cm^{-3}), we might expect it to be more optically thick and therefore we cannot assume that the ionized masses of the two PN to be the same. However, since the photoionization modelling of the two PN indicated that they are both still optically thick, we can trust the total number of recombinations ($\epsilon N_e^2 R^3$) to be the same (assuming that the ionizing fluxes are the same). From this we deduce that the linear radius of M 4–18 should be only 5 times larger than that of He 2–113, and not 20 times larger as we calculated by imposing that the two stars are identical.

We can also approach the argument from the PN point of view, and *not* impose the condition that the two stars must have similar luminosities. As we have already seen, conservation of the total number of recombinations imposes that the linear radius of M 4–18 is 5 times that of He 2–113. From this, and the measured angular diameters of the two PN, the distance to M 4–18 should be 1.6 times the distance to He 2–113. If this is the case, given the different observed (dereddened) V magnitudes and the distance of 1.5 kpc obtained for He 2–113 in Chapter 5, the central star of M 4–18 would be much less luminous than He 2–113, making it a very different star, and making it difficult to understand why such different stars should have such amazingly similar spectra! In brief,

there is no way of reconciling the difference in the PN of these two stars without falling in some contradiction. This was also noticed by Pottasch (1996) who put it forward as one of the puzzles of WR central stars of PN[8].

Photoionization modelling of the PN of M 4–18 and He 2–113 has indicated that indeed the two PN are very different. While we have seen (Section 8.5.3) that the non–LTE WR model stellar atmosphere of He 2–113, scaled to the dereddened V magnitude of 12.7 for M 4–18, reproduces the observed nebular properties of this PN to a satisfactory degree, for He 2–113 a gross overestimation of the hydrogen ionizing flux was evident. This would indicate that the nebular Hβ flux of He 2–113 is somehow suppressed, as it is also confirmed by the Zanstra temperatures being lower than predicted by the WR model code (Chapter 6). This behaviour (which is also encountered for the PN of CPD–56°8032) is very different from M 4–18. To explain this fact, we have pointed out in Chapter 6 that competition between the gas and dust in absorbing the ionizing photons might have to be invoked.

8.9.2 SwSt 1

As to the evolutionary stage of SwSt 1 there is little doubt that the star has only recently left the AGB and it is on its way to become a white dwarf. As also confirmed by the WR modelling modelling of Leuenhagen, Hamann and Jeffery (1996) and Leuenhagen and Hamann (1997), its effective temperature is hotter than those of M 4–18, He 2–113 and CPD–56°8032, although not quite as hot as a WC9 star (Leuenhagen, Hamann and Jeffery 1996 and Leuenhagen and Hamann 1997). Consistent with this conclusion is the fact that its PN is more highly ionized but is still compact (hence the high electron density), optically thick (as we have seem from the photoionization models), and presents a fair amount of neutral (e.g. sodium) and molecular (Dinerstein et al. 1995) material. The infrared fluxes and the spectroscopic observations of Aitken et al. (1979) demonstrate the

[8] Pottasch, however, was comparing dynamical ages of the two PN, which we do not think appropriate since we do not know the extent of the ionized regions in either PN.

presence of dust, although the nature of the grains might be different from the majority of PN since, with silicate features, they are oxygen–rich rather than carbon–rich. This was corroborated in the past (de Freitas Pacheco and Veliz 1987; Flower, Goharji Cohen 1984 and this work) by the derived C/O gas ratio of <1. Our own empirically derived C/O ratio is 0.98±0.39, consistent with oxygen–rich material.

The PN morphology shows a slightly elongated structure which could be interpreted as a ring seen at an angle from its plane. From a comparison of the Hβ and [O III] HST images we confirm that the [O III] emission derives from a smaller, inner part of the PN, once again supporting the interpretation (Section 8.2) that the forbidden lines from doubly ionised species, with smaller FWHMs than the lines from neutral and once ionised ions, come from an inner part of the PN.

There is no compelling evidence for Hβ or radio variability; the observed scatter can probably be attributed to measurement errors. As to the visual lightcurve, it appears likely (see Appendix A) that the variations are caused by observational effects. However we will await more data before we finalise our conclusion. Below we carry out a detailed comparison of the spectroscopy obtained since 1940. Changes were noticed by the different authors and it is important to decide whether they can be interpreted as real changes or as due to measurement errors.

The nebular carbon abundances of both M 4–18 (C/O=2.0) and SwSt 1 (C/O=0.98) are not very easy to measure, but do not appear to be as enhanced as for CPD–56°8032 and He 2–113 (Chapter 5).

8.9.2.1 The Variability Properties of SwSt 1

SwSt 1 was observed spectroscopically on 5 distinct occasions: in 1938 by Payne Gaposchkin (as reported by Carlson and Henize 1979), in 1940 by Swings and Struve (1940; in the range 3600–6680 Å at a dispersion of 100 and 50 Å/mm) in 1962 by Carlson and Henize (1979; in the range 3700–6600 Å at a dispersion of 177 Å/mm blue–ward of 5000 Å and 94 Å/mm red–ward of 5000 Å), in 1985 by de Freitas Pacheco and Feliz (1987; in the

range 3600–6930 Å at a resolution of 6.5 and 0.5 Å) and finally by us in 1993 (in the range 3700–9500 Å at a resolution of 0.15 Å).

Two trends of change have been pointed out in the literature: a weakening of the stellar wind lines and an increasing degree of ionization of the stellar wind and of the PN since 1940. The former trend was pointed out by Carlson and Henize (1979), who noted the possible disappearance of several weak stellar O III and C III lines between 1940 and 1962 along with the appearance of [Fe II] and [Fe III] (although these lines were reported by Payne Gaposchkin in 1938). They also reported the diminishing of P–Cygni profiles from a total of 10 lines (as counted by Swings and Struve) to 4 lines, finally concluding that the wind's density and mass loss rate must have decreased between the two observations. Undoubtedly before comparisons are made one has to note the different resolutions and detectors used by different studies, especially when dealing with 1940s photographic plates! However the spectroscopy of Carlson and Henize and of Swings and Struve were both obtained photographically and at similar dispersions, reinforcing the conclusions made by Carlson and Henize, based on a comparison of the two spectra.

Overall we feel that the conclusion that SwSt 1's wind has weakened is entirely plausible. To support the weakening of the wind theory, we would also like to note that many of the lines observed by Swings and Struve are observed by us to be so weak that unless in 1940 the whole spectrum was stronger than it is now, many of these lines could not have been observed. Weakening of the stellar lines in entirely consistent with a weakening wind (i.e. diminishing mass loss and decreasing wind density) and indeed SwSt 1 might be on its way to become a *weak emission line star* (Tylenda, Acker and Stenholm 1993) as it increases its gravity on its journey to becoming a white dwarf. As to the number of observed P–Cygni profiles, in our spectrum we can see only two prominent P–Cygni absorptions (see Table E.1 in Appendix E), reinforcing the hypothesis that the wind is losing strength. Most of the P–Cygni lines counted by Swings and Struve, however, were Balmer lines, indicating that the hydrogen lines might have had a stellar component which is no longer obvious. Since no stellar hydrogen lines are observed in our own spectrum,

this might show that the star has now lost its hydrogen or that the wind has weakened too much to see the Balmer lines any longer.

Carlson and Henize 1979 observed three He I P–Cygni absorptions (at 3819.6, 3964.7 and 4471.5 Å) and one on the blue–side of the C III line at 4650 Å. Although we do see the P–Cygni absorption on the blue–side of the C III line at 4650 Å, we note that the three helium lines mentioned do not exhibit absorption features. From our spectrum we can cast little doubt on these lines being of nebular origin, excluding the presence of P–Cygni absorption. However, if in 1962 the He I lines presented a stellar counterpart to the nebular component, the chance is that they might have had a P–Cygni absorption. This would then mean that the star might have warmed up in the intervening years, losing its stellar He I lines in favour of He II lines (we note however that the He I lines $\lambda\lambda$5876,3889 might show weak stellar components).

The advocates of the second trend, the increasing ionization of the stellar wind and of the PN, are de Freitas Pacheco and Veliz (1987), who claimed not to be able to see any nebular [Fe II] lines in their spectra despite the far superior resolution of their data, and noticed instead weak lines which they attributed to [Fe IV]. They also noted that the C IV lines at 5801 and 5811 Å were not observed by Carlson and Henize[9], although we would like to point out that they were present in the spectra of Swings and Struve (1940). They concluded that the nebula must have increased in ionization as the star evolved from cooler to hotter.

Increasing ionization with time could be expected, although the timescales seem very short for a normally evolving star. However, the observation of Payne Gaposchkin (1938, in Carlson and Henize 1979), indicating the presence of the [Fe III] lines as far back as 1938, together with the presence of [Fe II] lines in our own spectrum, disqualify a clear trend of increasing ionization. This is also supported by the C IV lines, supposedly absent

[9]It is an oddity that Carlson and Henize do not observe strong lines like C III λ5696 or C IV $\lambda\lambda$5801,11. Their spectroscopy longward of 5000 Å, however, comes from a different set of observations which might be causing the problem.

in 1962, but present in 1987 *and* in 1940.

Although de Freitas Pacheco and Veliz do not show any of the spectral region containing [Fe II] lines, from the quality of their published spectroscopy we see that they would not have been able to observe the weak [Fe II] lines. However, since the 1940 and 1962 spectroscopy is likely to have been of poorer S/N than their 1987 data, we can conclude that indeed [Fe II] lines have weakened and that the fact that we did observe them in 1993 is only because of our superior resolution. Based on the possibility of weakening nebular [Fe II] lines and stellar He I lines, we conclude that the wind and PN *might* have increased their level of ionization, although we attach a large uncertainty to this statement.

Returning to the issue of the wind's lost strength we would like to underline the peculiarity of the behaviour of SwSt 1. As we have already pointed out (Chapter 6) a post–AGB star has two competing processes: hydrogen is stripped from the envelope by mass loss, at the same time as the star is heating up, contracting and increasing its gravity. If the former process dominates, the star might develop a WR wind, while if the second process dominates the hydrogen–depleted star will tend to develop a *weak emission line* rather then a proper WR spectrum. For SwSt 1, it appears that the loss of hydrogen has coincided with a weakening of the wind, leading us to believe that the increasing gravity must have hampered the development of a full–blown WR wind that would have ensued from the loss of the hydrogen envelope. However, SwSt 1 is still a fairly cool object (in the [WCL] domain), while the gravities needed to determine weakening of the WR wind would be expected in hotter parts of the HR diagram (see Chapter 9). In conclusion, we feel that to try and resolve this issue we should retrieve and scan the old spectroscopy (1940 and 1962) for this bizarre object, a task that will be saved for future work.

Chapter 9

Thesis Conclusions, Ongoing and Future Work

In Section 9.1, I will summarise the main results reached in the course of the preceding 8 Chapters. In Section 9.2, I will draw a final conclusion and list the points that support it, cross–correlating them with relevant conclusions from the literature. I will also pose a few questions which might be answered by undertaking some of the suggested projects I list in Section 9.3.

9.1 Summary of Chapters

In **Chapter 4** major achievements have been:

- The definition of a robust classification system for central stars with WC spectra, consistent with the scheme of Smith et al. (1990) designed for massive WC stars. This scheme can also be applied to central stars showing a significant nebular contribution to the stellar continuum, a feature that can be useful in the classification of distant (e.g. extragalactic) central stars.

- Our WC classification criteria have been thoroughly compared with past schemes and, in particular, emphasis has been placed on the identification of a correspondence

between and unification of WO and WCE classifications.

- Within the new scheme, the 'gap' between the [WCL] and [WCE] groups has been reduced from [WC4]–[WC8] to [WC5]–[WC8].

- Partial criteria for *weak emission line stars* (Tylenda et al. 1993) have also been defined. These do not provide a full classification scheme for the *wel* stars, but help to exclude them from the WC sequence.

- The star IRAS 21282+5050 has been classified as O9–9.5 (it was classified by Cohen and Jones (1987) as a [WC11]); the star SwSt 1 has been identified as a peculiar object ([WC9pec]), and the hot R Cor Bor star V 348 Sgr, which was classified as a [WC12] star (van der Hucht et al. 1981, Leuenhagen et al. 1994), has been excluded from the WC system and given a peculiar EHe star classification.

- Finally, theoretical WC colours have been applied to the determination of the stellar reddenings. The reddening constants derived in this way can be readily compared with those obtained using empirical methods.

Chapter 5 dealt with the distance and nebular parameters of the [WC10] central stars CPD–56°8032 and He 2–113. For these two objects we have determined that:

- The most likely origin of the broad pedestal observed at the base of the Hα and Hβ profiles of both stars is due to nebular emission rather than hydrogen being present in the stellar wind. This reinstates WC central stars within their former hydrogen–free status (Leuenhagen et al. 1996) so that the overlap between hydrogen–rich and hydrogen–poor central stars sequences (Stanghellini 1996) is no longer obvious.

- The presence of high velocity components in the nebulae of CPD–56°8032 and He 2–113 has been inferred, supporting the conclusion below that the asymmetrically shaped nebular lines are caused by the irregular PN geometry.

- HST images of both objects have confirmed the asymmetry of the PN. Despite the low quality of these pre–COSTAR images, a ring is evident in the Hβ image

of CPD–56°8032, while the possibility of ansae is determined for He 2–113. From these images, and the fact that the PN of CPD–56°8032 and He 2–113 are young, compact, high density objects, we might also interpret these PN as having been shaped very early after ejection. While no dynamical age can be determined from the outer ionized radius of these PN, the age of ~100 yr determined for the inner ring structure of CPD–56°8032, might indicate when the ejection terminated. No halo or second larger shell, which reveal an association with the *born–again* scenario, is observed in these images.

- The presence of significant quantities of internal dust had previously been inferred from the high infrared fluxes, from the possibility of an abnormal reddening law and from our modelling of the PN (see also Chapter 6). On the HST image of CPD–56°8032, we notice more emission on the east than on the west side of the star, possibly due to dust obscuration.

- Distances were calculated using two independent methods, which agree within 0.5 kpc of each other. The IR bolometric luminosity method is subject to the assumption that these WR central stars have the same masses (~0.62 $M_{\odot}$) as a group of LMC WR central stars and that the circumstellar dust completely absorbs and reradiates the stellar flux. However, there is no reason why all WC central stars should have the same mass, as proven by the existence of massive and non massive WC stars; this limits the validity of the LMC calibration method.

- Nebular C/H number ratios of more then 10 times the mean PN value (Kingsburgh and Barlow 1994) have been derived for CPD–56°8032 and He 2–113. Carbon enrichment can be expected if the base of the ejected PN comes from the inter–shell region, where helium and carbon are abundant. Alternatively it might show that the third dredge–up has been at work and raised into the H–rich envelope, substantial amounts of carbon from the helium shell. A third possibility is that the high carbon abundance might be due to contamination of the PN from the stellar wind. A high

C/O ratio is consistent with the strong UIR bands (although the O/H number ratio was assumed to be the same as for the mean PN value derived by Kingsburgh and Barlow (1994), who found no significant variation in O/H amongst various classes of PN and H II regions).

In Chapter 6 stellar and nebular modelling of CPD–56°8032 and He 2–113 were carried out. From this exercise:

- The independently developed models of the Kiel (now Potsdam) group and of D.J. Hillier are shown to yield comparable results.
- The difficulty of fitting the wings of Hα and Hβ simultaneously, might show (as in Chapter 5) that the origin of the asymmetric shapes of the Balmer lines is not due to the presence of stellar wind hydrogen.
- Photoionization modelling of the PN was ineffective in reproducing the observed characteristics. This might indicate inadequacy of the input stellar flux distributions, although it is more likely (since the same modelling of M 4–18, Chapter 8, was successful) that the presence of dust–gas competition in absorbing the Lyman continuum photons is responsible for the misfits.
- The idea is introduced that some instability strip might exist for post–AGB stars which initiate/hampers the WR wind.

In **Chapter 7** we introduced the use of dielectronic recombination in the determination of the wind electron temperature of [WCL] stars. Stellar wind abundances were also derived and optical depth effects discussed. In particular:

- The method was outlined and applied to CPD–56°8032, He 2–113, M 4–18, IRAS 17514–1555 and K 2–16. It appears that the temperature determined for the C II line forming region always lies within a certain range (17 000–21 000 K), although we only applied the method to five [WC10] and [WC11] stars, the only ones that display

low–temperature dielectronic recombination lines. This is consistent with ionization stratification in the winds of WR stars. By comparison with the temperatures predicted by the wind models, this also constitutes the first confirmation of the assumption of radiative equilibrium in the winds of WR stars (see also Chapter 6).

- Stellar wind abundances of carbon and oxygen with respect to helium were obtained for the [WC10] stars CPD–56°8032, He 2–113 and M 4–18 from recombination line analyses, showing good agreement with abundances derived from wind modelling in Chapter 6 for CPD–56°8032 and He 2–113.

- Optical depth effects on C II bound–bound recombination lines were shown NOT to preclude their use for abundance determination. In fact, dielectronic lines of C II, previously thought to be the most optically thin and hence ideal for abundance analysis, have been shown to be more optically thick than some bound–bound recombination lines, and to systematically underestimate abundances.

In **Chapter 8** we have analysed the PN of the [WC10] star M 4–18 and the [WC9pec] star SwSt 1. We determined that:

- Their nebular C/H number ratios are much lower than for the nebulae of CPD–56°8032 or He 2–113. This might mean that above–average C/H nebular abundance ratios are not a prerogative of WC central stars. It is possible that carbon enrichment of the PN is at the hand of the stellar wind. If so, both the size and characteristics of the PN (M 4–18 might be much larger than either CPD–56°8032 and He 2–113) or a lower mass-loss (for SwSt 1 de Freitas Pacheco et al. (1993) find a mass–loss rate 10 times lower than for He 2–113) might explain the lack of carbon enrichment.

- The stellar spectrum of M 4–18 is remarkably similar to that of He 2–113. However, given this similarity (from which we constrain the distance), the PN of M 4–18 is very different from the PN of CPD–56°8032 and He 2–113, with a lower electron density and a much larger linear radius.

- Photoionization modelling of the PN around M 4–18 and SwSt 1 has shown their nebular spectral characteristics to be well reproduced with different stellar energy distributions, with the best fit to M 4–18 being obtained using the non–LTE WR model flux distribution derived for He 2–113 (which fits M 4–18's stellar line profiles to a very good degree of accuracy).

- The spectral appearance of SwSt 1 is likely to have changed in the years between 1940 and 1993. Hydrogen seems to have been lost, while the stellar spectral emission lines might have decreased in intensity. Pending confirmation of these spectral changes, this may be interpreted as quenching of a WR wind and the development of a *weak emission line* type spectrum.

In Table 9.1 we summarise the main parameters derived during the course of the preceding eight Chapters, while in Fig. 9.1 we have placed the four central stars on the HR diagram, along with results from Leuenhagen et al. (1996) and theoretical evolutionary tracks from Blöcker (1995).

9.2 Conclusion

Given the above results, evidence might be emerging that there is no *unique* evolutionary sequence for all post–AGB WC central stars of PN, in the sense that it does not appear that the [WC] stars are **either all** post–AGB **or all** created though a *born–again* scenario.

We support this claim with the following observations:

- To date, no thorough investigation of the entire parameter space (luminosity, effective temperature, gravity and metallicity) within which CSPN are observed has been carried out. However, the combination of gravity, composition and luminosity necessary for the formation of a strong WR stellar wind could readily arise in *either* an immediate post-AGB environment *or* after a final flash. To illustrate this, Schmutz, Hamann & Wessolowski (1989) established that identical WR spectral features may be predicted using a huge variety of stellar properties, provided that a

Table 9.1: Summary of the stellar and nebular parameters derived for the central stars and PN analysed during the course of this thesis

System	CPD-56°8032	He 2-113	M 4-18	SwSt 1
D(kpc)	1.35±0.3	1.50±0.3	9.5±1.0	2.8±0.5
Helio. RV(km s^{-1})	-58.7±3.0	-57.4±3.0	-51.6±1.0	-17.8±1.0
E(B-V)(mag)	0.68±0.03	1.00±0.03	0.45±0.02	0.46±0.02
		Nebular parameters		
v_{exp}(km s^{-1})	30±4	19±1	20±1	21±2
R_{PN}(pc)	0.006±0.0005	0.05±0.005	0.0031±0.0003	0.041±0.004
T_e(K)	8800±500	8400±400	8200±200	10500±500
$\log(N_e/cm^{-3})$	4.8±0.1	4.8±0.1	3.7±0.2	4.5±0.2
12+log(C/H)	9.80±0.70	9.70±0.70	8.90±0.30	8.40±0.30
12+log(N/H)	7.92±0.03	7.82±0.03	7.75±0.04	7.32±0.10
12+log(S/H)	7.00±0.03	7.59±0.03	6.21±0.06	6.61±0.10
C/O	13.1±4.0	10.4±3.0	2.0±0.6	0.98±0.5
		Stellar parameters		
V magnitude	11.1±0.1	11.9±0.1	14.1±0.1	11.5±0.1
M_V(mag)	-1.9±0.1	-1.8±0.1	-1.9±0.1	-
BC(mag)	-2.8±0.1	-2.8±0.1	-2.8±0.1	-
$R_*(R_\odot)$	2.0±0.2	2.5±0.2	2.5±0.2	3.5±0.3[a]
$M(M_\odot)$	0.62±0.05	0.62±0.05	0.62±0.05	0.62±0.05
$\log(L/L_\odot)$	3.72±0.20	3.72±0.20	3.72±0.20	3.86[a]
T_*(kK)	34.5±2.0	31.2±2.0	31.2±2.0	-
T_{eff}(kK)	30.0±2.0	30.9±2.0	30.9±2.0	34.0±3.0[a]
$\log(Q_o/s^{-1})$[Model]	47.23±0.10	46.51±0.10	46.51±0.10	-
$\log(Q_o/s^{-1})$[Hβ]	45.74±0.20	45.26±0.20	47.25±0.20	47.51±0.20
$\log(\dot{M}/M_\odot/yr)$	-5.40±0.05	-6.10±0.05	-6.10±0.05	-
v_∞(km s^{-1})	225±10	160±10	160±10	1400±100
H/He(by number)	$\lesssim$0.02	$\lesssim$0.02	$\lesssim$0.02	-
C/He(by number)	0.50±0.10	0.55±0.15	0.55±0.15	-
O/He(by number)	0.10±0.05	0.10±0.05	0.10±0.05	-

[a]For SwSt 1 these stellar parameters were obtained by the Zanstra analysis using a Kurucz model atmosphere flux distribution.

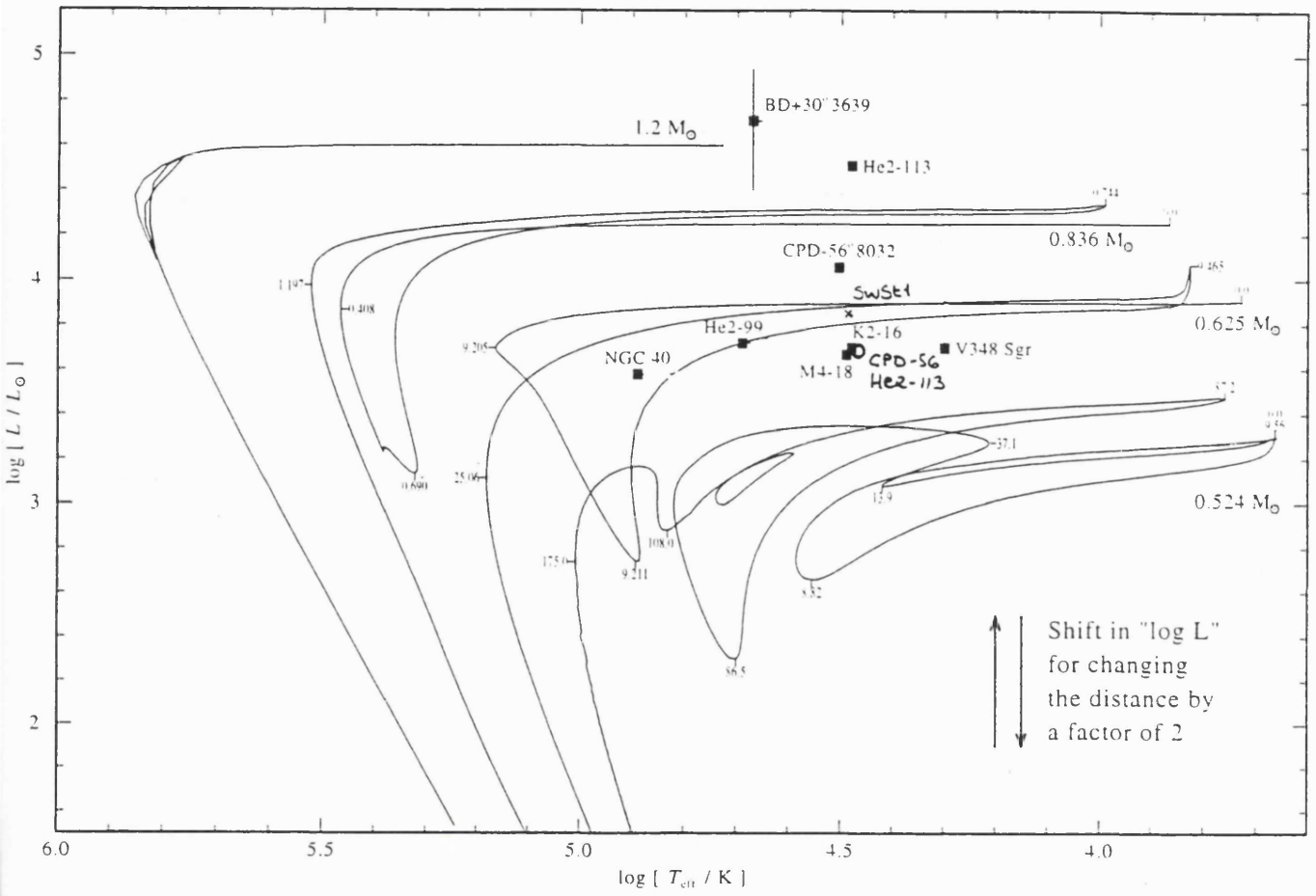

Figure 9.1: HR diagram with evolutionary tracks from Blöcker (1993, 1995) and Paczynski (1970) reproduced from Leuenhagen et al. 1996 (their Fig. 14). The ticks on the tracks denote the time (in 10^3 yrs) since leaving the AGB. The filled squares give the positions of the [WCL] stars analysed by Leuenhagen et al. (1996). The vertical line for BD+30°3639 represents the error bar on the distance according to Hajian et al. (1993). The positions of CPD–56°8032 and He 2–113 as deduced in this thesis, marked by a circle, are almost identical; M 4–18 was assumed to have the same position as He 2–113, while SwSt 1, marked by a cross is slightly hotter and more luminous (cf. Table 9.1)

single quantity, namely the 'transformed radius', R_t ($= R_* (v_\infty/\dot{M})^{2/3}$), is maintained. The very existence of massive and non–massive WR stars shows that the WR phenomenon does not occur only in one region of the HR diagram. Within the same excitation class, [WC] and WC stars can be surprisingly similar, as originally pointed out by Smith and Aller (1971) who showed that the [WC9] star He 2–99 and the WC9 WR 103, with different masses, luminosities and mass–losses, have almost identical spectra.

- The lack of segregation with respect to any of the studied parameters (i.e. PN composition, expansion velocity, morphology and galactic position (Gorny and Stasinska 1995)), might indicate that the groups of H–poor and H–rich central stars overlap. Moreover, it is obvious that not all the H–poor central stars (WC and *wel*) are *born–again*. *Born–again* stars have lost all their hydrogen and it is therefore not surprising that they show a hydrogen–deficient spectrum! However, the WR central stars analysed here are very unlikely to be the result of a final flash (Chapters 5 and 8). Open questions still remain like whether the abundances of WR central stars are consistent with post–AGB evolution.

- The gap between [WCL] and [WCE] stars (Tylenda et al. 1993) seems more than a coincidence, or the product of fast evolution. It appears instead more likely to be an instability strip, crossing which the [WCL] stars lose their wind. Tylenda et al. (1993) claim that if the same parameters that are used for the classification of WC stars are applied to the *wels* these stars would fall in the [WC8]–[WC5] gap. However, we have shown (Chapter 4) the need for consistency in the diagnostic lines used in the classification of central stars, and the lines required are not always observed in *wels*. This possibility needs however more consideration.

- Spectral transitions do occur. A transition between WR and *wel* type is possibly observed in SwSt 1, which seem to now have a considerably weaker wind since it was observed in 1940 (Chapter 8).

- Transitions between cool giant type spectra and WR–type spectra are observed in the central star of A 58, V 605 Aql. This star is known to have undergone a brightening event in 1919 (Wolf 1920) after which it temporarily developed an R Cor Bor spectrum (Lundmark 1921, Clayton and De Marco 1997). In 1985 the spectrum showed a line of C IV at 5800 Å, from which it was deduced that the central star possessed a WR–type spectrum (Seitter 1985, Guerrero and Manchado 1996).

- No matter what distance is adopted, certain differences between the spectroscopic twin WC10 central stars He 2–113 and M 4–18 cannot be reconciled. The possibility of a slower evolution for M 4–18 is opened. This further stresses the fact that even two members of the same subclass might have followed different evolutionary paths.

9.3 Ongoing and Future Work

- The main project I have underway at the moment is the analysis of the spectra of *weak emission line* and WC central stars obtained at the INT in 1996. Two main lines of investigation are being followed: the first concerns the stellar spectrum, mainly with the aim of studying the presence of nitrogen and hydrogen. The correlation between the presence of these two elements and stellar effective temperature (or degree of ionization) will be investigated, as will the correlation between abundances and general line strengths. Non–LTE WR modelling of some of these spectra might also be carried out. The second line of investigation concerns the nebular abundance ratios. In particular, for some of the more extended PN, the possibility of spatial variations in the abundances will be investigated (although only limited spatial resolution can be achieved with the particular instrumental set up used). This might constitute a precedent for a further, high–spatial resolution proposal to analyse the more compact PN. C/H abundance ratios will be derived for those PN for which IUE spectroscopy exists.

- The question of the origin of nebular carbon should be investigated with spatially

resolved spectroscopy of the PN (for the smallest PN the high spatial resolution of HST would be required). We might expect that if the carbon overabundance in CPD–56°8032 and He 2–113 originates from wind enrichment, we might find more carbon in the inner, star facing regions. This might be particularly advantageous to observe in young PN, for which there has not been much time for mixing of the nebular material to take place.

- A wider parameter space for the winds of [WCL] central stars should be investigated with the calculation of a grid of models. From this, we could carry out a more systematic study of the behaviour of emission lines in response to different parameters. The resultant WR continuum flux distributions would constitute a database to be used, for instance, to model PN instead of the inappropriate blackbody or Kurucz model atmospheres.

- WF/PC2 HST images of young PN can reveal to what extent the morphology of the PN is established. Since it is still not clear exactly when the PN morphology arises, and as it appears that the PN of CPD–56°8032 and He 2–113 already have particular characteristics (a ring in the case of CPD–56°8032 and ansae in the case of He 2–113), it might be useful to obtain post-COSTAR images. Imaging of these PN will also be important in carrying out photoionization modelling of the PN.

- The 1940 and 1962 spectra of SwSt 1 should be scanned to establish the nature and the extent of the changes that seem to have taken place.

- Spectroscopy of CPD–56°8032 at minimum light is advisable, to look for any spectral changes between minimum and maximum light phases. This might reveal more on the nature of the dust formation episodes.

- As the discrepancy between nebular abundances derived using forbidden and recombination lines is still open (Peimbert 1994), we suggest that the nebula of SwSt 1 be analysed in both ways since its recombination spectrum is particularly strong and easy to measure.

- Unfortunately, radiation-driven wind theory remains incapable of accounting for the observed mass–loss properties of WR stars (e.g. Schmutz 1997). WC–type CSPN may prove to be excellent test cases for any theory under development, so that further stellar wind studies are keenly sought. Ultimately, we would wish to unite atmospheric models and interior models (e.g. Vassiliadis & Wood 1994; Blöcker 1995ab), once radiation–driven theory becomes sufficiently advanced (Kudritzki 1998). This approach has been successfully implemented by Schaerer et al. (1996) for massive stars, and would be essential in directly comparing CSPN properties with evolutionary predictions.

References

1995, *HST Data Handbook*, Space Telescope Science Institute. 2.

Aaquist, O.B. & S., Kwok, 1990. *Astrophys. J.*, **262**, 183.

Acker, A., Stenholm, B. & Tylenda, R., 1989. *Astr. Astrophys. Suppl.*, **77**, 487.

Acker, A., Gorny, S.K. & Stenholm, B., 1996. *Astrophys. Space. Sci.*, **238**, 63.

Acker, A., Gorny, S.K. & Cusinier, F., 1996. *Astr. Astrophys.*, **305**, 944.

Acker, A., Grosdidier, Y. & Durand, S., 1997. *Astr. Astrophys.*, **317**, 51.

Aitken, D.K. & Roche, P.F., 1982. *Mon. Not. R. Astr. Soc.*, **200**, 217.

Aitken, D.K., Roche, P.F., Spenser, P.M. & Jones, B., 1979. *Astrophys. J.*, **233**, 925.

Aitken, D.K., Barlow, M.J., Roche, P.F & Spencer, P.M., 1980. *Mon. Not. R. Astr. Soc.*, **192**, 679.

Auer, L.H. & Mihalas, D., 1969. *Astrophys. J.*, **158**, 641.

Auer, L.H. & Mihalas, D., 1973. *Astrophys. J.*, **184**, 151.

Balick, B., 1987. *Astr. J.*, **94**, 671.

Balick, B., 1993. *Astr. Astrophys. Suppl.*, **183**, 5106.

Balick, B., 1994. *Astrophys. Space. Sci.*, **216**, 13.

Balick, B., Rodgers, B., Hajian, A., Terzian, Y. & Bianchi, L., 1996. *Astr. J.*, **111**, 834.

Barlow, M.J., 1983. In: *Planetary Nebulae, IAU Symposium 103*, ed. Flower, D.R., p. 105, Reidel, Dordrecht.

Barlow, M.J., 1987. *Mon. Not. R. Astr. Soc.*, **227**, 161.

Barlow, M.J. & Hummer, D.G., 1982. In: *Wolf-Rayet Stars: Observations, Physics, Evolution, IAU Symposium 99*, eds. de Loore, C.W.H. & Willis, A.J., Reidel, Dordrecht.

Barlow, M.J. & Storey, P.J., 1993. In: *Planetary Nebulae, IAU Symposium 155*, eds. Weinberger, R. & Acker, A., p. 92.

Barlow, M.J., Blades, J.C. & D.G., Hummer, 1980. *Astrophys. J.*, **241**, 27.

Beals, C.S., 1938. *Trans. I.A.U.*, **6**, 248.

Becker, S.A. & Iben, I. Jr, 1979. *Astrophys. J.*, **232**, 831.

Berrington, K.A., Fon, W.C. & Kingston, A.E., 1982. *Mon. Not. R. Astr. Soc.*, **200**, 347.

Berrington, K.A., Burke, P.G., Dufton, P.L. & Kingston, A.E., 1985. *A. T. and T.*, **33**, 195.

Berrington, K.A., Burke, P.G., Butler, K., Seaton, M.J., Storey, P.J., Taylor, K.T. & Yu Yan, ., 1987. *J. Phys. B: At. Mol. Phys.*, **20**, 6379.

Bidelman, W.P., MacConnell, D.J. & Bond, H.E., 1969. *IAU Circular*, **2089**.

Blaha, M., 1969. *Astrophys. J.*, **157**, 473.

Blöcker, T., 1993. *Acta Astron.*, **43**, 305.

Blöcker, T., 1995. *Astr. Astrophys.*, **297**, 727.

Blöcker, T., 1995. *Astr. Astrophys.*, **299**, 755.

Bond, H.E. & Livio, M., 1990. *Astrophys. J.*, **355**, 568.

Bond, H.E., R., Ciardullo & M., Meakes, 1993. In: *Planetary Nebulae, IAU Symposium 155*, eds. Weinberger, R. & Acker, A., p. 397, Kluwer, Dordrecht.

Bowers, R.L., 1984. *Astrophysics: I. Stars*, Jones and Bartlett, Boston.

Brand, J. & Blitz, L., 1993. *Astr. Astrophys.*, **275**, 67.

Burgess, A., 1959. *Mon. Not. R. Astr. Soc.*, **118**, 477.

Burgess, A., 1965. *Astrophys. J.*, **141**, 1588.

Cannon, C.J., 1973. *Astrophys. J.*, **185**, 621.

Carlson, E.D. & Henize, K.E., 1979. *Vistas in Astronomy*, **23**, 213.

Carrasco, L., Serrano, A. & Costero, R., 1983. *Rev. Mex. Astron. Astrof.*, **8**, 187.

Castor, J.I., 1970. *Mon. Not. R. Astr. Soc.*, **149**, 111.

Castor, J.I., Smith, L.F. & van Blerkom, D., 1970. *Astrophys. J.*, **159**, 1119.

Clayton, G.C., 1996. *Publ. Astr. Soc. Pacif.*, **108**, 225.

Clegg, R.E.S., 1987. *Mon. Not. R. Astr. Soc.*, **229**, 31.

Clegg, R.E.S., 1989. In: *Planetary Nebulae, IAU Symposium 131*, ed. Torres-Peimbert, S., p. 139.

Cochrane, D.M. & McWhirter, R.W.P., 1983. *Physica Scripta*, **28**, 25.

Cohen, M., 1975. *Mon. Not. R. Astr. Soc.*, **173**, 489.

Cohen, M. & Barlow, M.J., 1980. *Astrophys. J.*, **238**, 585.

Cohen, M. & Jones, B.F., 1987. *Astrophys. J.*, **277**, 648.

Cohen, M., Allamandola, L., Tielend, A.G.G.M., Bregman, J., J.P., Simpson, Witteborn, F.C., Wooden, D. & Rank, D., 1986. *Astrophys. J.*, **302**, 737.

Cohen, M., Tielens, A.G.G.M., Bregman, J.D., Witteborn, F.C., Rank, D.M., Allamandola, L.J., Wooden, D.H. & de Muizon, M., 1989. *Astrophys. J.*, **341**, 246.

Conti, P.S., 1976. In: *Proc. 20^{th} Colloq. Int. Ap. Liege*, p. 193.

Conti, P.S., Massey, P. & Vreux, J-M., 1990. *Astrophys. J.*, **354**, 359.

Cottrell, P.L. & Lambert, D.J., 1982. *Astrophys. J.*, **261**, 595.

Cowley, A.P. & Hiltner, W.A., 1969. *Astr. Astrophys.*, **3**, 372.

Crawford, I.A. & Barlow, M.J., 1991. *Astr. Astrophys.*, **249**, 518.

Crowther, P.A. PhD thesis, University of London, 1993.

Crowther, P.A., 1997. *Mon. Not. R. Astr. Soc.*, **209**, 59.

Crowther, P.A. & Bohanan, B., 1997. *Astr. Astrophys.*, **317**, 532.

Crowther, P.A., Hillier, D.J. & Smith, L.J., 1995. *Astr. Astrophys.*, **293**, 172.

Crowther, P.A., Smith, L.J. & Willis, A.J., 1995. *Astr. Astrophys.*, **304**, 269.

Crowther, P.A., Hillier, D.J. & Smith, L.J., 1995. *Astr. Astrophys.*, **293**, 403.

Cudworth, K.M, 1974. *Astr. J.*, **79**, 1384.

Dahari, O. & Osterbrock, D.E., 1984. *Astrophys. J.*, **277**, 648.

Davey, A.R. PhD thesis, University of London, 1995.

Dayal, A. & Beiging, J.H., 1996. *Astrophys. J.*, **472**, 703.

de Freitas Pacheco, J.A. & Veliz, J.G., 1987. *Mon. Not. R. Astr. Soc.*, **227**, 773.

de Freitas Pacheco, J.A., Costa, R.D.D., de Araujo, F.X. & Petrini, D., 1993. *Mon. Not. R. Astr. Soc.*, **260**, 401.

De Marco, O., Degree project, 1993.

Dinerstein, H.L., Sneden, C. & Uglum, J., 1995. *Astrophys. J.*, **447**, 262.

Dopita, M.A., 1997. In: *Planetary Nebulae, IAU 180.* in press.

Drilling, J.S., 1983. *Astrophys. J.*, **270**, 13.

Dufton, P.L., Berrington, K.A., Burke, P.G. & Kingston, A.E., 1978. *Astr. Astrophys.*, **62**, 111.

Eissner, W., Jones, M. & Nussbaumer, H., 1974. *Comput. Phys. Commun.*, **8**, 270.

Feibelman, W.A., 1996. *Publ. Astr. Soc. Pacif.*, **108**, 664.

Fich, M., Blitz, L. & Stark, A.A., 1989. *Astrophys. J.*, **342**, 272.

Flower, D.R., Goharji, A. & Cohen, M., 1984. *Mon. Not. R. Astr. Soc.*, **206**, 293.

Garcia-Berro, E. & Iben, I. Jr., 1994. *Astrophys. J.*, **434**, 306.

Giovanardi, C. & Palla, .F, 1989. *Astr. Astrophys. Suppl.*, **77**, 157.

Giovanardi, C., Natta, A. & Palla, F., 1987. *Astr. Astrophys. Suppl.*, **70**, 269.

Goodrich, R.W. & Dahari, O., 1985. *Astrophys. J.*, **289**, 342.

Gorny, S.K. & Stasinska, G., 1995. *Astr. Astrophys.*, **303**, 893.

Green, L.C., Rush, P.P. & Chandler, C.D., 1957. *Astrophys. J. Suppl.*, **3**, 37.

Greig, W.E., 1972. *Astr. Astrophys.*, **18**, 70.

Grevesse, N. & Anders, A., 1989. In: *Cosmic abundances of matter, AIP 183*, ed. Waddington, C.J., p. 1, American Ins. of Phys., New York.

Grevesse, N., Lambert, D., Sauval, A.J., Dishoeck, E.F., C.B., Farmer & Norton, R.H., 1990. *Astr. Astrophys.*, **232**, 225.

Grevesse, N., Lambert, D., Sauval, A.J., Dishoeck, E.F., C.B., Farmer & Norton, R.H., 1991. *Astr. Astrophys.*, **242**, 488.

Hajian, A.R., Terzian, Y. & Bignell, C., 1993. *Astr. J.*, **106**, 1965.

Hamann, W-R., 1981. *Astr. Astrophys.*, **93**, 353.

Hamann, W-R., 1985. *Astr. Astrophys.*, **148**, 364.

Hamann, W.-R., 1996. *Astrophys. Space. Sci.*, **23**, 31.

Hamann, W-R. & Kösterke, L., 1993. In: *Planetary Nebulae, IAU Symposium 155*, eds. Weinberger, R. & Acker, A., p. 87, Kluwer, Dordrecht.

Hamann, W-R. & Wessolowski, U., 1990. *Astr. Astrophys.*, **222**, 171.

Hamann, W-R., Leuenhagen, U., Koesterke, L. & Wessolowski, U., 1992. *Astr. Astrophys.*, **255**, 200.

Handler, G., 1996. *IAU Circular*, **4283**.

Harrington, J.P. PhD thesis, Ohio State University, 1967.

Harrington, J.P., 1968. *Astrophys. J.*, **152**, 943.

Harrington, J.P., 1972. *Astrophys. J.*, **176**, 127.

Harrington, J.P., Seaton, M.J., Adams, S. & Lutz, J.H., 1982. *Mon. Not. R. Astr. Soc.*, **199**, 517.

Hayes, M.A. & Nussbaumer, H., 1984. *Astr. Astrophys.*, **134**, 194.

Hazard, C., Terlevich, B., Morton, D.C., W.L.W., Sargent & G., Ferland, 1980. *Nature*, **285**, 463.

Hempe, K. & Schönberg, K., 1986. *Astr. Astrophys.*, **160**, 141.

Henize, K.G., 1967. *Astrophys. J. Suppl.*, **14**, 125.

Henry, R.J.W., 1970. *Astrophys. J.*, **161**, 315.

Herbig, G.H., 1995. *Ann. Rev. Astr. Astrophys.*, **33**, 19.

Herbig, G.H. & Boyarchuck, A.A., 1968. *Astrophys. J.*, **153**, 397.

Hidalgo, M., 1968. *Astrophys. J.*, **153**, 981.

Hillier, D.J. PhD thesis, Australian National University, Canberra, 1983.

Hillier, D.J., 1987. *Astrophys. J. Suppl.*, **63**, 947.

Hillier, D.J., 1988. *Astrophys. J.*, **327**, 822.

Hillier, D.J., 1989. *Astrophys. J.*, **347**, 392.

Hillier, D.J., 1990. *Astr. Astrophys.*, **231**, 116.

Hillier, D.J., 1990. *Astr. Astrophys.*, **231**, 111.

Hillier, D.J., 1991. *Astr. Astrophys.*, **247**, 455.

Hillier, D.J. & Miller, D.L., 1997. *Astr. Astrophys. Suppl.* in press.

Hoffleit, D., 1958. *Astrophys. J.*, **63**, 78.

Houziaux, L. & Heck, A., 1982. In: *Wolf-Rayet Stars: Observations, Physics, Evolution, IAU Symposium 99*, eds. de Loore, C.W.H. & Willis, A.J., p. 139, Reidel, Dordrecht.

Howard, J.W., Henry, R.B.C. & McCartney, S., 1997. *Mon. Not. R. Astr. Soc.*, **284**, 465.

Howarth, I.D., 1983. *Mon. Not. R. Astr. Soc.*, **203**, 301.

Howarth, I.D. & Murray, J., 1988. *Starlink User Note*, **50**.

Howarth, I.D. & Murray, J., 1991, *Starlink User Note*, Rutherford Appleton Laboratory. 50.13.

Hu, J.Y. & Bibo, E.A., 1990. *Astr. Astrophys.*, **234**, 435.

Huggins, P.J., Bachillier, R., Cox, P. & Forveille, T., 1996. *Astr. Astrophys.*, **315**, 284.

Hummer, D.G., Kunasz, C.V. & Kunasz, P.B., 1973. *Comput. Phys. Commun.*, **6**, 38.

Humphreys, R.M., 1987. *Astrophys. J. Suppl.*, **38**, 309.

Husfeld, D., Butler, K., Heber, U. & Drilling, J.S., 1989. *Astr. Astrophys.*, **222**, 150.

Iben, I. Jr., 1975. *Astrophys. J.*, **196**, 525.

Iben, I. Jr., 1984. *Astrophys. J.*, **277**, 333.

Iben, I. Jr., 1985. *Quart. J. R. astr. Soc.*, **26**, 1.

Iben, I. Jr., 1996. In: *Hydrogen-Deficient Stars*, eds. Jeffery, C.S. & Heber, U., p. 409, ASP Conf. Ser., San Francisco.

Iben, I. Jr. & Livio, M., 1993. *Publ. Astr. Soc. Pacif.*, **105**, 1373.

Iben, I. Jr. & Renzini, A., 1983. *Ann. Rev. Astr. Astrophys.*, **21**, 271.

Iben, I. Jr. & R.T., Rood, 1970. *Astrophys. J.*, **161**, 587.

Iben, I. Jr. & Tutukov, A.V., 1985. *Astrophys. J. Suppl.*, **58**, 661.

Iben, I. Jr. & Tutukov, A.V., 1986. *Astrophys. J.*, **311**, 742.

Iben, I. Jr. & Tutukov, A.V., 1993. *Astrophys. J.*, **418**, 343.

Iben, I. Jr., Kaler, J.B., Truran, J.W. & Renzini, A., 1983. *Astrophys. J.*, **264**, 605.

Iben, I. Jr., Tutukov, A.V. & Yungelson, L.R., 1996. *Astrophys. J.*, **456**, 750.

Ike, V., Balick, B. & Frank, A., 1992. *Astr. Astrophys.*, **253**, 224.

Ilmas, M. & Nugis, T., 1982. *Calculation of the Emission-line Spectrum of HeI*, Academy of the Sciences of the Estonian SSR, Tartu.

Jacoby, G. & Ford, H., 1983. *Astrophys. J.*, **266**, 298.

Jeffery, C.S., 1994. *CCP7 Newslett.*, **21**, 27.

Jeffery, C.S., 1995. *Astr. Astrophys.*, **299**, 135.

Kaufman, V. & Sugar, J., 1986. *J. Phys. Chem. Ref. Data*, **15**, 321.

Keenan, F.P., Aller, L.H., Bell, K.L., Hyung, S., McKenna, F.C. & Ramsbottom, C.A., 1996. *Mon. Not. R. Astr. Soc.*, **281**, 107.

Kingdon, J.B. & G.J., Ferland, 1995. *Astrophys. J.*, **442**, 741.

Kingsburgh, R.L. & Barlow, M.J., 1994. *Mon. Not. R. Astr. Soc.*, **271**, 257.

Kingsburgh, R.L., Barlow, M.J. & Storey, P.J., 1995. *Astr. Astrophys.*, **295**, 75.

Klein, R.I. & Castor, J.I., 1978. *Astrophys. J.*, **220**, 902.

Knapp. G. R., Phillips, T. G., Leighton, R. B., Lo, K.Y., Wannier, P.G., Wotten, H.A. & Huggins, P.J., 1982. *Astrophys. J.*, **252**, 616.

Koesterke, L., Hamann, W-R. & Kosmol, P., 1992. *Astr. Astrophys.*, **255**, 490.

Kohoutek, L., 1996. In: *Hydrogen-deficient Stars, ASP 96*, eds. Jeffery, C.S. & Heber, U., p. 219, Astronomical Society of the Pacific, San Francisco, CA.

Kösterke, L. & Hamann, W.-R., 1995. *Astr. Astrophys.*, **229**, 503.

Kösterke, L. & Hamann, W.-R., 1997. *Astr. Astrophys.*, **320**, 91.

Kudritzki, R.P., Pauldrach, A.W.A., Puls, J. & Abbott, D.C., 1989. *Astr. Astrophys.*, **219**, 205.

Kurucz, R.L., 1970. *Atlas: A Computer Program for calculating Model Stellar Atmospheres, SAO*, **Spec. Rept. 309**.

Kurucz, R.L., 1991. In: *Precision Photometry: Astrophysics of the Galaxy*, eds. Philips, D., Upren, & Jones, , L. Davis Press.

Kwok, S., 1981. In: *Physical Processes in Red Giants*, eds. Iben, I. Jr. & Renzini, A., p. 421.

Kwok, S., Purton, C.F. & Fizgerald, P.M., 1978. *Astrophys. J. (Letters).*, **219**, 127.

Kwok, S., Purton, C.R. & Keenan, D.W., 1981. *Astrophys. J.*, **250**, 232.

Langer, G.E., Kraft, R.P. & Anderson, K.S., 1974. *Astrophys. J.*, **189**, 509.

Lawson, W.A. & Jones, A.F., 1992. *Observatory*, **112**, 231.

Lawson, W.A. & Jones, A.F., 1996. In: *Hydrogen-deficient Stars, ASP 96*, eds. Jeffery, C.S. & Heber, U., p. 151, Astronomical Society of the Pacific, San Francisco, CA.

Le Bertre, T., Epchtein, N., Gouiffes, C., Heydari-Malayeri, M. & Perrier, C., 1989. *Astr. Astrophys.*, **225**, 417.

Leuenhagen, U. & Hamann, W.-R., 1994. *Astr. Astrophys.*, **283**, 567.

Leuenhagen, U. & Hamann, W.-R., 1997. *Astr. Astrophys.* in press.

Leuenhagen, U., Heber, U. & Jeffery, C.S., 1994. *Astr. Astrophys. Suppl.*, **103**, 445.

Leuenhagen, U., Hamann, W.-R. & Jeffery, C.S., 1996. *Astr. Astrophys.*, **312**, 167.

Leung, C.M., 1976. *J. Quant. Spectrosc. Radiat. Transfer.*, **16**, 559.

Liu, X.-W., Storey, P.J., Barlow, M.J. & Clegg, R.E.S., 1995. *Mon. Not. R. Astr. Soc.*, **272**, 369.

Loreta, E., 1934. *Astronomische Nachrichten*, **254**, 151.

Lucy, L.B. & Abbott, D.C., 1993. *Astrophys. J.*, **405**, 738.

Lundmark, K., 1921. *Publ. Astr. Soc. Pacif.*, **33**, 314.

Lynds, B.T., 1980. *Astr. J.*, **85**, 1046.

Manchado, A., Guerrero, M.A., Stanghellini, L. & Serra-Ricart, M., 1996. *The IAC Morphological Catalogue of Northern Galactic Planetary Nebulae*, p. 150. IAC, Tenerife, Spain.

Martin, W.C., Kaufman, V. & Mussgrove, A., 1993. *J. Phys. Chem. Ref. Data*, **22**, 1179.

McGraw, J.T., Liebert, J., Starrfield, S.G. & Green, R., 1979. In: *White Dwarfs and Variable Degenerate Stars, IAU Coll. 53*, p. 377.

Mellema, G., 1997. *Astr. Astrophys.*, **321**, 29.

Mendez, R. & V.S., Niemela, 1982. In: *Wolf-Rayet Stars: Observations, Physics, Evolution, Proc. IAU Symposium 99*, eds. De Loore, C.W.H. & Willis, A.J., p. 457, Reidel, Dordrecht.

Mendez, R.H., Miguel, L.H., Heber, U. & Kudritzki, R.P., 1986. In: *Hydrogen Deficient Stars and Related Objects*, eds. Hunger, K., Schönberner, D. & Rao, N.K., p. 323, Reidel, Dordrecht.

Mendez, R.H., Herrero, A., Manchado, A. & Kudritzki, R.-P., 1991. *Astr. Astrophys.*, **252**, 265.

Mendoza, C., 1983. In: *Planetary Nebulae, Proc. IAU Symposium 103*, ed. Flower, D.R., p. 143, Reidel, Dordrecht.

Mendoza, C. & Zeippen, C.J., 1982. *Mon. Not. R. Astr. Soc.*, **198**, 127.

Menzies, J.W. & Wolstencroft, R.D., 1990. *Mon. Not. R. Astr. Soc.*, **247**, 177.

Mihalas, D., 1967. *Astrophys. J.*, **149**, 169.

Mihalas, D., 1978. *Stellar Atmospheres*, W.H. Freeman, 2nd edition.

Mihalas, D. & Stone, M.E., 1968. *Astrophys. J.*, **151**, 293.

Mihalas, D., Kunasz, B. & Hummer, D.G., 1975. *Astrophys. J.*, **202**, 465.

Mihalas, D., Kunasz, B. & Hummer, D.G., 1976. *Astrophys. J.*, **206**, 515.

Milne, D.K. & Aller, L.H., 1975. *Astr. Astrophys.*, **38**, 183.

Milne, D.K. & Aller, L.H., 1982. *Astr. Astrophys. Suppl.*, **50**, 209.

Minkowski, R., 1965. *Galactic Structure*, p. 321.

Monk, D.J., Barlow, M.J. & Clegg, R.E.S., 1988. *Mon. Not. R. Astr. Soc.*, **234**, 583.

Moore, C.E., 1970. *Nat. Stand. Ref. Data Ser., Nat. Bur. Stand. (U.S.)*, **3**(3).

Nussbaumer, H. & Rusca, C., 1979. *Astr. Astrophys.*, **72**, 129.

Nussbaumer, H. & Storey, P.J., 1978. *Astr. Astrophys.*, **64**, 139.

Nussbaumer, H. & Storey, P.J., 1981. *Astr. Astrophys.*, **99**, 177.

Nussbaumer, H. & Storey, P.J., 1982. *Astr. Astrophys.*, **115**, 205.

Nussbaumer, H. & Storey, P.J., 1983. *Astr. Astrophys.*, **126**, 75.

Nussbaumer, H. & Storey, P.J., 1984. *Astr. Astrophys. Suppl.*, **56**, 293.

Oke, J.B., 1974. *Astrophys. J. Suppl.*, **27**, 21.

Oke, J.B., 1992. *Astr. J.*, **92**, 1621.

O'Keefe, J.A., 1939. *Astrophys. J.*, **90**, 294.

Olson, G.L., Auer, L.H. & Buckler, J.R., 1986. *J. Quant. Spectrosc. Radiat. Transfer.*, **35**, 431.

Osterbrock, D.E., 1974. *Astrophysics of Gaseous Nebulae*, Freeman, San Francisco.

Osterbrock, D.H., Tran, H.D. & Vielleux, S., 1992. *Astrophys. J.*, **389**, 305.

Pascoli, G., Leclercq, J. & Poulain, B., 1992. *Publ. Astr. Soc. Pacif.*, **104**, 182.

Pascoly, G., 1992. *Publ. Astr. Soc. Pacif.*, **104**, 350.

Pazcynski, B., 1970. *Acta Astron.*, **20**, 47.

Pazcynski, B., 1971. *Acta Astron.*, **21**, 417.

Peach, G., Saraph, H.E. & Seaton, M.J., 1988. *J. Phys. B: At. Mol. Phys.*, **21**, 3669.

Peimbert, M., 1994. In: *The analysis of emission lines*, eds. Williams, R. & Livio, M., p. 165, Cambridge Univ. Press, Cambridge.

Peimbert, M. & Torres-Peimbert, S., 1983. In: *Planetary Nebulae, IAU Symposium 103*, ed. Flower, D.R., p. 233, Reidel, Dordrecht.

Pembert, E. & Serrano, A., 1980. *Rev. Mex. Astron. Astrof.*, **5**, 9.

Perek, L., 1971. *Bulletin. Astr. Inst. Czech.*, **22**, 103.

Perek, L. & Kohoutek, L., 1967. *Catalogue of Galactic Planetary Nebulae*, Czechoslavakian Academy of Science, Prague.

Pollacco, D.L. & Hill, P.W., 1994. *Mon. Not. R. Astr. Soc.*, **267**, 692.

Pollacco, D.L., Kilkenny, D., Marang, F., van Wyk, F. & Roberts, G., 1992. *Mon. Not. R. Astr. Soc.*, **256**, 669.

Popper, D.M., 1942. *Publ. Astr. Soc. Pacif.*, **54**, 160.

Pottasch, S.R., 1996. *Astrophys. Space. Sci.*, **238**, 17.

Pottasch, S.R., 1997. In: *Planetary Nebulae, IAU 180.* in press.

Pottasch, S.R., Baud, B., Beintema, D., Emerson, J., Harris, S., Habing, H.J., Houck, J., Jennings, R. & Marsden, P., 1984. *Astr. Astrophys.*, **138**, 10.

Pradhan, A.K., 1976. *Mon. Not. R. Astr. Soc.*, **177**, 31.

Puls, J., 1991. *Astr. Astrophys.*, **248**, 581.

Purton, C.R., Fedelman, P.A., Marsh, K.A., Allen, D.A. & Wright, A.E., 1982. *Mon. Not. R. Astr. Soc.*, **198**, 321.

Rao, N.K., 1987. *Quart. J. R. astr. Soc.*, **28**, 261.

Rao, N.K., Giridhar, S. & Nandy, K., 1990. *Astr. Astrophys.*, **234**, 410.

Reimers, D., 1975. *Mem. R. Soc. Sci. Liege, 6e*, **8**, 369.

Robert, C., 1994. *Astrophys. Space. Sci.*, **221**, 137.

Roche, P.F., Allen, D.A. & Bailey, J.A., 1986. *Mon. Not. R. Astr. Soc.*, **220**, 7.

Rubin, R.H., 1989. *Astrophys. J. Suppl.*, **69**, 897.

Rybicki, G.B., 1991. In: *Stellar Atmospheres: Beyond Classical Models, NATO Advanced Research Workshop*, eds. Crivellari, L., Hubeny, I. & D.G., Hummer, p. 1, Kluwer, Dordrecht.

Sabbadin, F., 1980. *Astr. Astrophys.*, **84**, 216.

Sabbadin, F. & Bianchini, A., 1979. *Publ. Astr. Soc. Pacif.*, **91**, 276.

Sahai, R., Wotten, A. & Clegg, R.E.S., 1993. In: *Planetary Nebulae, IAU Symposium 155*, eds. Weinberger, R. & Acker, A., p. 229, Kluwer, Dordrecht.

Sakhibullin, N.A., Auer, L.H. & van der Hucht, K.A., 1982. *Sov. Astron.*, **26**, 563.

Sanduleak, N., 1971. *Astrophys. J.*, **164**, 71.

Sawey, P.M.J. & Berrington, K.A., 1993. *Atomic Data and Nuclear Data Tables*, **55**, 81.

Scharmer, G.B., 1981. *Astrophys. J.*, **249**, 720.

Schmutz, W., 1997. *Astr. Astrophys.*, **321**, 268.

Schönberner, D., 1975. *Astr. Astrophys.*, **44**, 381.

Schönberner, D., 1979. *Astr. Astrophys.*, **79**, 108.

Schönberner, D., 1981. *Astr. Astrophys.*, **103**, 119.

Schönberner, D., 1996. In: *Hydrogen-Deficient Stars*, eds. Jeffery, C.S. & Heber, U., p. 433, ASP Conf. Ser., San Francisco.

Schönberner, D. & Weidemann, V., 1981. In: *Physical processes in red giant*, p. 463, Reidel, Dordrecht.

Schulte-Ladbeck, R.E., Eenes, P.R.J. & Davis, K., 1995. *Astrophys. J.*, **454**, 917.

Schwartz, H.E., Corradi, R.L.M. & Melnik, J., 1992. *Astr. Astrophys. Suppl.*, **96**, 23.

Seaton, M.J., 1958. *Rev. Mod. Phys.*, **30**, 979.

Seaton, M.J., 1979. *Mon. Not. R. Astr. Soc.*, **187**, 73P.

Seitter, W.C., 1987. *Messanger*, **50**, 14.

Shaw, R.A. *The evolution of Planetary Nebula Nucleii.* PhD thesis, The University of Illinois at Urbana-Champaign, 1985.

Shklovsky, I.S., 1956. *Astr. Zh.*, **33**, 515.

Shull, J.M & Van Steenberg, M.E., 1985. *Astrophys. J.*, **294**, 559.

Sion, E.M., Liebert, J. & Wesemael, F., 1985. *Astrophys. J.*, **292**, 477.

Smith, L.F., 1968. *Mon. Not. R. Astr. Soc.*, **138**, 109.

Smith, L.F., 1968. *Mon. Not. R. Astr. Soc.*, **140**, 409.

Smith, L.F. & Aller, L., 1969. *Astrophys. J.*, **157**, 1245.

Smith, L.F. & Aller, L., 1971. *Astrophys. J.*, **164**, 275.

Smith, L.F. & Hummer, D.G., 1988. *Mon. Not. R. Astr. Soc.*, **230**, 511.

Smith, L.F. & Maeder, A., 1991. *Astr. Astrophys.*, **241**, 77.

Smith, L.F., Shara, M.M. & Moffat, A.F.J., 1990. *Astrophys. J.*, **358**, 229.

Smith, L.F., Shara, M.M. & Moffat, A.F.J., 1996. *Mon. Not. R. Astr. Soc.*, **281**, 163.

Smith, L.J., Crowther, P.A. & Prinja, R.K., 1994. *Astr. Astrophys.*, **281**, 833.

Snyder, , 1990. *The Restoration of HST Images and Spectra*, p. 56. STScI.

Sobolev, V.V., 1958. *Theoretical Astrophysics*, p. 511. Permagon Press, London.

Sobolev, V.V., 1960. *Moving Envelopes of Stars*. Harvard Uni. Press, Cambridge, Mass.

Soker, N., 1997. In: *Planetary Nebulae, IAU Symposium 188*, Kluwer, Dordrecht. in press.

Soker, N. & Harpaz, A., 1992. *Publ. Astr. Soc. Pacif.*, **104**, 923.

Soker, N. & Livio, M., 1989. *Astrophys. J.*, **339**, 268.

Stafford, R.P., Bell, K.L., Hibbert, A. & Wijesundera, W.P., 1994. *Mon. Not. R. Astr. Soc.*, **268**, 816.

Stanghellini, L., 1996. *Astrophys. Space. Sci.*, **238**, 137.

Stanghellini, L. & Pasquali, A., 1995. *Astrophys. J.*, **452**, 286.

Storey, P.J., 1981. *Mon. Not. R. Astr. Soc.*, **195**, 27.

Storey, P.J., 1983. In: *Planetary Nebulae, Proc. IAU Symposium 103*, ed. Flower, D.R., p. 199, Reidel, Dordrecht.

Storey, P.J. & Hummer, D., 1991. *Comput. Phys. Commun.*, **66**, 129.

Storey, P.J. & Hummer, D.G., 1995. *Mon. Not. R. Astr. Soc.*, **272**, 41.

Stoy, R.H., 1933. *Mon. Not. R. Astr. Soc.*, **93**, 588.

Surendiranath, R. & Rao, N.K., 1995. *Mon. Not. R. Astr. Soc.*, **275**, 685.

Swings, P. & Struve, O., 1940. *Proc. Natn. Acad. Sci.*, **26**, 454.

Swings, P. & Struve, O., 1943. *Astrophys. J.*, **97**, 194.

Thackeray, A.D., 1977. *Observatory*, **97**, 165.

Torres, A.V. & P., Massey, 1987. *Astrophys. J. Suppl.*, **65**, 459.

Turner, D.G., 1982. *Publ. Astr. Soc. Pacif.*, **94**, 655.

Tylenda, R., Acker, A. & Stenholm, B., 1993. *Astr. Astrophys. Suppl.*, **102**, 595.

Vacca, W.D., Garmany, C.D. & Shull, M.J., 1996. *Astrophys. J.*, **460**, 914.

van der Hucht, K.A., 1996. *Astrophys. Space. Sci.*, **280**, 963.

van der Hucht, K.A., Conti, P.S., Lundström, I. & Stenholm, B., 1981. *Space Sci. Rev.*, **28**, 227.

van der Hucht, K.A., Conti, P.S., Lundstrom, I. & B., Stenholm, 1981. *Space Sci. Rev.*, **28**, 227.

van der Hucht, K.A., Hidayat, B., Admiranto, A.G., Supelli, K.R. & Doom, C., 1988. *Astr. Astrophys.*, **199**, 217.

Van Regemorter, H., 1962. *Astrophys. J.*, **136**, 906.

Vassiliadis, E. & Wood, P.R., 1994. *Astrophys. J. Suppl.*, **92**, 125.

Walton, N.A., Pottasch, S.R., Reay, N.Y. & Taylor, A.R., 1988. *Astr. Astrophys.*, **200**, 21.

Warner, B., 1967. *Mon. Not. R. Astr. Soc.*, **137**, 119.

Webster, B.L. & Glass, I.S., 1974. *Mon. Not. R. Astr. Soc.*, **166**, 491.

Werner, K., Heber, U. & Hunger, K., 1991. *Astr. Astrophys.*, **251**, 147.

Wessolowski, U., Schmutz, W. & Hamann, W-R., 1988. *Astr. Astrophys.*, **194**, 160.

Weymann, R.J. & Williams, R.E., 1969. *Astrophys. J.*, **157**, 1201.

Whittet, D.C.B, 1992. *Dust in the galactic enviroment*, p. 11. Institute of Physics Publishing.

Wiese, L.L., Smith, M.W. & Glennon, B.M., 1966. *Atomic Transition Probabilities*, volume 1, NSRDS-NBS.

Wiese, L.L., Smith, M.W. & Miles, B.M., 1968. *Atomic Transition Probabilities*, volume 1, NSRDS-NBS.

Willis, A.J., Dessart, L., Crowther, P.A., Morris, P.W., Maeder, A., Conti, P.S. & van der Hucht, K.A., 1897. *Mon. Not. R. Astr. Soc.*, **290**, 371.

Willis, A.J., Schild, H. & Smith, L.J., 1992. *Astr. Astrophys.*, **261**, 419.

Woitke, P., Goeres, A. & Sedelmyr, E., 1996. *Astr. Astrophys.*, **311**, 927.

Wolf, C.J.E. & Rayet, G., 1867. *Comptes Rendues.*, **65**, 292.

Yungelson, L.R., Tutukov, A.V. & Iben, I. Jr., 1993. *Astrophys. J.*, **418**, 794.

Zanstra, H., 1931. *Publ. Dom. Astrophys. Obs.*, **4**, 209.

Zeippen, C.J., 1982. *Mon. Not. R. Astr. Soc.*, **198**, 111.

Zijlstra, A.A., Pottasch, S.R. & C., Bignell, 1989. *Astr. Astrophys. Suppl.*, **79**, 329.

Zuckerman, B. & Aller, L.H., 1986. *Astrophys. J.*, **301**, 772.

Appendix A

The lightcurves of CPD–56°8032, He 2–113 and SwSt 1

CPD–56°8032 was discovered to undergo light declines by Pollacco et al. (1992). Its lightcurve has been followed visually since early 1988 by Albert Jones. Since then the star has experience two declines (see Fig. A.1), the first in 1990–1991 and the second in May–June 1994. Both events have an amplitude of ~1.5 mag.

Superimposed on this variation Lawson and Jones (1996) noticed a persistent variability with amplitude 0.1–0.4 mag. A power spectrum analysis of the lightcurve (rectified to eliminate the deep declines see Figure A.2) revealed one significant periodicity with period 122.1 days and a mean half amplitude of 0.076 mag. However, Lawson et al. (in prep.) noticed that the visual photometry of A. Jones compares very badly with the data of Pollacco et al. (1992). Pollacco et al. detect a sharp minimum, followed by a 50 day period almost at constant luminosity, while A. Jones' data suggest, for the same period, that CPD–56°8032 is rising from minimum on the 122–day period. Lawson et al. suggest that the comparison star used by A. Jones is the actual 122–day variable.

The origin of the lightcurve declines is probably in the formation of dust in the stellar envelope. This phenomenon would then be equivalent to the episodes of dust formation experienced by R Cor Bor star (see Chapter 1), whereby dust condenses at about 2 R_*

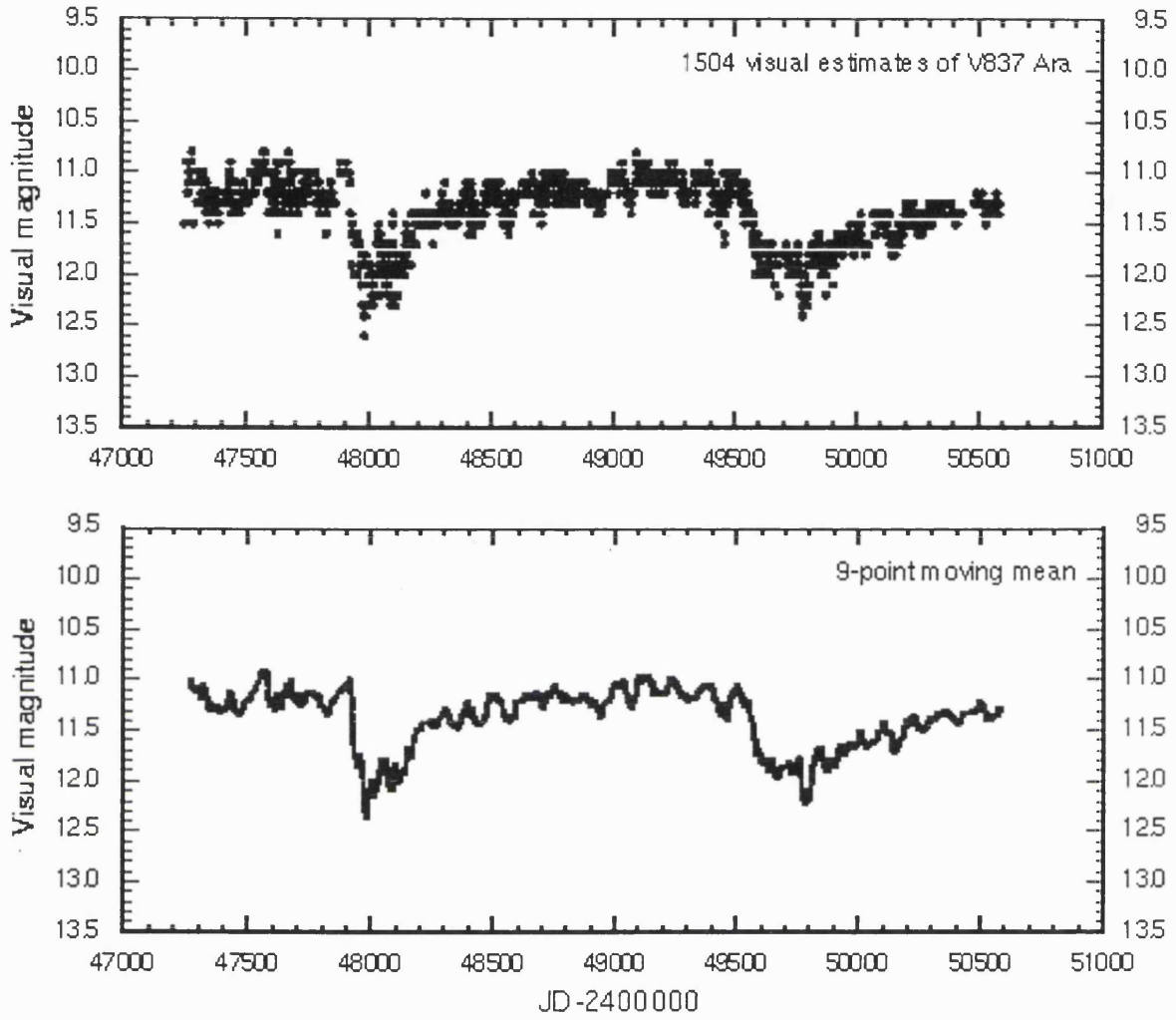

Figure A.1: Visual lightcurve and 9–point moving mean of CPD–56°8032

(Clayton 1996, Woitke, Gores and Sedelmayr 1996) and is blown off by photon pressure obliterating the photosphere. Support to this hypothesis is given by the WC–type star V 348 Sgr (see Chapter 4), which also exhibits similar, albeit deeper, declines (Hoffleit 1958, see also Leuenhagen, Heber and Jeffery 1994). Neither V 348 Sgr nor CPD–56°8032 appear to be spectroscopically variable, although our spectroscopy of CPD–56°8032 was obtained at maximum light and spectroscopy prior to 1992 cannot be checked against a lightcurve.

A lightcurve for He 2–113 is shown in Fig. A.3. The magnitude scale is the same as for CPD–56°8032 for comparison. As can be seen He 2–113 is fainter and in the early

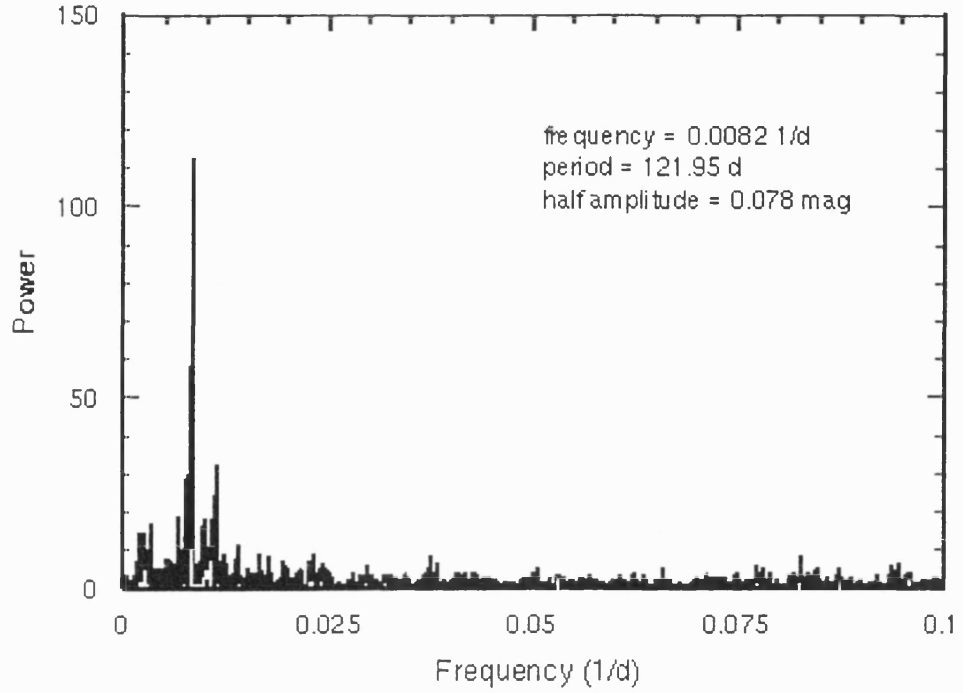

Figure A.2: Power spectrum obtained from the visual lightcurve of CPD–56°8032

data (prior to JD2449400) its variation shows a one–year cycle, due to a changing airmass with the star's position throughout the year. The later data provided by A. Jones, shows the seasonal variation only very weakly: the main factors are probably A. Jones' choice of comparison stars and that he's got used to the field. It's very hard to do good visual photometry on either very blue or red stars since the flux distribution of the stars is unlike the eye's response. This means that any change in colour, like airmass, is easily over–compensated by the eye.

We have no reason to believe that there is any further light variation in the visual curve of He 2–113, at least with amplitude greater than 0.1 mag. If the declines experienced by CPD–56°8032 are due, as for the R Cor Bor stars, to episodic dust formation in the stellar envelope, He 2–113 might not have experienced such an event in the time of the observations. Alternatively it might have ejected dust clouds in a different line of sight. This star is currently being monitored together with CPD–56°8032 and other southern WC central stars.

SwSt 1's lightcurve is shown in Figure A.4. It presents a fair amount of scatter. The

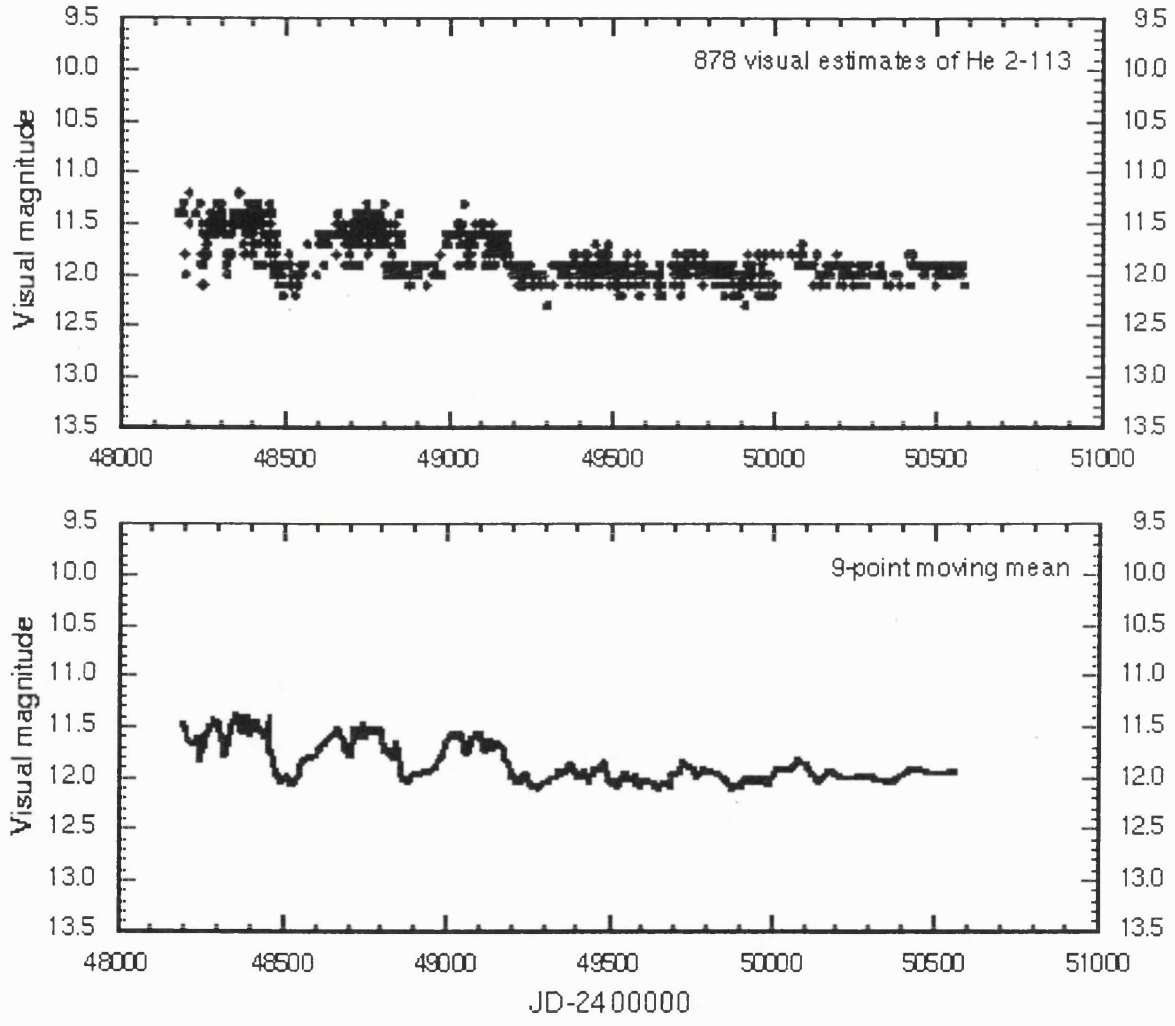

Figure A.3: Visual lightcurve and 9–point moving mean for He 2–113

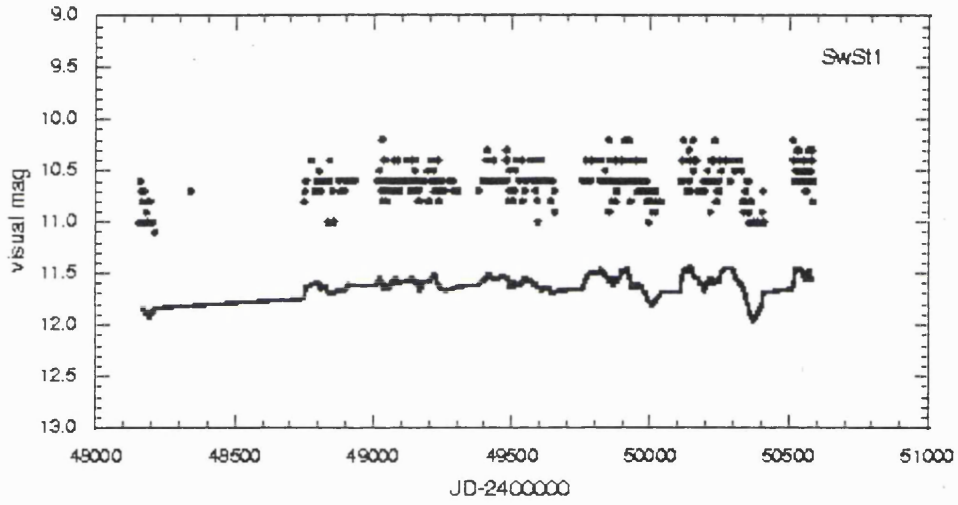

Figure A.4: Visual lightcurve and 9–point moving mean for SwSt 1

Fourier transform analysis (see Figure A.5) shows a 370–day peak (essentially 365 days, given the quality of the data and the resolution of the Fast Fourier Transform), a 185–day harmonic (because of the asymmetry of the yearly datasets), a 322–day and a 166–day cycles (probably from the width of the yearly datasets, i.e. from the window function), and then features of shorter period which we interpret as noise. The data are therefore dominated by airmass–related variations. We do not believe there to be any variation related to physical changes present in the star.

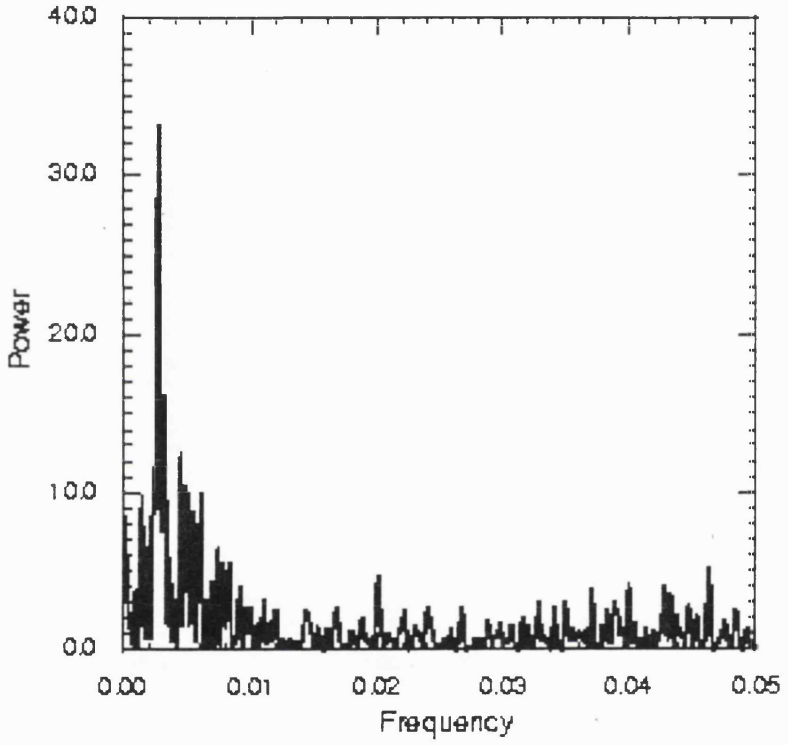

Figure A.5: Power spectrum of the lightcurve of SwSt 1

Appendix B

The energies of the $2s^2nf$ and $2s^2ng$ states of C^+

For the $2s^2nf$ series of C^+, energies are measured for $n \leq 7$, while for the $2s^2ng$ series measurements exist up to n=8. The quantum defect μ is defined by:

$$I_{nl} = \frac{-Z^2R}{(n-\mu^2)} \tag{B.1}$$

where I_{nl} is the ionization potential of state with principal quantum number n and orbital quantum number l, Z is the effective charge (Z=2 for C^+) and

$$R_C = \frac{R_\infty}{1 + m_e/Am_u}$$

is the Rydberg constant for carbon, where R_∞=109737.3, m_e is the electron mass, m_u is the atomic mass unit and A is the atomic mass number.

For a one–channel problem, the quantum defect, is related to the reactance matrix of quantum defect theory by (Seaton 1983)

$$\mathcal{R} = \tan(\pi\mu) \tag{B.2}$$

The reactance matrix for the $2s^2nf\,^2F^o$ series has poles at the energies of the C^+ $2s2p(^3P^o)nd$ states. Considering only the lowest of these poles, we fit the reactance matrix to a function

Table B.1: Energies for states $2s^2nf$ and $2s^2ng$ deduced by quantum defect extrapolation

State	Energy (cm^{-1})
8f	189759.7
9f	191211.1
10f	192248.8
9g	191238.3
10g	192269.8

of the energy variable $\epsilon = -1/(n-\mu)^2$,

$$\mathcal{R} = a + b\epsilon + \frac{c}{(\epsilon - \epsilon_0)}, \tag{B.3}$$

where $\epsilon_0 = 0.00752$ corresponds to the position of the $3d'(^2F^o)$ state. Values of $\mathcal{R}$ and hence μ can then be obtained for higher members of the $2s^2nf$ series. The resulting energies are given in Table B.1 relative the ground state of C^+.

For the $2s^2ng$ series a different procedure is used. The quantum defects for this series can only be perturbed by states of the $2s2p(^3P^o)nf$ series, whose lowest member $n = 4$ lies at sufficiently high energy that its effect can be neglected. We therefore analyse the quantum defects of the $2s^2ng$ in terms of the dipole polarizability, α_d of the $2s^2$ electron configuration. The quantum defect can expressed in terms of the polarizability by

$$\alpha_d = \frac{2\mu}{Z^2 n^3 P(nl)}, \tag{B.4}$$

where

$$P(nl) = \frac{(3n^2 - l^2 - l)}{2n^5(l-\frac{1}{2})l(l+\frac{1}{2})(l+1)(l+\frac{3}{2})}. \tag{B.5}$$

From the experimental energies for the 5g and 6g states we deduce $\alpha_d = 3.9$. Term energies for the higher members of the ng series can then be inferred from the above two equations and the results are given in Table B.1.

Appendix C

The Spectra of CPD–56°8032 and He 2–113

In this Appendix we present the optical spectra of CPD–56°8032 and He 2–113, taken at the AAT in May 1993 with UCL Echelle Spectrograph. Details of the observations and data reduction are presented in Chapter 3. In this atlas the spectra are rectified and the spectrum of CPD–56°8032 is offset by an additional constant of 1.

Spectral lines are identified and labeled in the figures by their wavelength, ion and multiplet number. For carbon we used tables of Moore (1970), for O II lines we used the tables of Martin, Kaufman and Mussgrove (1993). Other lines were identified with the help of tables by Wiese, Smith and Glennon (1966) and Wiese, Smith and Miles (1968).

Ideally all the components of each multiplet would individually be labeled, but this could be done only in non–crowded regions. When space did not allow, we adopted one of two methods: we either marked all the multiplet components with dashes joined by a horizontal line above which only ion and multiplet number where written, or we simply marked the strongest and/or unblended multiplet components.

For strong lines (i.e. nebular lines) the dash marking the exact position is inside the line, while the label is offset horizontally. Unidentified lines are labeled with the feature's wavelength and a questionmark .

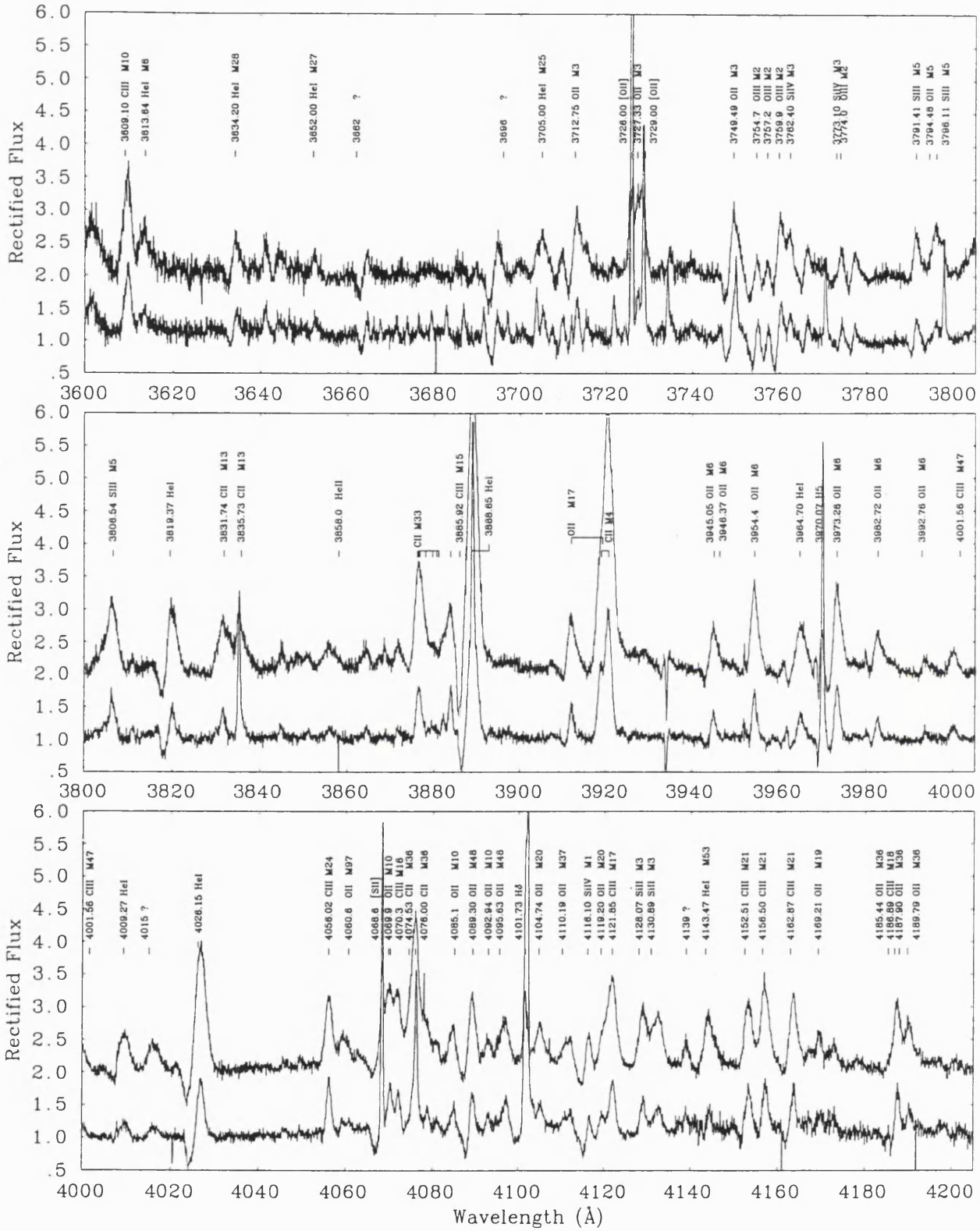

Figure C.1: UCLES spectra of CPD–56°8032 (upper) and He 2–113 (lower) between 3600 and 4200 Å

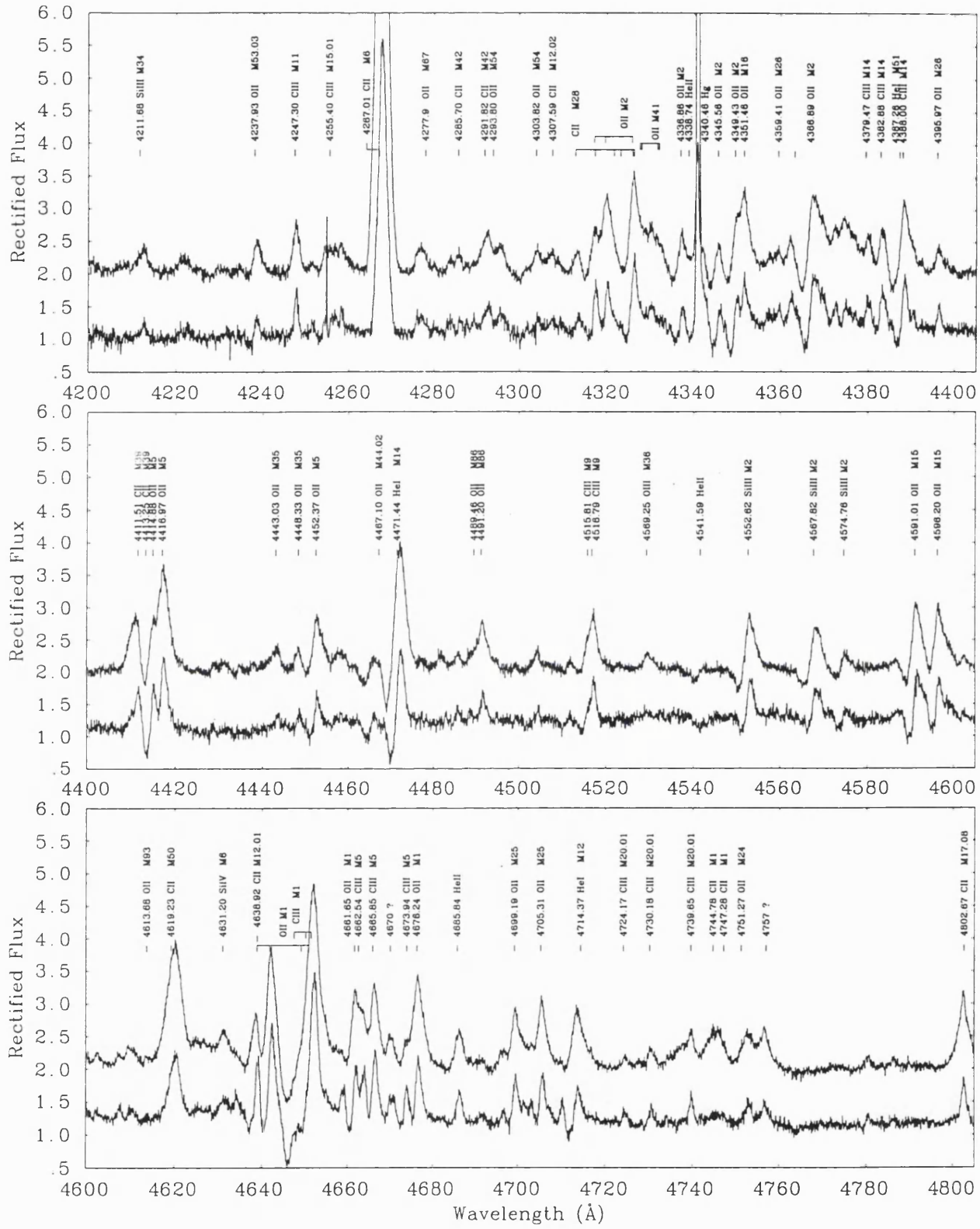

Figure C.2: UCLES spectra of CPD–56°8032 (upper) and He 2–113 (lower) between 4200 and 4800 Å

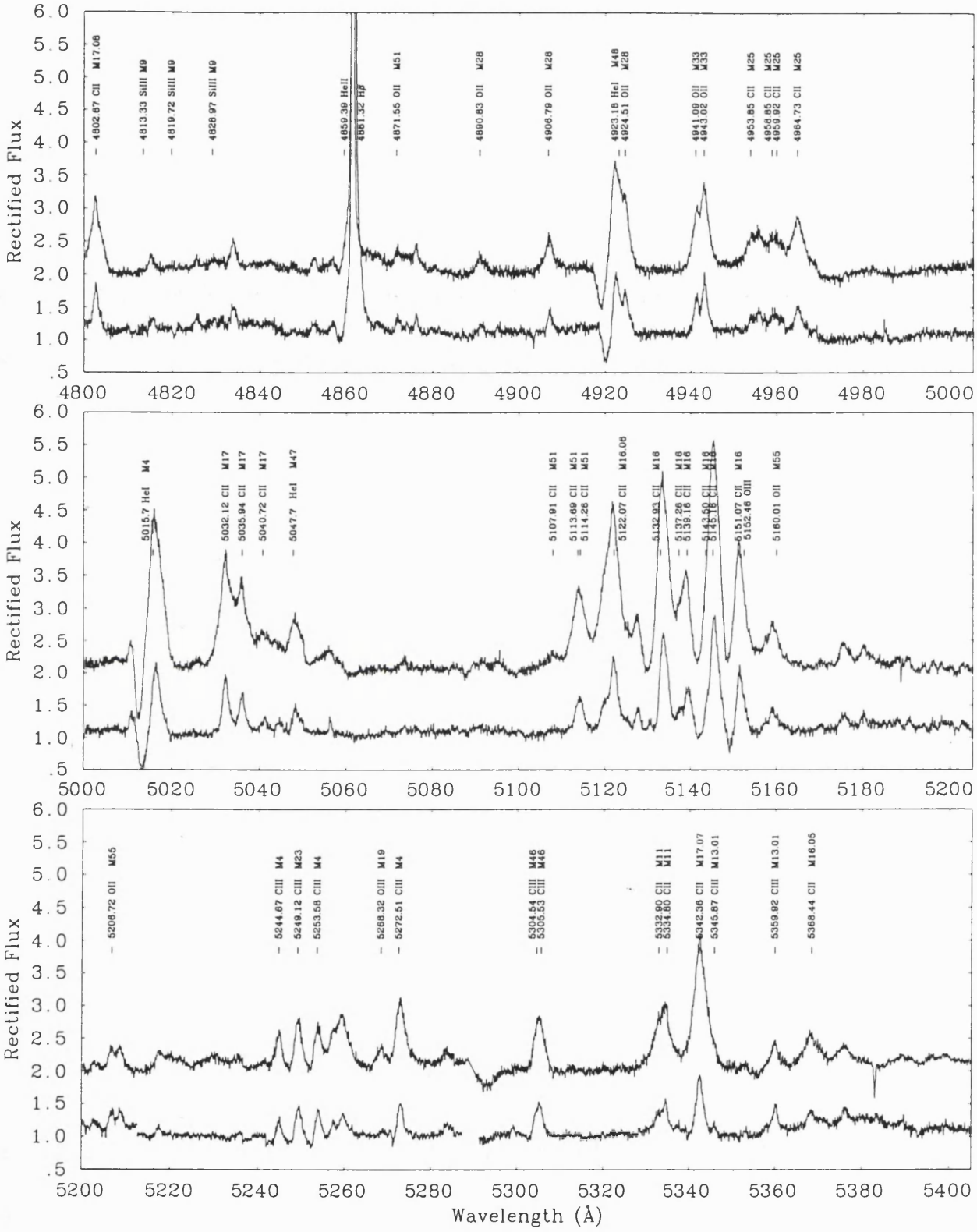

Figure C.3: UCLES spectra of CPD–56°8032 (upper) and He 2–113 (lower) between 4800 and 5400 Å

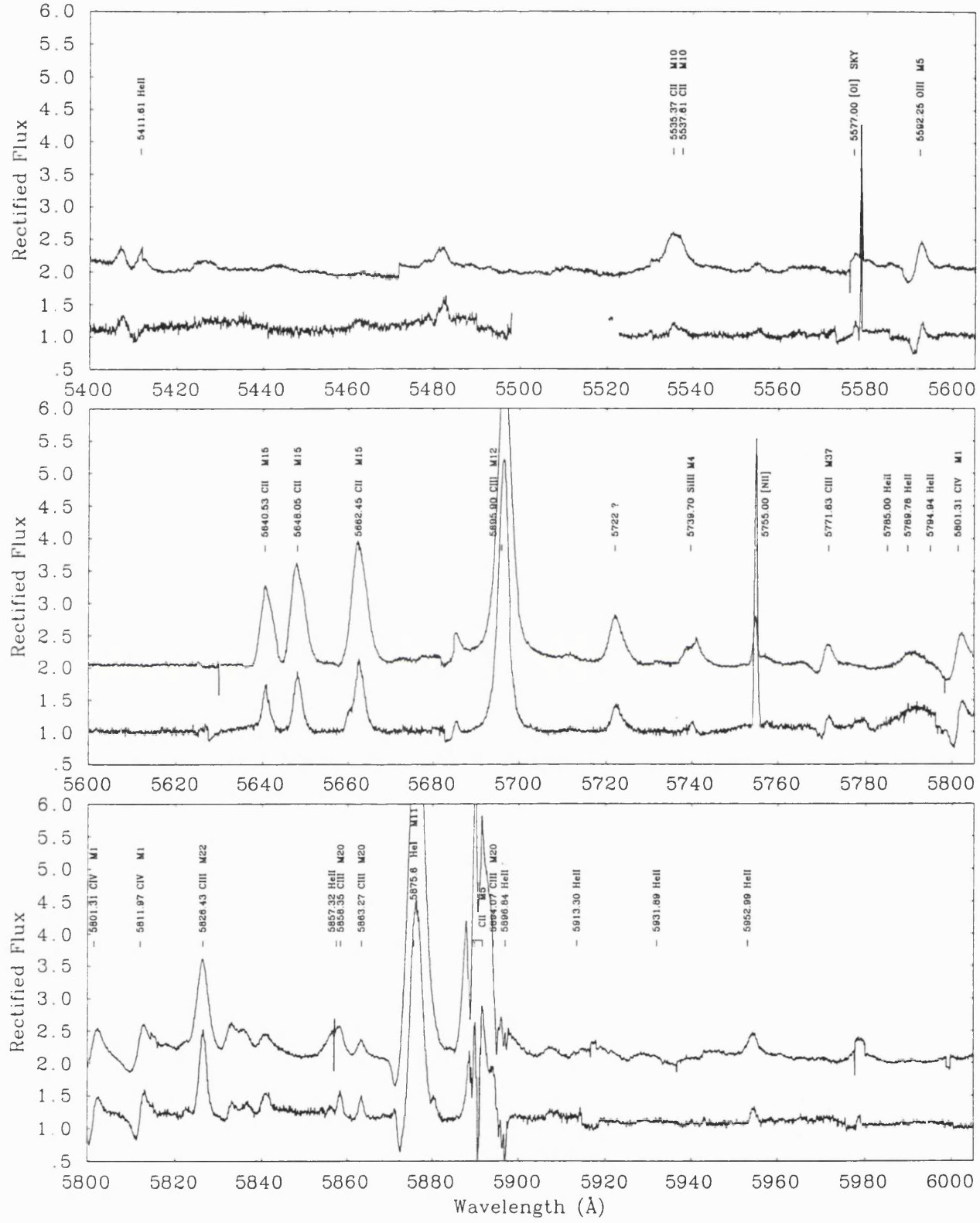

Figure C.4: UCLES spectra of CPD–56°8032 (upper) and He 2–113 (lower) between 5400 and 6000 Å

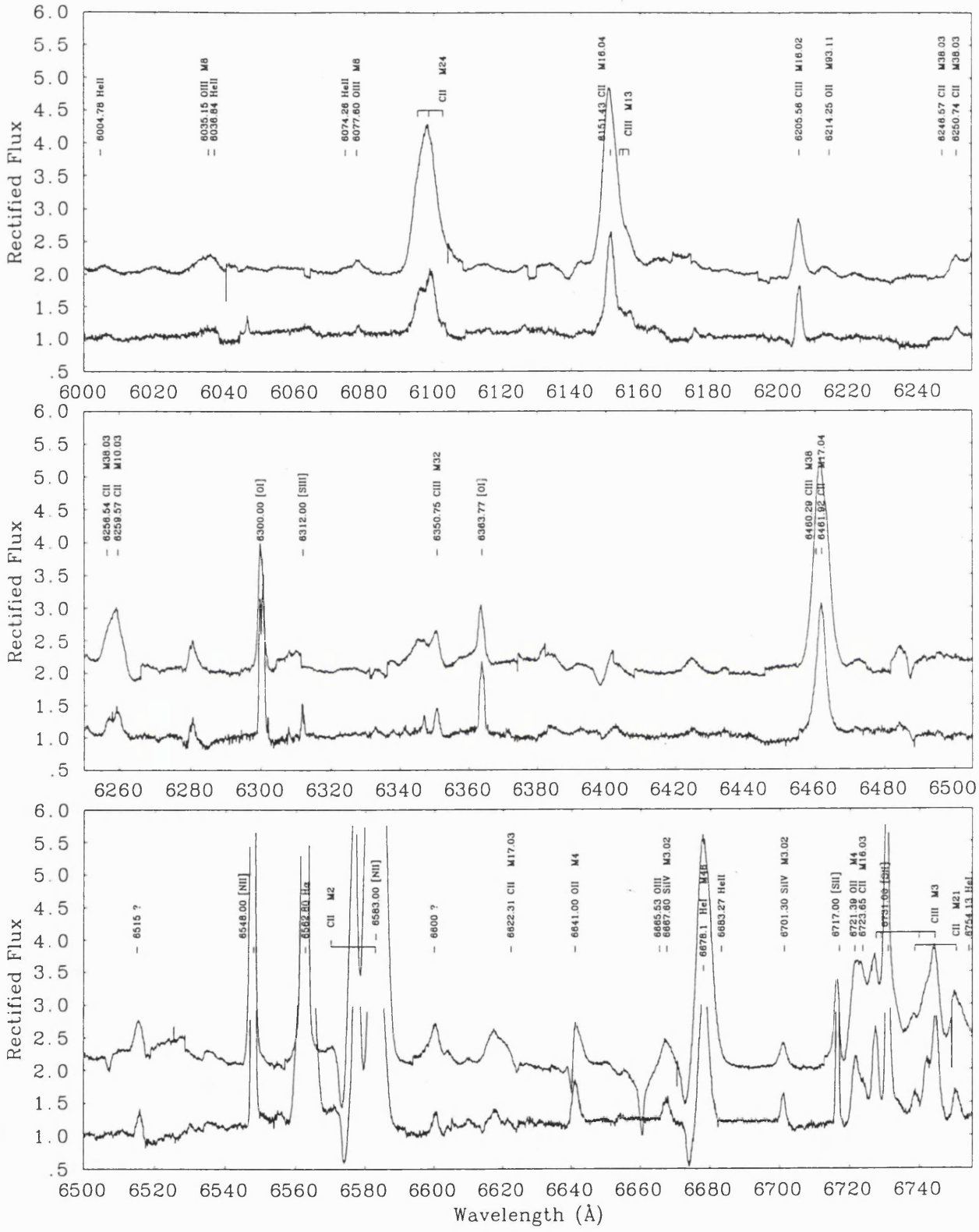

Figure C.5: UCLES spectra of CPD–56°8032 (upper) and He 2–113 (lower) between 6000 and 6750 Å

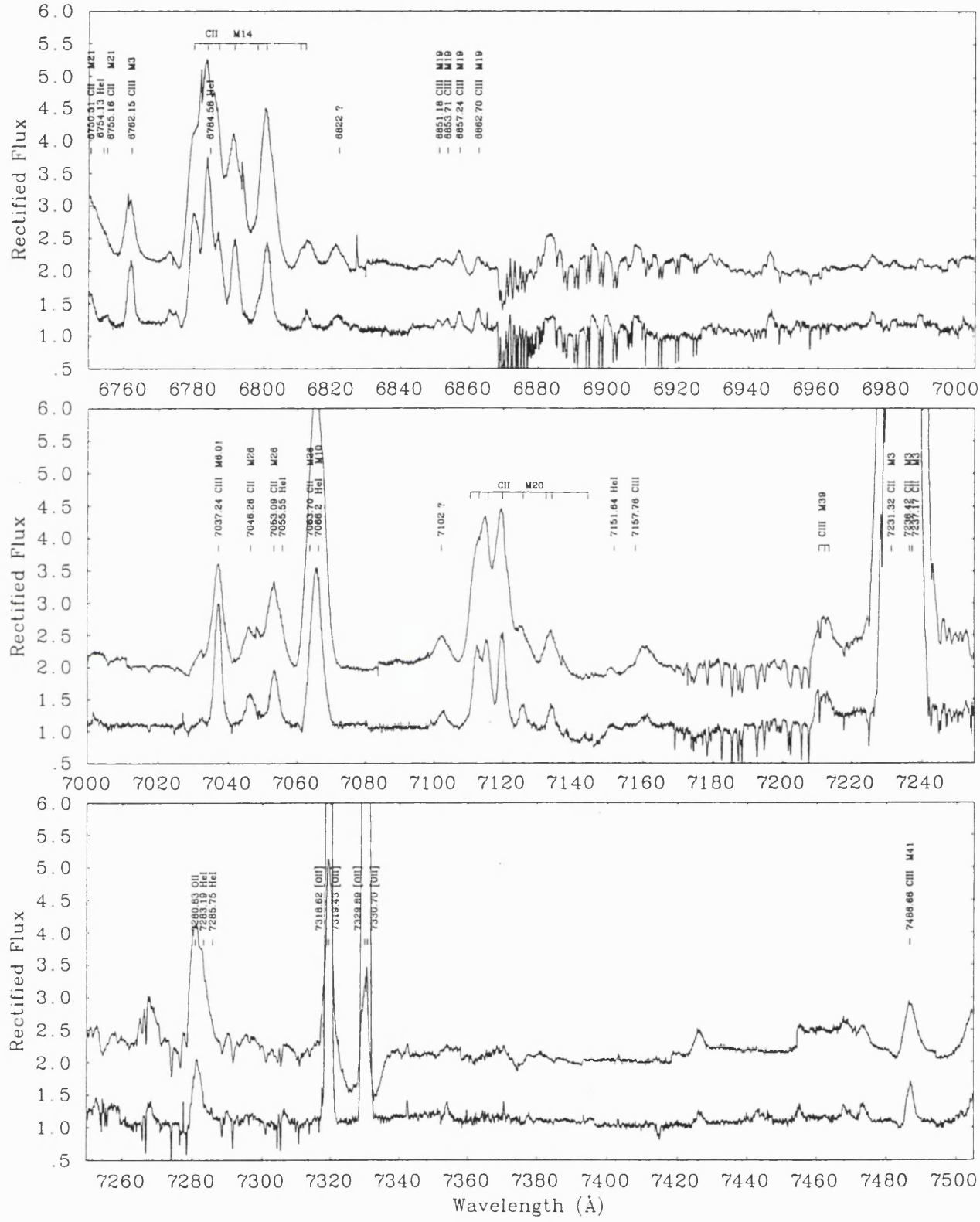

Figure C.6: UCLES spectra of CPD–56°8032 (upper) and He 2–113 (lower) between 6750 and 7500 Å

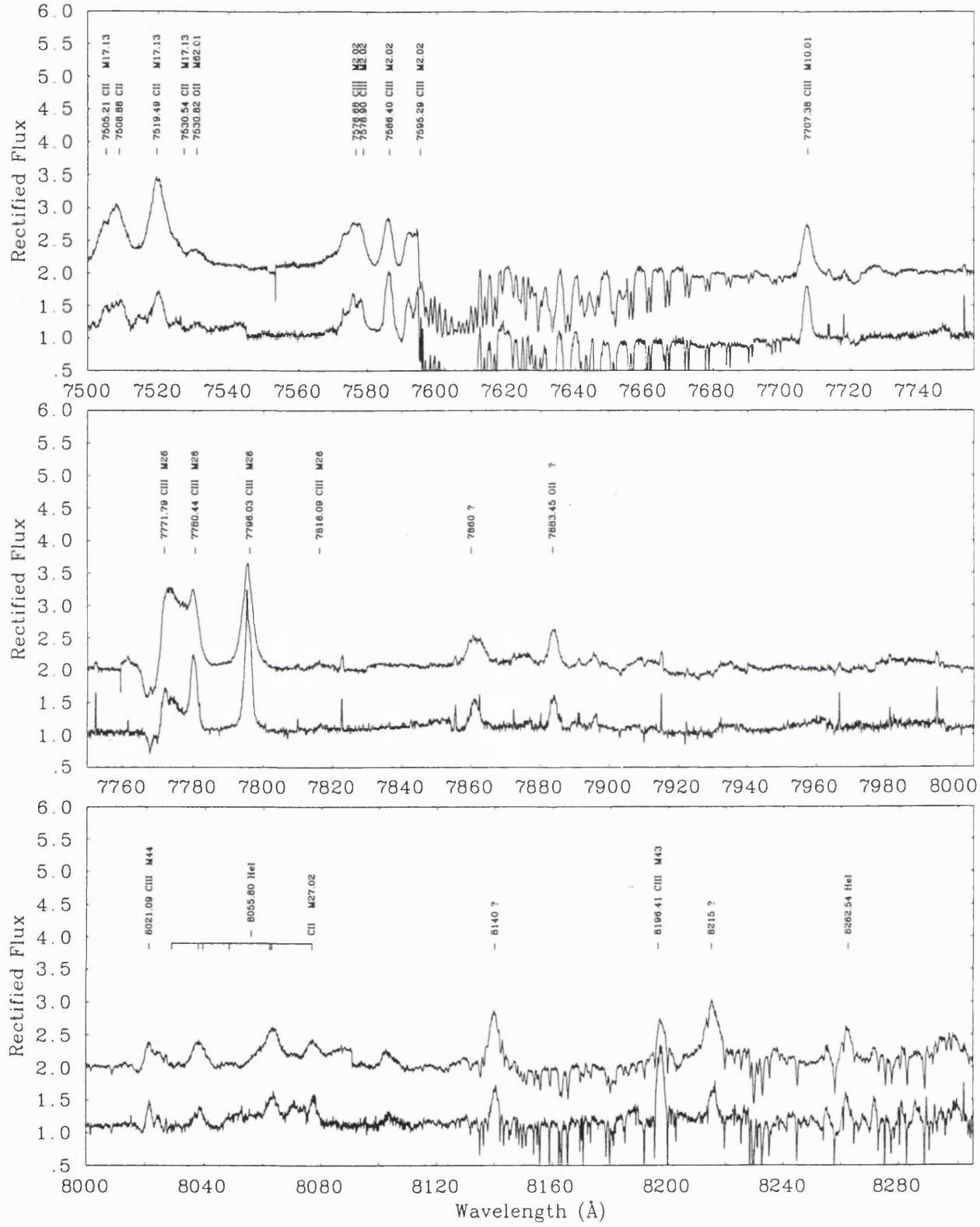

Figure C.7: UCLES spectra of CPD–56°8032 (upper) and He 2–113 (lower) between 7500 and 8300 Å

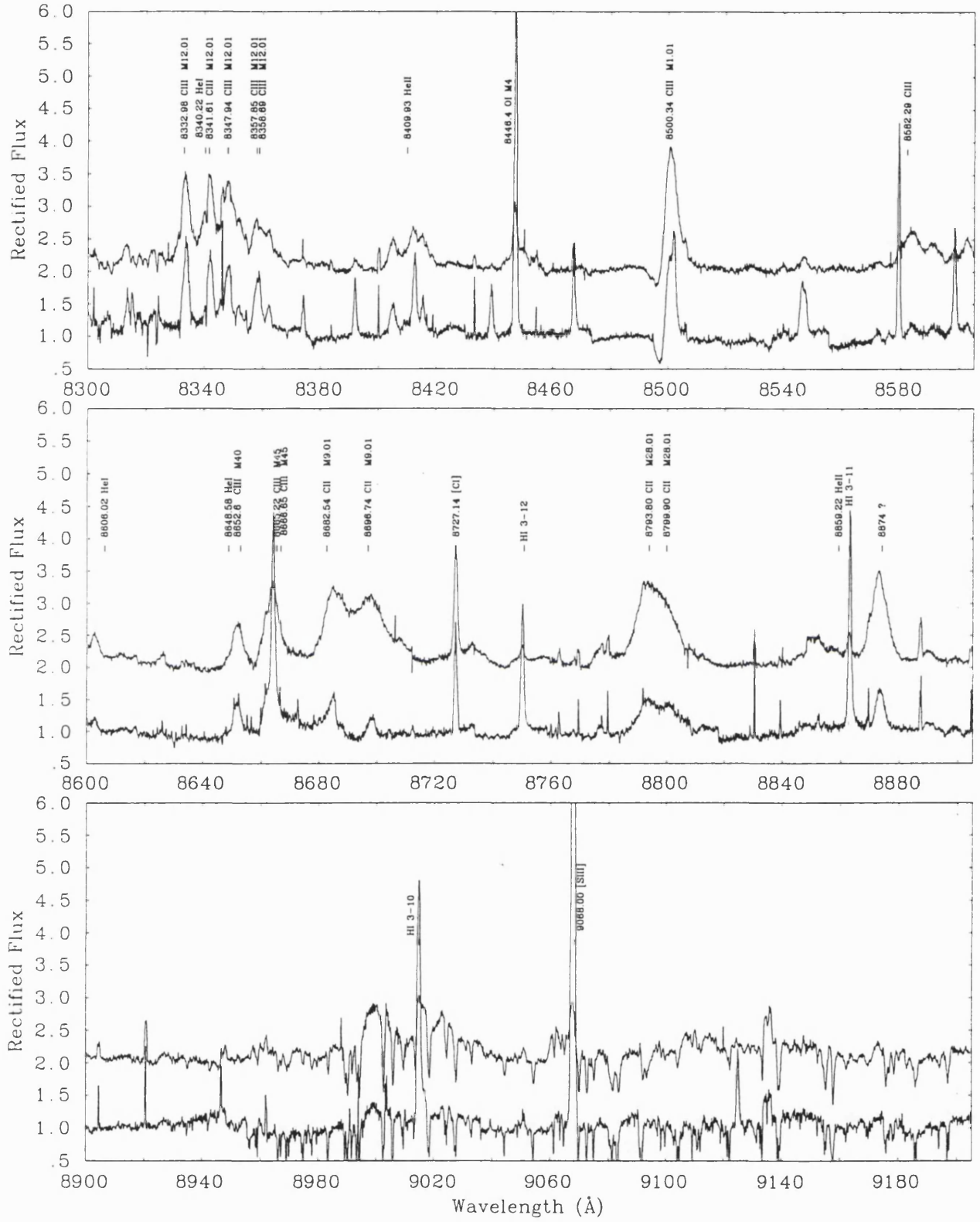

Figure C.8: UCLES spectra of CPD–56°8032 (upper) and He 2–113 (lower) between 8300 and 9200 Å

Appendix D

The Spectrum of M 4–18

In this Appendix we present the rectified optical spectrum of M 4–18 between 3700 Å and 6800 Å. The higher resolution WHT spectrum (4200–5800 Å) is spliced into the lower resolution INT one and compared with the UCLES spectrum of He 2–113. Details of all the observations and data raduction are presented in Chapter 3. Only the most prominent spectral lines are indicated, since a complete spectral identification was carried out for CPD–56°8032 and He 2–113 in Appendix B, and, as can be seen from the spectral comparison of M 4–18 and He 2–113 in the range 4200–5800 Å, besides the slightly stronger stellar lines presented by M 4–18 and its much brighter nebular spectrum, there is a perfect match of all spectral features.

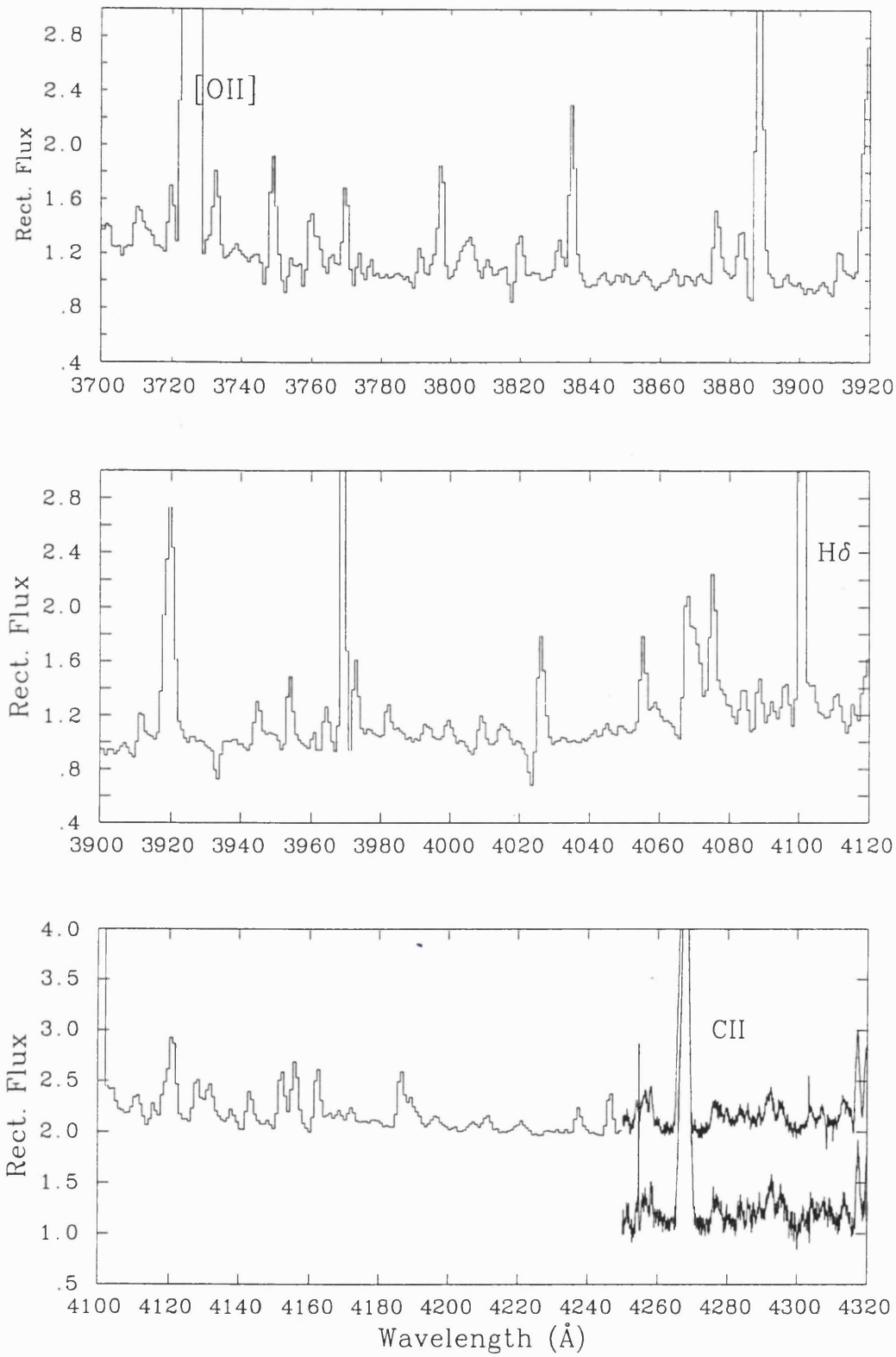

Figure D.1: The INT (3700–4200 Å) and WHT (4200–4320 Å) spectra of M 4–18 (above) compared with the UCLES spectrum of He 2–113 (below)

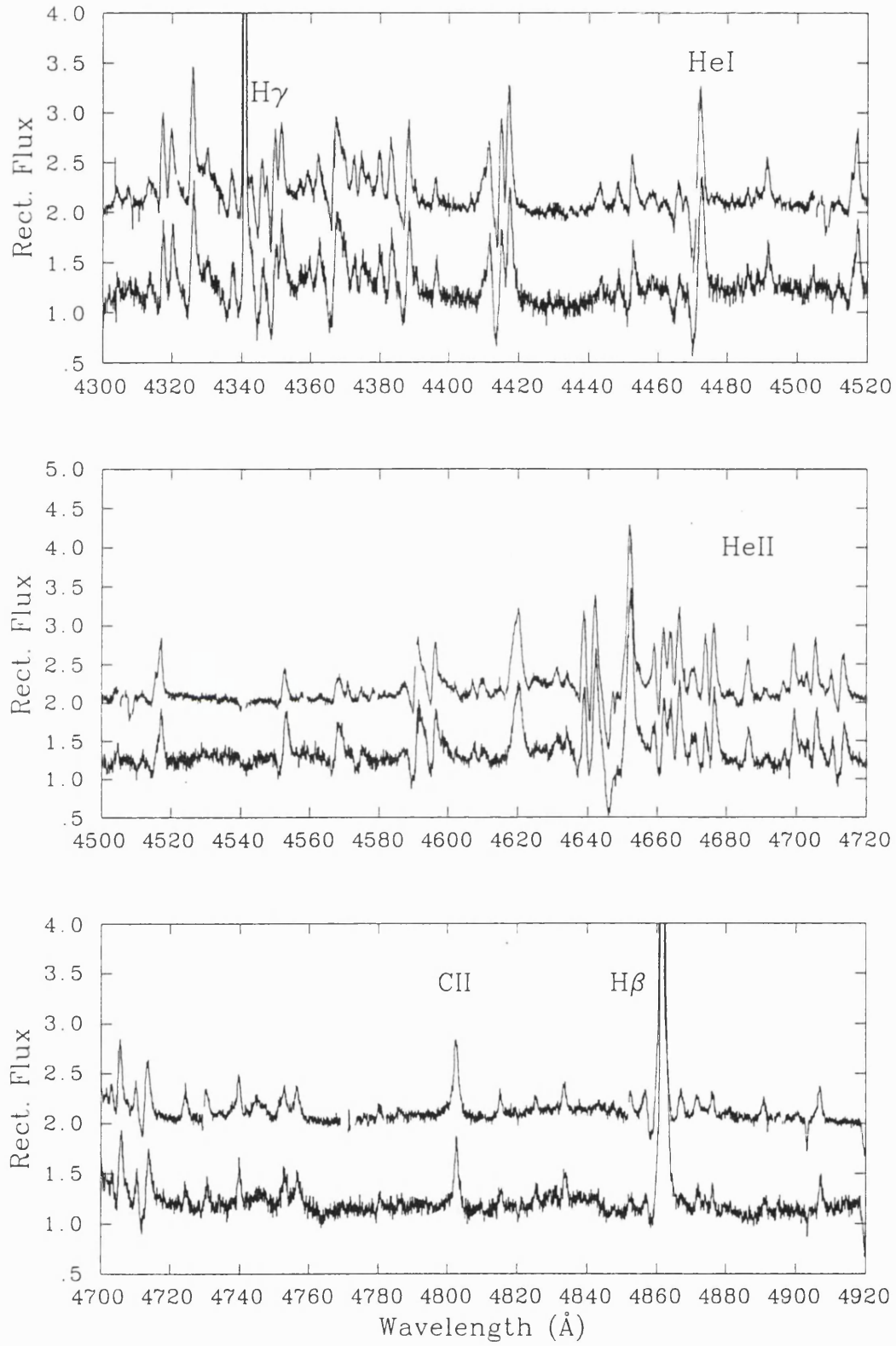

Figure D.2: The WHT spectrum of M 4–18 (above) between 4300 and 4920 Å compared with the UCLES spectrum of He 2–113 (below)

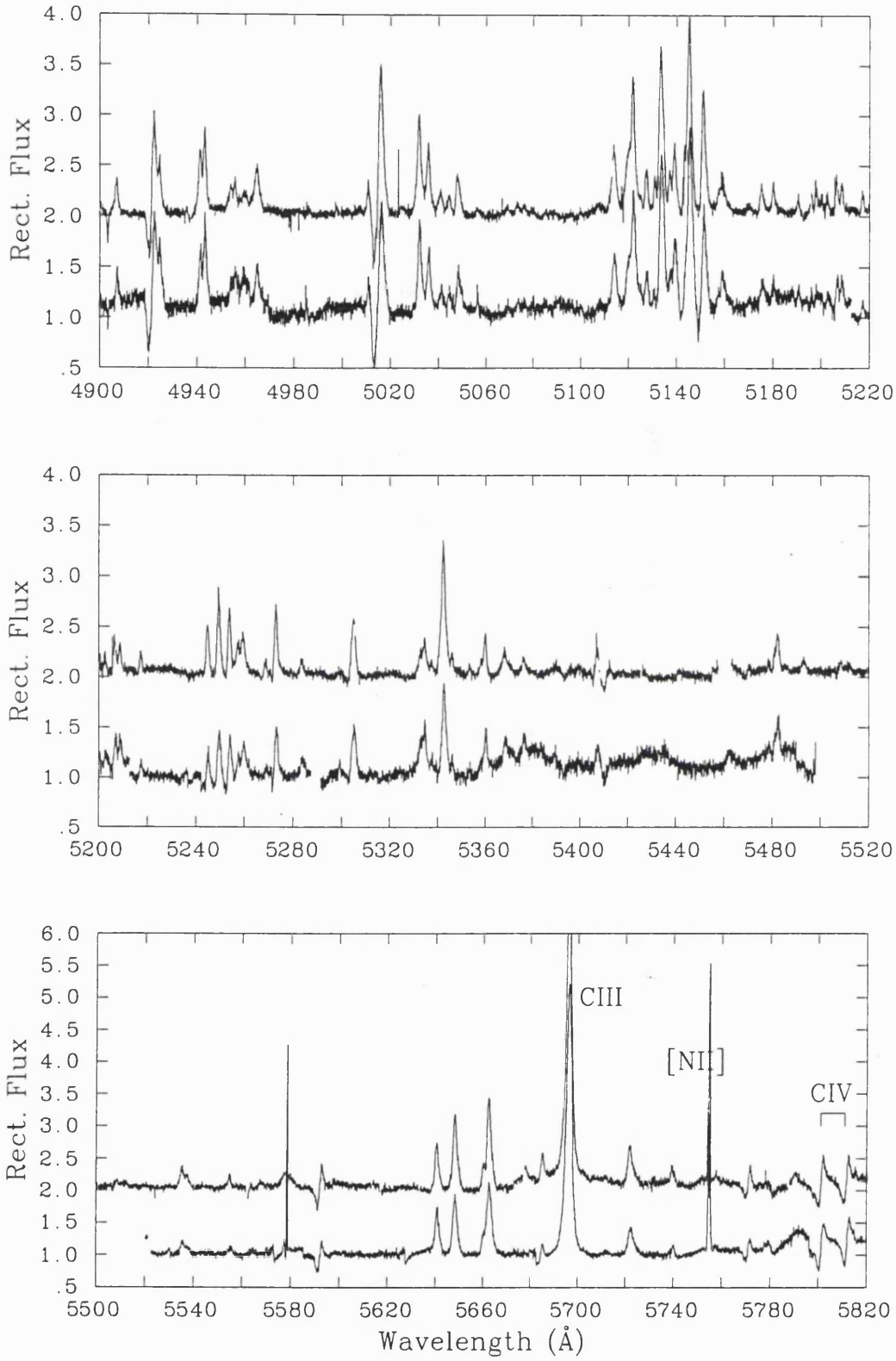

Figure D.3: The WHT spectrum of M 4–18 (above) between 4900 and 5820 Å compared with the UCLES spectrum of He 2–113 (below)

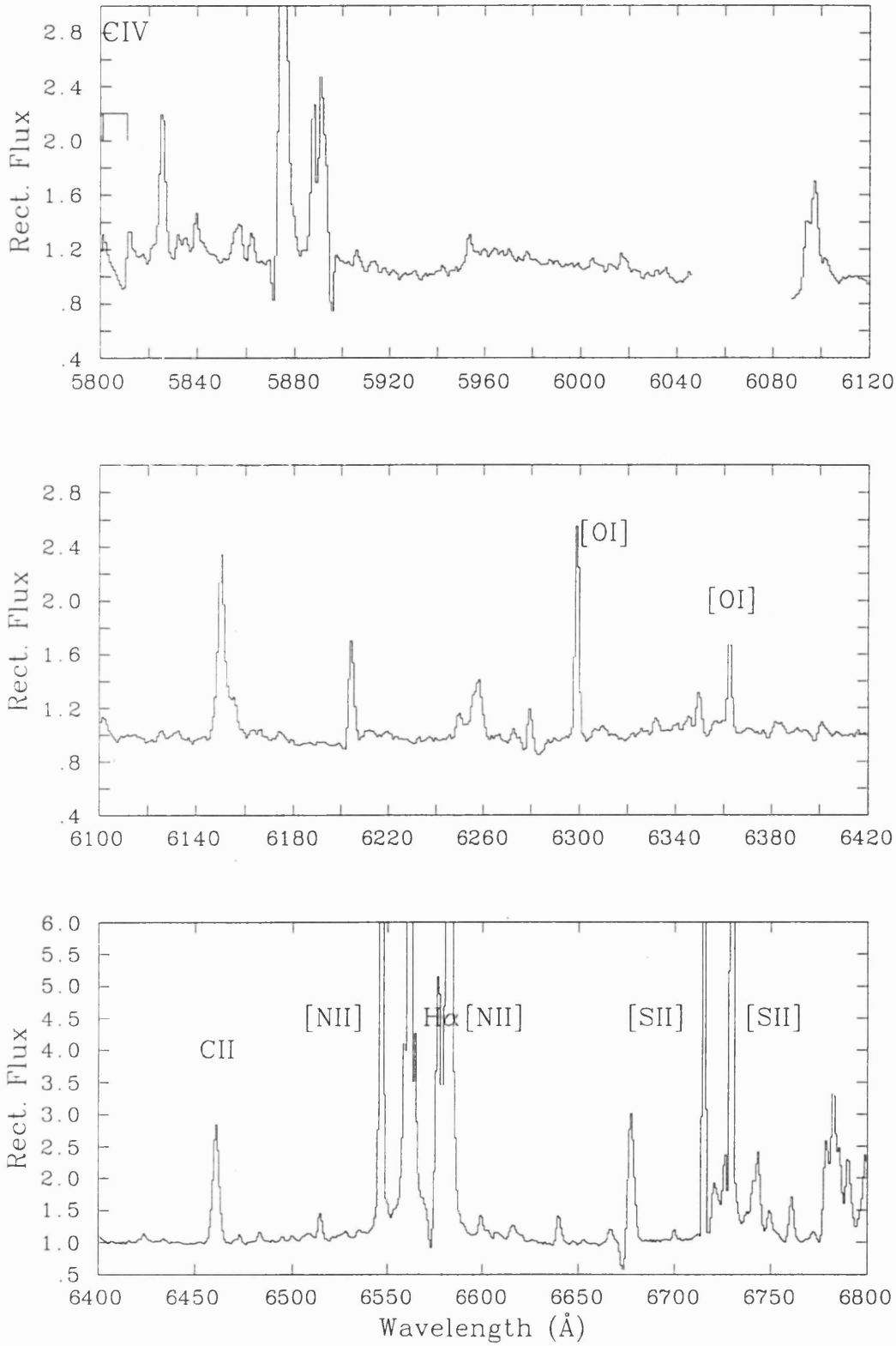

Figure D.4: The INT spectrum of M 4–18 between 5800 and 6800 Å

Appendix E

The AAT UCLES Spectrum of SwSt 1

In this Appendix we present the UCL Echelle spectrum of SwSt 1 obtained at the Anglo–Australian Telescope in May 1993 (details of the data acquisition and reduction are presented in Chapter 3). Due to the strength of the nebular lines compared to the stellar lines, we present the rectified spectrum on a log scale.

The stellar spectrum is dominated by lines of C III. The only stellar C II feature is observed at λ4267 blended with its nebular counterpart. Stellar C IV is also present at 5801,11 Å. C IV λ4658 might be present, although severely blended with C III λ4650 (Multiplet 1). No (or very week) stellar He I features are observed in the spectrum. Swings and Struve (1940) deduced that the He I lines were of both nebular and stellar origin from a comparison of the nebular [N II] λ5755 line and the He I λ5876 line; they observed He I λ5876 to have a broader pedestal than the nebular line. Our higher resolution spectrum shows the pedestal clearly, but we attribute it to the C III line at 5871.6 (Multiplet 20), whose other two components ($\lambda\lambda$5894.2,5857.9) are also present. Since no other He I line displays the same broad base, we conclude that He I features are produced mainly by the nebula. The He II line at 4686 Å presents a strong and symmetric broad profile of clear stellar origin, while the He II line at 5411 Å has a P–Cygni absorption. Lastly, the He II

line at 4541.6 Å is present in absorption, although the absorption is not photospheric since its radial velocity–corrected central wavelength (4540.2 Å; the heliocentric radial velocity is 17.8±1 km s^{-1}), is blue–shifted with respect to the line's rest wavelength (4541.6 Å). Stellar lines of O III can also be identified, while no stellar O II nor O IV lines are observed.

The nebular spectrum presents very strong forbidden lines (discussed in Chapter 8), along with a number of weaker recombination lines. Neutral helium recombination lines produce a well defined spectrum. No nebular He II lines are observed. Only the strongest C II recombination lines are visible in the nebular spectrum (e.g. λ4267, $\lambda\lambda$6578,82 and λ7236), while there is no clear indication that recombination lines of C I are present. We do not observe a nebular counterpart to the stellar C III recombination spectrum. O I Multiplet 4 (with mean wavelength 8446.5 Å) is observed in the nebylar spectrum along with very weak nebular recombination lines of O II; the two strongest components of O II Multiplet 2 can be seen on either sides of Hγ, at 4349.4 and 4336.9 Å (we do not label them due to their faintness). Some of the very weak narrow features could be identified as N II recombination lines, although it is difficult to measure their wavelength with precision. The [Ne III] line λ3868.7 was mistaken by Swings and Struve (1940) for He I λ3867.5. From our echelle spectroscopy we can determine that the wavelength of the observed feature matches the neon and not the helium line. The other optical [Ne III] line at 3967.5 Å (predicted to be 0.42 times the strength of λ3867.5) is only barely visible. The forbidden lines of [Fe III] are particularly strong in the spectrum of this PN. The forbidden lines of [Fe II] are much weaker, although it is worth noting that they seem particularly broad, with FWHM$\sim$100 km s^{-1}, which may indicate a stellar wind origin.

In Table E.1 we present a list of the lines we identified in the spectrum of SwSt 1. In Column 4 we indicate the origin of the line (*s* for stellar, *n* for nebular, *is* for interstellar), while in Column 5 we list the initials of the authors who have identified those lines in the past. The intensities of the most important nebular lines are presented in Chapter 8.

Table E.1: Lines identified in the spectrum of SwSt 1 between 3700 and 9550 Å

Ion	Wavelength (Å)	Multiplet No.	Origin	Comments
H16	3703.8		n	SS,CH
He I	3705.0	25	n	CH
H15	3711.9		n	SS,CH
O III	3715.0	14	s	SS
H14	3721.8		n	SS,CH,dFV
[O II]	3726.2	1F	n	SS,CH,dFV
[O II]	3728.9	1F	n	SS,CH,dFV
H13	3734.2		n	SS,CH
H12	3750.4		n	SS,CH
O III	3761.0	30	s	SS
O III	3774.0	2	s	
O III	3791.3	2	s	
H11	3770.9		n	SS,CH,dFV
O III	3791.9	2	s	SS
H10	3797.9		n	SS,CH,dFV
He I	3819.4	22	n	SS,CH
H9	3835.4		n	SS,CH,dFV
He I	3888.7	2	n	SS
H8	3889.1		n	SS,CH,dFV
C II	3919.0	4	n	CH
C II	3920.7	4	n	CH
He I	3964.7	5	n	SS,CH
Hϵ	3970.2		n	SS,CH,dFV
HE I	4009.4	55	n	
He I	4026.3	18	n	SS,CH
C III	4056.1	24	s	SS,CH
[S II]	4068.6	1F	n	SS,CH,dFV
[S II]	4076.3	1F	n	SS,CH,dFV
Hδ	4101.7		n	SS,CH,dFV
He I	4120.8	16	n	
C III	4121.8	17	s	
Si II	4128.0	3	s	CH
Si II	4130.9	3	s	
He I	4143.8	53	n	SS,CH
C III	4152.5	21	s	
C III	4156.5	21	s	SS
C III	4162.8	21	s	
He I	4169.0	52	n	
C III	4186.9	18	s	SS,CH
C III	4247.3	11	s	
C II	4267.0	6	n+s	CH,dFV
[Fe II]	4287.4	7F	n	CH
C III	4315.4	48	s	

Ion	Wavelength (Å)	Multiplet No.	Origin	Comments
C III	4325.6	7	s	CH
Hγ	4340.5		n	SS,CH,dFV
[Fe II]	4359.3	7F	n	CH
[O III]	4363.2	2F	n	SS,CH,dFV
O I	4368.0		n	dFV
C III	4379.0	14	s	
C III	4382.0	14	s	
He I	4388.1	51	n	SS,dFV,CH
[Fe II]	4416.3	6F	n	CH
C III	4443.1	23.01	s	
He I	4471.5	14	n	SS,dFV,CH
C III	4516.0	9	s	SS,CH
He II	4541.6	4-9	s	
[Fe II]	4606.0		n	
C III	4647.4	1	s	SS,CH
C III	4650.3	1	s	SS,CH
C III	4651.5	1	s	SS,CH
[Fe III]	4657.0	3F	n	dFV,CH
C III	4663.6	5	s	
C III	4667.0	5	s	SS
C III	4673.9	5	s	
He II	4685.7	3-4	s	SS,CH
[Fe III]	4701.0	3F	n	CH,dFV
He I	4713.2	12	n	CH,dFV
[Fe III]	4733.9	3F	n	CH,dFV
[Fe III]	4754.0	3F	n	dFV
[Fe III]	4769.4	3F	n	
[Fe III]	4777.7	3F	n	
Hβ	4861.3		n	SS,CH,dFV
[Fe III]	4881.0	2F	n	
He I	4921.9	48	n	CH,dFV
[Fe III]	4930.5	1F	n	
[O III]	4958.9	1F	n	SS,CH,dFV
[O III]	5006.8	1F	n	SS,CH,dFV
He I	5015.7	4	n	dFV
He I	5047.7	47	n	
Si II	5056.0	5	n?	
?	5130.8		s	
[Fe II]	5158.8	19F	n	
[Ar III]	5191.8	3F	n	
[N I]	5197.9	1F	n	
[N I]	5200.3	1F	n	
C III	5244.6	4	s	
C III	5249.1	23	s	
C III	5253.5	4	s	
[Fe III]	5270.0	1F	n	dFV

Ion	Wavelength (Å)	Multiplet No.	Origin	Comments
C III	5272.5	4	s	
C III	5305.1	46	s	
He II	5411.5	4-7	s	
[Cl III]	5517.7	1F	n	dFV
[Cl III]	5537.9	1F	n	dFV
[O I]	5577.3	3F	n	sky
OIII	5592.4	5	s	
He I	5675.0	?	n	
C III	5695.9	12	s	SS
[Fe II]	5721.4	33F	n	
[N II]	5754.6	3F	n	SS,dFV
C III	5771.7	?	s	
C IV	5801.0	1	s	SS,dFV
C IV	5811.0	1	s	dFV
C III	5826.4	22	s	
C III	5857.9	20	s	
C III	5871.6	20	s	
He I	5875.7	11	n	SS,CH,dFV
Na I D2	5889.9		n+is	
C III	5894.2	20	s	
Na I D1	5895.9		n+is	
C III	6205.5	17	s	
[O I]	6300.3	1F	n	SS,dFV
[S III]	6312.1	3F	n	SS,dFV
[O I]	6363.8	1F	n	dFV
[N II]	6548.0	1F	n	SS,CH,dFV
Hα	6562.8		n	SS,CH,dFV
C II	6578.1	2	n	
[N II]	6583.4	1F	n	SS,CH,dFV
He I	6678.1		n	SS,dFV
[S II]	6716.5	2F	n	dFV
C III	6727.4	3	s	
[S II]	6730.8	2F	n	dFV
C III	6744.4	3	s	
C III	6762.2	3	s	
C III	7037.2	6.01	s	
He I	7065.7	10	n	
[Ar III]	7135.8	1F	n	
C II	7231.3	3	n	
C II	7236.4	3	n	
He I	7281.3	45	n	
[O II]	7319.9	2F	n	
[O II]	7330.1	2F	n	
C III	7486.5	41	s	
C III	7586.4	2.02	s	
C III	7707.4	10.01	s	

Ion	Wavelength (Å)	Multiplet No.	Origin	Comments
[Ar III]	7751.1	1F	n	
C III	7771.8	26	s	
C III	7780.4	26	s	
C III	7796.0	26	s	
C III	8196.2	43	s	
H3-20	8392.4		n	
H3-19	8413.3		n	
H3-18	8438.0		n	
H3-17	8467.3		n	
C III	8500.3	1.01	s	
H3-16	8502.5		n	
H3-15	8545.4		n	
[Cl II]	8578.7		n	
H3-14	8598.4		n	
H3-13	8665.1		n	
H3-12	8750.5		n	
H3-11	8862.7		n	
H3-10	9014.9		n	
[S III]	9068.9	1F	n	
H3-9	9229.0		n	
[S III]	9531.0	1F	n	

SS=Swings and Struve 1940; range 3600–6680 Å; dispersion 100 and 50 Å/mm.
CH=Carlson and Henize 1979; observations taken in 1962, range 3700–6600 Å, resolution 177 Å/mm up to 5000, 94 Å/mm after.
dFV=de Freitas Pacheco and Veliz 1984; range 3600–5900 Å resolution 6.5 Å and 0.5 Å;NB some lines observed by them might be missing.

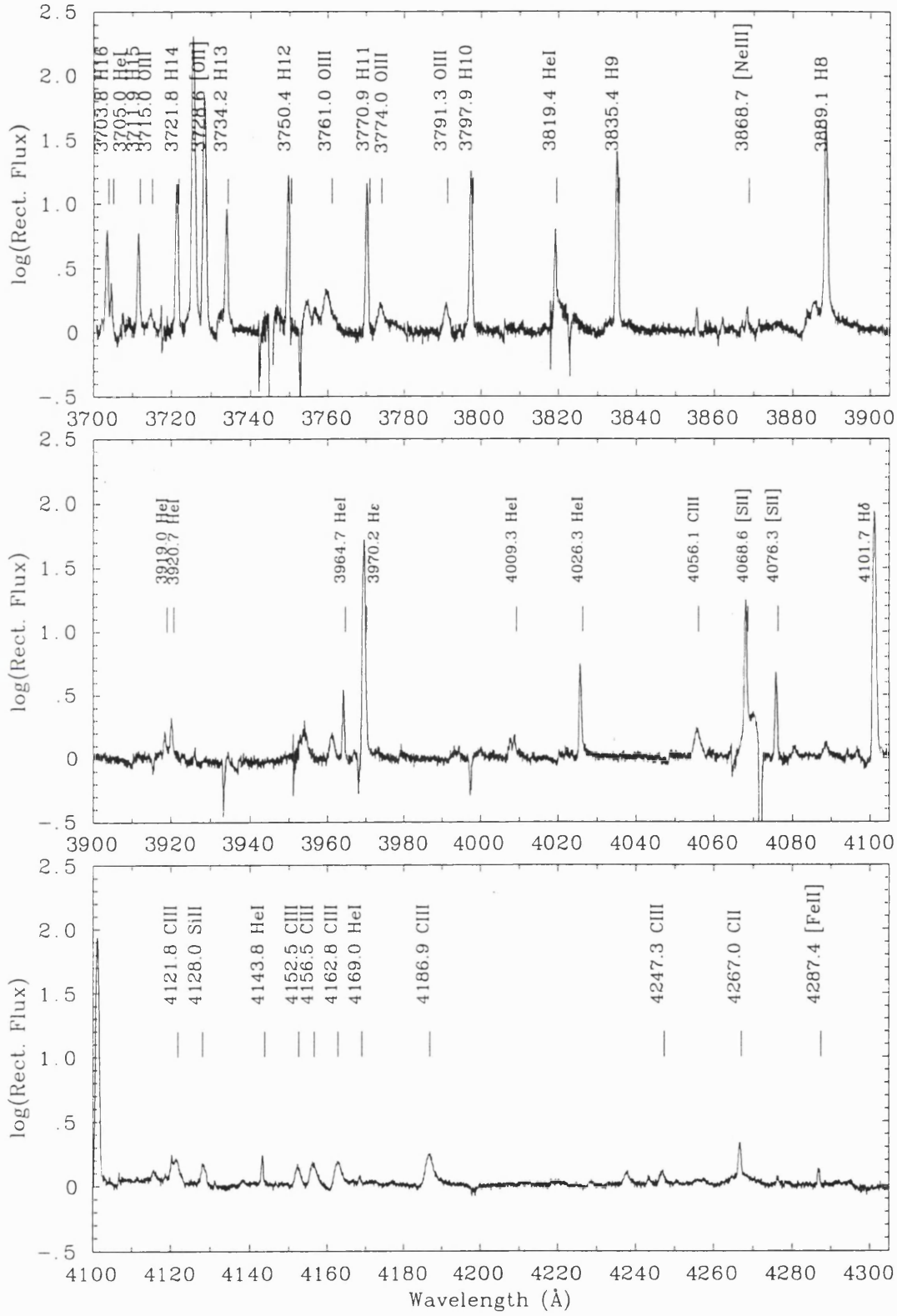

Figure E.1: The AAT spectrum of SwSt 1 between 3700 and 4300 Å

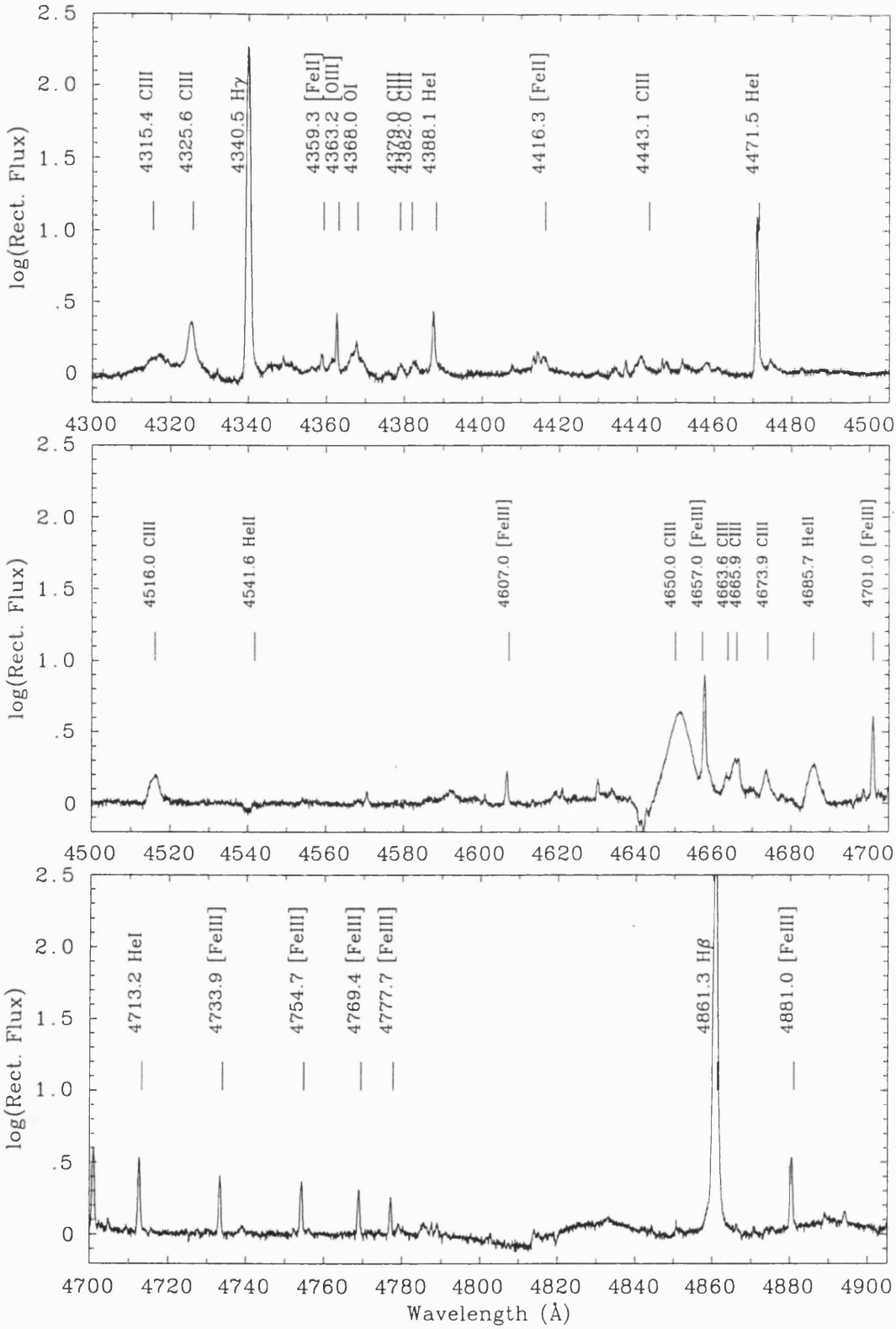

Figure E.2: The AAT spectrum of SwSt 1 between 4300 and 4900 Å

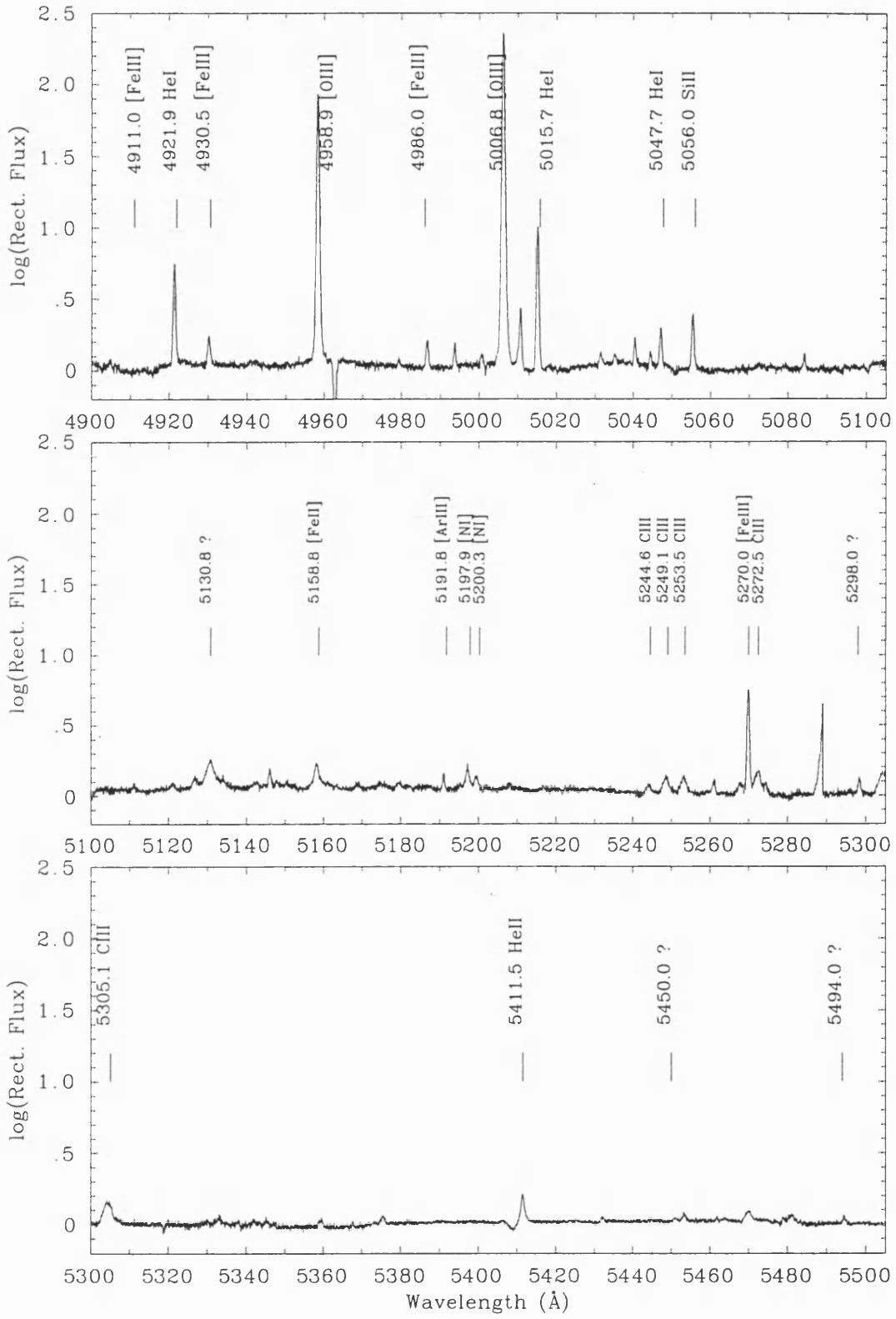

Figure E.3: The AAT spectrum of SwSt 1 between 4900 and 5500 Å

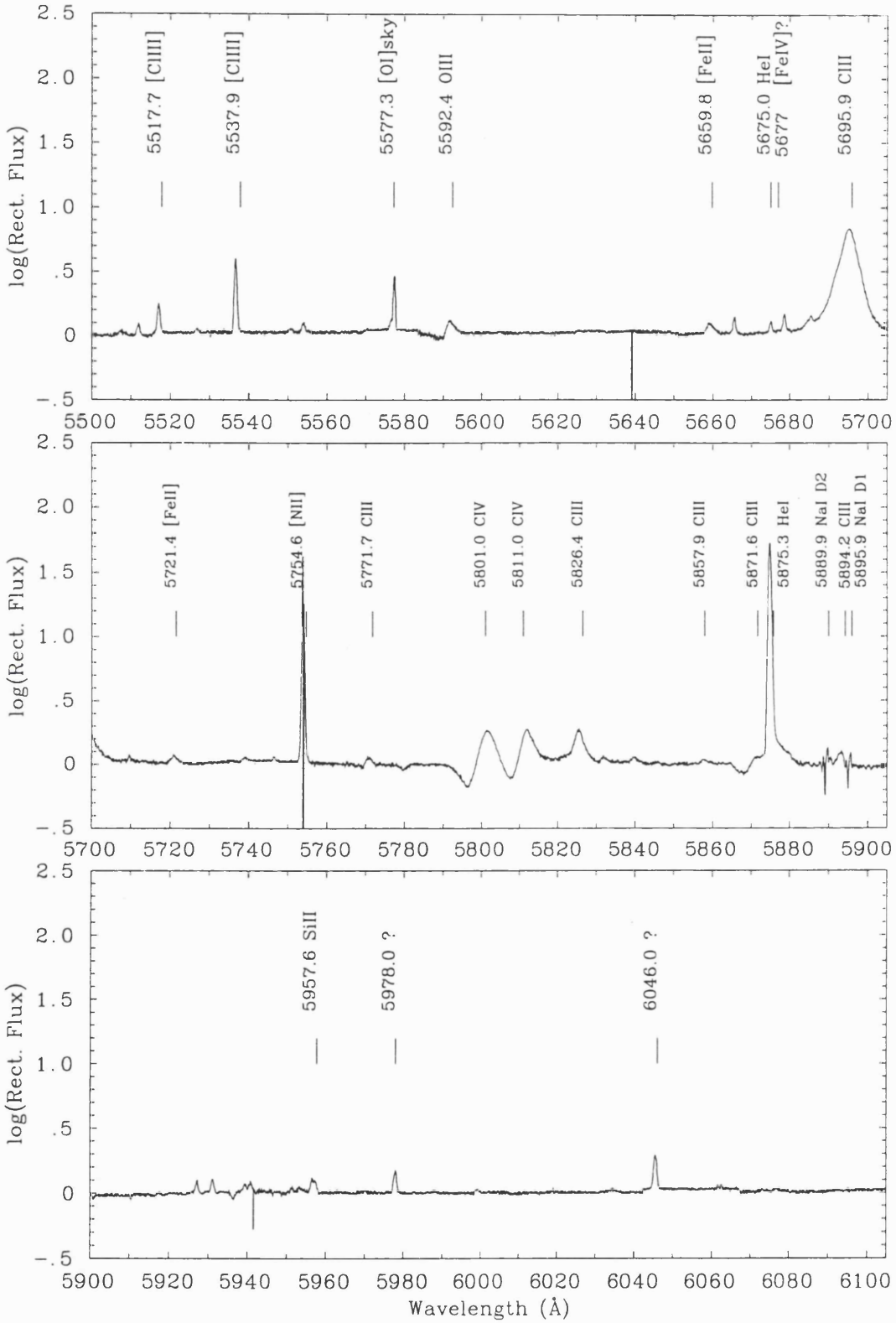

Figure E.4: The AAT spectrum of SwSt 1 between 5500 and 6100 Å

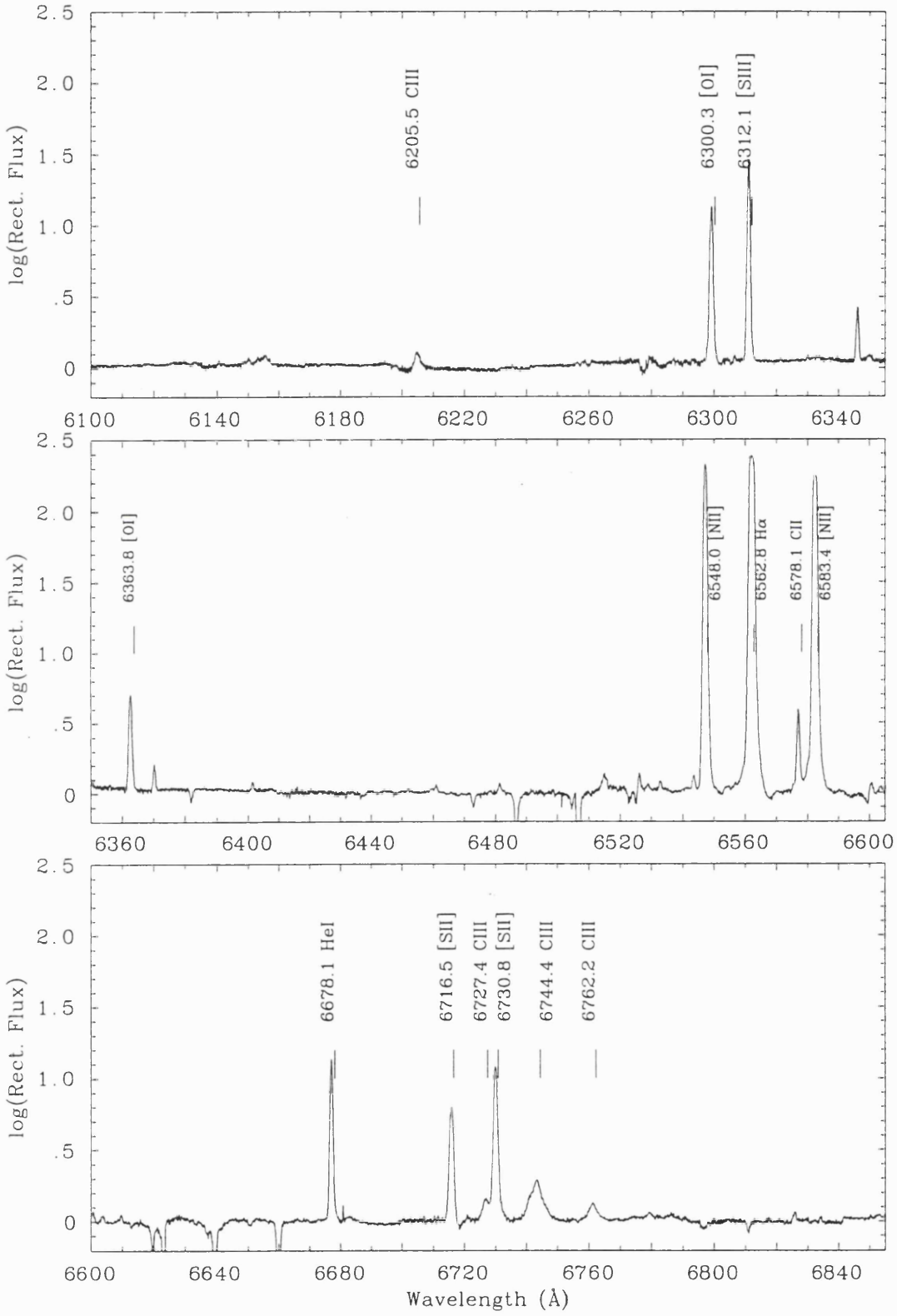

Figure E.5: The AAT spectrum of SwSt 1 between 6100 and 6850 Å

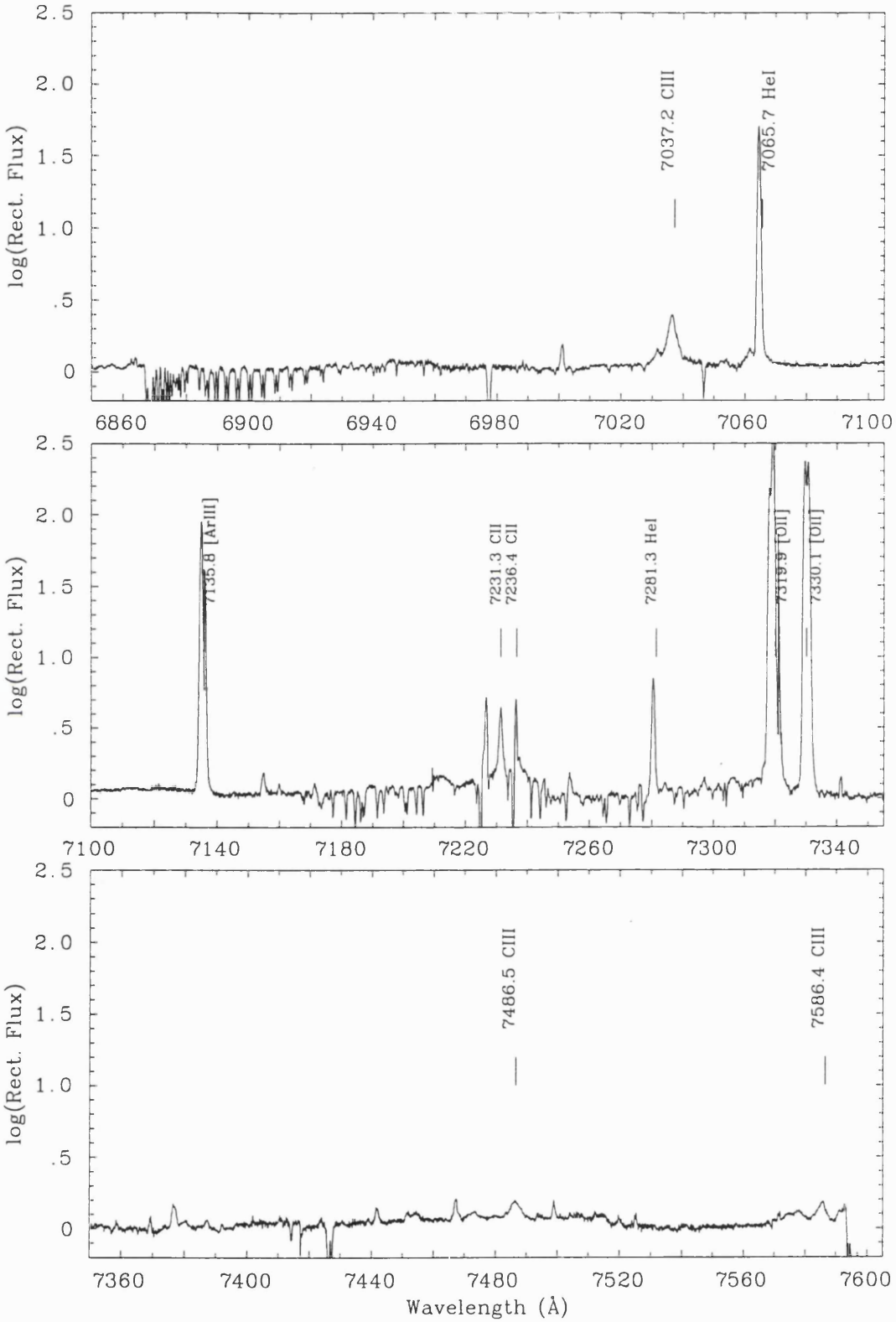

Figure E.6: The AAT spectrum of SwSt 1 between 6850 and 7600 Å

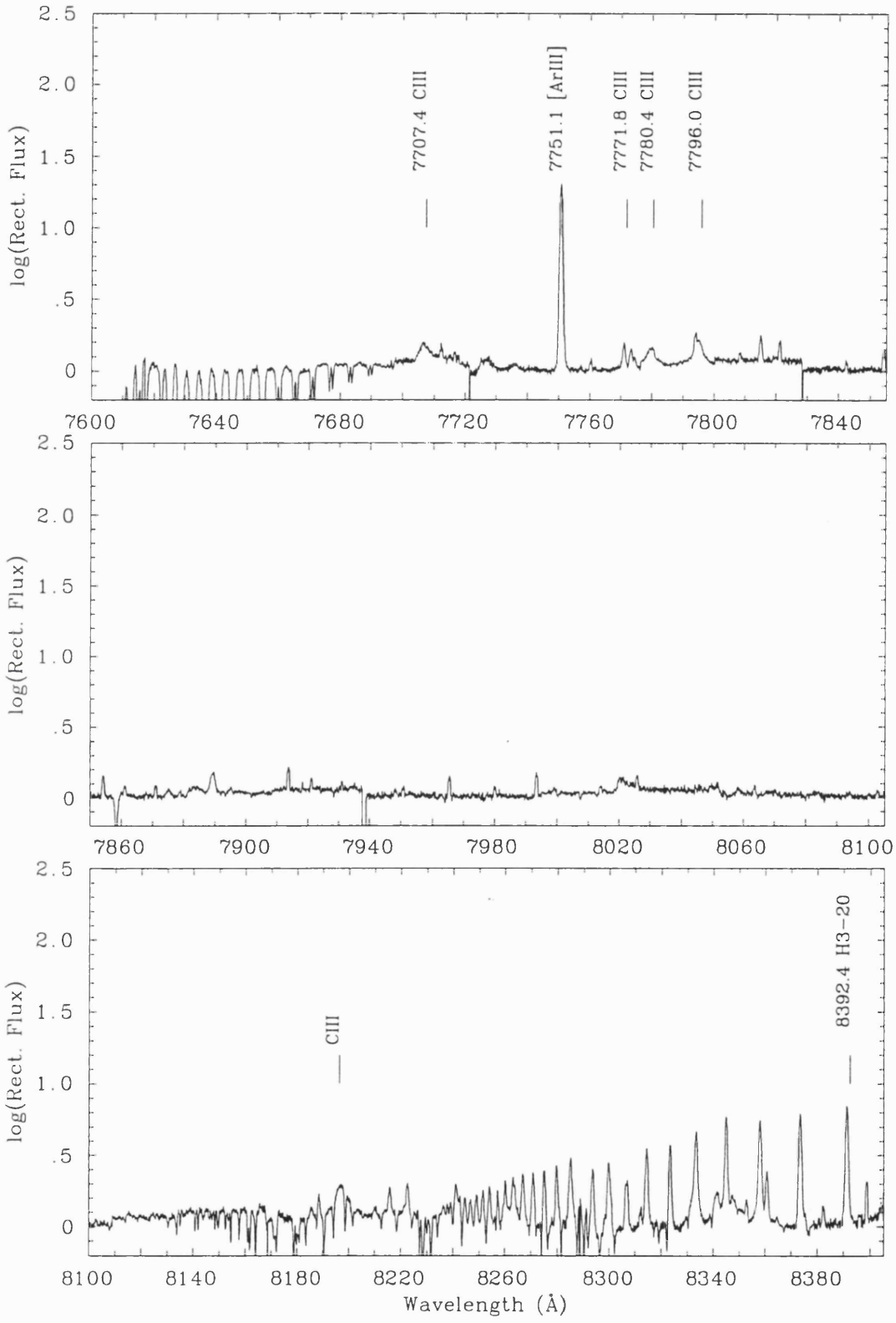

Figure E.7: The AAT spectrum of SwSt 1 between 7600 and 8400 Å

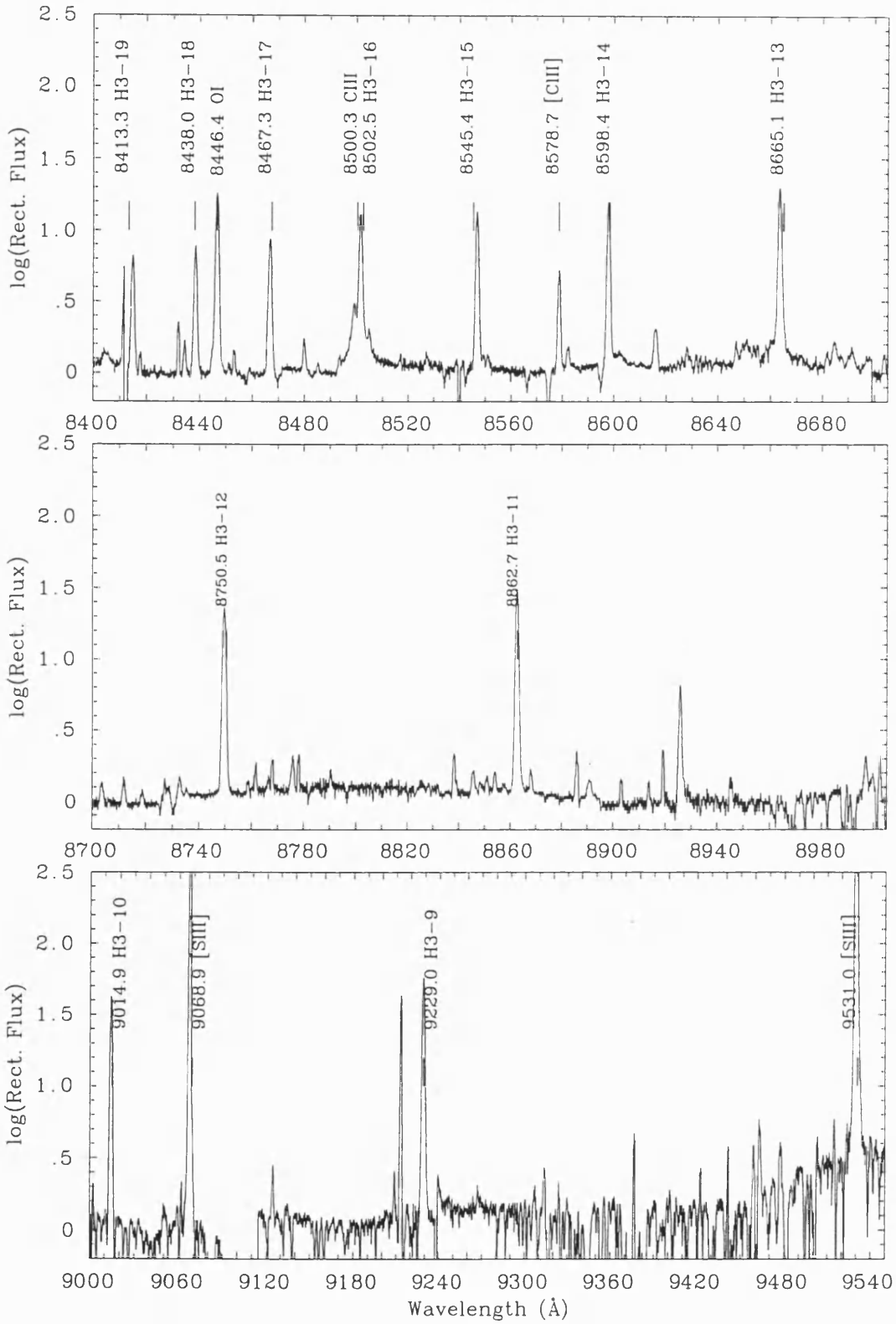

Figure E.8: The AAT spectrum of SwSt 1 between 8400 and 9550 Å

Publications

- O. De Marco, M.J. Barlow and P.J. Storey, *The WC10 Central Stars CPD-56°8032 and He 2-113: I. Distances and Nebular Parameters*, 1997, MNRAS, in press. Chapter 5.

- O. De Marco and P.A. Crowther, *The WC10 Central Stars CPD-56°8032 and He 2-113: II. Model Analysis and Comparison with Nebular Properties*, 1997, MNRAS, submitted. Chapter 6.

- O. De Marco, P.J. Storey and M.J. Barlow, *The WC10 Central Stars CPD-56°8032 and He 2-113: III. Wind Electron Temperature and Abundances*, 1997, MNRAS, submitted. Chapter 7.

- P.A. Crowther, O. De Marco and M.J. Barlow, *Quantitative Classification of WC Stars*, 1997, MNRAS, in press. Chapter 4.

- C.G. Clayton and O. De Marco, *The Evolution of the Final Helium Shell Flash Star V 605 Aql, from 1917 to 1997*, 1997, AJ, in press.

- G.H. Jacoby, O. De Marco, D.M. Sawyer, *The Velocity Field of the Old PN A 58 Measured with the DENSEPACK/WYNN Configuration*, in preparation.

- A. Jones, W.A. Lawson, O. De Marco, *The Light Variability Properties of the [WCL] Central Stars*, in preparation. Appendix A.

- O. De Marco, *The Planetary Nebula of the [WC10] Central Star M 4-18*, in preparation, Chapter 8.

- O. De Marco, P.A. Crowhter, M.J. Barlow and P.J. Srorey, *The life and miracles of SwSt 1* in preparation, Chapter 8.

- O. De Marco, M.J. Barlow and P.J. Storey, *The Winds of WC10 Central Stars of Planetary Nebulae*, 1996, Ap.Sp.Sci 238, 91.

- P.A. Crowther, O. De Marco, M.J. Barlow and P.J. Storey, *A Quantitative Analysis of the Prototype [WCL] Star CPD-56° 8032*, 1996, Ap.Sp.Sci 238, 119.

- O. De Marco, P.J. Storey and M.J. Barlow, *A Method for the Direct Determination of the Wind Electron Temperature of WC10 Central Stars of Planetary Nebulae*, 1996, ASP No. 96, 145.

- P.A. Crowther, O. De Marco, M.J. Barlow and P.J. Storey, *A Quantitative Analysis of the [WCL] Star CPD-56° 8032*, 1996, ASP No. 96, 149.

- O. De Marco, M.J. Barlow and P.J. Storey, *An Empirical Analysis of the Stellar Wind and Planetary Nebulae of the [WC10] central stars CPD-56° 8032 and He 2-113*, 1997, IAU 180, in press.

- O. De Marco and P.A. Crowther, M.J. Barlow and P.J. Storey, *Modelling the Stellar Winds of the [WC10] central stars CPD-56° 8032 and He 2-113*, 1997, IAU 180, in press.

- O. De Marco and P.A. Crowhter, *Quantitative Spectral Classification of Late WC Stars*, 1997, IAU 180, in press.